Studies
for the
ALICE Inner Tracking System Upgrade

Felix Reidt

European Organization for Nuclear Research (CERN)
and
Physikalisches Institut,
University of Heidelberg

A thesis submitted for the degree
Doctor of Natural Sciences
Heidelberg 2016

Dissertation
submitted to the
Combined Faculties for Natural Sciences and Mathematics
of the Ruperto-Carola University of Heidelberg, Germany
for the degree of
Doctor of Natural Sciences

put forward by

Felix Reidt (M.Sc. Physics)

born in Schwetzingen, Germany

Oral examination: April 28th, 2016

Studies
for the
ALICE Inner Tracking System Upgrade

Referees: Prof. Dr. Johanna Stachel
               Prof. Dr. Peter Fischer

Studies for the ALICE Inner Tracking System Upgrade

The ALICE experiment at the CERN LHC identifies D^0 mesons via secondary-vertex reconstruction and topological cuts to reduce the corresponding combinatorial background in heavy-ion collisions. The D^0 meson is produced promptly in initial, hard scatterings via the strong interaction or as feed-down from weakly decaying B hadrons. Within this thesis, a novel method for the separation of prompt and feed-down D^0 mesons using cut variations was implemented and applied to data from p–Pb collisions at $\sqrt{s_{NN}} = 5.02\,\text{TeV}$. The effectiveness of the secondary-vertex reconstruction strongly depends on the performance and in particular the pointing resolution of the Inner Tracking System. The upgrade of the ALICE Inner Tracking System for the Long Shutdown 2 of the LHC in 2019/2020 will significantly improve its vertex-reconstruction and tracking capabilities. It will be equipped with Monolithic Active Pixel Sensors manufactured using the Tower-Jazz 180 nm CMOS process on wafers with a high-resistivity epitaxial layer. In another part of this thesis, several pixel-chip prototypes of the ALPIDE architecture with in-pixel amplification and discrimination as well as in-matrix data reduction were characterised. The pALPIDE-2 prototype was measured to fulfil the requirements in terms of detection efficiency, fake-hit rate, position resolution and tolerance to irradiation with non-ionising energy loss.

Based on simulations modelling the tracking and vertex-reconstruction performance of the upgraded Inner Tracking System, the perspective of the feed-down separation using cut variations after the upgrade was assessed within this thesis.

Studien zum ALICE Inner Tracking System Upgrade

Das ALICE Experiment am CERN LHC identifiziert D^0-Mesonen durch Sekundärvertexrekonstruktion sowie topologische Auswahlkriterien, um den kombinatorischen Untergrund in Schwerionenkollisionen zu reduzieren. Diese D^0-Mesonen werden direkt in initialen, harten Interaktionen mittels starker Wechselwirkung oder in schwachen Zerfällen von B-Hadronen, sogenanntem Feed-Down, erzeugt. Als Teil dieser Dissertation wurde eine neuartige Methode zur Separation von direkt erzeugten und Feed-Down D^0-Mesonen basierend auf Variationen der Auswahlkriterien implementiert und auf Daten von p–Pb-Kollisionen bei $\sqrt{s_{NN}} = 5.02\,\text{TeV}$ angewandt.

Die Effektivität der Sekundärvertexrekonstruktion wird maßgeblich von der Leistungsfähigkeit des Inner Tracking Systems bestimmt. Das Upgrade des ALICE Inner Tracking Systems während des zweiten langen Wartungsstops des LHC in 2019/2020 wird dessen Vertex- und Spurrekonstruktion deutlich verbessern. Es wird aus Monolithischen Aktiven Pixel Sensoren bestehen, welche im TowerJazz 180 nm CMOS Prozess auf Wafern mit einer hochresistiven Epitaxieschicht hergestellt werden. Als Teil dieser Dissertation wurden mehrere Pixelchip-Prototypen, die basierend auf der ALPIDE-Architektur für das Inner Tracking System Upgrade entwickelt wurden, charakterisiert. Das Design dieser Pixelchip-Prototypen basiert auf In-Pixel-Verstärkung und -Diskriminierung sowie In-Matrix-Datenreduktion. Die charakterisierten pALPIDE-2 Prototypen erfüllen die Anforderungen hinsichtlich Detektionseffizienz, Rauschtrefferrate, Ortsauflösung und Strahlungshärte bei nicht-ionisierender Bestrahlung.

Als ein weiterer Teil dieser Dissertation wurde, basierend auf Simulationen, welche die Vertex- und Spurrekonstruktionseigenschaften des neuen Inner Tracking Systems beschreiben, die Verbesserung der Methode zur Feed-Down-Separation basierend auf Variationen der Auswahlkriterien studiert.

Contents

1. Introduction

The Standard Model is the very successful and well-tested theory of high-energy particle physics [1]. It combines the electromagnetic, the weak and the strong force employing locally gauge-invariant Quantum Field Theories (QFTs). The strong interaction part of the Standard Model is described by Quantum Chromodynamics (QCD) [1–3]. The peculiarity of QCD is its inherent SU(3) colour symmetry resulting in the self-interactions of gluons. The QCD coupling constant $\alpha_s(q^2)$ is running from strong coupling at small momentum transfer q^2 corresponding to large distances of bare colour charges to weak coupling at high q^2 and small distances. The weak coupling of bare colour charges at small distances is a distinct feature of QCD, called asymptotic freedom. The self-interaction of gluons, the number of active light-flavour quarks and the number of colours define the direction of the running of the strong coupling constant $\alpha_s(q^2)$. While quarks and gluons are only observed bound into nuclear matter such as protons and neutrons, the closer two partons (quarks or gluons) get, the weaker their attraction becomes. As a consequence, nuclear matter should be deconfined at very high temperatures or densities - the Quark-Gluon Plasma (QGP) [4, 5]. In the standard cosmological picture, this state of matter is assumed to be present from about 10 ps to 10 μs after the formation of the universe [6]. However, the evolution of the universe makes the cosmological QGP inaccessible. Hence, the method of choice is the study in the laboratory. In ultra-relativistic heavy-ion collisions as available at the CERN Large Hadron Collider (LHC) [7] the necessary extreme temperatures and densities are reached [8–10]. The main purpose of ALICE (A Large Ion Collider Experiment) [11] is the measurement of signatures and properties of the QGP. Moreover, also the LHC experiments ATLAS [12], CMS [13] and LHCb [14] study heavy-ion physics.

1.1. The Quark-Gluon Plasma

Although QCD has been proposed as the theory of strong interaction in 1973 [15, 16] and has been very successful in describing experimental data at high q^2 [17], there are open questions on very basic aspects. These concern the transition between the phase of confined and deconfined matter in the thermodynamic picture of QCD, the nature of confinement and QCD matter at high temperatures.

Below a critical temperature, QCD matter is described by hadronic degrees of freedom. In this phase, the fundamental QCD degrees of freedom, quarks and gluons, are confined into colour-neutral objects. The QGP state is assumed to be reached by a phase transition from colour-neutral objects into unbound quarks and gluons at the critical temperature [18–20]. A second phase transition, the chiral phase
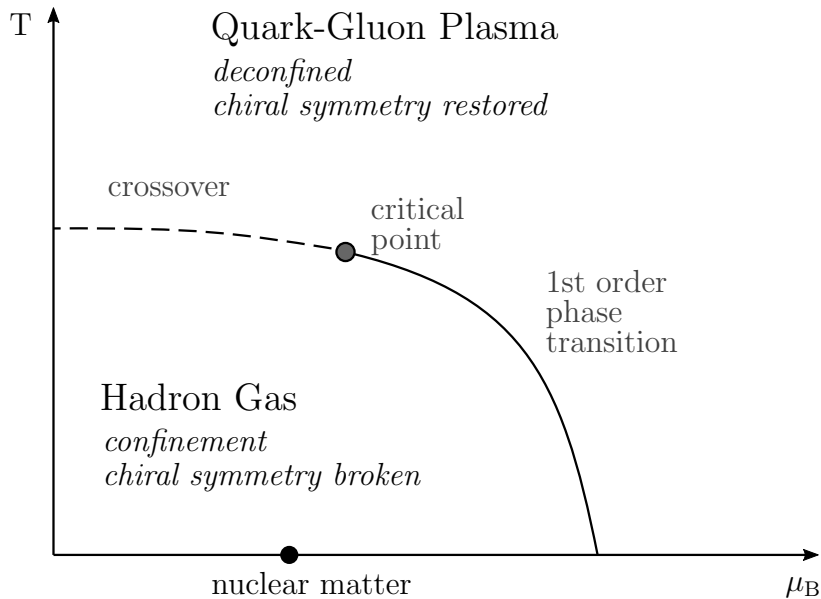
Figure 1.1.: Exemplary schematic phase diagram of strongly interacting matter.

transition, is connected to the mass generation mechanism of hadrons. At low temperatures the spontaneous symmetry breaking of the chiral symmetry of the strong interaction leads to the formation of a quark-antiquark condensate in the vacuum which generates the constituent quark masses. This effect is crucial for light quarks, whereas the mass of heavy quarks is dominated by the current masses. At high temperatures the vacuum condensate decreases and the masses of the quarks drop to their bare current-quark mass values. The underlying reason for this crossover phase transition is the restoration of approximate chiral symmetry[1].

Using the principles of thermodynamics and a phenomenological model like the MIT Bag model [22, 23], which describes confinement by the necessity of additional energy to release quarks and gluons from their bound state, a phase diagram for hadronic matter can be drawn. In such a phase diagram, the control parameters are the temperature T and the baryochemical potential[2] μ_B. Lattice QCD predicts the transition between QGP and hadronic matter at zero baryochemical potential to be a smooth crossover [9, 10]. For higher values of the baryochemical potential the nature of the phase transition between hadronic matter and QGP is not settled [24]. It could be a thermodynamic phase transition of first order or of second order instead of a crossover transition. This would imply the existence of a critical endpoint at which the properties of the phase transition change. A schematic drawing of a QCD phase diagram is shown in Fig. 1.1.

---

[1]In the limit of zero quark masses the chiral symmetry is exact. See e.g. [21] for a review.

[2]The baryochemical potential is a measure for the net baryon density and quantifies the energy necessary to add another baryon to the particle ensemble. This energy does not cover the energy required to create the particle itself.

Heavy-ion collisions at the LHC create systems at high temperatures and low net baryon densities [25]. In these systems the microscopic degrees of freedom are expected to interact strongly enough to constitute a system in local thermodynamic equilibrium. Right after the collision ($\tau < 1\,\mathrm{fm}/c$), the system is in a pre-equilibrium state and quickly thermalises locally [26, 27]. The following expansion can be well described by hydrodynamics [26, 28]. When temperature and density decrease, the phase transition to hadronic matter occurs. At the chemical freeze-out temperature, inelastic reactions cease and the hadron abundances are determined. Statistical models can describe these abundances over a wide range of centre-of-mass energies based on a single temperature and a single baryochemical potential [25, 29]. These models are based on a hadron-resonance gas described by a grand-canonical ensemble and are an established method to locate the system in the phase diagram at chemical freeze-out. After the chemical freeze-out, the momentum spectra are still subject to changes until the kinetic freeze-out is reached and elastic collisions no longer occur [6].

1.2. Signatures of the QGP

Due to confinement, only colour-neutral particles are observed in the detector. As a consequence and due to its short lifetime, the QGP can only be investigated by the hadrons remaining after the phase transition and hadronisation as well as other particles, which are not subject to the strong interaction. Therefore, a direct observation of the QGP is impossible. Furthermore, assuming a phase transition from a thermalised QGP has occurred, strongly interacting particles are frozen out as hadrons after the phase transition and do not carry any direct information about the QGP, but only about the moment of the freeze-out.

In the following, the most important signatures and measurements will be briefly introduced. In general, the observables are classified in bulk and single-particle observables. Bulk observables are based on all or the of majority particles in the detector and characterise the collision as a whole. By contrast, single-particle observables are based only on a certain particle species or underlying process. A more comprehensive summary can be found in [6] or [30].

A very important concept for characterising heavy-ion collisions is the centrality, which is a bulk observable providing a measure for the spatial overlap of the colliding nuclei. The volume of the interaction region depends on the displacement of the nuclei's centres in the plane perpendicular to the beam direction. This displacement is specified by the impact parameter b. Events with zero impact parameter b correspond to a centrality of $0\,\%$. On average the centrality of a collision is proportional to its multiplicity and can be determined using the abundance of particle production in a phase-space element. A smaller b leads to a larger interaction region and correspondingly to higher particle multiplicity. The exact approach for the

centrality determination in heavy-ion collisions in ALICE is described in [31]. Using a Glauber model [32, 33] one can furthermore deduce geometrical properties of the collision such as the number of participating nucleons N_{part}, which are involved in interactions, and the number of binary nucleon-nucleon collisions N_{coll}.

One of the first measurements published by the ALICE collaboration on Pb–Pb collisions is the pseudorapidity density of primary charged particles, which is also a bulk observable. In heavy-ion collisions at a centre-of-mass energy of $\sqrt{s_{\text{NN}}} = 2.76\,\text{TeV}$ per nucleon pair, in the $5\,\%$ most-central collisions it has been measured to be $\mathrm{d}N_{ch}/\mathrm{d}\eta = 1584 \pm 4(\text{stat}) \pm 76(\text{syst})$ at mid-rapidity [31]. The multiplicity per participating nucleon is with $8.3 \pm 0.4(\text{syst})$ about a factor 1.9 higher than in pp collisions at similar collision energies [31]. The size of the system at the kinetic freeze-out (radii of about $4\,\text{fm}$ to $8\,\text{fm}$) can be inferred using femtoscopy [34].

Another important bulk observable to study are the expansion dynamics of the system. Due to a pressure gradient, the system expands during the cool-down. Collective flow [28] is an observable that provides experimental information on the equation of state and the transport properties of the system. The asymmetric overlap of the colliding nuclei in non-central collisions leads to e.g. the so-called anisotropic flow (v_2). Recently, fluctuations in the initial state have been included into the hydrodynamical calculations improving the description of triangular flow (v_3) and higher harmonics. Measurements by ALICE confirm that the expansion dynamics can be described by nearly ideal hydrodynamics [35].

A further important probe are direct photons which carry information on the initial value and the space-time evolution of the temperature in the thermalised medium created in heavy-ion collisions [36]. Direct photons are photons not originating from hadron decays. In an exponential fit to the low-p_{T} part of the direct photon spectrum in Pb–Pb collisions at $\sqrt{s_{NN}} = 2.76\,\text{TeV}$ the inverse slope parameter is found to be $296 \pm 12(\text{stat}) \pm 40(\text{syst})\,\text{MeV}$ [37]. Contributions from various stages in the space-time evolution of the thermalised medium to the direct photon spectrum and a blue shift due to radial flow complicate the interpretation of the fit result as a temperature. However, it indicates the presence of temperatures above the phase transition and can be used to infer the initial temperature using assumptions on the expansion dynamics of the system [38].

Furthermore, partons which are produced in initial, hard scatterings interact with the medium via inelastic processes [39, 40] (medium-induced gluon radiation) and elastic processes [41, 42] (collisional energy loss). The nuclear modification factor R_{AA} is an observable comparing heavy-ion collisions to pp collisions. It is defined as the ratio of particle production measured in nucleus-nucleus (AA) collisions to that expected from incoherent superposition of pp collisions, here as function of p_{T}:

$$R_{\text{AA}} = \frac{1}{\langle N_{\text{coll}} \rangle} \frac{\mathrm{d}N_{\text{AA}}/\mathrm{d}p_{\text{T}}}{\mathrm{d}N_{\text{pp}}/\mathrm{d}p_{\text{T}}} \ . \tag{1.1}$$

The corresponding scaling factor is the average number of binary nucleon-nucleon collisions $\langle N_{\text{coll}} \rangle$ obtained using the Glauber model [32, 33].

In absence of a QGP and so-called Cold Nuclear Matter (CNM) effects, it is expected that the R_{AA} is equal to unity. These CNM effects are a consequence of the presence of a nucleus instead of a bare proton and are not related to deconfinement. CNM effects can be studied by comparing p–Pb collision and pp collision measurements. An important effect is the modification of the parton density of the incoming hadrons by shadowing or saturation which can be described using modified Parton Distribution Functions (PDFs) [43] or the Colour Glass Condensate (CGC) effective theory [44], respectively. Further CNM effects under discussion are the energy loss of the produced colour-dipole [45] in the initial and final states and a separate treatment of the Cronin effect [46] due to multiple scattering [45, 47]. The measurement and understanding of CNM is crucial for the interpretation of the R_{AA}. A recent review of CNM effects can be found in [48].

1.3. Heavy Flavour Probes

Assuming a QGP temperature of the order of a few hundred MeV at LHC [37], mainly light quark pairs ($u\bar{u}$, $d\bar{d}$, $s\bar{s}$) at low p_{T} can be thermally produced. The thermal production of heavy quarks like charm (c) and beauty (b) quarks is on the other hand heavily suppressed due to their large masses of about $1.3\,\text{GeV}/c^2$ and $4.5\,\text{GeV}/c^2$ [1], respectively. Heavy quarks are dominantly[3] produced during the initial, hard interactions of the nucleons before the formation of the QGP. Due to the minimum virtuality Q^2 needed to produce a quark-antiquark pair, these hard processes take place on a time scale $\Delta t \sim 1/2m_{c(b)} \sim 0.07(0.02)\text{fm}/c$ for c(b) quarks. According to recent model-dependent estimates [51], the formation time of the QGP is similar or slightly larger with about $0.3\,\text{fm}/c$. Additionally, the masses of c and b quarks and respective q^2 are large compared to Λ_{QCD}, allowing perturbative calculations of their production cross sections. Moreover, their masses are still small enough to let them significantly interact with their environment. As a consequence they are sensitive to the properties of the medium. The dependence of the energy loss in a strongly interacting medium on the parton nature (quark/gluon) and the parton mass could reveal insights into the underlying mechanism. In the experiment, hadrons are used to probe the partonic energy loss. At LHC energies, pions up to a few tens of GeV/c in p_{T} are mainly produced from gluon fragmentation. The comparison of the nuclear modification factors of hadrons with charm (R_{AA}^{D}) and beauty (R_{AA}^{B}) with that of pions (R_{AA}^{π}) was predicted to show an ordering pattern like $R_{\text{AA}}^{\pi}(p_{\text{T}}) < R_{\text{AA}}^{\text{D}}(p_{\text{T}}) < R_{\text{AA}}^{\text{B}}(p_{\text{T}})$ [52–57]. However, recent results as shown in Fig. 1.2, show an equal suppression of the hadrons containing light and charm quarks

---

[3]Depending on the exact initial temperature of the QGP partonic transport model calculations predict sizeable thermal c quark production [49, 50].
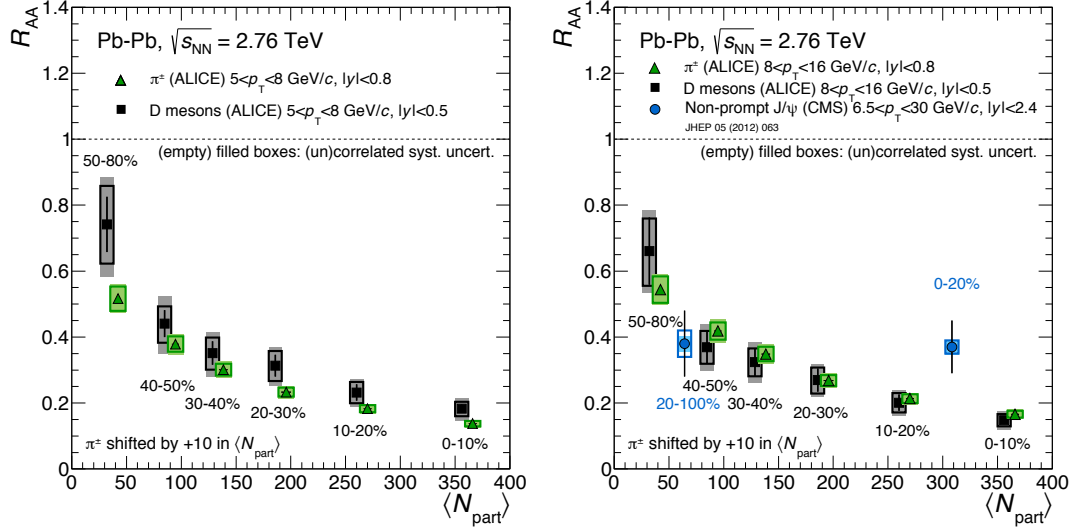
Figure 1.2.: Comparison of the D meson R_{AA} and the charged pion R_{AA} [62] in $5 < p_T < 8\,\text{GeV/c}$ (left) and $8 < p_T < 16\,\text{GeV/c}$. The right panel additional contains the R_{AA} of non-prompt J/Ψ mesons in $6.5 < p_T < 30\,\text{GeV/c}$ measured by the CMS Collaboration [59]. This figure has been taken from [58].

in the p_T regime of $5\,\text{GeV}/c$ to $16\,\text{GeV}/c$ [58]. By contrast, non-prompt J/Ψ mesons originating from B meson decays seem to be less suppressed [59] in central collisions. However, it has to be noted that the interpretation of the nuclear modification of different particles species is not straightforward. The R_{AA} depends on the input spectra and fragmentation functions which are expected to be different for charm quarks and light quarks or gluons [60]. Furthermore, the pion yield could contain a sizeable contribution from soft production processes up to a p_T of about $2\,\text{GeV}/c$ to $3\,\text{GeV}/c$ due to the strong radial flow at LHC energies [61]. A more comprehensive discussion on the interpretation of the R_{AA}^D in comparison to the R_{AA}^π can be found in [61]. Their properties make heavy-flavour quarks a particularly suitable probe for the underlying mechanisms of in-medium energy loss. A recent review on the current understanding on heavy-flavour production and energy loss can be found in [48].

In order to obtain a better and more quantitative understanding, however, more precise measurements are needed. In addition to the prompt production of D^0 mesons in initial hard scatterings, a substantial fraction D^0 mesons originates from B mesons decays [63]. For a more precise measurement, these contributions need to be disentangled. The separation of prompt and feed-down D^0 mesons allows to study in addition to the energy loss of c quarks using prompt and that of b quarks using feed-down D^0 mesons. With the current ALICE detector, however, prompt and feed-down D^0 meson production is difficult to distinguish. With regard to this aspect, the upgrade of the ALICE Inner Tracking System (ITS) [64] will lead to significant progress. The improved pointing resolution as well as tracking efficiency and p_T

resolution at low p_T will improve the secondary and tertiary vertex reconstruction used to measure charm and beauty decays in particular at small displacement and low p_T. Furthermore, the D^0 meson is the lightest charmed meson having the largest production cross sections as well as the largest branching ratio in B hadron decays. Its decay into two charged tracks leads to a high reconstruction efficiency compared to other charmed mesons involving more decay particles.

1.4. Thesis Outline

This thesis is organised as follows. Chapter 2 introduces the D^0 meson along with its production mechanisms and decay properties. The technical introduction to the current ALICE detector is given in Ch. 3. The new analysis method for the separation of prompt and feed-down D^0 mesons using variations of topological cuts implemented within this thesis is described in Ch. 4. The performance of this analysis method is shown on the basis of p–Pb data. In Ch. 5, the ALICE Inner Tracking System upgrade is introduced. Within this thesis, small-scale and full-scale Monolithic Active Pixel Sensor (MAPS) prototypes for the ALICE ITS Upgrade were characterised. The corresponding characterisation results based on the analysis of measurements in the laboratory and at test beam are discussed in Ch. 6. The physics performance for the separation of prompt and feed-down D^0 mesons after the upgrade of the ITS assessed within this thesis is presented in Ch. 7. Chapter 8 summarises the results and shows prospects for future measurements after the installation of the upgraded ITS.

Additionally, a readout system for small-scale analogue-output and digital-output MAPS prototypes was designed, implemented and commissioned as part of this thesis (cf. App. C).

2. The D^0 Meson

In this chapter, the D^0 meson and its general properties are summarised. The production mechanisms in the case of prompt and feed-down production are compared. Furthermore, the most important decay mode of the D^0 meson is presented. Additionally, the theoretical background for production cross section calculations is outlined.

The valence quarks of the D^0 are a c and $\bar{u}$ and its rest mass m_{D^0} was measured to be $(1864.86 \pm 0.13)\,\text{MeV}/c^2$ [1]. With about $(122.9 \pm 0.4)\,\mu\text{m}$, its mean proper decay length $c\tau$ is short compared to other weakly decaying particles like the D^+ and B^0 with $(311.8 \pm 0.2)\,\mu\text{m}$ and $(457.2 \pm 2.7)\,\mu\text{m}$ [1], respectively, leading to a more challenging determination of decay vertices from D^0 at low p_T.

2.1. D^0 Meson Production

The major fraction of c quarks at the LHC is produced in initial, hard scatterings via strong interactions [65, 66]. The resulting D^0 mesons are called prompt D^0 mesons. A non-negligible amount of D^0 mesons is, however, produced in weak decays of B mesons. This fraction of the total production constitutes the so-called non-prompt or feed-down contribution to the D^0 spectrum.

2.1.1. Prompt D^0 Production

Example Feynman diagrams for the prompt production of heavy quarks, the so-called pair creation at Leading Order (LO), gluon splitting and flavour excitation, both at Next-to-Leading Order (NLO) are shown in Fig. 2.1 [3, 67].
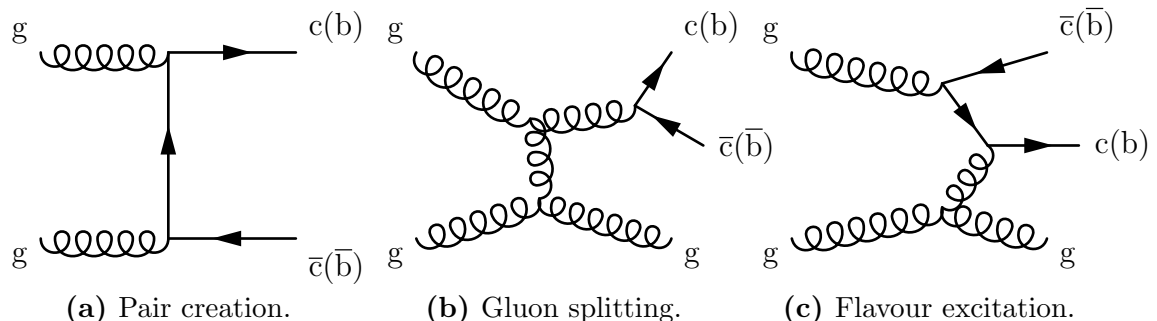

(a) Pair creation.   **(b)** Gluon splitting.   **(c)** Flavour excitation.

Figure 2.1.: Example Feyman diagrams for the production of charm and beauty quarks at the LHC.

In pp collisions, the production of charmed hadrons can be calculated using perturbative Quantum Chromodynamics (pQCD) based on collinear factorisation using Eq. 2.1 [3]:

$$\sigma_{\text{p+p}\rightarrow\text{D}+X} = \sum_{i,j,k} \int \mathrm{d}x_1 \mathrm{d}x_2 \mathrm{d}z \; f_i(x_1, \mu_{\text{F}}) f_j(x_2, \mu_{\text{F}})$$
$$\times \left| \mathcal{M}_{ij\rightarrow k} \left(\mu_f, \alpha_{\text{s}}(\mu_{\text{R}}), m_{\text{c}} \right) \right|^2 \times D_k^{\text{D}}(z) \tag{2.1}$$

The interacting partons in the colliding protons are denoted by i and j. The Parton Distribution Functions (PDFs) $f(x, \mu_{\text{F}})$ depend on the Björken-x of the partons x_1 and x_2 as well as on the factorisation scale μ_{F}. The actual pQCD matrix element $\mathcal{M}_{ij\rightarrow k}$ for the production of the charm quark k is a function of μ_{F}, the strong coupling constant α_{s} which in turn depends on the renormalisation scale μ_{R}, and the mass of the charm quark m_{c}. The non-perturbative fragmentation function $D_k^{\text{D}}(z)$ describes the probability of the quark k to hadronise to a D meson and is a function of the relative four-momentum z of the charm quark and the D meson.

FONLL calculations [68, 69] reproduce the p_{T} dependence of the cross sections for the production of heavy quarks measured at RHIC, the Tevatron and the LHC [65, 66]. The FONLL framework is based on fixed next-to-leading order (NLO) QCD calculations which are matched with all-order resummation to next-to-leading logarithm (NLL) in the limit where the p_{T} of the heavy-quark is much larger than its mass. The non-perturbative fragmentation functions are obtained from the analysis of data acquired in e^+e^- annihilation [70]. The default PDF set is CTEQ6.6 [71]. A summary of theoretical predictions for charm and bottom production at the LHC including FONLL calculations and a comparison to measurements can be found in [65, 66].

In Pb–Pb collisions the production of heavy quarks is expected to scale with the average number of binary (nucleon-nucleon) collisions $\langle N_{\text{Coll}} \rangle$. Using the Glauber model [32, 33] one can obtain the nuclear overlap function $\langle T_{\text{AA}} \rangle$ which provides the appropriate scaling factor. A cross section scaled using $\langle T_{\text{AA}} \rangle$, however, does not contain corrections for in-medium energy loss or possible changes in the fragmentation. Furthermore, as mentioned in Ch. 1, so-called Cold Nuclear Matter (CNM) effects due to the presence of the nucleons in a nucleus have to be taken into account.

2.1.2. Feed-Down from B Mesons

About $56\,\%$ of the B^0 and about $86\,\%$ of the B$^+$ decays involve a D^0 or its charge conjugate [1]. The contribution from B$_s^0$ meson decays is negligible due to the combination of branching ratio and fragmentation. The dominant Feyman diagrams for B meson decays are the spectator diagrams in which the valence b quark undergoes a transition to another quark type under emission of a W boson and the
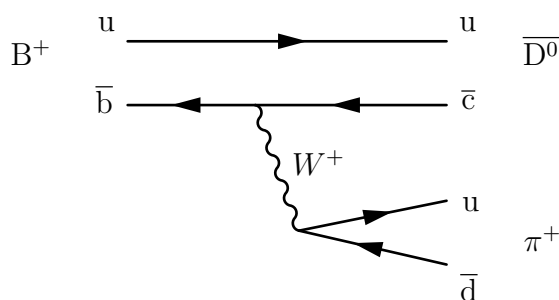
Figure 2.2.: Example spectator-type Feynman diagram for the B$^+$ → $\overline{\text{D}^0}$ π^+ decay.

other valence quark is only spectating as shown in Fig. 2.2 [72]. In these tree-level decays, the transition of the b quark to either an on-shell c quark or an on-shell u quark is allowed. The transition amplitude, given by the Cabibbo-Kobayashi-Maskawa (CKM) matrix [1, 73, 74], is about a factor ten larger from a b quark to c quark than to a u quark [1]. In case of a B$^+$ decay, the spectator is a u quark, which has automatically the right colour and allows to form D^0 meson at tree level as shown in Fig. 2.2. In a B^0 meson, which consists of a $\overline{\text{b}}$ and d quark, the necessary u quark needs to originate from the W^+-vertex. Hence, this diagram is colour suppressed reducing the branching ratio into D^0 in those decays.

Quite often, instead of direct production of a D^0 meson, an exited D* meson is formed which decays via the emission of a photon or a pion to the ground-state D^0 [1]. While the D*(2007) always decays into a D^0 and π^0 or a photon, the D*(2010), D$_1$(2420)^0, D$_2^*$(2460)^0 and D$_2^*$(2460)$^\pm$ can decay into both a neutral or a charged D meson [1].

Due to the large probability of a B meson decaying into a D^0 meson, non-prompt D^0 mesons are an excellent possibility to study the energy loss of b quarks. At LHC energies, about 10 % of the D^0 are estimated to originate from weakly decaying B hadrons [63]. The downside of this measurement, however, is the variety of decay channels containing a D^0 meson due to the large mass difference of the B hadron and the D^0 meson of more than $3\,\text{GeV}/c^2$. Only a few of these decay channels have a branching ratio of 1 % or slightly larger.

In addition to that, B meson decays feature high decay-particle multiplicity. A study of the charged track multiplicity in B meson decays of the CLEO Collaboration lead to a mean value of $5.36 \pm 0.01^{+0.11}_{-0.08}$ for a single B meson [75]. This multiplicity can also be attributed to the mass difference of the B meson and its decay particles, allowing additional gluon radiation producing quark-antiquark pairs or the decay into excited D mesons. In Fig. 2.3 (left), the number of stable decay particles in addition to the D^0 daughters are shown. Although the distribution peaks at four B meson decay particles in addition to the D^0, decays with at least 15 additional particless are frequent enough to be of importance for the efficiency determination. The contributions from B$_s^0$ mesons and Λ_b baryons are small compared to the B^0 and B$^+$ mesons. The large spread in the decay multiplicity leads to a huge variation
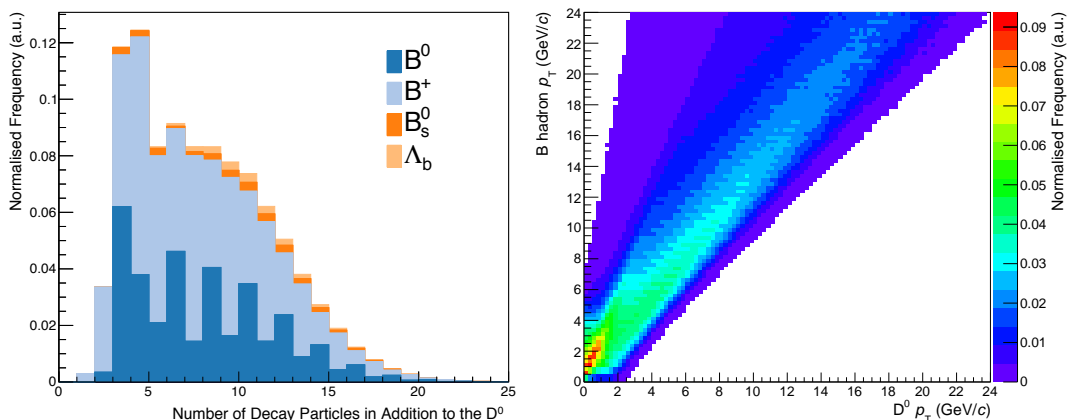
Figure 2.3.: Left: distribution of B hadron decay particles. Right: correlation of B hadron p_T with the D^0 p_T. Both plots obtained using PYTHIA6 [76] MC simulations.
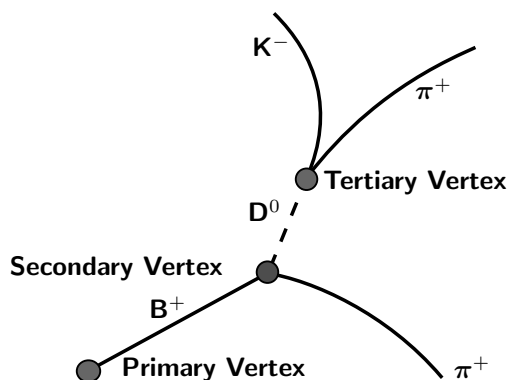
Figure 2.4.: Triple vertex topology of a $B^+ \to \overline{D^0}\pi^+$ as an example decay in the xy or $r\varphi$-plane. Distances and curvatures are not to scale.

in the momentum carried by the D^0 meson originating from the B meson decay. On the other hand, especially for the B meson decays with many particles, there is a good chance to associate one of these particles to the vertex where also the D^0 meson originates from. This is a further potential measure to identify feed-down D^0 mesons.

The mass difference of the B hadron and the D^0 meson also explains the moderated correlation of the B hadron p_T with the D^0 p_T in feed-down production (cf. Fig. 2.3, right). A wide range of B hadron p_T contributes to the same D^0 p_T. Additionally, in order to be sensitive to B hadrons produced at rest, one needs to measure D^0 mesons down to less than $2\,\text{GeV}/c$ in p_T.

The full reconstruction of a B^+ meson with an identification of all decay particles would be possible for the channel $B^+ \to \overline{D^0}\pi^+$ (cf. Fig. 2.2). The branching ratio of only $(4.81 \pm 0.15) \times 10^{-3}$ [1] requires a significantly larger data sample than an inclusive measurement using feed-down D^0 mesons.

Such an inclusive measurement of feed-down D^0 mesons can be achieved by exploiting the three-vertex topology of the decay chain with the vertices of the primary interaction, the B meson decay and the D^0 meson as depicted in Fig. 2.4. While prompt D^0 mesons point directly to the primary vertex, feed-down D^0 mesons point to the displaced B hadron decay vertex instead of the primary vertex.

2.2. The $D^0 \to K^- \pi^+$ Decay and Kinematics

The D^0 meson decays weakly in mainly two decay particles with a total branching ratio $BR = (70 \pm 6)\,\%$ [1]. The hadronic decay mode with the largest branching ratio is $D^0 \to K^- \pi^+$ with $(3.88 \pm 0.05)\,\%$.

As shown in Fig. 2.5, at low D^0 p_T the decay kinematics are governed by the Q value of the decay defined as the difference of the D^0 and the sum of the K and π mass. In this D^0 p_T regime, the momentum distribution of the decay particles in the laboratory frame is not flat. Below about $2\,\mathrm{GeV}/c$ in D^0 p_T, cases in which one of the decay particles is emitted in the opposite direction of the D^0 momentum vector, lead to a very asymmetric p_T of the decay particles in the laboratory frame. This contributes to the shape of the decay-particle momentum distribution which shows sizeable amount of decay particles below $0.5\,\mathrm{GeV}/c$. Together with the steep slope of the D^0 spectrum, this leads to difficulties in the reconstruction and the estimation of acceptance and efficiency especially as a function of p_T in this D^0 p_T regime. At about a D^0 p_T of $2\,\mathrm{GeV}/c$, the boost of the D^0 meson starts dominating the momentum distribution of the daughter particles in the laboratory frame. The momentum distribution of the D^0 daughters becomes flatter with increasing p_T.
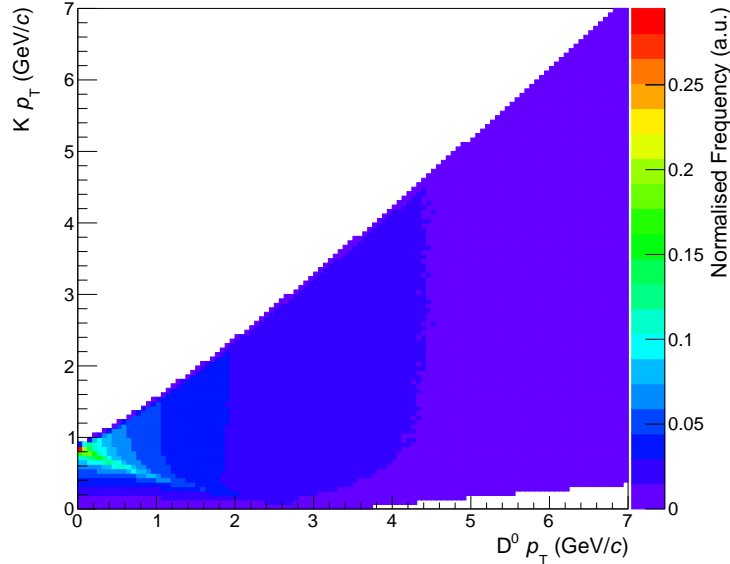
Figure 2.5.: Daughter kaon p_T versus the mother D^0 p_T, based on a uniform D^0-p_T distribution, obtained using PYTHIA6 [76].

3. The ALICE Detector

The ALICE experiment [11] at the CERN LHC [7] is focused on heavy-ion collision. The LHC is a hadron accelerator and collider with superconducting magnets designed for a maximum centre-of-mass energy of 14 TeV in pp collisions. In the design of ALICE, large emphasis was put on its capabilities to cope with high particle densities as present in central Pb–Pb collisions. This design goal lead to a highly granular detector. Furthermore, the importance of bulk observables and thus low-p_T particles lead to a material budget in the central region which is the lowest among the four main LHC experiments. A particle in ALICE has to traverse 11-13% of radiation length until it leaves the Time-Projection Chamber (TPC) [77] in contrast to about 40% before the calorimeters of ATLAS [78] and CMS [13] at mid-rapidity. The low material is achieved by using the TPC, a large gas detector, for tracking. On the other hand, the TPC drift time of about 100 µs [79] leads to a limitation in interaction rate. A solenoidal magnet with a B-field of 0.5 T allows tracking at lower p_T than ATLAS [78] and CMS [13] which use fields of 2 T and 3.8 T, respectively. The combination of low material budget and magnet field allow ALICE to track particles down to a p_T of about 80 MeV/c using only the Inner Tracking System (ITS) [80]. In addition to that, ALICE exploits a variety of Particle Identification (PID) techniques up to about 20 GeV/c in p_T [80]. These features of ALICE allow for a proton-proton physics programme of its own, which is complementary to the one of ATLAS and CMS.

1. ITS
2. FMD, T0, V0
3. TPC
4. TRD
5. TOF
6. HMPID
7. EMCAL
8. PHOS
9. MAGNET
10. ACORDE
11. ABSORBER
12. MUON TRACKER
13. MUON WALL
14. MUON TRIGGER
15. DIPOLE MAGNET
16. PMD, V0
17. ZDC

a. ITS SPD Pixel
b. ITS SDD Drift
c. ITS SSD Strip
d. V0 and T0
e. FMD

Figure 3.1.: ALICE detector cut view, adapted from [11].

The ALICE detector layout is shown in Fig. 3.1. The ALICE detector subsystems can be subdivided into three groups: the central barrel, forward detectors and the

muon arm. The central-barrel detectors cover the pseudorapidity range $|\eta| < 0.9$ and most of them cover the full azimuth. The forward detectors are located outside the central-barrel acceptance at $|\eta| > 0.9$. The muon arm (items 11 to 15 in Fig. 3.1) has a pseudorapidity acceptance of $-2.5 < \eta < -4.0$.

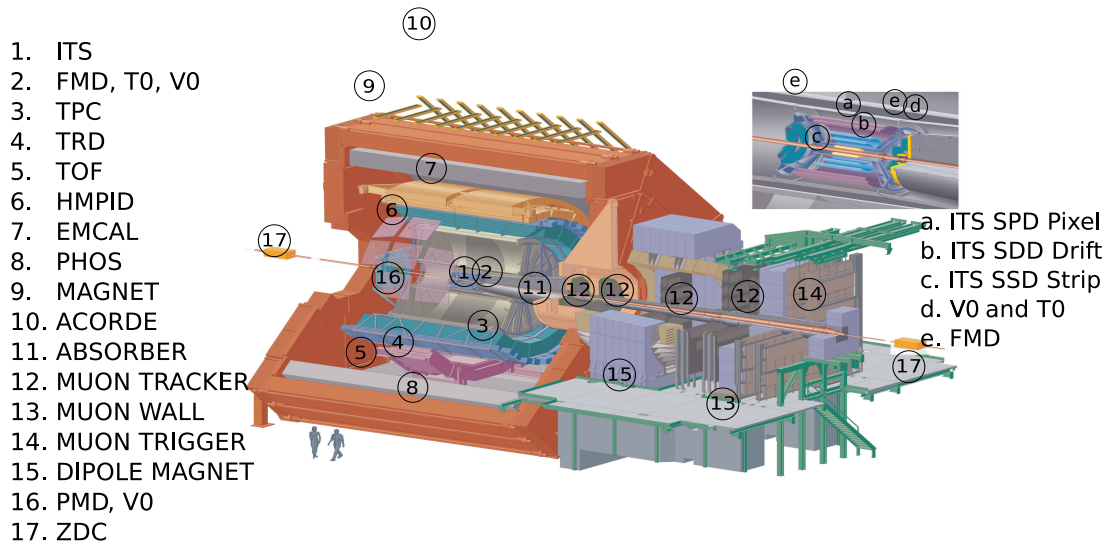The physics analysis carried out within the course of this thesis was based on data acquired using the central barrel. The detector systems relevant as well as the overall tracking and PID capabilities of the central barrel are described in more detail below. Additional information on the detector systems themselves or their performance during the first years of operation at the LHC can be found in [11] and [80], respectively.

3.1. Detector System Overview

Inner Tracking System (ITS)

The current ITS consists of six cylindrical detector layers at radial positions ranging from 4 cm to 43 cm. A combination of three different silicon detector technologies is deployed. In order to cope with the high occupancies present close to the interaction point, the innermost two layers are silicon pixel sensors, called the Silicon Pixel Detector (SPD). The pixels of the SPD feature a rectangular shape of $50\,\mu\mathrm{m} \times 425\,\mu\mathrm{m}$ in $r\varphi \times z$ resulting in intrinsic resolutions of $12\,\mu\mathrm{m}$ and $100\,\mu\mathrm{m}$ in the $r\varphi$ and z-direction, respectively [81]. The material budget is about $1.14\,\%\,\mathrm{X_0}$ per layer. The readout electronics of the SPD provide a trigger signal which fires if at least one pixel of the readout chip indicates a hit [82, 83]. The middle two layers are made of silicon drift detector arrays (SDD) having a material budget of $1.13\,\%\,\mathrm{X_0}$ and $1.26\,\%\,\mathrm{X_0}$. The outermost two layers are Silicon Strip Detectors (SSDs) both featuring a material budget of only $0.83\,\%\,\mathrm{X_0}$. The analogue readout of the SDD and SSD detectors together provide four energy loss samples for PID.

Being the detector closest to the interaction point, the ITS provides tracking for low-p_T tacks and pointing resolution towards the interaction point. The pointing resolution is important for the secondary-vertex reconstruction. The capabilities in resolving secondary vertices are fundamental for the measurement of heavy-flavour hadrons based on their decay topologies. The track points close to the interaction point furthermore increase the lever arm improving the p_T resolution in the combined central-barrel tracking.

Time Projection Chamber (TPC)

The Time-Projection Chamber (TPC) is the main tracking device of the ALICE central barrel. Its active volume extends from 0.85 m to 2.5 m and from $-2.5\,\mathrm{m}$

to 2.5 m in r and z direction, respectively. It covers the pseudorapidity interval $|\eta| < 0.9$ and the full azimuth and its central electrode splits its volume of 88 m^3 into halves. The readout is located at end caps using Multi-Wire Proportional Chambers (MWPCs) and with a drift voltage of 100 kV, the drift time is about 100 μs for electrons. This value is large compared to interaction rates of several 100 kHz interaction rate in pp collisions [80] leading to multiple events in the drift volume. 159 pad rows in radial direction can provide track points and energy-loss information for PID. For the operation at high particle multiplicities in heavy-ion collisions, the top priority is the reduction of space-charge effects. In the ALICE TPC a gating grid in front of the MWPCs is used to limit the ion back flow from the amplification region to the drift region as the majority of ions is generated in the amplification region. The maximum opening frequency of the gating grid of about 3.5 kHz is determined by the time needed to collect all ions in the amplification region and represents the limiting factor in the TPC in terms of readout rate in pp collisions [84]. In heavy-ion collisions, the bandwidth of the readout electronics is also a limiting factor. While the size of a typical pp event is usually less than 1 MByte, a fully central heavy-ion collision can amount to about 70 MByte compared to few hundred kByte from the ITS [80]. The material budget of the TPC including the gas is only about 3.5 % X$_0$ at $\eta \approx 0$ [79].

Time-Of-Flight Detector (TOF)

The Time-of-Flight detector (TOF) provides PID based on the measurement of the time of flight of the particles from the interaction point to the detector itself. It consists of a large array of Multi-gap Resistive Plate Chambers (MRPCs). It is located at a radius of 3.7 m to 4.0 m covering the full azimuth and a pseudorapidity range $|\eta| < 0.9$. The start time for the TOF can be determined either using the T0 Cherenkov counters or based on a self-calibrated approach using the earliest arrival time of particles after the collision. The time resolution is about 80 ps for pions with about 1 GeV/c in p_T in central and semi-peripheral heavy-ion collisions [85]. The granularity of the detector allows to keep the occupancy below 15 % even in central heavy-ion collisions at 2.76 TeV.

3.2. Triggering System and Data Acquisition

In ALICE the Central Trigger Processor (CTP) is responsible for the trigger handling. The triggering is based on a three level scheme. The first level (L0) is generated based on observables generating fast signals such as the signal height in the plastic scintillators of V0 or the T0 Cherenkov counters within 0.9 μs after the interaction. Input signals with higher latency due to computing time or propagation times are

taken into account at L1 level (about 6.5 µs). The L0 and L1 decisions are propagated to the detectors with a delay of about 0.3 µs to trigger the buffering of event data in the detector front-end electronics. The third level (L2) decision is taken about 100 µs after the interaction corresponding to the TPC drift time. Upon a L2 trigger, the detectors send their data to the ALICE Data Acquisition system (DAQ) and, in parallel, to the High-Level Trigger system (HLT). Currently, all positive L1 trigger decisions are succeeded by a L2 trigger. There is, however, the possibility of implementing a past-future-projection in order to limit pile-up at L2 level. In addition to the information from the trigger detectors, CTP does also use information on the LHC bunch filling scheme to suppress background. The HLT can subsequently filter and compress the data from events with an L2 trigger.

In all collision modes (pp, p–Pb, Pb–Pb), various triggers have been deployed [80]. In general, minimum-bias triggers were used for data-taking to obtain a basic data sample. In addition to that in Pb–Pb also centrality triggers derived from the signal height in the V0 scintillators were used to enhanced the sample of semi-central and central events. On top of these samples triggers for rare probes and on general event properties like multiplicity are used. An overview of the major ALICE triggers can be found in [80].

3.3. Vertex and Track Reconstruction

In this section, the vertex and track reconstruction are briefly outlined. A detailed description can be found in [80].

Tracking and vertex reconstruction are carried out in several steps as shown in Fig. 3.2. The clustering is performed separately for all detectors. A preliminary vertex is searched based on track segments using clusters in the two layers of the SPD.
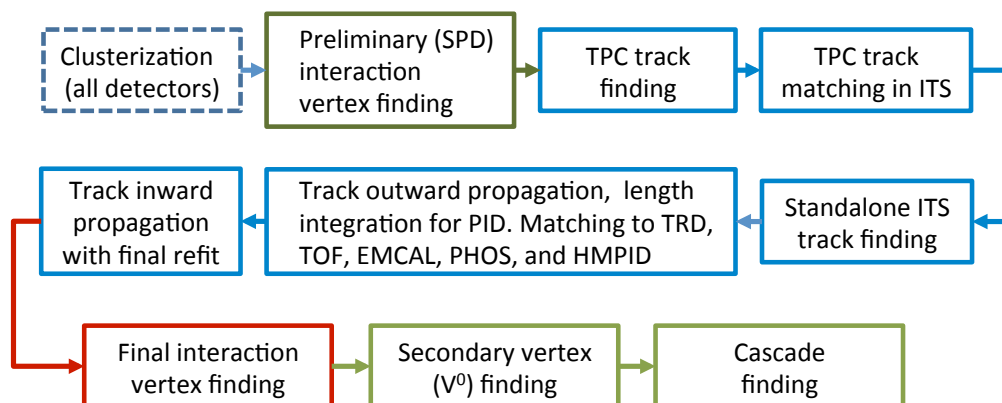

Figure 3.2.: Event reconstruction flow, taken from [80].

The tracking itself is performed using a Kalman filter [86, 87] which provides simultaneous track finding and fitting. It follows an inward-outward-inward scheme [88, 89]. Starting with short track candidates called seeds found at larger radii in the TPC, it proceeds radially inwards. Reaching the inner TPC wall, the algorithm continues by matching clusters in the ITS to extend the tracks towards the preliminary vertex. In order to extend the tracking to lower p_T, standalone ITS tracks are searched using the remaining clusters in the ITS beginning at the innermost layer proceeding radially outwards. Tracks traversing the dead regions of the TPC or below its p_T cut-off can be found this way. In the next step, the standard tracking is then restarted from the innermost ITS layer outwards. During this step the particle is assigned with a most-probable mass which is determined based on the TPC energy-loss information obtained for the track. During the outward propagation the track is prolonged by track points of the TRD, TOF, EMCAL, PHOS and HMPID which are, however, currently only used to match the PID information to a track but not for fitting. After the track reconstruction is completed, the primary vertex is recalculated based on the track information. Then, secondary vertices and cascade decays are searched.

The TPC track-finding efficiency peaks at a value of about $85\,\%$ at roughly $0.7\,\text{GeV}/c$ to $0.8\,\text{GeV}/c$ [80]. Below $0.5\,\text{GeV}/c$ the efficiency drops due to energy loss in the detector material. The p_T dependence above the peak is dominated by the loss of clusters in the dead zones of the TPC. The p_T resolution for tracks using combined ITS and TPC fitting is about 1% for tracks up to a momentum of a few GeV/c [80].

The resolution of the impact parameter in the xy-plane, $d_{0,xy}$, is shown in Fig. 3.3. The contribution from the primary-vertex resolution leads to a collision-system dependence (cf. Fig. 3.3, left). In Pb–Pb the higher charged-particle multiplicity leads to better primary vertex resolution and in turn to a better $d_{0,xy}$ resolution [80]. Furthermore, the contribution of a single track is less significant in events with higher multiplicity reducing the influence of tracks originating from a decay vertex which are erroneously assigned to the primary vertex. At a track p_T of $1\,\text{GeV}/c$ the $d_{0,xy}$ resolution is about $70\,\mu\text{m}$. Below a p_T of $1\,\text{GeV}/c$, the $d_{0,xy}$ resolution increasingly depends on the particle species as shown in the right part of Fig. 3.3. The $d_{0,xy}$ resolution for identified particles is well described by Monte-Carlo simulations. The resolution of the z distance $d_{0,z}$ is shown in Fig. 3.4. Due to the larger pixel pitch in z-direction, the $d_{0,z}$ is about $170\,\mu\text{m}$ at a p_T of $1\,\text{GeV}/c$.

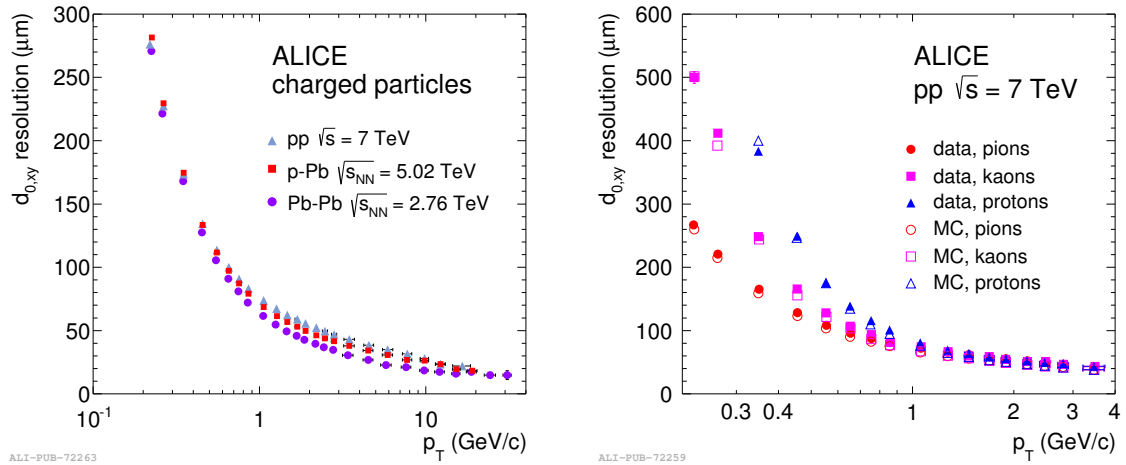**Figure 3.3.:** Resolution of the transverse distance to the primary vertex for all charged ITS–TPC tracks in different collision systems (left) and for identified particle ITS–TPC tracks in pp collisions (right). The resolution is not corrected for the vertex resolution. Taken from [80].
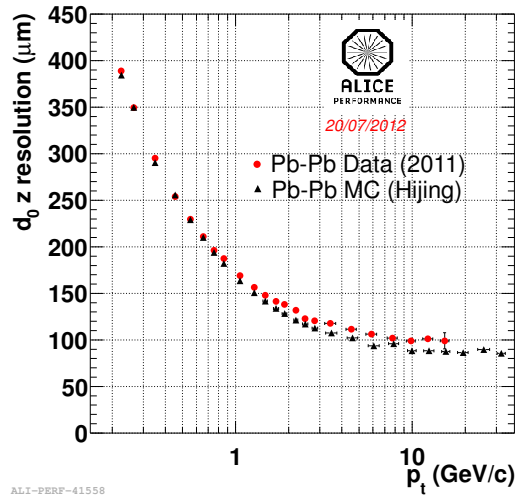
Figure 3.4.: Resolution of the z distance to the primary vertex for all charged ITS–TPC tracks in Pb–Pb collisions.

3.4. Particle Identification

ALICE exploits several Particle Identification (PID) methods. For the analysis of D^0 mesons, the PID capabilities of TPC and TOF are used. Both provide full azimuthal coverage leading to a good geometrical acceptance.

In Fig 3.5 (left) the specific energy loss dE/dx is shown as a function of the particle momentum. The black curves are parametrisations of the expected mean energy loss as a function of the momentum for different particle species. Due to the crossing of these lines, there are momentum ranges, e.g., at about $1\,\mathrm{GeV/c}$ for pions and kaons shown in Fig. 3.5 (left), where a PID decision is not possible. Depending on the purity requirements and the relative abundance, one can still use the PID information. In order to obtain a track-by-track response, bands around the parametrisation are used to assign a species hypothesis to a track. The widths of these bands depend on the analysis and are often chosen to be a few times the resolution σ (the so-called $n\sigma$-method). This resolution is about $5\,\%$ to $7\,\%$ depending on the occupancy [80].

The TOF PID capability of measuring the velocity β as a function of the momentum is complementary to the PID capability of the TPC. TOF is able to separate kaons from pions at momenta of up to about $2.5\,\mathrm{GeV/c}$, and protons from kaons up to $4\,\mathrm{GeV/c}$ (cf. Fig. 3.5 left) [80]. Also for TOF a band around the parametrised response is used to assign the tracks to a species.

The ambiguities in the PID response of the single detector can to some extent be resolved by a combination of the response TPC and TOF. A simple approach is to use the information of the detector which is unambiguous for a given track by excluding crossings or regions in which the bands are to close. A more sophisticated approach is the Bayesian PID [90] using the information from several detectors and folding the probabilities with the expected abundances of the particle species.
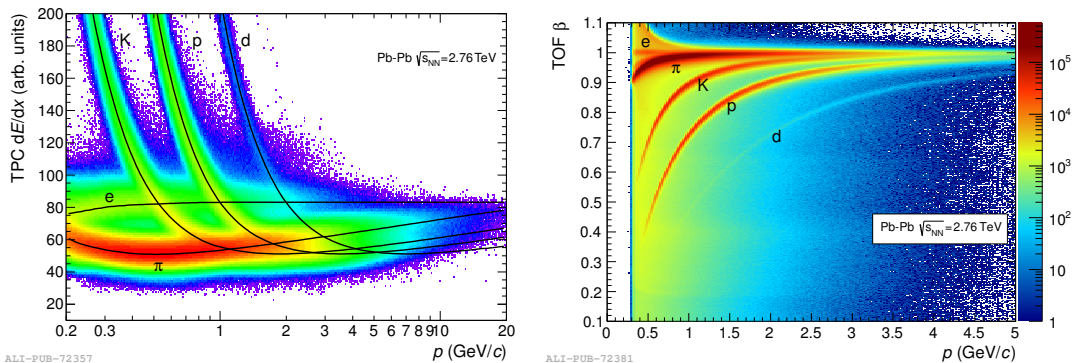
Figure 3.5.: Specific energy loss (dE/dx) in the TPC (left) and the particle velocity β by TOF (right) versus the momentum in Pb–Pb collisions, both taken from [80].

4. Measurement of Prompt and Feed-Down D^0 Mesons in the $\mathrm{K}^-\pi^+$ Decay Channel

In this chapter, a novel analysis method for the measurement of prompt and feed-down D^0 mesons in the decay channel $\mathrm{D}^0 \to \mathrm{K}^-\pi^+$ and its charge conjugate is presented. The first section of this chapter recapitulates the secondary-vertex reconstruction method used to measure D^0 mesons in ALICE and emphasises the peculiarities of the measurement of D^0 from B hadrons. In the second part of this chapter, the feed-down-separation method using cut variations is introduced. In the last part of this chapter the results obtained by applying this method to data from p–Pb collisions are shown.

In the measurements of D^0 mesons carried out by ALICE on data from pp [63, 91–93], p–Pb [94] and Pb–Pb [58, 61, 95–98] collisions, a feed-down subtraction using theoretical predictions of production cross sections for charm and beauty hadrons based on FONLL calculations [68, 69] was used. Kinematics and branching ratios are obtained using the EvtGen package [99]. Together with the acceptance times efficiency (Acc × ϵ) for feed-down D^0 mesons from Monte Carlo (MC) simulations, the expected feed-down contribution to the raw yield can be computed. The resulting fraction of prompt D^0 mesons contributing to the raw yield, f_{prompt}, in pp
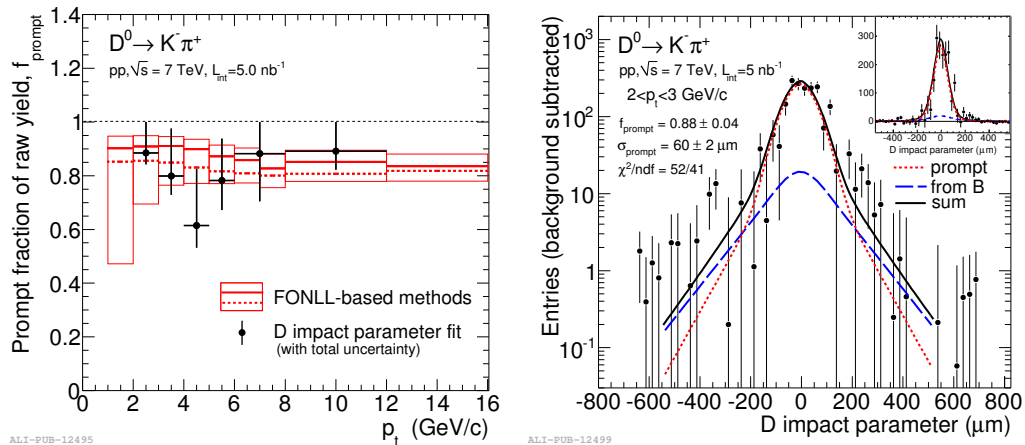
Figure 4.1.: Left: prompt fraction, f_{prompt}, of the D^0 raw yield as a function of p_{T} using the theory-based methods (solid and dashed red lines, see text for more details) and using the impact-parameter fit (black data points). Right: example of the D^0 meson impact-parameter distribution and its decomposition in the transverse plane after background subtraction. Figures taken from [63].

collisions at $\sqrt{s} = 7\,\mathrm{TeV}$ is shown with a solid red line in Fig. 4.1 (left). The f_{prompt} obtained using an alternative theory-based method is shown with a dashed red line. The alternative method is based on the $(\mathrm{Acc} \times \epsilon)$ from MC simulations times predicted cross section for feed-down D^0 mesons divided by the corresponding $(\mathrm{Acc} \times \epsilon)$ times predicted cross section for prompt D^0 mesons. As systematic uncertainty, the envelope of the uncertainties of both theory-based methods is used. A more detailed description of the methods can be found in [63]. The uncertainty of f_{prompt} is large, reaching about $45\,\%$ in the p_{T} range from $1\,\mathrm{GeV}/c$ to $2\,\mathrm{GeV}/c$. In addition to this large uncertainty, this approach has the clear disadvantage of exploiting theoretical predictions. Furthermore, for the application of a theory-based feed-down subtraction approach in nuclear collisions, assumptions must be made on the nuclear-modification factors of prompt and feed-down D^0 mesons, which are the measurement goals. A data driven approach is therefore desirable.

An experimental approach is the so-called impact-parameter fit which exploits the different shapes of the impact parameter distributions of prompt and feed-down (displaced) D mesons (cf. Fig. 4.1, right). The prompt fraction obtained using the impact-parameter fit is shown in Fig. 4.1 (left). A further detailed description of this method can be found in [63]. Due to its large uncertainties, this method is so far only used as a crosscheck of the theory-based method described above.

Within this thesis, a new data-driven technique for the measurement of prompt and feed-down D^0 mesons based on cut variations was studied.

4.1. $\mathrm{D}^0 \rightarrow \mathrm{K}^-\pi^+$ Reconstruction

For the reconstruction of D^0 mesons, secondary-vertex reconstruction using topological cuts is performed. The so-called cuts are selection criteria used to classify the D^0 mesons. This approach has been used for several publications based on data obtained in pp [63, 91–93], p–Pb [94] and Pb–Pb [58, 61, 95–98] collisions. For data from Pb–Pb collisions, this method achieves a significant reduction of the combinatorial background improving the signal-over-noise ratio [80]. Within the scope of this thesis, the potential of the current D^0 meson reconstruction for the measurement of the feed-down contribution is evaluated.

In Fig. 4.2, the topology of a D^0 meson decaying into a pion (π) and a kaon (K) in the plane perpendicular to the beam axis is shown. The reconstructed secondary vertex is the point at which the tracks of the π and K are closest to each other. The two tracks have to be of opposite charge. The D^0 flight line is the direct connection of the primary and the secondary vertex. The pointing angle $\theta_{\mathrm{pointing}}$ denotes the angle between the flight line and the reconstructed momentum of the D^0. d_0^{K} and d_0^{π} denote the impact parameters defined as the shortest distance of a track to the primary vertex in the plane perpendicular to the beam axis. The sign of the impact
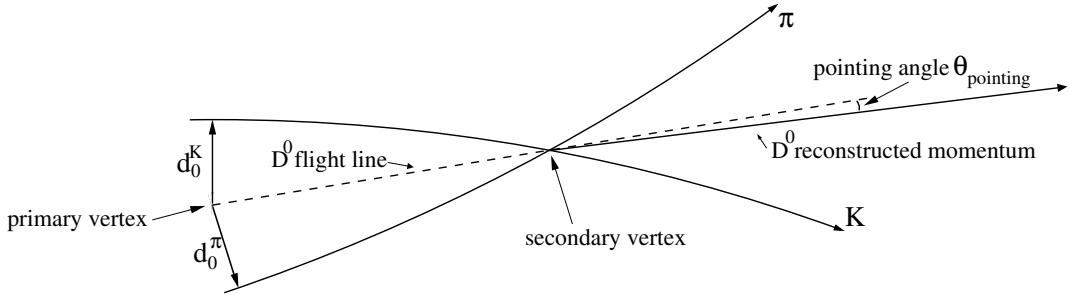
Figure 4.2.: D^0 decay topology in the transverse plane, taken from [64].

parameter depends on the handedness of the track helix and whether the vertex is inside or outside the helix.

4.1.1. D^0 Meson Selection Criteria

In this section, the selection criteria called cuts for D^0 candidates are discussed with regard to their background discrimination power and selection of feed-down D^0 mesons. The following cuts are applied after a cut on the invariant mass of D^0 candidate, which is required to be in an invariant-mass range of $\pm 250 \, \text{MeV}/c^2$ around the nominal D^0 mass.

Cosine of the Decay Angle $\cos(\theta^*)$:
   The angle between the K momentum vector in the rest frame of the D^0 meson and the flight line of the D^0 meson is denoted θ^*. The distribution of $\cos(\theta^*)$ from signal candidates of both prompt and feed-down D^0 mesons is flat, as the D^0 meson decays isotropically. Acceptance effects and additional cuts lead to a depletion at $|\cos(\theta^*)| \approx 1$. The combinatorial background from primary tracks accumulates close to $|\cos(\theta^*)| \approx 1$, leading to a cut rejecting candidates outside $|\cos(\theta^*)| > \epsilon$.

Daughter p_T:
   An important measure for the background rejection is the minimum-p_T cut on the daughter tracks of the D^0 candidates. As the majority of particle production is soft and the production cross section rapidly decreases with increasing p_T [100, 101], this cut can effectively decrease the combinatorial background. Furthermore, this cut ensures a good impact-parameter resolution, which is about $100 \, \mu\text{m}$ at a p_T of $500 \, \text{MeV}/c$, about the $c\tau$ of the D^0 meson, and degrades rapidly towards lower values of p_T (cf. Fig. 3.3). A minimum track p_T of $400 \, \text{MeV}/c$ to $500 \, \text{MeV}/c$ ensures good energy-loss description and PID, especially in the case of the K. However, it also cuts into the acceptance for low-p_T D^0 mesons (cf. Fig. 2.5).

Absolute value of the impact parameter $|d_0^X|$ of the daughter tracks:
The impact parameter $|d_0^X|$ of the daughter tracks is useful to discard primary tracks requiring a minimum distance cut from the primary vertex and maximum distance cut to discard tracks from strange decays which decay even further away from the primary vertex than charm and beauty hadrons. A minimum cut on the daughter p_T ensures a sufficient impact-parameter resolution to make this cut effective for low-p_T D^0 mesons, as the impact-parameter resolution degrades for low-p_T tracks.

Product of the impact parameter of the two daughter tracks $d_0^\mathrm{K} \times d_0^\pi$:
For signal D^0 candidates pointing to the primary vertex as shown in Fig. 4.2, the impact parameters point in opposing directions leading to a negative product of the impact parameters of the two daughter tracks $d_0^\mathrm{K} \times d_0^\pi$. Finite detector resolution leads, however, to a wide distribution which remains highly asymmetric with respect to zero. For background composed by random charged primary tracks, this distribution is found to be symmetric.

Distance of Closest Approach of the two daughter tracks $\mathrm{dca}_{\mathrm{K},\pi}$:
The Distance of Closest Approach (DCA) of the π and K is defined as the minimum distance of the two track helices. Due to the finite detector resolution, they do not always meet. This variable is closely correlated with the impact-parameter resolution. An upper limit rejects pairs which are unlikely to originated from the same vertex.

Cosine of the Pointing Angle $\cos\left(\theta_\mathrm{pointing}\right)$:
As depicted in Fig. 4.2, the pointing angle θ_pointing is defined as the angle between the D^0 flight line and its momentum vector. For prompt D^0 mesons, the $\cos(\theta_\mathrm{pointing})$ distribution peaks at 1 and has an exponential tail towards lower values due to finite detector resolution. For feed-down D^0 meson, the exponential tail becomes more prominent and the peak at 1 less pronounced. This is due to the D^0 momentum vector pointing to the B decay vertex which is not necessarily located on the line connecting the primary and the D^0 vertex. For background pairs, the pair momentum vector and the flight line are not correlated, as these are mostly pairs of primary tracks and the displacement of the secondary vertex is a consequence of the finite detector resolution. Background pairs hence dominate for $|\cos(\theta_\mathrm{pointing})| < 1 - \epsilon$ with ϵ being of order of magnitude of 10^{-2} depending on the corresponding resolution. Most of the prompt and feed-down D^0 mesons show a $|\cos(\theta_\mathrm{pointing})|$ close to 1. Only a small range of $|\cos(\theta_\mathrm{pointing})|$ is dominated by feed-down D^0 candidates and can be used to enhance their contribution to the candidate set, as for too low values of $|\cos(\theta_\mathrm{pointing})|$ the background candidates start to dominate.

Normalised Decay Length L:
The distance from the primary vertex to the secondary D^0 vertex is the decay length l. In order to obtain the normalised decay length L, the decay length l is normalised by its resolution σ_l. Effectively, the normalisation leads to

distributions only weakly depending on the D^0 p_T. An increasing D^0 p_T leads to an increase in l and a smaller opening angle in the laboratory frame. The smaller opening angle leads to a reduction of the secondary vertex resolution in direction of the D^0 momentum vector and in turn an increased σ_l. The quality of the description of the resolution in the MC simulation is important in order not to introduce a systematic bias.

PID of the daughter tracks:
For the particle identification, the TPC and TOF as described in Ch. 3.4 with a band of three times the resolution above and below the parametrised response are used ($n\sigma$-method). Both daughter particles are checked for both the K and the π hypotheses in both detectors. If both detectors confirm the same particle species, a particle is called 'identified'. If both detectors veto a species, the particle is marked 'incompatible'. If both detectors disagree or one or both are not able to confirm the species, the particle is called 'compatible' with a hypothesis. A D^0 candidate must be formed by a track pair of opposite charge, for which one track is compatible with the K hypothesis or identified as K and the other track is compatible with the π hypothesis or identified as π. Using this approach, combinatorial background is reduced by vetoing pairs which do not match a D^0 meson or its charge conjugate.

4.2. Feed-Down Separation Using Cut Variations

The feed-down-separation method using cut variations is based on the idea of using several cut sets with different sensitivities to prompt and feed-down D^0 mesons. The corresponding (Acc $\times \epsilon$) of the cut sets for prompt and feed-down D mesons are obtained from MC simulations. In the following mathematical derivation, the abbreviation

$$\xi := (\text{Acc} \times \epsilon) \tag{4.1}$$

is used. The mathematical formalism used to obtain the corresponding corrected yield for the two contributions is outlined below [102].

In the following, n different cut sets with an index $i \in 1 \dots n$ are used. The raw yields Y_i can be written as column vector $\boldsymbol{Y}$:

$$\boldsymbol{Y} := \begin{pmatrix} Y_1 \\ Y_2 \\ \vdots \\ Y_n \end{pmatrix}. \tag{4.2}$$

The ξ of a cut set i for the reconstruction of prompt D^0 mesons and feed-down D^0 mesons is denoted by $\xi_{\text{Prompt,i}}$ and $\xi_{\text{FD,i}}$, respectively. In the following, they will be

used in form of a matrix $\boldsymbol{\xi}$ defined as:

$$\boldsymbol{\xi} := \begin{pmatrix} \xi_{\text{Prompt},1} & \xi_{\text{FD},1} \\ \xi_{\text{Prompt},2} & \xi_{\text{FD},2} \\ \vdots & \vdots \\ \xi_{\text{Prompt},n} & \xi_{\text{FD},n} \end{pmatrix}. \tag{4.3}$$

The result of this method are the corrected yields for prompt and feed-down D^0 mesons, N_{Prompt} and N_{FD} which are combined to a vector $\boldsymbol{N}$ defined as:

$$\boldsymbol{N} := \begin{pmatrix} N_{\text{Prompt}} \\ N_{\text{FD}} \end{pmatrix}. \tag{4.4}$$

Together, this allows to write down the matrix equation

$$\boldsymbol{\xi} \times \boldsymbol{N} - \boldsymbol{Y} = \boldsymbol{\delta} . \tag{4.5}$$

The $\boldsymbol{\delta}$ here denotes the vector of residuals, which in an ideal case with $\boldsymbol{Y}$ in the range of $\boldsymbol{\xi}$ corresponds to a null vector. In detail, the matrix equation looks the following way:

$$\begin{pmatrix} \xi_{\text{Prompt},1} & \xi_{\text{FD},1} \\ \xi_{\text{Prompt},2} & \xi_{\text{FD},2} \\ \vdots & \vdots \\ \xi_{\text{Prompt},n} & \xi_{\text{FD},n} \end{pmatrix} \times \begin{pmatrix} N_{\text{Prompt}} \\ N_{\text{FD}} \end{pmatrix} - \begin{pmatrix} Y_1 \\ Y_2 \\ \vdots \\ Y_n \end{pmatrix} = \begin{pmatrix} \delta_1 \\ \delta_2 \\ \vdots \\ \delta_n \end{pmatrix}. \tag{4.6}$$

For the usage of more than two cut sets $(n > 2)$ selecting disjoint sets of D^0, this equation is likely to be overdetermined. In order to determine the corrected yields $\boldsymbol{N}$, an approach based on the minimisation of a χ^2 can be used. The χ^2 is defined as

$$\chi^2 = \boldsymbol{\delta}^T \boldsymbol{C}^{-1} \boldsymbol{\delta} \tag{4.7}$$

with the weighting matrix $\boldsymbol{C}^{-1}$ defined by

$$\boldsymbol{C} := \begin{pmatrix} \sigma_1^2 & & & \\ & \sigma_2^2 & & \\ & & \ddots & \\ & & & \sigma_n^2 \end{pmatrix}. \tag{4.8}$$

The entries σ_i of the matrix are calculated according to the following equation:

$$\sigma_i^2 = \sigma_{Y_i}^2 + \sigma_{\xi_{\text{Prompt},i}}^2 \cdot N_{\text{Prompt}}^2 + \sigma_{\xi_{\text{FD},i}}^2 \cdot N_{\text{FD}}^2 \tag{4.9}$$

with the statistical uncertainty of the raw yield σ_{Y_i}, and the statistical uncertainties of the acceptance times efficiency $\sigma_{\xi_{\text{Prompt},i}}$ and $\sigma_{\xi_{\text{FD},i}}$. At the beginning, the corrected yields are unknown and hence set to zero. In order to take the efficiency uncertainties

properly into account, the minimisation is iterated several times. However, using MC simulations with sufficiently large statistics, the statistical uncertainties on ξ are typically negligible and a single iteration is sufficient. Systematic uncertainties are assessed separately as described in Ch. 4.7. The weighting matrix will only be diagonal, if the cuts split the data sample into disjoint sets.

Algebraic minimisation of $\mathrm{d}\chi^2/\mathrm{d}N_i$ leads to

$$N = (\xi^T C^{-1} \xi)^{-1} \xi^T C^{-1} Y = \mathrm{Cov}(N) \xi^T C^{-1} Y \; . \qquad (4.10)$$

The covariance matrix $\mathbf{Cov}(N) = (\epsilon^T C^{-1} \epsilon)^{-1}$ contains the corresponding statistical uncertainties of the corrected yields.

In the analysis software, the inversion of $\epsilon^T C^{-1} \epsilon$ is performed using Cramer's rule [103]. The numerically critical calculation of the determinant is monitored and found to not distort the result.

Before applying the method to experimental data, the stability of the algorithm for the feed-down separation against statistical fluctuations and potential systematic uncertainties in the yield extraction and efficiency determination was studied. The stability studies are described in more detail in App. A.3.

4.3. Analysis of p–Pb Data

Within this thesis, the cut-variation feed-down separation using the D^0 meson reconstruction is applied to data from p–Pb collisions. This analysis method is studied with data from p–Pb collisions, as the statistics of this data sample is larger than that of central Pb–Pb collisions and of the same order of magnitude as the minimum-bias pp data sample at $\sqrt{s} = 7\,\mathrm{TeV}$. Additionally, due to the average $\langle N_{\mathrm{coll}} \rangle \approx 7$ [104] and the resulting event multiplicity, the primary-vertex resolution is significantly better than in data from pp collisions. Moreover, the study of p–Pb collision is necessary for the measurement of Cold Nuclear Matter (CNM) effects.

4.3.1. p–Pb Data Sample

The p–Pb data sample used for this analysis was acquired in January 2013 using a minimum-bias trigger. The p and Pb beams are bent by the same magnets leading to a fixed beam energy fixed to $4\,\mathrm{TeV}$ per nuclear charge Z for both the proton and the $^{208}_{82}\mathrm{Pb}$-ion beams. The different ratio of nuclear charge to mass number Z/A leads to a beam energy per nucleon of $4\,\mathrm{TeV}$ and $1.58\,\mathrm{TeV}$ resulting in a centre-of-mass energy of $\sqrt{s_{\mathrm{NN}}} = 5.02\,\mathrm{TeV}$. Due to the asymmetric beam energies, the rapidity range of $-0.5 < y_{\mathrm{lab}} < 0.5$ in the detector reference frame corresponds to $-0.96 < y_{\mathrm{cms}} < 0.04$ in the centre-of-mass frame.

The data sample consists of two periods: `LHC13b` and `LHC13c`. The corresponding MC simulations are `LHC13d3` and `LHC13d3_plus` which are used to compute the (Acc $\times$ ϵ) corrections. These simulations reproduce the detector performance and beam conditions during the data-taking periods. The simulations are based on HIJING [105] p–Pb events and additional signals from PYTHIA6 [76]. HIJING is used to simulate the underlying p–Pb event. The additional signals are obtained using PYTHIA6 events fulfilling the following requirements:

1. A $c\bar{c}$ pair with at least one of the quarks within $|y| < 1.5$; the hadronisation is not modified; however, D mesons are forced to decay in hadronic channels considered for analysis.

2. A $b\bar{b}$ pair with at least one of the quarks within $|y| < 1.5$; the B hadron decay itself is not modified; however, the D mesons that are produced by the decay of a B hadron are forced to decay in hadronic channels considered in the analysis.

3. A $c\bar{c}$ pair which decays via a channel involving an electron within $|y| < 1.2$;

4. A $b\bar{b}$ pair which decays via a channel involving an electron within $|y| < 1.2$;

The embedding of events fulfilling the requirements above results in a modification of the underlying event leading to a different shape and integral of the background in the invariant-mass range of the D^0 meson compared to minimum-bias events.

4.3.2. Event Selection

Background events originating from interactions of the beam with gas remaining in the beam pipe were rejected on the basis of timing information from the V0 detectors and the LHC bunch crossing scheme [80]. Furthermore, the primary vertex is required to be reconstructed using ITS+TPC tracks with a z-coordinate in the range $|z| < 10\,\mathrm{cm}$. The events are triggered online with the requirement of signals being present in both the V0-A and the V0-C detector. About 10^8 events passed the selection criteria, corresponding to an integrated luminosity $\mathcal{L}$ of roughly $50\,\mu\mathrm{b}^{-1}$. The event selection criteria used in this analysis are identical to those used for [94].

4.3.3. Track Selection

Within this thesis, the track selection used in [94] was adopted. Tracks are required to be within the pseudorapidity interval of $|\eta| < 0.8$ and to have at least 70 space points in the TPC. The fit of the TPC space points has to fulfil $\chi^2/\mathrm{ndf} < 2$. Furthermore, the tracks must have a hit in one of the SPD layers in order to reject secondary particles originating from strange decays or photon conversions as well

as to improve the pointing resolution of the track. The track p_{T} is required to be $400\,\mathrm{MeV}/c$ or larger.

The track-selection requirement of $|\eta| < 0.8$ leads to a steep drop in the acceptance for D^0 mesons with $|y|$ larger than about 0.7 to 0.8 depending on the D^0 p_{T}. In order to avoid y regions with a steep drop in the $(\mathrm{Acc} \times \epsilon)$, a p_{T}-dependent y_{fid} cut is applied on the D^0 candidates in order to maintain an $(\mathrm{Acc} \times \epsilon)$ flat in y.

4.4. Choice of Cut Sets

In the presented analysis, the feed-down-separation method using cut variations based on three sets of cuts was studied. As the cuts need to generate disjoint sets of events, the introduction of further cut sets leads to a reduction of the statistics in the existing sets. The following three cut sets were defined:

Maximised Prompt Contribution:
> This cut set is used to obtain a maximised prompt D^0 contribution. As the topological cuts favour feed-down D^0 which are intrinsically more displaced, the design goal for this cut is to achieve the same efficiencies for both prompt D^0 mesons as for feed-down D^0 mesons. Equal efficiencies and the larger production cross section of the prompt D^0 mesons lead to the desired enhancement in the D^0 candidate set.

Mixed:
> The mixed cut set has the highest efficiency among the three cut sets and features cuts very similar to the standard analysis. This cut set shows the best performance for the reconstruction of D^0 mesons in terms of significance. The efficiency is higher for feed-down than for prompt D^0 mesons.

Maximised Feed-Down Contribution:
> The maximised feed-down cut set is aiming at suppressing prompt D^0 mesons by at least a factor of ten in terms of efficiency. The trade-off for this cut set is between suppression prompt D^0 mesons and maintaining a statistically significant feed-down D^0 signal to be able to fit the invariant-mass distributions.

All three cut sets share the same basic cuts shown in Tab. 4.1 which are used in [94]. The D^0 candidates are subdivided into sets using additional cuts on the normalised decay length in the xy-plane L_{xy} and on $\cos(\theta_{\mathrm{Pointing,xy}})$ summarised in Tab. 4.2. The L_{xy} distributions (cf. Fig. 4.3, left) allow for a separation of the data set in three sub sets which are close to the desired ratio of prompt and feed-down contributions. The $\cos(\theta_{\mathrm{Pointing,xy}})$ (cf. Fig. 4.3, right) is used only for additional refinement. The smaller pixel size in the $r\varphi$-direction leads to a higher resolution in the $xy(r\varphi)$-plane compared to the z-direction (cf. Fig. 3.3 and Fig. 3.4). Consequently, only the $xy(r\varphi)$-components of the pointing angle and the normalised

Table 4.1.: Common selection cuts for D^0 candidates.

Cut variable	D^0-p_{T} range (GeV/c)				
	1–2	**2–4**	**4–8**	**8–12**	**12–16**
$\mathrm{dca}_{\mathrm{K},\pi}$ (cm)	< 0.03	< 0.03	< 0.03	< 0.03	< 0.03
$\lvert\cos(\theta^*)\rvert$	< 0.8	< 0.8	< 0.8	< 0.8	< 1.0
$p_{\mathrm{T}}^{\mathrm{K}}$ (GeV/c)	> 0.4	> 0.7	> 0.7	> 0.7	> 0.7
p_{T}^{π} (GeV/c)	> 0.4	> 0.7	> 0.7	> 0.7	> 0.7
$\lvert d_0^{\mathrm{K}}\rvert$ (cm)	< 0.1	< 0.1	< 0.1	< 0.1	< 0.1
$\lvert d_0^{\pi}\rvert$ (cm)	< 0.1	< 0.1	< 0.1	< 0.1	< 0.1
$d_0^{\mathrm{K}} \times d_0^{\pi}$ (cm^2)	< -0.00035	< -0.0003	< -0.0001	< -0.00005	< 0.0001
$\cos(\theta_{\mathrm{Pointing}})$	> 0.93	> 0.93	> 0.9	> 0.9	> 0.8
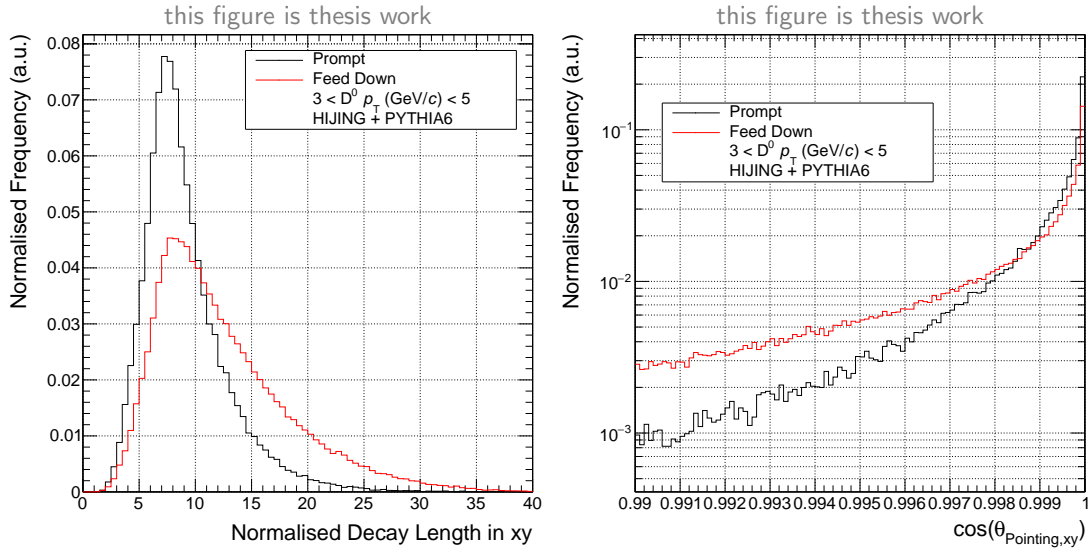
Figure 4.3.: Normalised decay length in the xy-plane L_{xy} (left) and $\cos(\theta_{\mathrm{Pointing,xy}})$ (right) of the p_{T} bin $3\,\mathrm{GeV}/c$ to $5\,\mathrm{GeV}/c$.

Table 4.2.: Cut set specific cuts for the D^0 candidates.

Cut Set	Cut variable	D^0-p_T range (GeV/c)				
		1–2	**2–3**	**3–5**	**5–8**	**8–16**
Max. prompt	L_{xy}	0–7	0–7	0–7	0–7	0–7
	$\cos(\theta_{Pointing,xy})$	> 0.998	> 0.996	> 0.996	> 0.998	> 0.998
Mixed	L_{xy}	7–12	7–12	7–12	7–12	7–12
	$\cos(\theta_{Pointing,xy})$	–	–	–	–	–
Max. feed-down	L_{xy}	–	> 12	> 12	> 12	> 12
	$\cos(\theta_{Pointing,xy})$	–	< 0.997	< 0.9985	< 0.999	< 0.9995

Table 4.3.: p_T bins used in the analysis of the data from p–Pb collisions.

Bin	1	2	3	4	5
p_T range (GeV/c)	1–2	2–3	3–5	5–8	8–16

decay length are exploited for the definition of the cut sets. The choice of the cut values is driven by two aspects: achieving the desired prompt and feed-down D^0 contributions while maintaining an approximate minimum significance of 5 of the signal. The p_T intervals chosen for the analysis are summarised in Tab. 4.3. The L_{xy} and $\cos(\theta_{Pointing,xy})$ distributions for all cut sets can be found in App. A.

4.5. Invariant-Mass Distributions

The invariant-mass distributions for the prompt-enhanced, mixed and feed-down-enhanced cut sets are shown in Fig. 4.4, Fig. 4.5 and Fig. 4.6, respectively. The most critical cut set with regard to the available statistics is the feed-down-enhanced set (cf. Fig. 4.6). The raw yields for each set of cuts and each p_T interval are obtained by fitting the invariant-mass distribution with a function composed of a Gaussian term describing the signal and an exponential term for the background. As start values for the Gaussian term of the fit, the peak position and peak width from MC simulations are used. For the feed-down-enhanced cut set, the width of the Gaussian distribution is fixed to the value obtained from MC simulations. This measure was taken as the fluctuations due to the low number entries per bin lead to very unstable behaviour of a fit with free width. For the two other cut sets, the width obtained from the MC simulations and the p–Pb data are in agreement.

In the first p_T bin from $1\,\text{GeV}/c$ to $2\,\text{GeV}/c$, it was not possible to find a cut configuration leading to a reliable invariant-mass fit with the desired significance and the desired prompt D^0 suppression. Above $p_T = 5\,\text{GeV/c}$, the invariant-mass bin size is doubled to $10\,\text{MeV}/c^2$ in order to increase the counts per bin and to
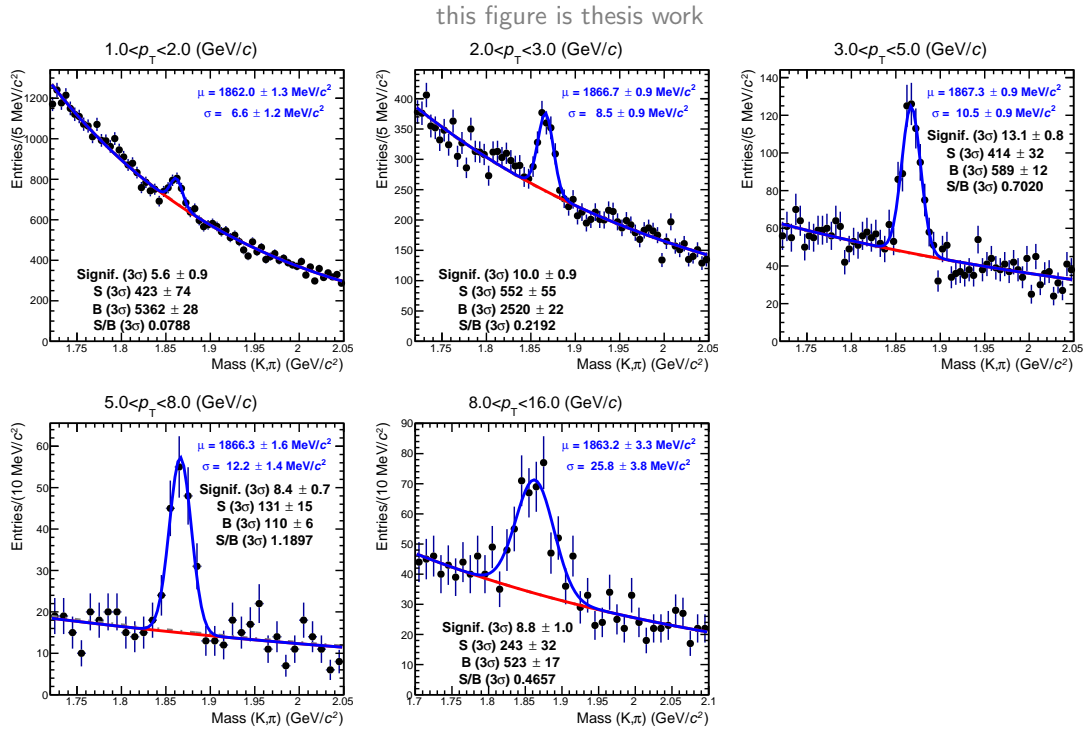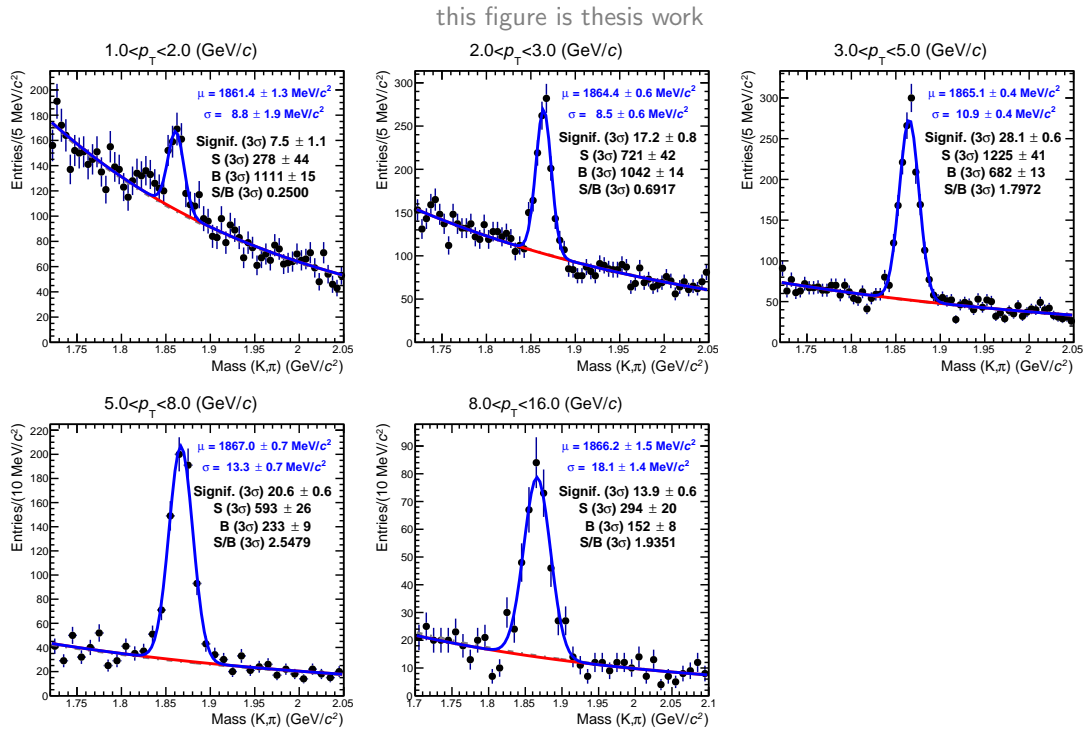
Figure 4.4.: Invariant-mass distributions of D^0 candidates for the prompt-enhanced cut set.

Figure 4.5.: Invariant-mass distributions of D^0 candidates for the mixed cut set.
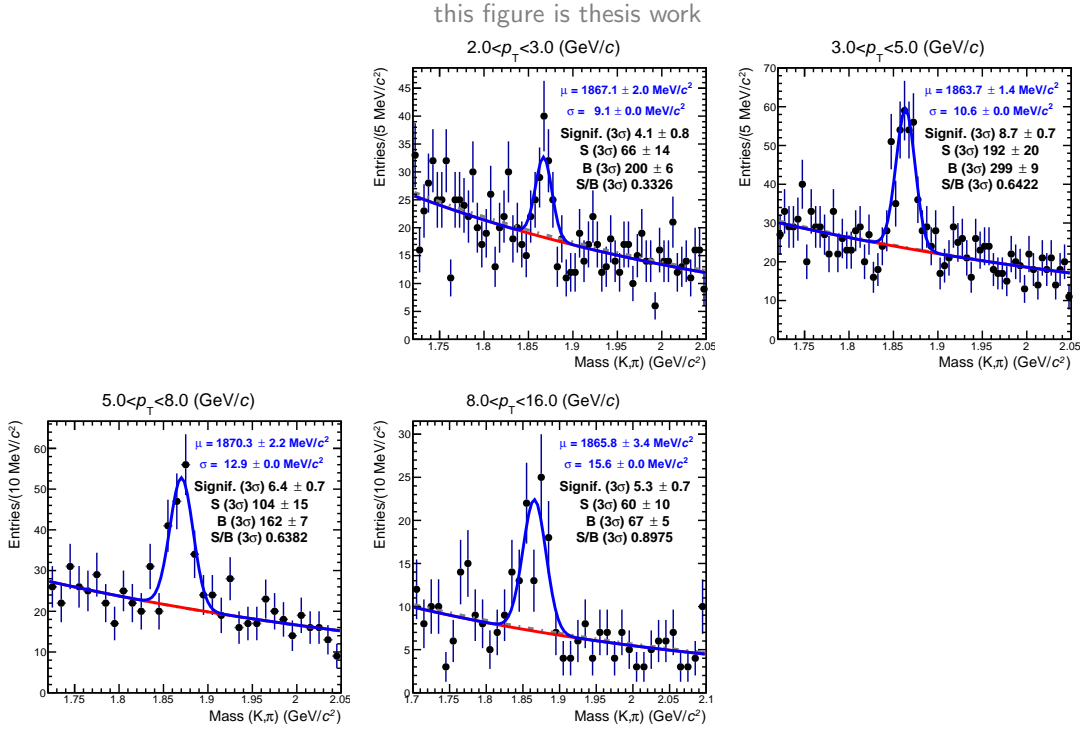
this figure is thesis work

Figure 4.6.: Invariant-mass distributions of D^0 candidates for the feed-down-enhanced cut set.

reduce bin-by-bin fluctuations.

In general, the invariant-mass distributions of all cut sets follow similar trends. The slope of the background decreases with increasing p_T. At the same time the signal over background increases. The significance is the highest in the p_T bin from $3\,\mathrm{GeV}/c$ to $5\,\mathrm{GeV}/c$ and decreases towards higher and lower p_T. A table containing all significance and signal values can be found in App. A.

The amount of signal within $\pm 3\sigma$ as well as the statistical uncertainties extracted from the fit are used as input for the determination of the prompt and feed-down component.

4.6. Acceptance times Efficiency

The acceptance times efficiency ($\mathrm{Acc}\times\epsilon$) needed for the χ^2-minimisation (cf. Ch. 4.2) are obtained from MC simulations. The p_T spectra of D^0 mesons and B hadrons are matched to the distributions predicted by FONLL. The signal enhancement in the MC simulations results in negligible statistical uncertainties of the ($\mathrm{Acc}\times\epsilon$) leading to a instantaneous convergence of the minimisation as the influence of the corrected yields is negligible (cf. Ch. 4.2). Potential systematic biases caused by the signal enhancement are assessed in Ch. 4.7.2.
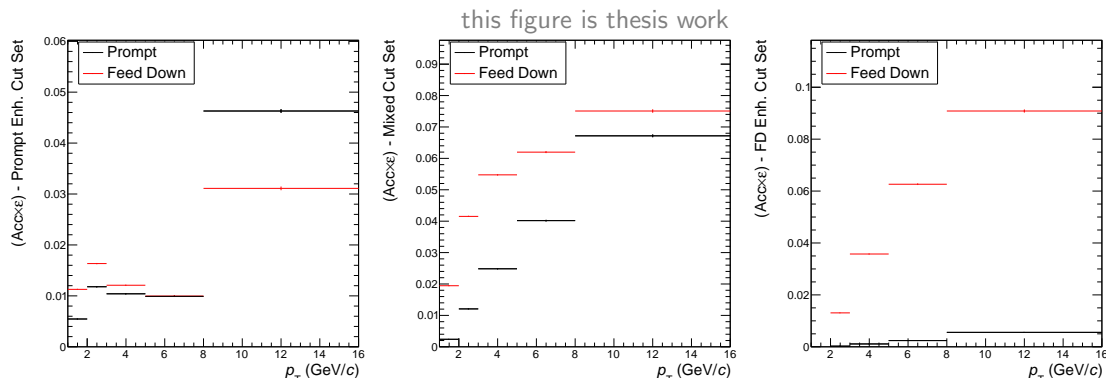
Figure 4.7.: Prompt and feed-down D^0 (Acc $\times$ ϵ) for the prompt-enhanced cut set (left), the mixed cut set (centre) and feed-down-enhanced cut set (right).

The resulting (Acc $\times$ ϵ) for the prompt-enhanced cut set are shown in Fig. 4.7 (left). For a p_T smaller than $5\,\mathrm{GeV}/c$, the resulting (Acc$\times$$\epsilon$)$_{\mathrm{FD}}$ for feed-down D^0 mesons is higher than the corresponding (Acc$\times$$\epsilon$)$_{\mathrm{Prompt}}$ for prompt D^0 mesons by up to a factor two. Taking into account the higher production cross section for prompt D^0 mesons, this leads nevertheless to a sample which is dominated by prompt production. At p_T of $5\,\mathrm{GeV}/c$ and higher, the (Acc $\times$ ϵ)$_{\mathrm{Prompt}}$ is larger than (Acc $\times$ ϵ)$_{\mathrm{FD}}$. Below a p_T of $8\,\mathrm{GeV}/c$ the (Acc $\times$ ϵ) is about $1\,\%$, increasing with p_T to about $5\,\%$ and $3\,\%$ for prompt and feed-down D^0 mesons, respectively.

The (Acc $\times$ ϵ) values of the mixed cut set shown in Fig. 4.7 (centre) increase monotonically with p_T ranging from about $0.2\,\%$ to $6.8\,\%$ and from $2\,\%$ to $7.5\,\%$ for prompt and feed-down D^0 mesons, respectively. This cut set shows large (Acc $\times$ ϵ) for prompt and feed-down D^0 mesons, which are comparable to the values in the corresponding enhanced cut sets, leading to the highest significance of the corresponding invariant-mass distributions.

The cuts used to enhance the feed-down component lead to an even stronger p_T dependence of the (Acc $\times$ ϵ) values for both feed-down and prompt D^0 mesons (cf. Fig. 4.7, right). The achieved prompt D^0 meson suppression factors in terms of (Acc $\times$ ϵ) decrease from about 50 to 17 with increasing p_T. In the last p_T bin, the (Acc $\times$ ϵ) for feed-down D^0 mesons matches approximately that of the mixed cut set. The strong decrease of (Acc $\times$ ϵ)$_{\mathrm{FD}}$ with decreasing p_T explains why it is impossible to find a viable feed-down-enhanced cut set in the p_T range of $1\,\mathrm{GeV}/c$ to $2\,\mathrm{GeV}/c$.

The dependencies of (Acc $\times$ ϵ) on other observables than p_T have been checked for [94] and the MC simulations were found to be reliable. A summary of all (Acc $\times$ ϵ) figures is given in Tab. 4.4.

Table 4.4.: $(\text{Acc} \times \epsilon)$ values for the reconstruction of D^0 candidates.

p_T (GeV/c)	Cut Set	$(\text{Acc} \times \epsilon)_{\text{Prompt}}$	$(\text{Acc} \times \epsilon)_{\text{FD}}$
1 to 2	max. prompt	$(5.460 \pm 0.064) \times 10^{-3}$	$(1.1280 \pm 0.0094) \times 10^{-2}$
	mixed	$(2.395 \pm 0.042) \times 10^{-3}$	$(1.945 \pm 0.012) \times 10^{-2}$
2 to 3	max. prompt	$(1.179 \pm 0.011) \times 10^{-2}$	$(1.689 \pm 0.012) \times 10^{-2}$
	mixed	$(1.207 \pm 0.011) \times 10^{-2}$	$(4.283 \pm 0.019) \times 10^{-2}$
	max. feed-down	$(2.59 \pm 0.16) \times 10^{-4}$	$(1.326 \pm 0.011) \times 10^{-2}$
3 to 5	max. prompt	$(1.0406 \pm 0.0094) \times 10^{-2}$	$(1.2392 \pm 0.0094) \times 10^{-2}$
	mixed	$(2.484 \pm 0.014) \times 10^{-2}$	$(5.533 \pm 0.020) \times 10^{-2}$
	max. feed-down	$(1.100 \pm 0.031) \times 10^{-3}$	$(3.623 \pm 0.016) \times 10^{-2}$
5 to 8	max. prompt	$(9.90 \pm 0.12) \times 10^{-3}$	$(1.013 \pm 0.012) \times 10^{-2}$
	mixed	$(4.018 \pm 0.024) \times 10^{-3}$	$(6.246 \pm 0.030) \times 10^{-2}$
	max. feed-down	$(2.398 \pm 0.061) \times 10^{-3}$	$(6.326 \pm 0.030) \times 10^{-2}$
8 to 16	max. prompt	$(4.630 \pm 0.037) \times 10^{-2}$	$(3.148 \pm 0.036) \times 10^{-2}$
	mixed	$(6.717 \pm 0.044) \times 10^{-2}$	$(7.600 \pm 0.055) \times 10^{-2}$
	max. feed-down	$(5.56 \pm 0.13) \times 10^{-3}$	$(9.272 \pm 0.060) \times 10^{-2}$

4.7. Systematic Uncertainties

In this section, the systematic uncertainties on the corrected yields obtained using the feed-down-separation method using cut variations are discussed. The influence of the individual systematic biases is assessed by rerunning the minimisation after variation of the raw yield and $(\text{Acc} \times \epsilon)$ according to the systematic bias.

4.7.1. Yield Extraction

In order to assess the stability of the yield extraction, the fitting procedure is varied as follows. For the description of the background, a linear, exponential and polynomial function of 2nd, 3rd and 4th order are used. The linear function is not used for the invariant-mass distribution of the p_T bin from $1\,\text{GeV}/c$ to $2\,\text{GeV}/c$ for the prompt-enhanced cut set as it does not describe the shape of the background. The polynomial of 3rd and 4th order are only used for bins with $p_T < 5\,\text{GeV}/c$. For higher p_T, the data points become too few due to the coarser binning and hence the background function is not constrained enough. The range for the fit cannot be extended, as below an invariant mass of about $1.72\,\text{GeV}/c^2$ incompletely reconstructed D mesons cause a bump structure. For example, D^0 mesons decaying into $K^-\pi^+\pi^0$, for which the neutral π^0 is not reconstructed, contribute to this bump.

The fit is varied using fixed and free mean μ as well as fixed and free width σ in the Gaussian signal term. In addition, a fixed width varied by $\pm 5\,\%$ and $\pm 10\,\%$

Table 4.5.: RMS of the raw yields obtained in the yield extraction study.

p_T range	RMS(Y) (%)		
(GeV/c)	Max. Prompt	Mixed	Max. Feed-Down
1 to 2	8.9	11	–
2 to 3	6.8	5.0	11.0
3 to 5	2.9	1.5	3.6
5 to 8	4.3	2.0	6.1
8 to 16	19.0	7.2	8.4

within the p_T range of $3\,\text{GeV}/c$ to $8\,\text{GeV}/c$ and outside of this range, respectively, are used. In the p_T range from $3\,\text{GeV}/c$ to $8\,\text{GeV}/c$, a variation of σ by $10\,\%$ is found not to describe the data well. Furthermore, the variations for the free σ are found to be smaller than $5\,\%$. As a crosscheck the signal is additionally obtained using bin counting within $3\,\sigma$ to $5\,\sigma$ using steps of $0.5\,\sigma$. In the bin counting approach, the entries of all bins within a specified range around μ are summed up and the background function is used to subtract the counts expected from background in this range.

The range of the fit is varied using different upper and lower bounds of $1.72\,\text{GeV}/c^2$, $1.74\,\text{GeV}/c^2$ and $1.76\,\text{GeV}/c^2$ as well as $2.06\,\text{GeV}/c^2$, $2.04\,\text{GeV}/c^2$ and $2.02\,\text{GeV}/c^2$, respectively.

The effect of the choice of binning is assessed by using three different binnings of $3\,\text{MeV}/c^2$, $4\,\text{MeV}/c^2$ and $5\,\text{MeV}/c^2$ and $9\,\text{MeV}/c^2$, $10\,\text{MeV}/c^2$ and $11\,\text{MeV}/c^2$ for a p_T smaller and larger than $5\,\text{GeV}/c$, respectively. A rebinning factor of 5 corresponds to a bin size of $5\,\text{MeV}/c^2$.

All combinations of the variations listed above are used independently for all invariant-mass distributions. The systematic uncertainties calculated using the Root Mean Square (RMS) of the raw-yield distributions are shown in Tab. 4.5.

4.7.2. Efficiency Determination

Depending on the list of decay channels included in the simulation, as well as how the generator simulates the decay kinematics, the distribution of the number of decay particles, as well as of their p_T, varies. The (Acc $\times$ ϵ) of reconstructing a feed-down D^0 meson depends on the B hadron decay properties. Depending on the number of decay particles, the momentum of the D^0 meson in the B hadron centre-of-mass system varies. Furthermore, the correlation of the B hadron and D^0 meson momentum vectors differs. In the following, the studies quantifying these effects are presented.

In the heavy-flavour enhanced MC simulation, particles generated outside $|y| < 1.5$ are removed to save the computing time needed for propagating them through the detector volume. As a consequence, only a subset of the B hadron decay particles are available to describe a decay at analysis level. In order to have a well-defined reference, only charged particles within the geometrical acceptance of ALICE with an absolute value of pseudo-rapidity $|\eta| < 0.9$ are used to characterise a decay.

The distributions of additional particles in acceptance n_i^{Gen} are obtained from the existing MC data sample (`LHC13d3` and `LHC13d3_plus`) and three additional MC data samples generated using `TPythia6Decayer` from ROOT [106], `AliPythiaDecayer` from AliRoot and EvtGen [99]. `TPythia6Decayer` and `AliPythiaDecayer` slightly differ in terms of decay tables, but use the same underlying MC generator, namely `PYTHIA6` [76]. On the other hand, EvtGen is a completely independent generator. The $(\text{Acc} \times \epsilon)_{\text{FD}}$ as a function of the number of decay particles in addition to the D^0 meson in the acceptance i together with the generator specific distribution of additional decay particles n_i^{Gen} is used to calculate the generator specific efficiency

$$(\text{Acc} \times \epsilon)_{\text{FD}}^{\text{Gen}} = \sum_i n_i^{\text{Gen}} (\text{Acc} \times \epsilon)_{FD,i}. \tag{4.11}$$

The systematic uncertainty is set to the maximum deviation of one of the generator specific values from the MC data sample. The $(\text{Acc} \times \epsilon)$ as a function of the number of additional decay particles in acceptance $(\text{Acc} \times \epsilon)_{\text{FD},i}$ as well as the distributions of additional decay particles in acceptance n_i^{Gen} can be found in App. A.

Due to the signal enhancement described above, the MC data sample furthermore contains unphysically many B hadrons decaying into an electron and a D^0 meson as well as possibly additional particles. This decay channel is used as a test for the potential bias caused by an individual decay channel. In order to study the bias of this enhancement, the $(\text{Acc} \times \epsilon)$ is obtained separately excluding decays involving an electron. The deviation of the $(\text{Acc} \times \epsilon)$ is used as an estimate for the systematic bias due to the enhancement cocktail.

The systematic uncertainties on the $(\text{Acc} \times \epsilon)$ are shown in Fig. 4.8 for the prompt-enhanced cut set (left), mixed cut set (centre) and feed-down-enhanced cut set (right). Furthermore, they are summarised in Tab. 4.6.

The two contributions to the systematic uncertainty of $\text{Acc} \times \epsilon$ are to some extend correlated, as the enhancement of certain decay channels also changes the decay-particle distribution. As the amount of correlation is difficult to assess with the present MC data sample and given the small size of the effect found, they are treated as independent uncertainties in the following.

An important crosscheck allowing to safely reduce these uncertainties are dedicated MC simulations based on two different generators such as PYTHIA [76, 107] and EvtGen [99] using an underlying p–Pb event from HIJING [105] in which the full decay information is kept to do a more differential study. As the uncertainty from
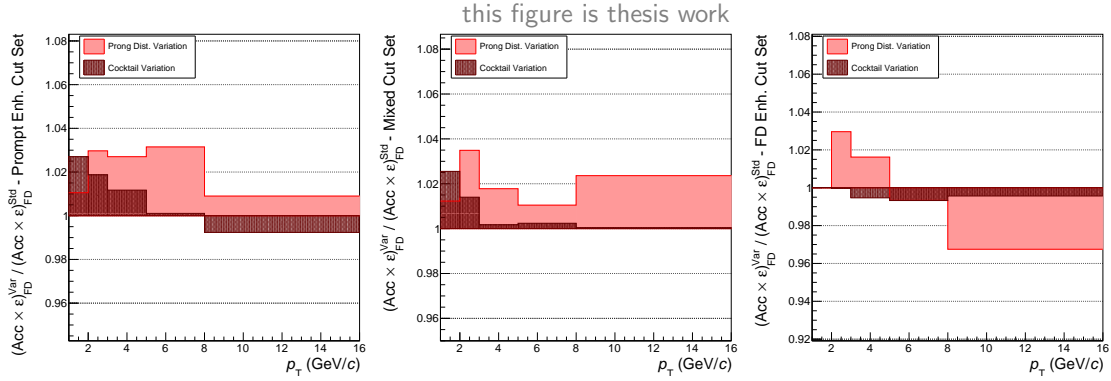
Figure 4.8.: Relative systematic uncertainties on $(Acc \times \epsilon)$ for the prompt-enhanced (left), mixed (centre) and feed-down-enhanced (right) cut sets.

Table 4.6.: Systematic uncertainty on the $(Acc \times \epsilon)$ for feed-down D^0 mesons.

p_T Bin (GeV/c)	Cut Set	$(Acc \times \epsilon)$ Systematic Uncertainty	
		Decay Description (%)	Cocktail (%)
1 to 2	Max. prompt	+1.1	+2.7
1 to 2	Mixed	+1.2	+2.6
2 to 3	Max. prompt	+3.0	+1.9
2 to 3	Mixed	+3.5	+1.4
2 to 3	Max. feed-down	+3.0	−0.03
3 to 5	Max. prompt	+2.7	+1.2
3 to 5	Mixed	+1.8	+0.17
3 to 5	Max. feed-down	+1.6	−0.54
5 to 8	Max. prompt	+3.1	+0.11
5 to 8	Mixed	+1.0	+0.24
5 to 8	Max. feed-down	−0.67	−0.68
8 to 16	Max. prompt	+0.90	−0.76
8 to 16	Mixed	+2.4	+0.04
8 to 16	Max. feed-down	−3.2	−0.44

the yield extraction was found to be larger and these simulations require a large amount of CPU time and storage, they have not been carried out within the course of this thesis.

4.7.3. Propagation of Yield Extraction and Acceptance times Efficiency Systematic Uncertainties

In order to estimate their combined influence on the minimisation results, the raw yields and the $(Acc \times \epsilon)$ values are varied inside the estimated uncertainties and the minimisation is repeated for all combinations of variations. For each raw yield, three

Table 4.7.: Systematic uncertainty on the corrected yield derived from the systematic uncertainty of the yield extraction and the feed-down efficiency determination.

	Corrected Yield Systematic Uncertainty			
p_T (GeV/c)	Prompt D^0 (%)		Feed-Down D^0 (%)	
1 to 2	-18.6	$+7.7$	-64.8	$+39.6$
2 to 3	-17.4	$+16.6$	-35.0	$+35.4$
3 to 5	-5.9	$+5.5$	-10.9	$+10.2$
5 to 8	-8.6	$+8.1$	-8.6	$+18.3$
8 to 16	-21.7	$+20.7$	-30.1	$+35.6$

different cases are evaluated: unmodified raw yield N_X, $N_X - \sigma_\mathrm{syst.}$ and $N_X + \sigma_\mathrm{syst.}$ with the systematic uncertainty $\sigma_\mathrm{syst.}$. The systematic uncertainties on the $(\mathrm{Acc} \times \epsilon)$ from the decay description are used only with their actual sign or the respective $(\mathrm{Acc} \times \epsilon)$ stays unmodified. The extrema of the resulting cross section values are used to define the combined systematic uncertainty shown in Tab. 4.7. The systematic uncertainty on the yield extraction is dominating the uncertainty on the corrected yields.

4.7.4. Cut Variation

An exact description of the cut variables by the MC simulations leads to analysis results independent of the cut values. If the dependence on a cut variable in the data is not reproduced in the MC simulation the analysis results are biased. With the help of a cut variation, the influence of the cut-value choice on the analysis results can be assessed. The cut variation is done for L_xy as well as $\cos(\theta_\mathrm{Pointing,xy})$. In the plane of L_xy and $\cos(\theta_\mathrm{Pointing,xy})$ as shown in Fig. 4.9, the D^0 candidate sets have two variable borders defined by cuts each in L_xy and $\cos(\theta_\mathrm{Pointing,xy})$. L_xy is varied by $\pm 2.5\,\sigma_{L_\mathrm{xy}}$ in steps of $0.5\,\sigma_{L_\mathrm{xy}}$. The $\cos(\theta_\mathrm{Pointing,xy})$ is varied by ± 0.002, ± 0.001, ± 0.0006, ± 0.0004, ± 0.0002 and ± 0.0001. A trial will be only considered if all invariant-mass fits have a significance larger than 2. The resulting systematic uncertainties from the cut variation are listed in Tab. 4.9.

4.7.5. Normalisation of the Decay Length

The cut on the normalised decay length in the xy-plane L_xy is the essential point of this analysis, as it is used to define the disjoint D^0 candidate sets.
The normalisation by the resolution of L_xy at low p_T depends highly on the quality of the description of the secondary-vertex reconstruction and the underlying impact-parameter resolution by the MC simulation. In order to estimate the influence of resolution of L_xy, the analysis has been repeated twice, cutting on either
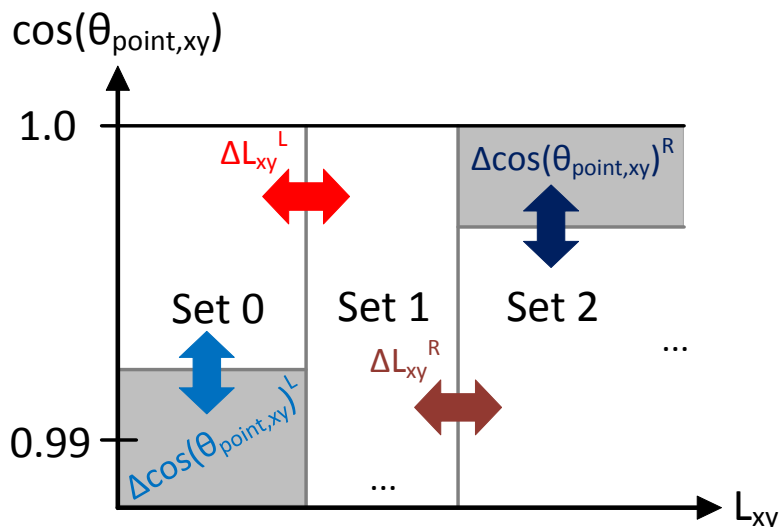
Figure 4.9.: Schematic drawing of the D^0 sets in the L_{xy}-cos($\theta_{\mathrm{Pointing,xy}}$)-plane with the applied cut variations.

Table 4.8.: Maximum cross section deviation found using the decay length and the decay length in xy as alternative cut variables.

	Systematic Uncertainty (%)			
p_{T} (GeV/c)	Prompt D^0		Feed-Down D^0	
1 to 2	-0	$+16$	-28	$+25$
2 to 3	-0	$+11$	-25	$+0$
3 to 5	-0	$+14$	-26	$+0$
5 to 8	-0	$+19$	-24	$+0$
8 to 16	-0	$+5.2$	-7.9	$+3.0$

the decay length l or the decay length in the xy-plane l_{xy} instead of L_{xy}. The maximum deviation from the results based on L_{xy} are presented in Tab. 4.8. The variations caused by the normalisation indicate an imperfection in the description of the vertex-reconstruction performance in the simulation which defines the decay length resolution. This was not relevant for previously published D^0 analyses, as L_{xy} was used to reject background with marginal influence on (Acc $\times$ ϵ) for D^0 mesons [63].

4.7.6. Total Systematic Uncertainty

The different contributions to the systematic uncertainties are added quadratically to obtain the total systematic uncertainty shown in Tab. 4.9. The PID as well as

the tracking uncertainties are taken from [94] as the corresponding cuts are also adopted from this analysis.

In general, the systematic uncertainties on the corrected yield for feed-down D^0 mesons is larger than that for prompt D^0 mesons. The systematic uncertainty in the first p_T bin is clearly dominated by the cut variation. The contribution to uncertainty from the cut variation on the corrected feed-down D^0 yield is 153 %. This can be attributed to the fact, that in this p_T bin only two cut sets are used. Without the feed-down-enhanced set, the corrected feed-down D^0 yield is only constrained by the minor contribution in the mixed and prompt-enhanced cut sets and hence more sensitive to fluctuations. As a consequence, the corrected feed-down D^0 yield in this p_T bin is not reliable. On the other hand, the corrected prompt D^0 has an uncertainty of 20 %. Above $p_T = 2\,\mathrm{GeV}/c$, the other contributions to the systematic uncertainty dominate.

In the p_T range between $3\,\mathrm{GeV}/c$ to $8\,\mathrm{GeV}/c$, the systematic uncertainty is at its minimum. The systematic uncertainty due to the normalisation of the decay length is dominant. This is a clear indication, that the description of the decay length and its resolution needs to be studied in further detail. The overall smallest systematic uncertainty is achieved for the p_T bin ranging from $3\,\mathrm{GeV}/c$ to $5\,\mathrm{GeV}/c$.

Above $p_T = 8\,\mathrm{GeV}/c$, the systematic uncertainty is dominated by the yield extraction suffering from low statistics.

Dedicated simulations without enhancements of single B hadron decay channels from at least PYTHIA and EvtGen may allow to reduce the systematic uncertainty on the $(\mathrm{Acc} \times \epsilon)$ determination. In order to reduce the systematic uncertainty due to the dependence of the analysis results on the cuts and the normalisation of the decay length, the description of the secondary-vertex properties needs to be studied in further detail in both data and MC simulations. With the present data set, it is not obvious how to reduce the systematic uncertainty on the yield extraction. However, in this study the uncertainty resulting from each mass fit was considered to be independent. This is a conservative assumption. With more statistics, more detailed studies could be performed. A further study which could lead to an improvement of the systematic-uncertainty handling is the integration of the systematic uncertainties of, e.g., the yield extraction into the weighting matrix used for the calculation of the χ^2 (cf. Ch. 4.2).

Table 4.9.: Summary of all systematic uncertainties of the corrected yield of prompt and feed-down D^0.

p_T (GeV/c)	1 to 2		2 to 3		3 to 5		5 to 8		8 to 16	
Production mechanism	**Prompt**	**FD**	**Prompt**	**FD**	**Prompt**	**FD**	**Prompt**	**FD**	**Prompt**	**FD**
Cut variation (%)	20	153	6.9	18	2.1	7.5	3.3	17	4.0	14
Yield extraction and FD efficiency (%)	−13 +4.6	−39 −27	−11 +17	−24 +22	−4.1 +3.8	−7.6 +6.8	−4.4 +4.0	−9.9 +12	−15 +14	−22 +28
Decay Length Normalisation	−0 +16	−28 +25	−0 +11	−25 +0	−0 +14	−26 +0	−0 +19	−24 +0	−0 +5.2	−7.9 +3.0
PID[1] (%)	5	5	0	0	0	0	0	0	5	5
Tracking efficiency[1] (%)	6	6	6	6	6	6	6	6	6	6
Total (%)	−25 +27	−161 +168	−15 +15	−40 +29	−7.6 +16	−28 +12	−8.1 +21	−31 +21	−17 +17	−28 +32

[1]Taken from [94].

4.8. Cross Sections

In this section, the production cross section for prompt and feed-down D^0 mesons obtained with the feed-down-separation method using cut variations are presented. The cross sections are calculated as follows:

$$\frac{\mathrm{d}\sigma_X^{D^0}(p_T)}{\mathrm{d}p_T} = \frac{1}{2 \cdot 2y_{\mathrm{fid}}} \frac{N_X(p_T)|_{|y|<y_{\mathrm{fid}}}}{(\mathrm{Acc} \times \epsilon) \cdot \mathrm{BR} \cdot \mathcal{L}} \tag{4.12}$$

with the prompt or feed-down production denoted by X. The factor of two in the denominator is needed as the corrected yield N_X contains both particles and antiparticles, the rapidity interval $\Delta y = 2y_{\mathrm{fid}}$ depends on the p_T of the D^0 mesons (cf. Ch. 4.3.3). The cross section is provided for the rapidity interval of $-0.96 < y_{\mathrm{cms}} < 0.04$. BR denotes the branching ratio of analysed decay channel $D^0 \rightarrow K^-\pi^+$ which is $(3.88 \pm 0.05)\,\%$ [1]. The integrated luminosity $\mathcal{L}$ can be determined by using the number of inelastic interactions $N_{\mathrm{V0AND}}^{\mathrm{tot}}$ triggered using the coincidence of V0-A and V0-C whose cross section $\sigma_{\mathrm{V0AND}}^{\mathrm{tot}} = (2.09 \pm 0.07(\mathrm{syst}))\,\mathrm{b}$ was measured using a van-der-Meer scan [108] and calculated according to

$$\mathcal{L} = \frac{N_{\mathrm{V0AND}}^{\mathrm{tot}}}{\sigma_{\mathrm{V0AND}}^{\mathrm{tot}}} \ . \tag{4.13}$$

4.8.1. Prompt D^0 Production

The cross section for the production of prompt D^0 mesons is shown in Fig. 4.10. The data points obtained using the method developed within this thesis are shown in black. The corresponding statistical uncertainty and the systematic uncertainty are depicted using error bars and a light grey box, respectively. The result published in [94] is shown in blue and has been rebinned for direct comparison. Furthermore, the FONLL prediction [65, 66] scaled using a Glauber model [32, 33] and the corresponding total uncertainty are shown in purple. The scaling using a Glauber model is based on an incoherent superposition of binary collisions not taking into account potential CNM effects. The result published in [94], is consistent with the absence of CNM effects. Both methods agree within their systematic uncertainties. The measurement results are consistently above the central value of the FONLL predictions. Except for the first p_T, the feed-down-separation method using cut variations is lower than the published results. In Fig. 4.11, the ratio of the production cross sections obtained using this and the published method is shown. The statistical uncertainties are calculated assuming the two methods to be uncorrelated. The correlated component of the statistical uncertainty is approximately that of the mixed cut set, which is much smaller than the dominant statistical uncertainties of the prompt and feed-down-enhanced cut sets. This hypothesis is supported by the statistical uncertainties of this method being significantly larger

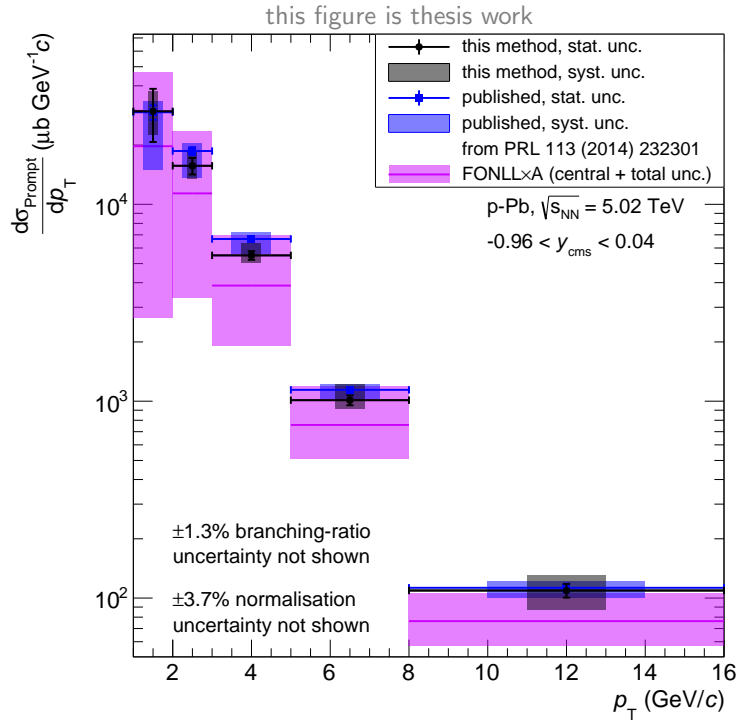**Figure 4.10.:** Production cross section for prompt D^0 measured in p–Pb collisions at $\sqrt{s_{NN}} = 5.02\,\text{TeV}$ within $-0.96 < y_{cms} < 0.04$. The published results are taken from [94].
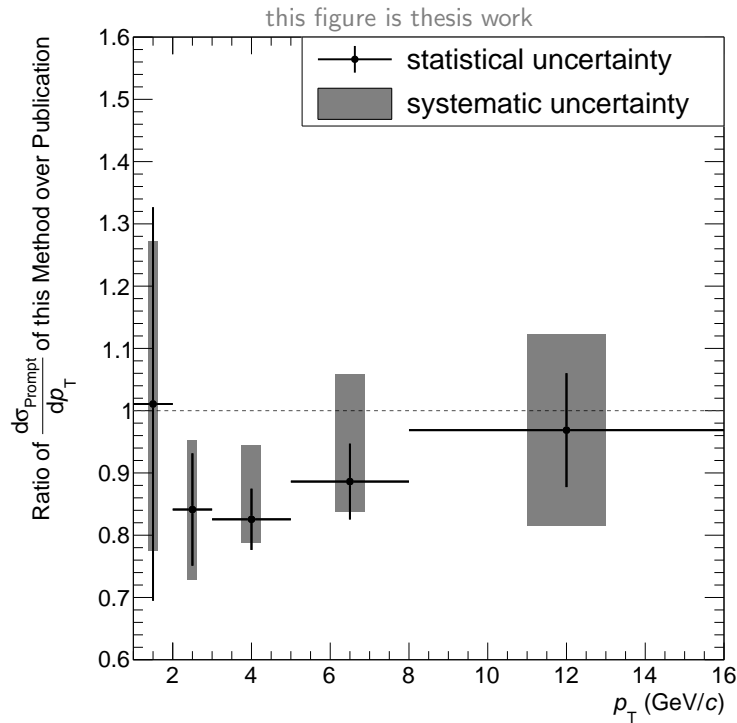

Figure 4.11.: Ratio of the production cross section for prompt D^0 obtained with feed-down-separation method based using cut variations and the method published in [94] for data from p–Pb collisions at a centre-of-mass energy of $\sqrt{s_{NN}} = 5.02\,\text{TeV}$ in the rapidity range from $-0.96 < y_{cms} < 0.04$.
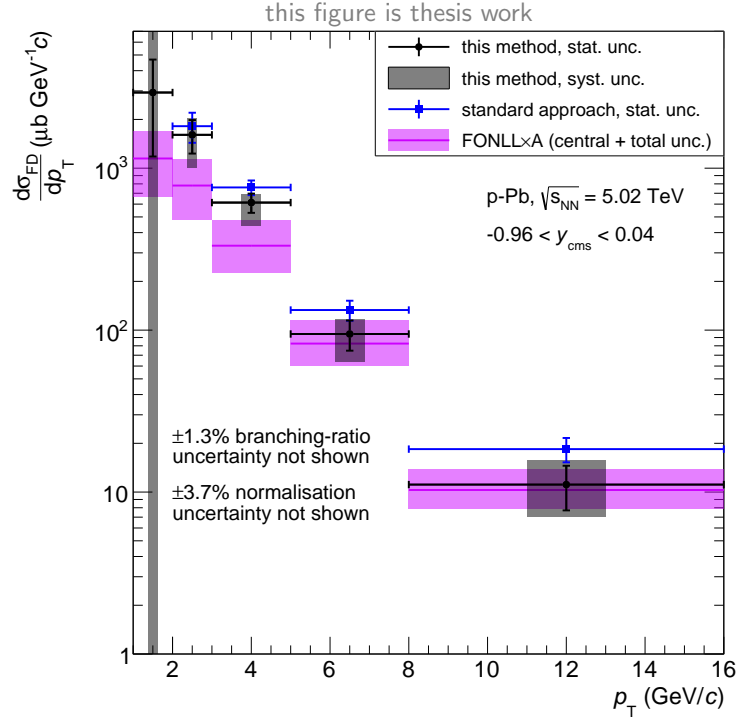
Figure 4.12.: Production cross section for feed-down D^0 measured in p–Pb collisions at $\sqrt{s_{\mathrm{NN}}} = 5.02\,\mathrm{TeV}$ within $-0.96 < y_{\mathrm{cms}} < 0.04$.

than that of the published method. Furthermore, the systematic uncertainties specific to this method are shown, excluding the systematic uncertainty on the PID and the tracking efficiency. At low p_{T}, the cut-variation method has smaller systematic uncertainties than the published results. This is explained by the large uncertainty on the FONLL calculations at low p_{T} used for the feed-down subtraction of the published results (cf. Fig. 4.1).

4.8.2. Feed-Down D^0 Production

The cross-section for the feed-down production of D^0 mesons is shown in Fig. 4.12. The data points obtained using this analysis method are shown in black. The corresponding statistical uncertainty and the systematic uncertainty are depicted using error bars and a light grey box, respectively. The blue data points are derived by correcting the feed-down-enhanced cut set for $(\mathrm{Acc} \times \epsilon)$ without subtracting the residual contribution from prompt D^0 production. As a consequence, these data points are always above the correct feed-down D^0 production cross section. In the first p_{T} bin it is not possible to define a feed-down-enhanced cut set and hence the corresponding data point is missing. Furthermore, the FONLL prediction [65, 66] scaled using a Glauber model [32, 33] not taking into account CNM effects with the central value and the corresponding total uncertainty is shown in purple.

Although the first p_{T} bin is in agreement with FONLL according to its statistical uncertainty, the large systematic uncertainty does not allow any statement on this data point. In the p_{T} range from $2\,\mathrm{GeV}/c$ to $5\,\mathrm{GeV}/c$, the measurement is higher than the FONLL prediction. Above $5\,\mathrm{GeV}/c$ in p_{T}, the measurement value is with in the total uncertainty of the prediction and matches the central value within the statistical uncertainty. The systematic and statistical uncertainty of the measurement in this p_{T} range are of a comparable size.

4.9. Summary

The prompt D^0 cross-section obtained using the feed-down separation using cut variation method is in agreement with the published results in [94]. The usage of disjoint cut sets leads to higher demand in statistics compared to the published analysis and therefore p_{t} bins have to be merged. At low p_{T}, the systematic uncertainties of this method are smaller than the published results. Above a p_{T} of $5\,\mathrm{GeV}/c$, the FONLL calculations used for feed-down subtraction in the publication become more precise and the systematic uncertainties shrink drastically. The feed-down D^0 cross section is in agreement with the predictions from FONLL calculations [65, 66] using a Glauber model based scaling. In order to extend the measurement at low p_{T}, either more statistics or an increased secondary-vertex resolution improving the separation of the contributions and the secondary-vertex reconstruction efficiency is needed to allow the definition of a cut set isolating the feed-down component with sufficient statistical precision.

A quantitative statement on CNM effects using the cut-variation method is not feasible given the size of the uncertainties and without a reference measurement in pp collisions.

The clear advantage of the cut-variation feed-down-separation method is that it gives access to both prompt and feed-down D^0 mesons. Feed-down D^0 mesons can be used to study new physics observables as e.g. correlations of feed-down D^0 mesons.

5. ALICE Inner Tracking System Upgrade

During the Long Shutdown 2 (LS2) of the LHC in 2019/2020, the ALICE detector will be substantially upgraded to enhance its physics capabilities with a focus on high-precision measurements of rare processes at low p_T. This chapter introduces the ALICE upgrade plans and in particular the ITS upgrade. Based on the design objectives of the upgraded ITS, the pixel chip requirements are outlined and the technology choice is motivated. Furthermore, the Monolithic Active Pixel Sensor (MAPS) Research and Development (R&D) with a focus on the prototypes of the ALPIDE family is discussed.

5.1. ALICE Upgrade

In order to enable the high precision measurement of rare probes at low p_T, the ALICE upgrade programme [109] is built along two lines: the improvement of the vertex-reconstruction and tracking capabilities, in particular at low p_T, and the preparation for a significant increase in interaction rate. The LHC foresees a luminosity increase for Pb–Pb collisions to $L = 6 \times 10^{27}\,\mathrm{cm}^{-2}\mathrm{s}^{-1}$ resulting in a Pb–Pb interaction rate of 50 kHz [110]. The vast amount of combinatorial background in heavy-ion collision makes triggering inefficient [111]. As a consequence, the strategy of ALICE is to read out all Pb–Pb interactions which is impossible with the current readout rate of 500 Hz in Pb–Pb collisions [112]. The integrated luminosity to be recorded after the upgrade will amount to $10\,\mathrm{nb}^{-1}$, corresponding to a factor 100 increase in terms of statistics of minimum-bias events compared to the physics programme until LS2. The reference data samples in pp and p–Pb collisions will be of $6\,\mathrm{pb}^{-1}$ and $50\,\mathrm{nb}^{-1}$, respectively.

In summary, the detector upgrade consists of the following sub-system upgrades:

- The beam-pipe radius will be reduced from 29.8 mm to 19.2 mm, allowing the innermost layer of the central-barrel silicon tracker to be moved closer to the interaction point.

- New high-resolution, high-granularity, low material-budget silicon trackers:

  - The Inner Tracking System (ITS) [64] covering $-1.2 < \eta < 1.2$ will feature an improved pointing resolution, tracking efficiency and p_T resolution at low p_T, and an increased readout rate.

- The Muon Forward Tracker (MFT) [113] covering $-3.6 < \eta < 2.45$ will add additional tracking planes in front of the absorber of the Muon Spectrometer (cf. Fig. 3.1).

- The TPC wire chambers will be replaced by Gas Electron Multiplier (GEM) detectors and new electronics allowing for a continuous readout will be installed [84, 114].

- The forward trigger detectors and the Zero-Degree Calorimeter (ZDC) [112] will be upgraded to cope with the increased interaction rate.

- The readout electronics of the Transition Radiation Detector (TRD), TOF detector, Photon Spectrometer (PHOS) and Muon Spectrometer will be upgraded for high rate operation and increased the readout rate [112].

- The online and offline systems (O^2 project) [115] will be upgraded to cope with the expected data volume during data-taking, reconstruction and simulation.

5.2. Inner Tracking System Upgrade Design Objectives

In order to improve the vertex-reconstruction capabilities with a focus on secondary vertex identification from decays and the tracking at low p_T, the following design objectives were specified [64]:

Impact parameter resolution:
   The impact parameter resolution will be improved by a factor of 3 and 5 in the $r\varphi$ and z-coordinate, respectively, at a p_T of $500 \, \text{MeV}/c$ as shown in Fig. 5.1 (left). To achieve this performance, the innermost detector layer will be moved closer to the interaction point from $39 \, \text{mm}$ to $23 \, \text{mm}$. Furthermore, the material budget of the inner layers will be reduced to $0.3 \, \% \, X_0$ per layer. For the outer layers, a value of $1.0 \, \% \, X_0$ is aimed for. The pixel size will be reduced from $50 \, \mu\text{m} \times 425 \, \mu\text{m}$ to about $30 \, \mu\text{m} \times 30 \, \mu\text{m}$.

Tracking efficiency and p_T resolution at low p_T:
   The tracking efficiency and the p_T resolution at low p_T will be improved. This will be achieved by using 7 instead of 6 layers, resulting in an additional track point. Furthermore, the deployment of silicon pixel sensors instead of silicon drift sensors and silicon strip sensors as in the SDD and in the SSD, leads to a better single-point resolution for the entire ITS. The expected performance gain in terms of tracking efficiency is outlined in Fig. 5.1 (right).

Readout rate:
   The readout rate of the ITS will be increased from about $1 \, \text{kHz}$ to $50 \, \text{kHz}$ and $200 \, \text{kHz}$ in Pb–Pb and pp collisions, respectively.
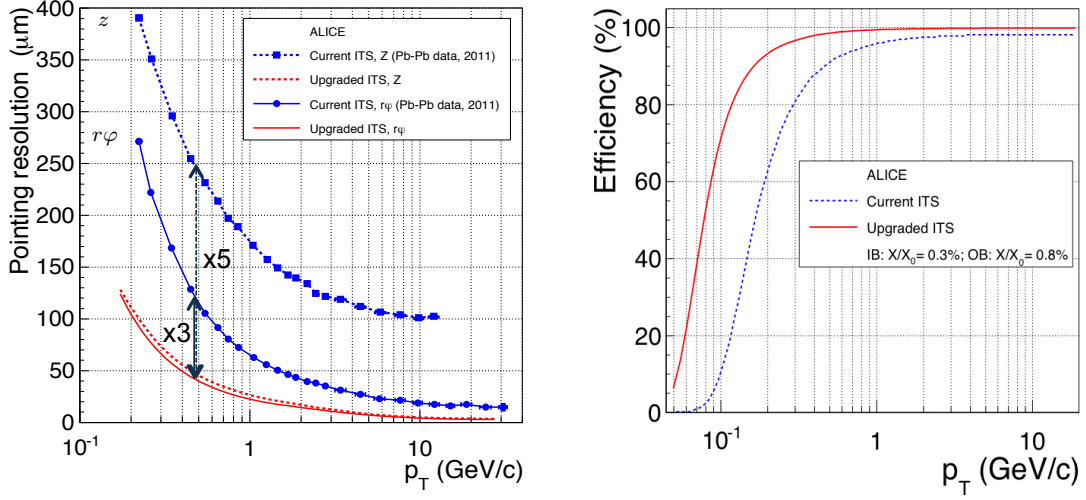
Figure 5.1.: Pointing resolution (left) and tracking efficiency (right) of the upgraded ITS obtained from MC simulations, taken from [64].

Maintenance:

> The upgraded ITS is designed to allow easy removal and insertion during the yearly shutdown periods.

5.3. Layout and Environment of the Upgraded Inner Tracking System

The upgraded ITS, as shown in Fig. 5.2, consists of seven layers. The innermost three layers form the Inner Barrel (IB). The middle and the outer layers form

Table 5.1.: Dimensions of the upgraded ITS [64].

	Layer	Radius (mm)	Stave length (mm)
Inner Barrel (IB)	0	23	
	1	31	271
	2	39	
Outer Barrel (OB)	3	194	843
	4	247	
	5	353	1475
	6	405	
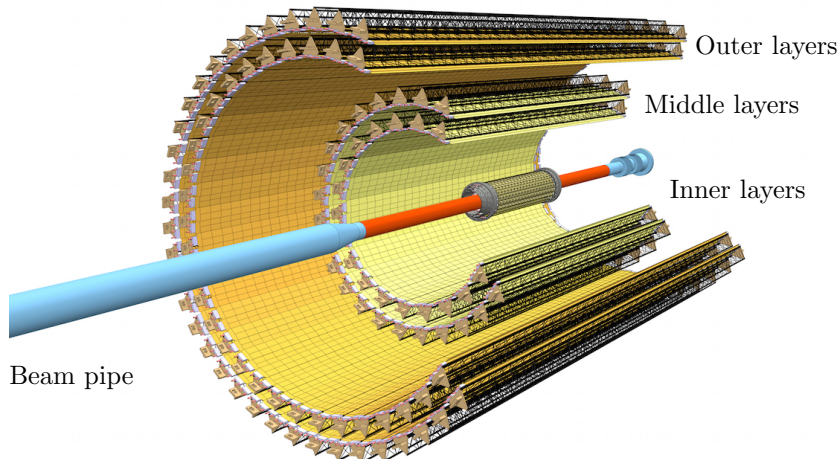
Figure 5.2.: Layout of the upgraded ITS, taken from [64].

together the Outer Barrel (OB). The radii of the layers and the length of the staves forming the layers are summarised in Tab. 5.1.

The requirements on the pixel chips are shown in Tab. 5.2. Although these requirements are slightly different for the IB and OB, the goal is to deploy the same chip on all seven layers. The upgraded ITS will cover the pseudo-rapidity range of $|\eta| < 1.22$ for 90 % of the most luminous beam interaction region. The radial positions of the layers were optimised in order to achieve the best combined performance in terms of pointing resolution, p_{T} resolution and tracking efficiency as well as matching efficiency to TPC tracks in Pb–Pb collisions. The recurring hit rate of a single pixel was estimated to be about 10 Hz and the hit densities will be a few $10 \, \mathrm{cm}^{-2}$/event. At a fake-hit rate of 10^{-5}/pixel/event, the hit density in the outer barrel is dominated by fake hits. The total detector surface will amount to $10.3 \, \mathrm{m}^2$ containing about 12.5×10^9 pixels with binary readout. The new detector will be operated at room temperature (20 °C to 30 °C) and cooled using water. The expected radiation load accumulated during the six years of operation at the innermost layer is expected to be 2700 krad of Total Ionising Dose (TID) and $1.7 \times 10^{13} \, 1 \, \mathrm{MeV} \, \mathrm{n}_{\mathrm{eq}}/\mathrm{cm}^2$ of Non-Ionising Energy Loss (NIEL) including a safety factor of ten. In order to meet the material-budget requirements, the silicon sensors will be thinned down to $50 \, \mu\mathrm{m}$. The material-budget requirements furthermore impose limitations on the power budget [64].

5.3.1. Choice of Pixel Chip Technology

In order to achieve the desired physics performance, the upgraded ITS has to combine very thin sensors, very high granularity and cover an area of about $10 \, \mathrm{m}^2$. Additionally, a maximum power density of $100 \, \mathrm{mW/cm}^2$ can be tolerated, but the radiation levels are only moderate compared to the other LHC experiments like

Table 5.2.: General pixel-chip requirements [64].

Parameter	Inner Barrel	Outer Barrel
Chip dimensions	15 mm × 30 mm ($r\varphi \times z$)	
Sensor thickness	50 µm	
Spatial resolution	5 µm	10 µm
Detection efficiency	> 99 %	
Fake-hit rate	$< 10^{-5}$ event^{-1}pixel^{-1}	
Integration time	< 30 µs	
Power density	$< 300\,\mathrm{mW/cm^2}$	$< 100\,\mathrm{mW/cm^2}$
Temperature	20 °C to 30 °C	
TID radiation hardness[a]	2700 krad	100 krad
NIEL radiation hardness[a]	$1.7 \times 10^{13}\,1\,\mathrm{MeV\,n_{eq}/cm^2}$	$1 \times 10^{12}\,1\,\mathrm{MeV\,n_{eq}/cm^2}$

[a]These values include a safety factor of ten, updated according to latest estimates [116].

ATLAS preparing for a maximum of $1.4 \times 10^{16}\,1\,\mathrm{MeV\,n_{eq}/cm^2}$ NIEL and 770 Mrad TID after the Phase-II upgrade [117].

Monolithic Active Pixel Sensor (MAPS), integrating both sensor and readout electronics on the same die, fulfil these requirements. In the last years, there has been significant progress on the development of MAPS. Today, MAPS are used e.g. in the STAR PXL detector [118]. By accommodating detection volume and readout circuitry on the same die, MAPS allow for very thin sensors and make an interconnection of readout and sensor chip obsolete. MAPS can be implemented cost effectively using a commercial CMOS process without the need for an expensive interconnect.

The stringent requirements of the ITS upgrade compared to previous applications as in the STAR experiment in terms of integration time ($\approx$200 µs), power consumption ($\approx 170\,\mathrm{mW/cm^2}$) and radiation hardness ($\lesssim 90\,\mathrm{kRad}$ TID and $\lesssim 10^{12}\,1\,\mathrm{MeV\,n_{eq}/cm^2}$ NIEL, both per year of operation) necessitates further R&D [119].

5.4. MAPS for the ALICE ITS Upgrade

The pixel chips for the upgraded ITS will be manufactured using the commercial 0.18 µm CMOS Imaging Sensor process by TowerJazz [120]. The process provides up to six metal layers which allow together with the small feature size of 180 nm for a high-density, low-power circuitry. Furthermore, the gate oxide thickness of about 3 nm provides a sufficient TID radiation tolerance [121]. The features most relevant for the use in ALICE are the possibility to use high-resistivity epitaxial layers and the deep p-well.

A high resistivity ($\approx$ kΩcm), 18 µm to 40 µm thick epitaxial layer serves as sensitive volume. The depletion volume of the pn-junction formed by the collection n-well

(a) Default configuration.

(b) Thicker epitaxial layer.

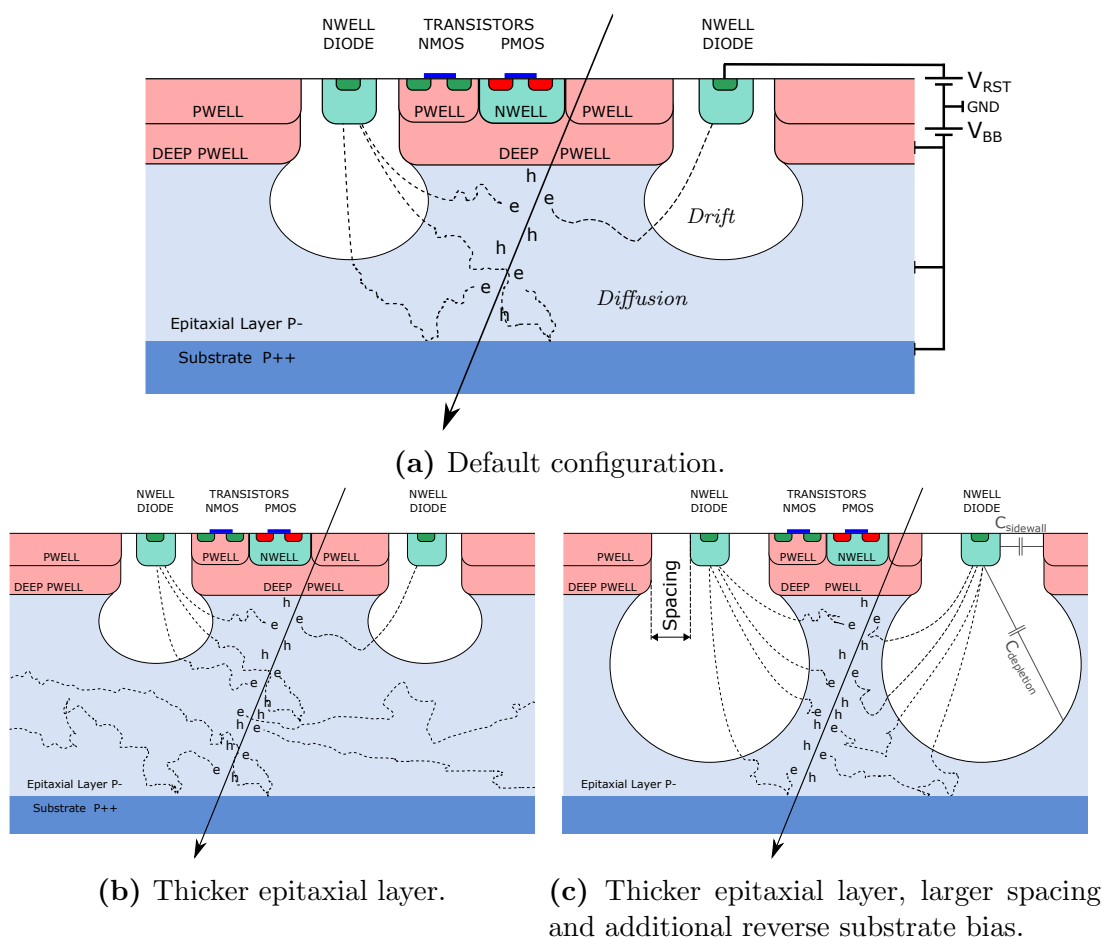**(c)** Thicker epitaxial layer, larger spacing and additional reverse substrate bias.

Figure 5.3.: Schematic cross section of a MAPS sensor on a high-resistivity epitaxial layer and different optimisation steps.

and the p-type active volume increases monotonically with the resistivity, leading to an advantage compared to a low resistivity epitaxial layers or substrate. For a further increase of the depletion volume, a moderate reverse substrate bias V_{BB} of $-6\,V$ to $-8\,V$ can be applied.

The n-wells of PMOS transistors are embedded in additional deep p-wells as shown in Fig. 5.3a in order to avoid competition in charge collection with the collection n-well reducing the efficiency of the collection n-well. Hence, CMOS logic can be used within the matrix and as consequence, complex in-pixel circuitry is possible.

5.4.1. Charge Generation and Collection in MAPS

The mean energy deposited by particles crossing material is described by the Bethe-Bloch formula [1, 122, 123]. The energy loss depends on the path length of the particle in the material and is minimal for particles with $\beta\gamma \approx 3-4$, so-called

Minimum Ionising Particles (MIPs). The Bethe-Bloch formula only describes the mean energy loss but not its fluctuations. For an absorber of about $300\,\mu m$ silicon, the fluctuations around the mean value are well described by a Landau distribution [124]. These fluctuations increase for thinner absorbers and at an absorber thickness of about $20\,\mu m$ to $30\,\mu m$ the energy loss is more accurately described by the Bichsel model [125]. A part of the energy deposit in the silicon is used for the generation of free electron-hole pairs. The remaining energy goes into the excitation of phonons, which dissipate thermally.

In contrast to hybrid pixel sensors, which feature an active layer of about $200\,\mu m$ to $300\,\mu m$ thick, the epitaxial layer used in the MAPS for the upgraded ITS is $18\,\mu m$ to $30\,\mu m$. This leads to a comparably small average charge generated by a traversing MIP of $1000\,e^-$ at an epitaxial-layer thickness of $18\,\mu m$. Due to the fluctuations, a single particle can deposit less energy. The smaller collected charge Q leads to a reduction in terms of signal voltage $\Delta V_{\mathrm{IN}} = Q/C$ for a given pixel capacitance C. In order to achieve a high signal voltage, the combination of charge collected by the central pixel in a cluster[1], called seed, and the capacitance of the pixel C needs to be optimised in order to increase the Q/C ratio. A high Q/C ratio leads to an improved signal-to-noise ratio and as a consequence reduced power consumption of the circuitry [126].

The signal induced on the electrode can be described using the Ramo-Shockley theorem [127, 128]. The small diameter of $2\,\mu m$ to $3\,\mu m$ of the collection electrode compared to the epitaxial-layer thickness leads to a weighting field only non-negligible in the close vicinity of the collection electrode [129]. Consequently, only for charge travelling close the collection electrode a signal is induced. After the arrival of the charge at the electrode, the integral of the induced signal corresponds to the collected charge. The charge collection time is with less than $100\,ns$ [130] small compared to the shaping time of $O(1\,\mu s)$ and in first approximation only the total collected charge at a pixel has to be taken into account [131].

The small size of the collection n-well ($2\,\mu m$ to $3\,\mu m$) compared to the pixel pitch of the order of $30\,\mu m$ leads to a small capacitance of the electrode of a few fF [130] as compared to what is generally done in, e.g., HV-MAPS[2] [132, 133] with an input capacitance of the order of $100\,fF$ [132].

As shown in Fig. 5.3a, in MAPS the charge is collected by two mechanisms. In the vicinity of the collection n-well, charge is collected by drift in the electric field of the depletion zone of the pn-junction formed by the collection n-well and epitaxial layer. In the undepleted part of the epitaxial layer, the charge is collected by diffusion. In the MAPS prototypes for the ITS upgrade, full depletion of the

---

[1]If the charge of a traversing particle is shared by several pixels, all pixels collecting charge form a cluster. The pixel collecting the majority of the charge is called the seed pixel.

[2]High-Voltage MAPS (HV-MAPS) are based on a commercial (HV-)CMOS process on a low resistivity substrate or epitaxial layer. The collection electrodes of these MAPS are of a similar size as the pixel itself. Depletion is achieved by applying a reverse substrate bias of up to about $100\,V$.

epitaxial layer is not reached. Potential barriers at the borders between the deep p-well ($N_A \approx 10^{18}\,\mathrm{cm}^{-3}$) and the epitaxial layer ($N_A \approx 10^{13}\,\mathrm{cm}^{-3}$) as well as between the substrate ($N_A \approx 10^{16}\,\mathrm{cm}^{-3}$) and the epitaxial layer keep the charge contained in the epitaxial layer. The potential V_{bi} at the borders can be calculated using

$$V_{\mathrm{bi}} = \frac{k_B T}{q} \ln \left(\frac{N_{\mathrm{A,p^+}}}{N_{\mathrm{A,p^-}}} \right) \tag{5.1}$$

where $N_{\mathrm{A,p^+}}$ and $N_{\mathrm{A,p^-}}$ are the doping concentrations of p-wells or substrate and the epitaxial layer, respectively [131, 134]. The factor $k_B T/q$ is the thermal potential which is about $25\,\mathrm{mV}$ at about $300\,\mathrm{K}$. The resulting potential barriers are about 7 and 12 times the thermal potential at the border to the substrate and the p-wells, respectively. The charge-collection efficiency depends on the charge-carrier lifetime and thus indirectly on the charge-collection time. The charger-carrier life time is mainly determined by impurities causing energy levels within the band gap [131]. Additionally, charge is also produced in the substrate which, however, depending on the lifetime and the path length in the substrate stays mainly uncollected [135].

A possibility to increase the amount of collected charge is increasing the epitaxial-layer thickness leading to more initial charge generation as depicted in Fig. 5.3b. For a thicker epitaxial layer and a constant depletion volume, this on the other hand leads to an increased diffusion volume. The increased diffusion leads in turn to more pixels sharing the generated charge and therefore less relative signal in the seed. Thus, the actual benefit of a thicker epitaxial layer depends on the absolute amount of charge collected in the seed pixel, which, in turn, depends on shape and size of the depletion volume. In a configuration, for which the depletion zone reaches the border of epitaxial layer and substrate, an increased epitaxial-layer thickness can lead to an increased depletion zone.

An approach to increase the signal voltage at the seed pixel is to reduce the charge sharing and concentrating it in fewer pixels. This can be achieved by enlarging the depletion volume. As mentioned above, the depletion volume can be increased by increasing the reverse bias voltage V_{RB} between the collection electrode and the substrate as the depletion volume monotonically increases as function of V_{RB}. As depicted in Fig. 5.3a, the total reverse bias voltage is $V_{\mathrm{RB}} \approx V_{\mathrm{RST}} - V_{\mathrm{BB}}$, measuring both voltages relative to the chip ground potential. In the MAPS for the upgraded ITS, the reset voltage V_{RST} cannot exceed the supply voltage of $1.8\,\mathrm{V}$. The reverse-substrate bias V_{BB} is applied via a p-guard ring surrounding the pixel matrix to the epitaxial layer and the substrate. Without the presence of a depletion zone isolating the (deep) p-wells in the matrix from the epitaxial layer, the p-wells cannot be set to a potential different from the substrate. The maximum voltage here is determined by the breakdown point of the junction of the NMOS transistors which are housed in a p-well [130].

The input capacitance C is the sum of the circuit capacitance and the junction capacitance. The circuit capacitance consists of the routing line capacitance of the
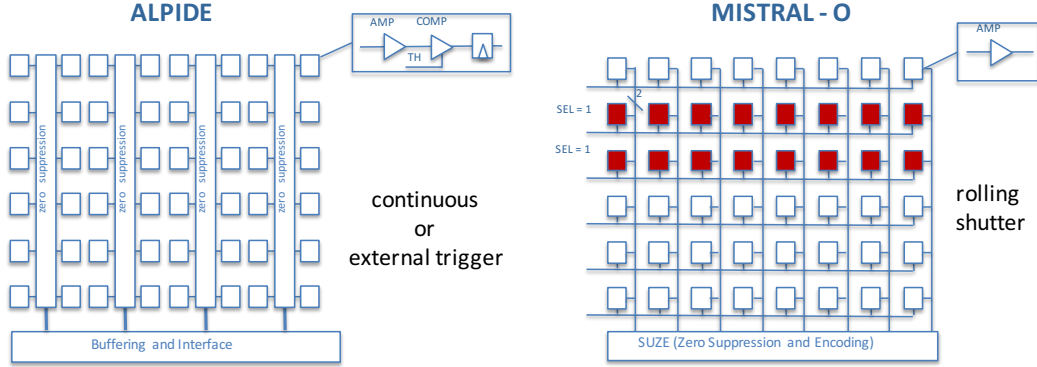
Figure 5.4.: Sketch of the architectures deployed in the ALPIDE (left) and MISTRAL (right) design stream, taken from [116].

connection from the electrode to the input transistor, the input capacitance of the input transistor and the capacitance of the reset mechanism. The junction capacitance is built up between the n-well and the undepleted epitaxial-layer volume ($C_{\mathrm{depletion}}$) as well as the surrounding p-well (C_{sidewall}) (cf. Fig. 5.3c). As the capacitance is inversely proportional to their distance, the junction capacitance can be decreased by increasing the depletion volume and increasing the spacing between the n-well diode and the surrounding p-well as sketched in Fig. 5.3c. The maximum spacing is limited mainly by the surface needed by in-pixel and general readout circuitry.

The combined optimisation is shown in Fig. 5.3c, where the epitaxial-layer thickness, the spacing and the reverse substrate bias are increased.

5.4.2. Chip Architectures

For the upgrade of the ITS, currently, two independent R&D design streams are under development. Their architectures are depicted in Fig. 5.4 showing the ALPIDE on the left and the MISTRAL on the right hand-side. The full-scale prototypes of both architectures will feature the same electrical and mechanical interfacing.

The ALPIDE architecture is based on the approach to move as much as needed complexity inside the pixel or the matrix. Each ALPIDE pixel contains its own amplifier and shaper, followed by a comparator and multiple hit buffers. The zero-suppression is performed within the matrix. In order to do this, an Address-Encoder Reset-Decoder (AERD) circuit is employed. This circuit takes care of propagating the addresses of hit pixels to the end-of-column logic and resetting the corresponding in-pixel hit buffers. As a consequence of this approach, the end-of-column logic is reduced to buffering and interface. This architecture allows to read all pixels in a global-shutter mode. This shutter can either be controlled by an external trigger

signal combined with short shutter windows, or operated in continuous acquisition mode, only being closed in between frames to move to the next hit-buffer.

The MISTRAL-O chip is based on a rolling-shutter architecture, which is, e.g., also deployed in the ULTIMATE chip for the STAR PXL detector [118]. In a rolling-shutter architecture, a row of pixels is read simultaneously and rows are read sequentially. The integration time is defined by the matrix readout time corresponding to the time the shutter needs to return to the same row. The special feature of the MISTRAL-O chip is the readout of two neighbouring rows of pixels at the same time. In the MISTRAL-O architecture, the pixel contains only an amplifier. Therefore, the analogue signals have to propagated to the end-of-column circuitry for discrimination and zero-suppression.

For a rolling shutter architecture, integration time, pixel pitch, shutter clock and power consumption are closely coupled. The integration time is the ratio of pixels per column over shutter frequency. The number of pixels per column depends on the pixel pitch for a fixed column length. The power consumption increases with the shutter frequency, as the necessary shorter signal rise times of clock and analogue signals lead to an increased current consumption. The minimum pixel pitch in the ALPIDE architecture is determined by the surface needed for the in-pixel and in-matrix circuitry. Furthermore, the hit-oriented ALPIDE architecture is by design less power-consuming, as only digital signals have to be propagated across the chip, and only the addresses of hits are propagated to the end-of-column circuitry. In summary, the ALPIDE architecture allows for smaller pixels pitches, smaller power consumption and shorter integration time in comparison to the MISTRAL architecture. At the time of writing, the ALPIDE architecture is the baseline for the upgraded ITS.

5.5. The ALPIDE family

The various ALPIDE prototypes and their key specifications are summarised in Tab. 5.3. The main goal of the R&D was to minimise the power-consumption exploiting all features provided by the TowerJazz CMOS process. The submission of the final ALPIDE chip is envisaged for the first quarter of 2016.

Within this thesis, the pALPIDEss and the pALPIDE-2 prototypes are discussed in further detail. For a discussion of the analogue prototypes see [130]. The pALPIDE-1 prototype is discussed in [130] and [136].

Table 5.3.: The prototypes of the ALPIDE family and their goals.

| Submission	Prototype	Specification & Purpose
Jul. 2012	Explorer-0	• analogue readout • $20 \times 20\,\mu m^2$ and $30 \times 30\,\mu m^2$ pixels • pixel and collection-electrode geometry • reverse substrate bias • radiation hardness
Mar. 2013	Explorer-1	• epitaxial-layer properties (thickness and resistivity)
	pALPIDEss-0	• 64×512 pixels of $22 \times 22\,\mu m^2$ • first variant of ALPIDE architecture • front-end circuit verification • verification in-matrix sparsification
Jan. 2014	Investigator-0	• parallel analogue output of 8×8 pixels • 135 mini-matrices • pixel-pitch and electrode-geometry studies • charge-collection time measurement
	pALPIDEss-1	• front-end optimisation and variations
	pALPIDE-1	• first full-scale prototype • 1024×512 pixels ($28 \times 28\,\mu m^2$) • in-pixel masking • pads over matrix • on-chip bias DACs
Dec. 2014	pALPIDE-2	• epitaxial-layer properties • final interface except high-speed link
Jun. 2015	pALPIDE-3	• front-end optimisation • three in-pixel hit buffer per pixel • high-speed link
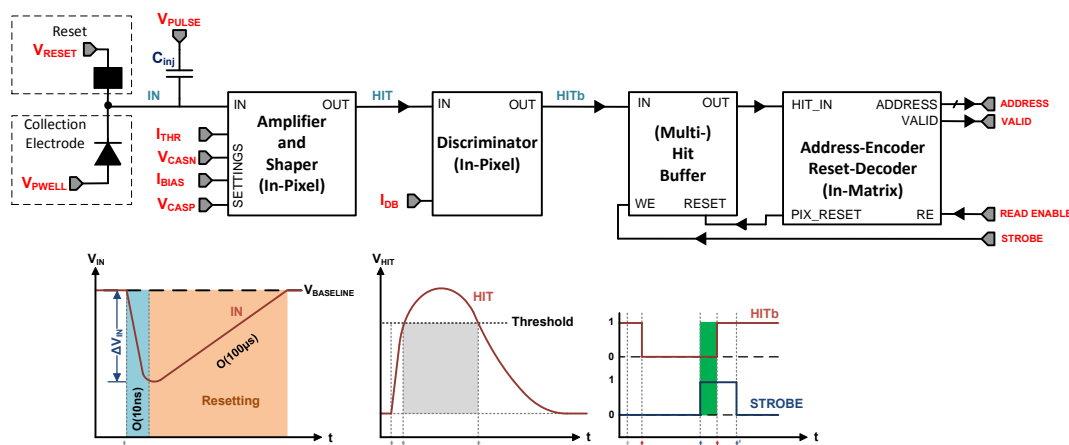
Figure 5.5.: Schematic drawing of the ALPIDE circuitry and signal flow.

5.5.1. ALPIDE Front-End Circuit

All prototypes based on the ALPIDE architecture feature a similar front-end circuitry. Below, the front-end of the pALPIDEss, pALPIDE-1 and pALPIDE-2 are explained. For a description of the optimisations deployed in pALPIDE-3 see [137].

The signal flow in the ALPIDE architecture is shown in Fig. 5.5. The voltage at the input node IN drops within the charge-collection time below 100 ns [130]. The reset mechanism lets IN return to the baseline voltage V_{BASELINE} in about 100 μs. The front-end acts as a memory to bridging the ALICE L0 trigger latency of about 1.2 μs (cf. Ch. 3.2). For this, the amplifier and shaper were designed to deliver a pulse which peaks in less than 2 μs, with a total pulse width of less than 10 μs. The relatively low speed leads to a reduction of the power consumption of the front-end. Due to the high granularity and small hit density, pile-up within a pixel is negligible. This low power consumption was also achieved by minimising the input capacitance and hence maximising the voltage excursion at the input. The discriminator transforms the analogue input signal HIT to a digital active-low signal HITb. The STROBE signal enables the input of the hit buffer. The Address-Encoder Reset-Decoder (AERD) provides the ADDRESS of the hit pixel and whether the current address is VALID to the chip periphery.

For the pALPIDE-1/2, the circuitry is shown in more detail in Fig. 5.6. In both prototypes two different pixel reset mechanisms are implemented.

The PMOS-reset is a constant-current reset mechanism which provides the current I_{RESET} when V_{IN} deviates from the baseline value. The reset current I_{RESET} can be adjusted to achieve the desired reset time and to adapt to the leakage current of the pixel. The baseline of the pixel can be regulated using V_{RESET}.

The diode reset is based on a single forward-biased diode. The advantages of the
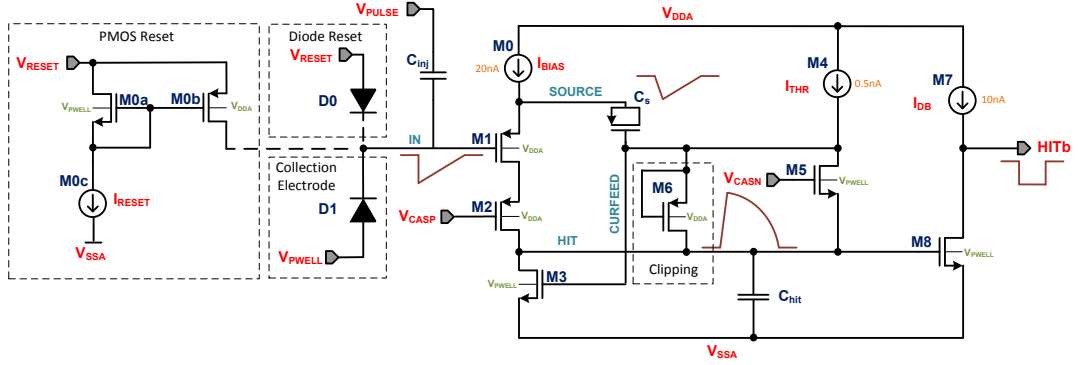
Figure 5.6.: Front-end circuitry of the pALPIDE-1/2.

diode reset are its smaller contribution to the input capacitance and its smaller dimensions. However, in contrast to the PMOS reset, the conductance of the diode increases exponentially with the voltage drop across the diode. As a consequence, the reset current depends on the leakage current and the signal voltage ΔV_{IN}. The exponential response of the reset mechanism can lead to a clipping effect, limiting the maximum difference of V_{IN} and V_{RST}, as above certain voltage drop the current is large enough to reset a signal before it is detected by the front-end circuitry. An increase of the leakage current shifts increases the baseline value of $V_{\text{RESET}} - V_{\text{IN}}$ and leads to clipping for smaller signals ΔV_{IN}.

The injection capacitor C_{inj} allows to inject a test charge into the pixel by applying a negative voltage step V_{PULSE}.

The amplifier and shaper stage consist of two current branches, one with I_{BIAS} and the one with I_{THR}. All transistors in the front-end are operated in weak inversion. As a consequence, the change in current flow is proportional to $\exp(\Delta V_{\text{gs}})$ with V_{gs} denoting the voltage between gate and source of the transistor. Without external stimulation, the input PMOS transistor M1 conducts the current I_{BIAS} provided by the current source M0. The NMOS transistor M5 conducts I_{THR} leading to a fixed voltage difference of V_{HIT} and V_{CASN}. Consequently, V_{CASN} can be used to change the baseline voltage of the HIT node V_{HIT}. M3 absorbs the sum of both current branches. As it is difficult to match M3 to M0 and M5, especially with them operating in weak inversion, a feed-back mechanism has been implemented to adjust the conductivity of M3. The cascode M2 circumvents the Miller effect [138] for the input transistor. The source of M1 (SOURCE) is capacitively coupled to the current-feedback node CURFEED. The capacitance of SOURCE is much larger than the capacitance of HIT. At arrival of a negative input pulse, the voltage drop at the gate of M1 increses its current which flows inbetween SOURCE and HIT. With some delay, V_{SOURCE} and consequently V_{CURFEED} follow V_{IN}. This leads to a reduced conductivity of M3 and V_{HIT} increases. The increase of V_{HIT} lets M5 close. Consequently, I_{THR} charges up C$_{\text{s}}$, leading to an increase of V_{CURFEED} and increases the conductivity of M3 again. The clipping transistor M6 limits the output signal once V_{HIT} exceeds approximately

V_{CURFEED}. The rise time of the pulse is defined by the time I_{THR} and I_{BIAS} need to charge the `HIT` node. Additional charge stored at `SOURCE` can speed up this process significantly. The pulse duration depends on the clipping point and how quickly `CURFEED` is charged up to increase the conductivity of `M3`.

The voltage gain of the input PMOS `M1` can be estimated under the assumption that it behaves like an ideal source follower, i.e. $\Delta V_{\text{IN}} \approx \Delta V_{\text{SOURCE}}$. This leads to charge transfer of $Q_{\text{SOURCE}} \approx C_{\text{SOURCE}} \cdot \Delta V_{\text{IN}}$ from C_{SOURCE} to C_{HIT} resulting in the following equation:

$$V_{\text{HIT}} \approx \frac{Q_{\text{SOURCE}}}{C_{\text{HIT}}} \approx \frac{C_{\text{SOURCE}} \cdot \Delta V_{\text{IN}}}{C_{\text{HIT}}} \tag{5.2}$$

$$\approx \frac{C_{\text{SOURCE}}}{C_{\text{HIT}}} \cdot \frac{Q_{\text{IN}}}{C_{\text{IN}}} \ . \tag{5.3}$$

The resulting voltage gain is

$$g = \frac{C_{\text{SOURCE}}}{C_{\text{HIT}}} \ . \tag{5.4}$$

Consequently, the capacitances of the circuitry are optimised to achieve

$$C_{\text{SOURCE}} \gg C_{\text{HIT}} \ . \tag{5.5}$$

`M7` and `M8` form a second stage which discriminates and inverts the `HIT` signal. I_{DB} is the maximum current consumed by this stage. In static operation, its current is close to zero. A pulse on `HIT` increase the transconductance of `M8` and the node `HITb` is discharged. When the `HIT` node returns to its baseline, the current through `M8` becomes smaller than I_{DB} and `HITb` is charged. This stage is not present in the pALPIDEss.

The power consumption of the front-end circuit per pixel is

$$P = V_{\text{DDA}} \cdot (I_{\text{BIAS}} + I_{\text{THR}}) \approx 40\,\text{nW} \ , \tag{5.6}$$

as the dynamic power consumption is negligible.

All bias parameters are supplied chip-wide and cannot be tuned on a pixel-by-pixel basis. As a consequence, special emphasis was put on the spatial uniformity during the design phase. For the selection of the bias parameters, an important aspect is the influence of the reverse substrate bias on the NMOS transistors, as they are housed in a p-well. While the n-wells are connected to the supply voltage V_{DDA}, the p-wells are connected to V_{BB}. Lowering the bulk voltage of an NMOS transistor results in an increase of its threshold voltage [139, 140], which on the circuit-level has to be compensated for by increasing V_{CASN} in order to achieve a similar baseline of V_{HIT}.
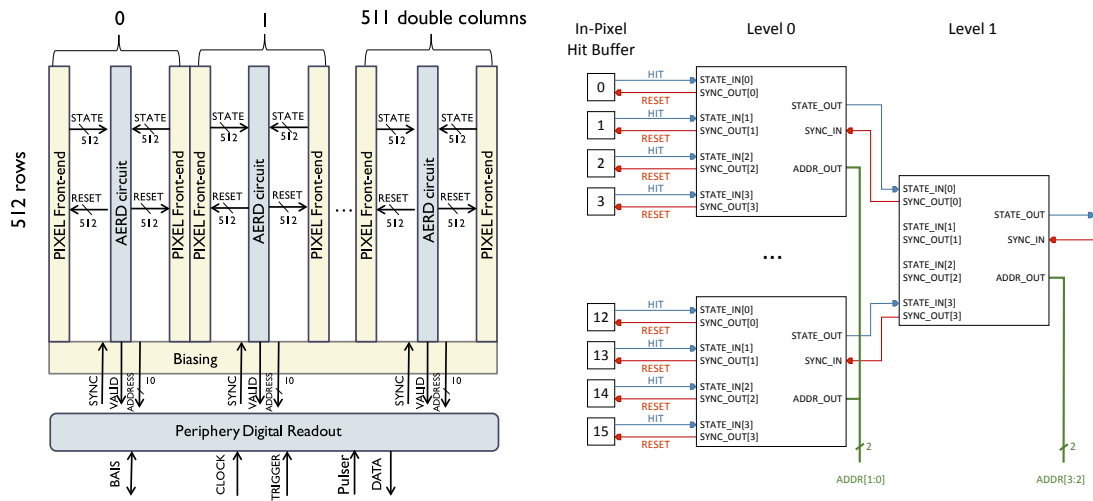
Figure 5.7.: Left: readout structure of the ALPIDE chip, taken from [141]. Right: hierarchical AERD scheme, adapted from [141].

5.5.2. Address-Encoder and Reset-Decoder Circuit

With the Address-Encoder Reset-Decoder (AERD) circuit a hit-oriented readout is achieved. Two neighbouring columns share the same readout-circuitry as depicted in Fig. 5.7 (left). The double-column structure of the AERD circuitry together with the hierarchic scheme (cf. Fig. 5.7, right) leads to a better usage of the available space for routing and circuitry.

Each hierarchy level consists of blocks combining four inputs. Four inputs is the best trade-off between numbers of transistors and routing lines required for the implementation [141]. The STATE_OUT signal is defined as the logical OR of the STATE_IN inputs. The SYNC_IN signal enables the ADDR_OUT output of the respective block. The SYNC_IN signal is forwarded to the SYNC_OUT signal with active STATE_IN and the highest priority. In the in-pixel hit buffer a falling edge of the RESET signal triggers its reset. This completely asynchronous circuit is operated with a frequency of 10 MHz in pALPIDE-1/2 and 40 MHz starting from pALPIDE-3. A more detailed description as well as an estimate of the power consumption of the AERD circuitry in the pALPIDE chips can be found in [141].

5.5.3. pALPIDEss

The pALPIDEss is a small-scale prototype implementing blocks of the ALPIDE architecture. It features pixels of 22 μm pitch arranged in 64 columns and 512 rows. The chip is split in four regions along the column direction (cf. Tab. 5.4). The collection electrode of all pixels is made of a n-well implant and Shallow-Trench Isolation (STI) to separate the collection n-well from the surrounding p$^+$

Table 5.4.: Pixel variants of the pALPIDEss.

Sector	Row	Column	Pixel Variant	Pulsing Capacitor
0	0 to 127	0 to 63	$2.53 \times 2.53\,\mu m^2$ octagon	no
1	128 to 255	0 to 63	$2.53 \times 2.53\,\mu m^2$ octagon	yes
2	256 to 383	0 to 63	$2.25 \times 1.98\,\mu m^2$ rectangle	yes
3	384 to 511	0 to 63	$2.25 \times 1.98\,\mu m^2$ rectangle	no

ring. All pixels have an opening of $5.56\,\mu m$ diameter of the p^+ square surrounding the collection electrode. Half of the pixel have injection capacitors which are $0.14\,fF$. This capacitance is small compared to the expected input node capacitance of the order of $1\,fF$ [130]. Only the injection capacitors in the rows 254 to 257 are connected to an analogue input pad, the other injection capacitors are connected to ground. The pixels are the same in all pALPIDEss generations and variants. All pixels of the pALPIDEss have a diode reset.

In the pALPIDEss a Dynamic Memory Cell (DMC) based on a capacitor of $80\,fF$ is used as in-pixel hit buffer. During reset, this capacitor is charged. The `HIT` signal from the front-end controls the discharging of the capacitor via a transistor. The length of the `HIT` pulse hence needs to be long and high enough to discharge the capacitor below threshold.

The pALPIDEss does not feature in-pixel masking. The priority encoder is based on standard CMOS logic cells.

The AERD implementation of the pALPIDEss is slightly different compared to the pALPIDE. In the pALPIDEss, single-column priority encoders with 512 inputs are deployed. Furthermore, an end-of-column priority encoder combines the 64 columns. The control signals of the priority encoder are directly accessible from IO-pads giving full control to the readout system.

pALPIDEss-0

The pALPIDEss-0 is the first version. In order to minimise the front-end capacitance, the PMOS input transistor was placed in the collection n-well (cf. Fig. 5.8a). This measure allowed for a very short input routing line, reducing its capacitance. In every transistor, parasitic diodes are connecting the source and drain implant to the bulk of the transistor. The pixel as sketched in Fig. 5.8a, however, has the disadvantage that these parasitic diodes of the input transistor are connected to the collection n-well which is on V_{IN} and not to a standard n-well, which is connected to the supply voltage V_{DDA}. This diode connecting source and the collection n-well competes with the reset diode and prevents the pixel from having a stable point of operation. This problem can be mitigated by either increasing the leakage of the collection diode itself by shining light on the chip, or by lowering the drain voltage to $0\,V$.
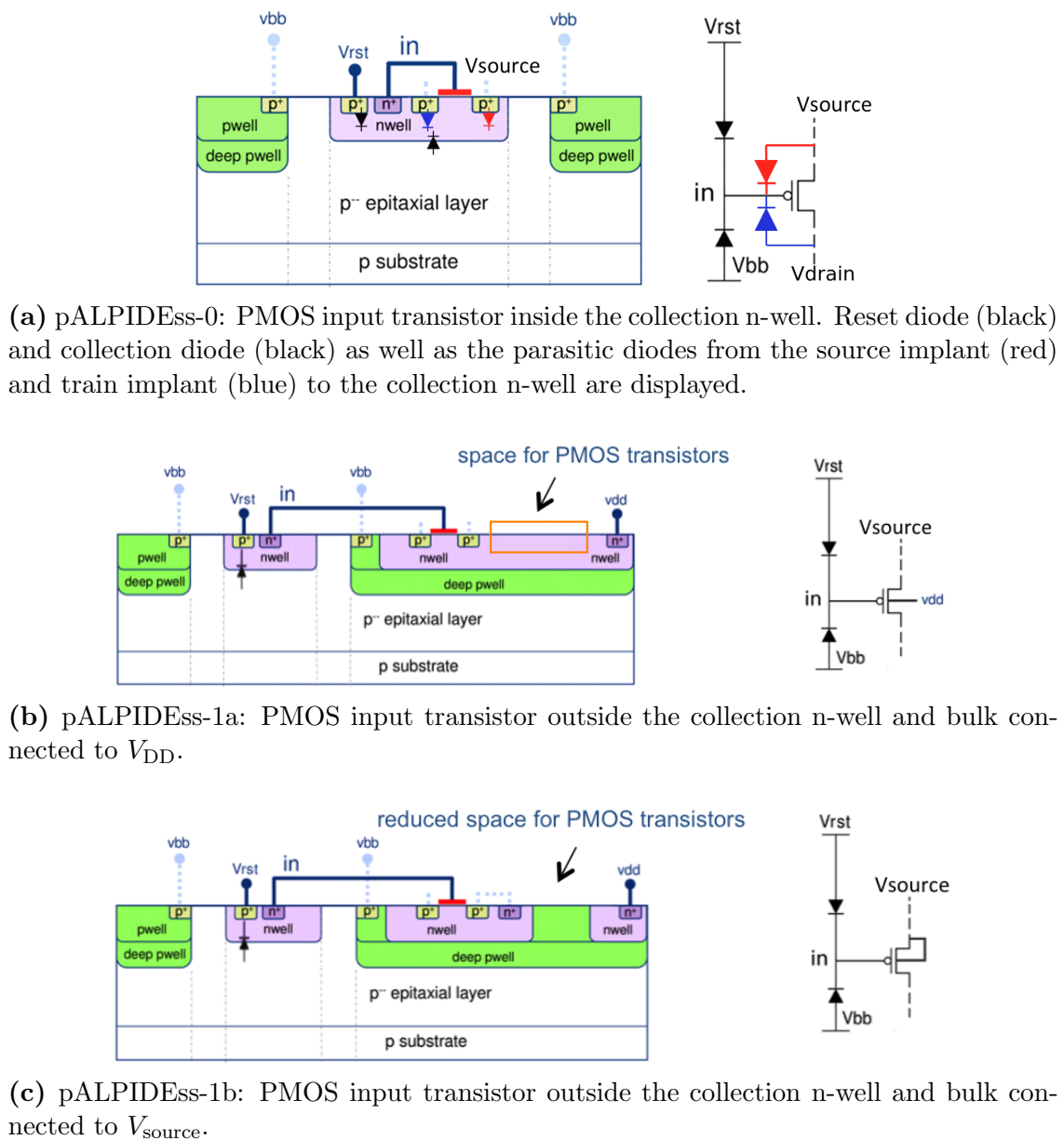
(a) pALPIDEss-0: PMOS input transistor inside the collection n-well. Reset diode (black) and collection diode (black) as well as the parasitic diodes from the source implant (red) and train implant (blue) to the collection n-well are displayed.

(b) pALPIDEss-1a: PMOS input transistor outside the collection n-well and bulk connected to V_{DD}.

(c) pALPIDEss-1b: PMOS input transistor outside the collection n-well and bulk connected to V_{source}.

Figure 5.8.: Schematic drawings of pixel and input transistor of the pALPIDEss prototypes.

Moreover, the chip showed problems under reverse substrate bias. This was attributed to the fact that the coupling capacitance C_s and the clipping mechanism were implemented using NMOS transistors. As NMOS transistors are embedded in a p-well which is on the reverse substrate bias potential, they see a changed reference potential and they are pushed out of their operational range.

pALPIDEss-1

In order to mitigate the biasing issue, in the next generation the PMOS input transistor was moved outside the collection n-well. Furthermore, the filtering capacitance C_s and clipping transistor were implemented using PMOS transistors.

pALPIDEss-1a

In the pALPIDEss-1a (cf. Fig. 5.8b) the bulk contact of the PMOS input transistor is connected to V_{DDA}. Since this is the usual n-well potential of PMOS transistors, the input transistor can share the n-well with the other PMOS transistors of the front-end circuitry. As a consequence, more space for PMOS transistors is available.

pALPIDEss-1b

In the pALPIDEss-1b (cf. Fig. 5.8c) the bulk contact of the PMOS input transistor is connected to V_{source}. This configuration mitigates the body-effect and leads to an increased gain [139, 140]. However, the transistor needs to be embedded in a separate n-well, reducing the available space for PMOS transistors in the pixel. As a consequence, the biasing PMOS transistors and the coupling capacitor C_s have a reduced size.

Biasing Parameters

The pALPIDEss chips do not contain on-chip biasing, all bias currents and voltages have to be supplied externally. The nominal values obtained using simulations of the circuitry of the most important biasing parameters are summarised in Tab. 5.5. The current biases are internally scaled to obtain the desired value at the pixel level. V_{CASN} has to be adjusted based on V_{BB} (cf. Ch. 5.5.1).

Table 5.5.: Summary of the most important pALPIDEss biases and their default values at the chip input pad and the pixel level.

| | Value | |
Name	Input Pad	Pixel Level
I_{Bias}	$5.12\,\mu A$	$20\,nA$
I_{THR}	$2.05\,\mu A$	$0.5\,nA$
V_{RST}	$1.6\,V$	
V_{CASN}	$0.4\,V$ at $V_{BB} = 0.0\,V$	
V_{CASP}	$0.6\,V$	
V_{BB}	$0\,V$ to $-6\,V$	

Table 5.6.: pALPIDE-2 pixel properties.

Sector	n-well diameter	Spacing	p-well opening	Reset	Input transistor width (W)
0	$2\,\mu m$	$2\,\mu m$	$4\,\mu m$	PMOS	Minimum
1	$2\,\mu m$	$2\,\mu m$	$6\,\mu m$	PMOS	$4\times$Minimum
2	$2\,\mu m$	$4\,\mu m$	$6\,\mu m$	PMOS	Minimum
3	$2\,\mu m$	$4\,\mu m$	$10\,\mu m$	Diode	Minimum

5.5.4. pALPIDE-2

The pALPIDE-2 is a full-scale prototype with a dimension of $30\,\text{mm} \times 15\,\text{mm}$ containing 1024×512 pixels of $28\,\mu m \times 28\,\mu m$. The change of pixel size compared to the pALPIDEss prototypes is driven by the need for more space for in-pixel circuitry. pALPIDE-2 features a masking register per pixel and a single in-pixel hit-buffer per pixel. Furthermore, the in-pixel hit-buffer is implemented as a latch. This latch reacts instantly to a hit in contrast to the time necessary for discharging the capacitor employed in the DMC of the pALPIDEss. Furthermore, the chip integrates a circuit for the pulsing of the injection capacitors.

The AERD circuitry of pALPIDE-2 is implemented using a full-custom logic in order to save space and routing resources within the matrix. In pALPIDE-3, the AERD circuit is built from standard CMOS cells again. Although it features the final interface, the high-speed serialiser is not integrated into pALPIDE-2. The pixel matrix of the pALPIDE-2 is grouped into 32 regions containing 16 double columns each.

The power consumption per pixel front-end is $40\,\text{nW}$ leading to a power density of $4.7\,\text{mW/cm}^2$. The total power density is about $20\,\text{mW/cm}^2$ without activity in the matrix.

In its current version, four sectors containing different pixel designs are implemented as outlined in Tab. 5.6. In particular, two different collection-diode geometries with different sizes of p-well openings are implemented. Furthermore, the width W of the input transistor is varied, while the gate length L is kept at the minimum value. Moreover, a PMOS and a diode reset mechanism are employed.

Biasing

With pALPIDE-1 on-chip bias Digital-to-Analogue Converters (DACs) were introduced. Both the current and the voltage DACs feature an 8 bit resolution. The most important biases and their default values from simulations are summarised in Tab. 5.7. Only the reverse substrate bias is applied using an external power supply.

Table 5.7.: Summary of the most important pALPIDE-2 biases and their default values.

Name	Value	
I_{Bias}	$20\,\text{nA}$	$64\,\text{DAC}$
I_{THR}	$0.5\,\text{nA}$	$51\,\text{DAC}$
I_{DB}	$10\,\text{nA}$	$64\,\text{DAC}$
I_{RST}	$5\,\text{pA}$	$50\,\text{DAC}$
V_{RST}	$1.2\,\text{V}$	$117\,\text{DAC}$
V_{CASN}	$0.4\,\text{V}$	$57\,\text{DAC}$
V_{CASP}	$0.6\,\text{V}$	$86\,\text{DAC}$
V_{BB}	$0.0\,\text{V}$ to $-6.0\,\text{V}$	external

6. Characterising MAPS for the ALICE ITS Upgrade

This chapter outlines and discusses the measurement techniques used to characterise the MAPS prototypes developed for the ITS upgrade, focusing on the pALPIDEss and pALPIDE-2 prototypes (cf. Ch. 5.5). Furthermore, the characterisation results and the impact of the main operational parameters are presented.

Within this thesis, the characterisation of the pALPIDEss prototypes was carried out and the full laboratory software framework for the pALPIDEss, as well as the corresponding readout system described in App. C, were developed. Furthermore, the pALPIDEss was integrated into the `EUDAQ` [142, 143] framework for test-beam data acquisition and the existing pALPIDE-1 test-beam analysis software [136] based on `EUTelescope` [142, 144] was adapted for the use with the pALPIDEss.
For the pALPIDE-2, the test-beam measurements for the epitaxial-layer study were carried out within this thesis. In laboratory measurements, the operational range of the test-beam Devices Under Test (DUTs) was explored and fake-hit rates and charge thresholds were obtained. The test-beam analysis software for the pALPIDE-2 was adapted from the existing pALPIDEss and pALPIDE-1 software. Furthermore, source code for the pALPIDE-1/2 integration into `EUDAQ` was contributed. Moreover, the telescope mechanics and settings as well as the triggering scheme were optimised.

For further information on the characterisation of the analogue-output prototypes of the ALPIDE family and pALPIDE-1 see [130]. A detailed description of the pALPIDE-1 test beam analysis using `EUTelescope` and corresponding results can be found in [136].

6.1. Measurement Techniques

In the following, the measurement techniques used for the characterisation of the ALPIDE prototypes are presented.
The sole available analogue information on the pulse shape at the `HIT` node of the front-end circuitry, is based on the pALPIDEss-0. Only the pALPIDEss prototypes contain eight isolated pixels surrounded with dummy pixels at the edge of the matrix. These pixels are not connected to the normal readout circuit, but feature an amplifier connected to the `HIT` node (cf. Ch. 5.5.1), driving an output pad, instead of the DMC. The amplifier leads to a baseline shift of $V_{\mathrm{HIT,out}}$ at the output pad compared to V_{HIT}. With the pixels not containing a pulsing capacitor, the injection of a defined charge is not possible. Response curves measuring $V_{\mathrm{HIT,out}}$
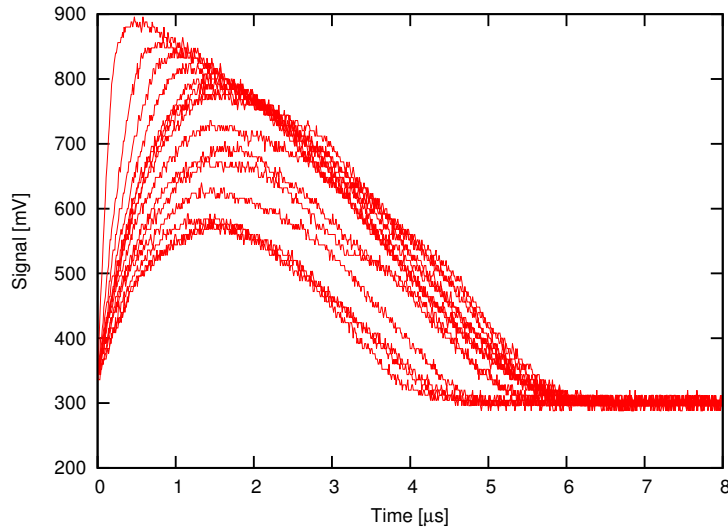
Figure 6.1.: 20 pALPIDEss in-pixel front-end responses ($V_{\text{HIT,out}}$) of a single pixel for signals created by an ^{55}Fe X-ray photon. Taken from [64].

of the front-end output using and oscilloscope are shown in Fig. 6.1. The signal was generated by an ^{55}Fe radioactive source, whose X-ray photons deposit a charge comparable to the charge generated by a MIP. The position of the pixel within the cluster and therefore the fraction of charge in such a measurement is, however, unknown as the neighbouring pixels are not read out. A 500 mV threshold was applied on $V_{\text{HIT,out}}$ for triggering.

The Full-Width Half Maximum (FWHM) of the majority of signals is seen to be 3.5 µs. The peaking time, which is defined as the time until the signal reaches its maximum voltage, varies from about 0.5 µs to 1.7 µs. A higher maximum voltage of the signal is correlated with a shorter peaking time.

The absence of pixels with analogue outputs in the matrix leads to measurement techniques using the digitised output of the pixels in order to perform systematic studies of the in-pixel front-end and the complete matrix. The measurements described below are subdivided into laboratory and test-beam measurements. In the laboratory, initial functional tests and the measurement of charge threshold, spatial uniformity and fake-hit rate are performed. At the test beam, the detection efficiency, position resolution and cluster size are measured.

6.1.1. Laboratory Measurements

Initial functional tests of the response of the pixel chip to particles are carried out using a radioactive source. As radioactive sources, ^{55}Fe emitting photons of 5.9 keV and 6.5 keV or ^{90}Sr emitting electrons with a maximum energy of about 2.3 MeV
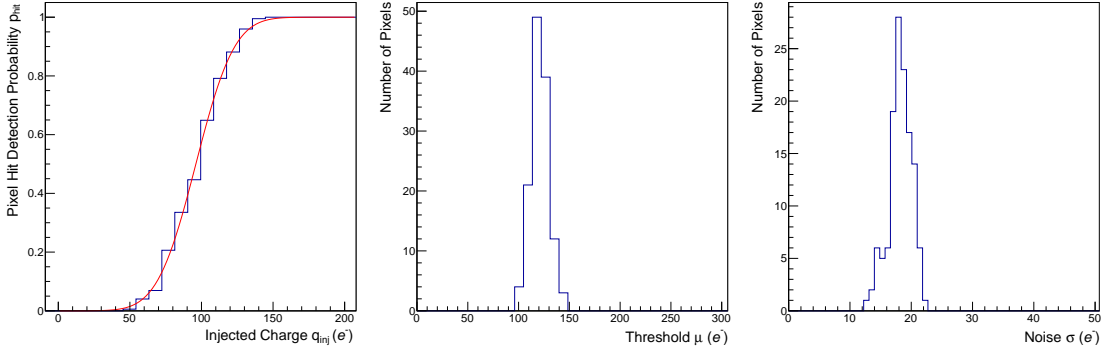
Figure 6.2.: Examples for an S-Curve of a pALPIDEss pixel (left), threshold distribution with a mean of $\overline{\mu} = 121.0\,e^-$ and an RMS $\Delta\mu = 8.6\,e^-$ (centre) and TN distribution with a mean of $\overline{\sigma} = 18.2\,e^-$ and an RMS $\Delta\sigma = 1.9\,e^-$ (right). All plots were acquired using a pALPIDEss-1a at $V_{\mathrm{BB}} = -2\,\mathrm{V}$, $I_{\mathrm{THR}} = 0.5\,\mathrm{nA}$ and $V_{\mathrm{CASN}} = 1.05\,\mathrm{V}$.

are used. Both radioactive source were selected as the particles emitted by them deposit a similar amount of charge as MIPs. While X-ray photons have a localised charge deposit, electrons lose energy along their path through the sensor leading to different cluster shapes and sizes. The radioactive-source measurements allow to study the matrix uniformity. In measurements with several tens of hits per pixel, the boundaries between sectors and dead pixels can be identified.

Threshold Measurement

For the ALPIDE prototypes, a so-called S-Curve scan is used to determine the charge threshold and Temporal Noise (TN) of the front-end circuit. In MAPS, the TN originates from various spots in the circuitry [135, 145]. An example for such a noise source is the reset mechanism producing shot noise. During an S-Curve scan, the front-end settings are kept at fixed values. A charge q_{inj} is injected into the front-end node `IN` by applying a negative voltage step on the injection capacitor C_{inj}. The injected charge q_{inj} is varied by adjusting the voltage step. For each injected charge, the hit-detection probability p_{hit} of the pulsed pixel is measured. Assuming a Gaussian distribution of the noise, the response function of the pixel based on a Gaussian error function:

$$p_{\mathrm{Hit}}(q_{\mathrm{inj}}) = \frac{1}{2}\left(1 + \mathrm{Erf}\left[\frac{q_{\mathrm{inj}} - \mu}{\sqrt{2}\cdot\sigma}\right]\right) \tag{6.1}$$

where q_{inj} is the injected charge, μ is the charge threshold and σ the TN. The measurement is called S-Curve scan due to the characteristic S-shape of the response function. The values for μ and σ are extracted using a pixel-by-pixel fit (cf. Fig 6.2, left). The sector average for the charge threshold and TN are denoted by $\overline{\mu}$ and $\overline{\sigma}$, respectively. Additionally, the RMS of both threshold and Temporal Noise (TN), $\Delta\mu$ and $\Delta\sigma$, are calculated to assess the uniformity (cf. Fig. 6.2, centre and right).
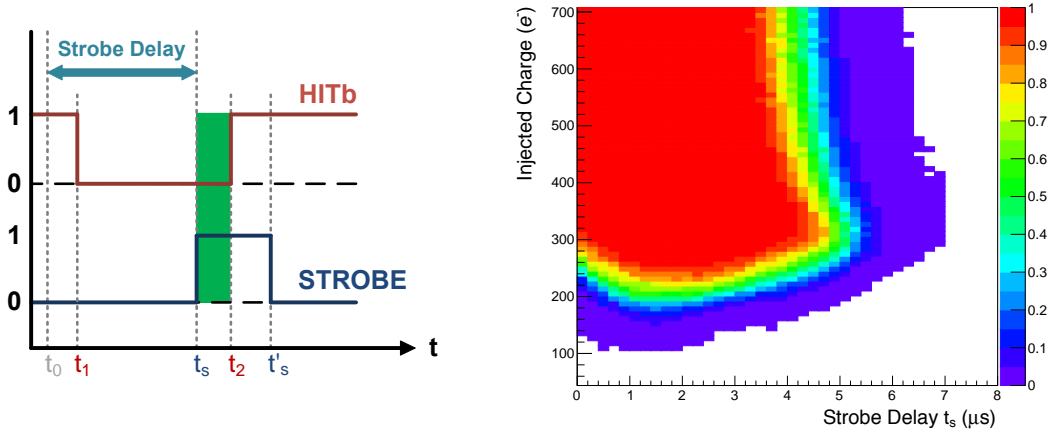
Figure 6.3.: Left: active-low hit output signal of the in-pixel front-end and active-high strobe signal. Right: Pixel hit-detection probability as a function of the strobe delay t_s and the injected charge for a pALPIDEss-1a ($V_{\mathrm{BB}} = 0.0\,\mathrm{V}$, $V_{\mathrm{CASN}} = 0.4\,\mathrm{V}$ and $I_{\mathrm{THR}} = 0.5\,\mathrm{nA}$).

$\Delta\mu$ contributes to the Fixed-Pattern Noise (FPN), as it leads to an additional variation of the μ/σ-ratio for a threshold setting which is constant across the chip. Commonly, FPN is assumed to originate from mismatches in the circuitry, leading to a stable spatial pattern. The stable FPN pattern allows to mask pixels with a particularly low μ/σ-ratio. The conversion from a voltage step to the injected charged is calculated using the design value of the injection capacitance[1].

Pulse-Shape Measurement

An alternative method to infer the output-signal shape is to vary the strobe delay t_s relative to the charge injection at t_0 as shown in Fig. 6.3 (left). In such a measurement, a threshold scan is repeated for different delays between charge injection at t_0 and the STROBE signal at t_s. This measurement results in a map of the hit-detection probability as a function of t_s and q_{inj}. From this map, a 50 %-hit-detection probability contour is extracted. The largest strobe delay t_s for which a hit-detection probability of 50 % is reached, is defined to be the maximum pulse width.

In Fig. 6.3 (right), the hit-detection probability of a pixel as a function of the strobe delay t_s and the injected charge q_{inj} for a pALPIDEss-1a at default settings ($V_{\mathrm{BB}} = 0.0\,\mathrm{V}$, $V_{\mathrm{CASN}} = 0.4\,\mathrm{V}$ and $I_{\mathrm{THR}} = 0.5\,\mathrm{nA}$) is shown. This distribution has several distinct features. The charge needed to trigger decreases with increasing t_s until a delay of about 1.5 μs and it increases again from about 2.5 μs on. This is explained by the longer peaking time for smaller charges (cf. Fig. 6.1). The lowest charge threshold corresponding to the highest sensitivity is achieved by a t_s of

---

[1]The MAPS of the ITS upgrade do not contain an additional circuit which allows to measure the size or variation of the injection capacitor.

about $2\,\mu s$ due to the peaking time of the smallest pulse exceeding the discriminator threshold. Consequently, the t_s with the highest sensitivity depends on the settings of the front-end circuit. For the interpretation the pulse shape results of the pALPIDEss, the `STROBE` length or acquisition time $t_{\text{ACQ}} = t'_s - t_s$ of $1.54\,\mu s$ being of the same order as the peaking time of pulse has to be taken into account. For charges higher than about $300\,e^-$, the pulse duration decreases again due to clipping (cf. Ch. 5.5.1). The on-set of the clipping depends on the potential difference between `CURFEED` and `HIT`. This potential difference depends on the settings of V_{CASN} and I_{THR}.

The time response of the circuit for highly-ionising particles such as low energetic protons or alpha particles cannot be probed in this measurement. The size of the injection capacitance and the restriction of the voltage pulse to the supply voltage, allow only to inject about $1600\,e^-$. This corresponds approximately to the most-probable energy loss of a MIP in a $25\,\mu m$ epitaxial layer. In order to asses the pulse shape for highly-ionising particles in the laboratory, a laser is a viable option to inject the desired amounts of charge into the pixel.

Fake-Hit Rate

To estimate the fake-hit rate, the chips are read out in a sequence of consecutive events without providing an external stimulus like a radioactive source, beam or external pulsing. The average fake-hit rate R_{FH} is calculated according to

$$R_{\text{FH}} = \frac{N_{\text{Hits}}}{N_{\text{Pixels}} \cdot N_{\text{Events}}} \tag{6.2}$$

with N_{Hits} denoting the number of hits detected by the number of pixels under study N_{Pixels} and the number of recorded events N_{Events}.

The impact of masking pixels is studied by excluding n pixels with the highest hit count in the fake-hit rate calculation. Masking is justified as long as the fake hits originate from a constant, small group of pixels featuring a significantly higher fake-hit rate than an average pixel. A possibility to study this, is to repeat measurements, keeping the conditions constant, checking whether the noisy pixels stay the same. As reference for comparison, the list of pixels sorted by the number of fake hits is used. For the pALPIDEss-1a at nominal settings, the first 200 noisy pixels were found to be the same in ten measurements. The DUT was powered down for an hour between measurements.

In addition to the bias-parameter dependence of the front-end, its dependence on the occupancy in the matrix needs to be studied. A fake-hit rate of 10^{-5}/pixel/event leads to an occupancy of $1\,\text{hit/event/cm}^2$ about the same as expected from particles for the OB [64]. As cross check, an occupancy of about $7\,\text{hit/event/cm}^2$ was generated by charge injections via the pulsing capacitors. This additional occupancy in the matrix was found not to influence the fake-hit rate.
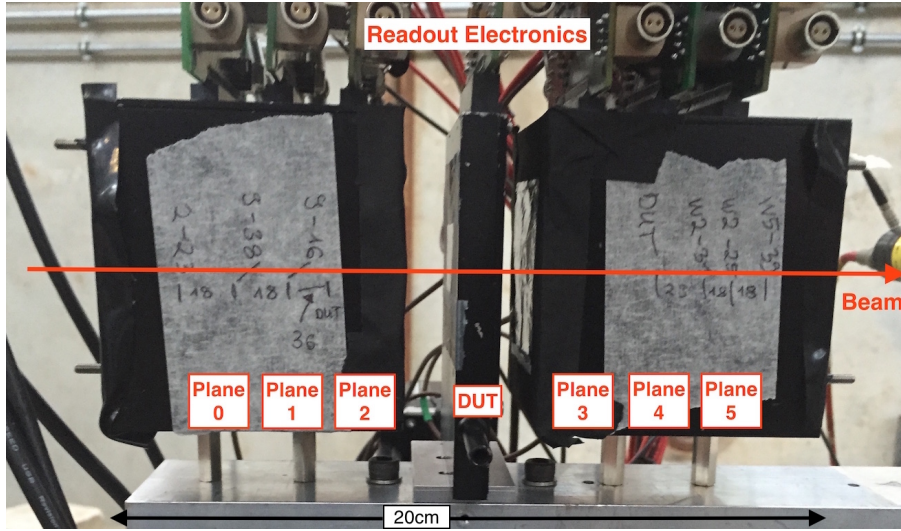
Figure 6.4.: ALPIDE telescope consisting of two arms with three pALPIDE-1 reference planes each and the pALPIDE-2 DUT in the centre.

Assuming a Gaussian distribution of the TN, the fake-hit probability can be estimated by integrating over the tail of the noise distribution from the μ to infinity:

$$p_{\mathrm{FH}}^{expected} = \frac{1}{2}\mathrm{Erfc}\left(\frac{\mu}{\sqrt{2}\cdot\sigma}\right) \tag{6.3}$$

This calculation is carried out on a pixel-by-pixel basis in order to take into account the FPN. At pixel level, a μ/σ of 5 leads to an estimated fake-hit rate of 2.9×10^{-7} /event/pixel.

6.1.2. Test-Beam Measurements

The test-beam measurements presented in this thesis were carried out at two different beam lines. The data for pALPIDEss and pALPIDE-2 was taken at the DESY test beam facility in Hamburg and the CERN Proton Synchrotron (PS) T10 beam line, respectively. In both cases, a telescope consisting of two arms containing three pALPIDE-1 chips with the DUT in the centre was used (cf. Fig. 6.4). The mechanical setup had to be adjusted to fit the different DUTs. At DESY and the PS, a $3.2\,\mathrm{GeV}/c\ e^+$-beam and $6\,\mathrm{GeV}/c\ \pi^-$-beam were used, respectively. At these momenta, the particles are slightly more ionising than MIPs and the multiple scattering is small enough to allow a position-resolution measurement.

The pALPIDEss measurement programme was focused on detection efficiency and pulse shape as function of the front-end settings. For the pALPIDE-2, the detection efficiency and position resolution and their dependence on the epitaxial-layer thickness and front-end settings were studied.
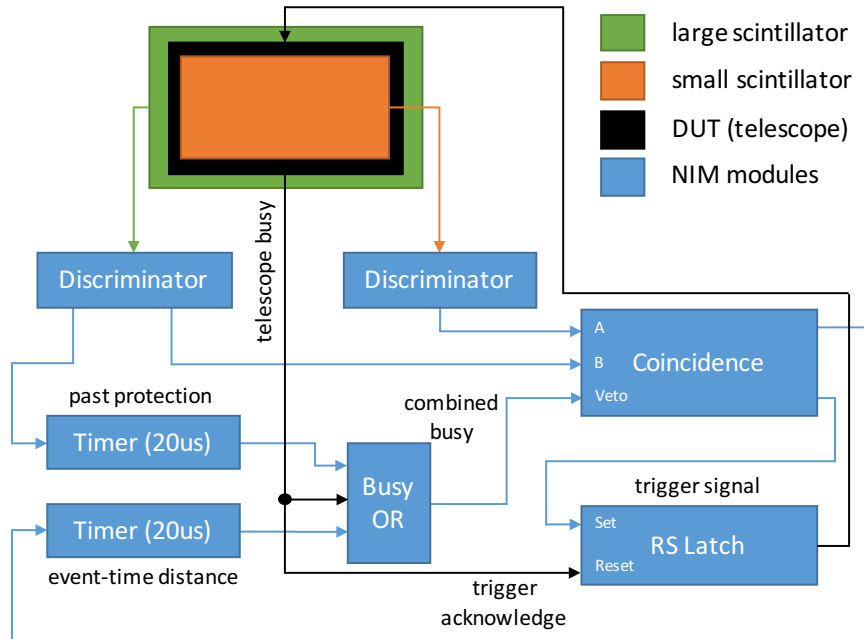
Figure 6.5.: Trigger logic used for the pALPIDE-2 test beams.

6.1.3. Trigger Setup

For the pALPIDE-2 test beam, scintillators and trigger logic as shown in Fig. 6.5 were used. In this trigger setup, a scintillator larger than the DUT is used to generate a busy signal of 20 µs after each particle or fake-hit in the scintillator. This busy signal is used as past protection in order to prevent triggers from particles too close in time. In coincidence a with the large scintillator, a small scintillator was used to generate a trigger. The second scintillator was chosen smaller than the pALPIDE-2 to ensure that a particle which crosses this scintillator also crosses the DUT. A trigger signal is only accepted in the absence of a busy signal from either the past protection or the DAQ boards reading out the reference planes and the DUT. Furthermore, a busy signal of 20 µs is generated after each accepted trigger.

The past protection is needed if the DUT has a shorter front-end response than the reference planes. A particle A crossing shortly before the particle B triggering an event thus could be seen by the reference planes but not by the DUT leading to an artificial loss in efficiency (cf. Fig. 6.6). As I_{THR}-scans are performed and this parameter is known to influence the pulse width, this measure is necessary. On the reconstructed data, a past-protection can be introduced by requiring an event-time distance which is larger than the average busy time of the readout system. However, depending on the beam structure, this leads to a significant loss of statistics.
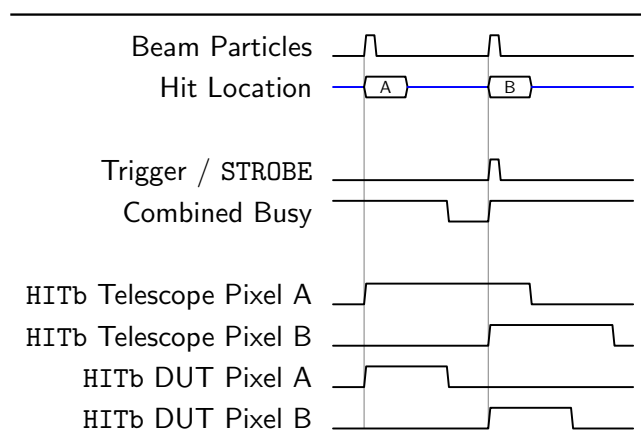
Figure 6.6.: Scenario of two particles crossing shortly after each other with different pulse widths in the reference planes and the DUT.

6.1.4. Software Framework and Measurement Technique

At test beam, the data acquisition is based on the `EUDAQ` framework [142, 143]. The `EUTelescope` framework [142, 144] interfaces `EUDAQ` for reading the raw data. The data flow in the analysis is shown in Fig. 6.7. In a first step, the data of the DUT is checked for disabled double-columns. The pALPIDE-1/2 prototypes automatically disable a double column if a pixel gets stuck and its hit-buffer is not reset during the readout. In a next step, all planes are searched for noisy pixels excluding all pixels with a hit frequency above 10^{-3}. Based on the hits after exclusion of noisy pixels, the clustering is performed. In the so-called hitmaker step, the clusters are transformed into hit positions on the planes. After this step, a pre-alignment is obtained from the correlations of the hits in the planes. The performance of the pre-alignment was found to be sensitive to noisy pixels. The final alignment of the planes using straight tracks is performed based on the pre-aligned data. Then the noisy pixel search, clustering and hitmaker step are repeated using a cut of 10^{-2} on the hit frequency of noisy pixels. The track fit is done using a General Broken Line (GBL) [146] based on hits in the reference planes, excluding the position information from the DUT. The advantage of the GBL fit compared to a straight line fit is that it takes into account the multiple scattering in the telescope material leading to a better resolution.

In the analysis step, a square region centred at the extrapolated impinging point in the DUT is scanned for a cluster. The probability to find a cluster in this region is defined as the detection efficiency. Furthermore, the size distribution of clusters assigned to a track and their geometrical distance from extrapolated impinging point, the residuals, are stored. To obtain the average position resolution σ_{pos}, the resolution of the extrapolation σ_{track} is quadratically subtracted from the RMS of
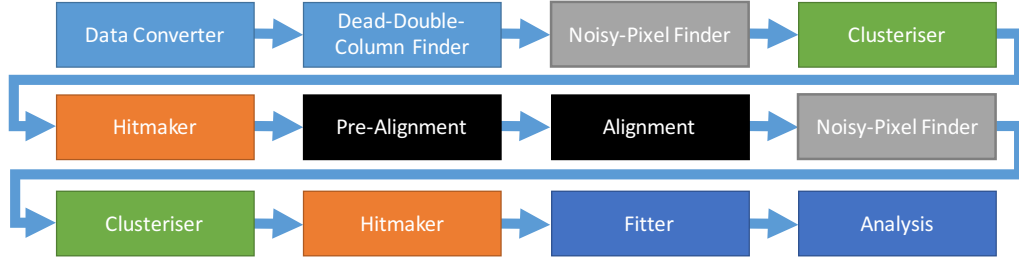
Figure 6.7.: `EUTelescope` analysis flow used for the pALPIDEss and pALPIDE-2.

the residual distribution σ_{res} according to

$$\sigma_{\text{pos}}^2 = \sigma_{\text{res}}^2 - \sigma_{\text{track}}^2 . \tag{6.4}$$

The track resolution σ_{track} is estimated from a special run using a pALPIDE-1 as DUT and the same settings in all seven planes. As a consequence, all planes have the same single-point resolution. Using the GBL model and the estimated material budget, as well as the beam energy, one can vary the single-point resolution to match the residual distribution from the simulation with that obtained from the data. As the different sectors of the pALPIDE-1 do not have the same single-point resolution, this has to be carried out sector-by-sector.

The full-scale pALPIDE prototypes are mounted on carrier Printed Circuit Boards (PCBs) with an opening behind a part of the chip. In order to minimise the impact of multiple scattering, only those regions of a sensor are used for the determination of the position resolution that have no PCB behind the sensor. The material taken into account in the track fit and simulation are the air, the aluminium foil, covering the beam entrance and exit windows of the reference arm as well as the DUT enclosure, and the sensors themselves. In the course of preparing the pALPIDE-2 test beam, the setup was optimised in terms of material budget and geometry (cf. Fig. 6.8) leading to an average track resolution estimated to be about 2.8 µm.
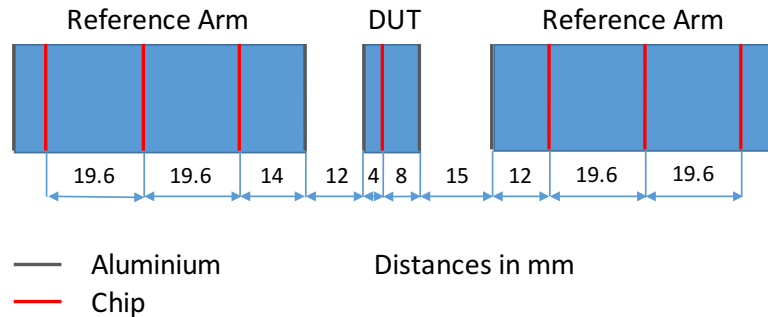
Figure 6.8.: Plane distances and scattering material positions in the ALPIDE telescope used for the pALPIDE-2 test beam.

6.2. Characterisation Results

6.2.1. Light Sensitivity of pALPIDEss-0

During the initial tests of pALPIDEss-0 at default settings, the chip did not reliably respond to pulsing via the injection capacitors. This problem was found to be solved by exposing the chip to light. In order to study this behaviour, an array of white LEDs was built to shine a well-defined amount of light onto the chip. In order to find an optimal working point, the number of reacting pixels and the reset current were studied as a function of the current supplied to the LEDs. In this study, a clear threshold behaviour was observed. Without light, the combined reset current of all pixels in the matrix is below the measurement range of the multimeter of $0.01\,\mathrm{nA}$. In this regime, the pALPIDEss-0 shows a threshold RMS which is about five times larger than with light. At about $5\,\mathrm{nA}$ combined reset current, all pulsed pixels reliably react and the threshold RMS decreases. The ambient light of the laboratory, corresponds to a slightly higher combined reset current of about $30\,\mathrm{nA}$ or about $1\,\mathrm{pA}$ per pixel. Within a combined reset current range from about $5\,\mathrm{nA}$ to $500\,\mathrm{nA}$, the front-end circuitry works reliably. In the following, for measurements with light, the supply current of the LEDs is adjusted to result in a leakage current of $30\,\mathrm{nA}$ for a pALPIDEss-0. Furthermore, lowering V_{CASP} can lead to an additional leakage current through the diode formed by the drain implant and collection electrode (cf. Ch. 5.5.3).

In order to find the optimal amount of light used to operate the pALPIDEss-0 chips, a measurement of threshold and noise as a function of the reset-current was carried out. This measurement was performed at nominal bias conditions. In the operational range from $5\,\mathrm{nA}$ to $500\,\mathrm{nA}$, the ratios of threshold RMS over threshold and noise RMS over noise stay approximately constant. However, the noise increases by $20\,\%$ with increasing reset current. This can be assumed to be caused by shot noise. The threshold increases by about $8\,\%$. A possible explanation for the threshold increase is signal clipping by the reset diode due to a shift of the front-end node `IN` to a different operation point. The reset is implemented using a forward-biased diode. At forward bias, the diode current depends exponentially on the voltage drop across the diode. The exponential dependence of the current on the voltage and the shift of the operation point can lead to fast clipping of the input charge.

In pALPIDEss-1a/b, the dependence on an additional leakage current induced by light has been mitigated by moving the input transistor out of the collection electrode (cf. Ch. 5.5.3). Light still increases the leakage current in the pixel leading to an increased TN but the threshold RMS stays stable. It was verified in a test beam that the detection efficiency of pALPIDEss-0 is strongly increased by light. Moving the input transistor out of the collection electrode also eliminated this effect for pALPIDEss-1a and pALPIDEss-1b (cf. Ch. B.1).

6.2.2. Front-End Parameter Studies

In order to determine the sensitivity of the front-end circuit to bias variations, the influence of the parameters on threshold and TN are studied. The studies presented below are based on the pALPIDEss-1a. The qualitative behaviour of the front-end circuitry found in pALPIDEss-1a was found to be the same in pALPIDEss-1b and, with exception of the light sensitivity and the reverse-substrate-bias tolerance, also for the pALPIDEss-0. As the front-end circuity of the full-scale prototypes is based on that the small-scale prototypes, the influence of the parameters is comparable. The discriminator branch (cf. Ch. 5.5.1) and the PMOS reset were studied using a pALPIDE-1 and pALPIDE-2, respectively.

PMOS Cascode Voltage – V_{CASP}

The PMOS cascode voltage V_{CASP} was found to have little effect (few %), on threshold and noise, as long as it was chosen below the expected swing of the `IN` node. The circuit functioned well, from $0\,\mathrm{V}$ to $1.0\,\mathrm{V}$. As a consequence, the default setting of $0.6\,\mathrm{V}$ has been kept.

Diode Reset – V_{RST}

The reset voltage V_{RST} was found to show an on-set behaviour. Above a minimum voltage, the circuit behaviour did not change significantly. This minimum voltage, however, increases from about $1.2\,\mathrm{V}$ to about $1.4\,\mathrm{V}$ for an increase in reverse substrate bias from $0\,\mathrm{V}$ to $-6\,\mathrm{V}$. This is explained by the larger leakage current at increased reverse substrate bias absorbed by the resetting diode leading to a larger voltage drop across it. Hence, the default setting of $1.6\,\mathrm{V}$ is a safe choice. The on-set behaviour observed in threshold and noise is equally reflected in the analogue-pulse response of the pixels. As a consequence, pulsing at a single charge value above the threshold can be used to find the operational range.

Reverse Substrate Bias – V_{BB}

pALPIDEss-0 only works in the reverse-substrate-bias range from $0\,\mathrm{V}$ to $-2\,\mathrm{V}$. For larger reverse substrate bias, the NMOS coupling capacitor C_{s} in the pALPIDEss-0 stops working. This is caused by the increased transistor threshold voltage due to the reverse substrate bias and hence the transistor is not inverted anymore. However, the use of the transistor as capacitor is based on the capacitance built up between the gate and the inversion layer. In pALPIDEss-1a/b this is issue has been mitigated by using an PMOS coupling capacitor instead.
During the study of analogue-output small-scale prototypes, an exponential increase

on reverse-substrate-bias current was observed starting at about $-8\,\mathrm{V}$. $V_{\mathrm{BB}} = -6\,\mathrm{V}$ was chosen as limit to keep a safety margin. The current is expected to be due to a breakdown of the junction in the NMOS transistors, as they are embedded in p-wells. pALPIDE-2 was found to operate in a V_{BB} range from $0\,\mathrm{V}$ to $-6\,\mathrm{V}$.

Charge Threshold Setting – I_{THR} and V_{CASN}

The main parameters for influencing the threshold and noise were found to be V_{CASN} and I_{THR}, as expected from the circuit design (cf. Ch. 5.5.1). An increase of V_{CASN} leads to a lower threshold, as it corresponds to a higher baseline value of the output pulse at the HIT node. A decrease in I_{THR} leads to a lower threshold (cf. Fig. 6.9) as expected from the slower reaction of the feedback mechanism discharging HIT. V_{CASN}, however, has to be adjusted depending on V_{BB}. This can be explained by the NMOS transistor being embedded in a p-well, which is set to V_{BB}. V_{CASN} influences not only threshold and TN but also had a stronger influence on the fake-hit rate than I_{THR}.

In Fig. 6.10, the threshold in comparison to the fake-hit rate measured during an S-Curve scan is shown. The minimum threshold of about $90\,e^-$ can be reached starting with $V_{\mathrm{BB}} = -2\,\mathrm{V}$ at the default $I_{\mathrm{THR}} = 0.5\,\mathrm{nA}$. In general, increasing V_{CASN} leads to a decreased threshold as expected. Within the V_{BB} range from $0\,\mathrm{V}$ to $-2\,\mathrm{V}$, above a certain V_{CASN}, the threshold and its RMS start to increase. Comparing the S-Curves of individual pixels, some pixels do not show the expected decreased threshold due to the higher V_{CASN}, but instead the threshold increases until they stop responding to the analogue pulsing. The fake-hit rate increases with V_{CASN}. While from $0\,\mathrm{V}$ to $-2\,\mathrm{V}$ in V_{BB} a region with a slow increase, followed by a strong increase in fake-hit rate is measured, for larger reverse substrate bias the fake-hit rate starts to behave differently. The fake-hit rate is approximately constant within a small V_{CASN} range, before it slightly decreases in a V_{CASN} range of about $0.1\,\mathrm{V}$ and then exponentially increases. Only at V_{BB} from $0\,\mathrm{V}$ to $-3\,\mathrm{V}$, a fake-hit rate lower than 10^{-5} /event/pixel can be achieved.

In summary, the pALPIDEss-1a profits only up to V_{BB} of $-2\,\mathrm{V}$ and the minimum threshold with a fake-hit rate of 10^{-5} /event/pixel is about $120\,e^-$.

Acquisition time – t_{ACQ}

A further setting to tune is the STROBE signal duration or acquisition time t_{ACQ}. In the pALPIDEss, a few hundred nanoseconds are necessary to discharge the DMC and to write a hit depending on the pulse shape. A default value of $1.54\,\mathrm{\mu s}$ is used to exclude efficiency loss caused by a too short t_{ACQ}.
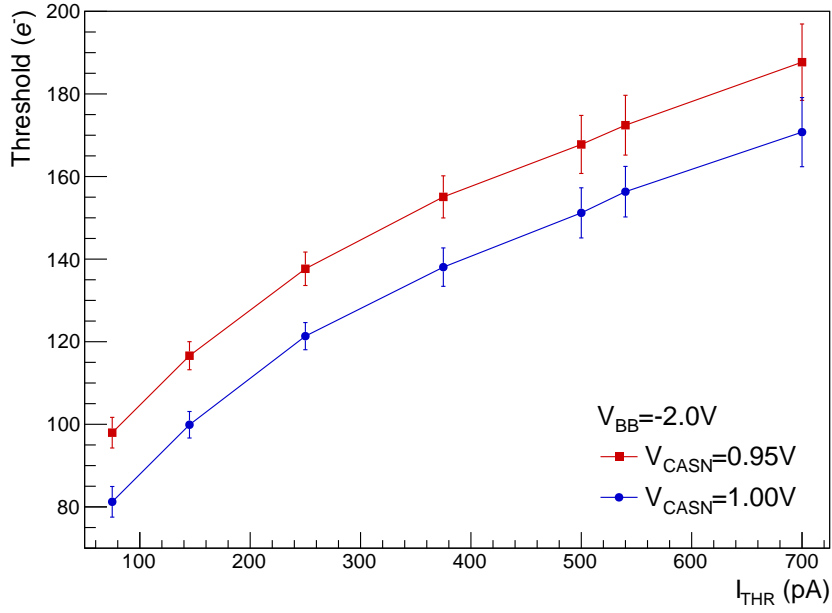
Figure 6.9.: Threshold for a pALPIDEss-1a as function of I_{THR} for $V_{BB} = -2.0\,\text{V}$. Error bars show the threshold RMS.
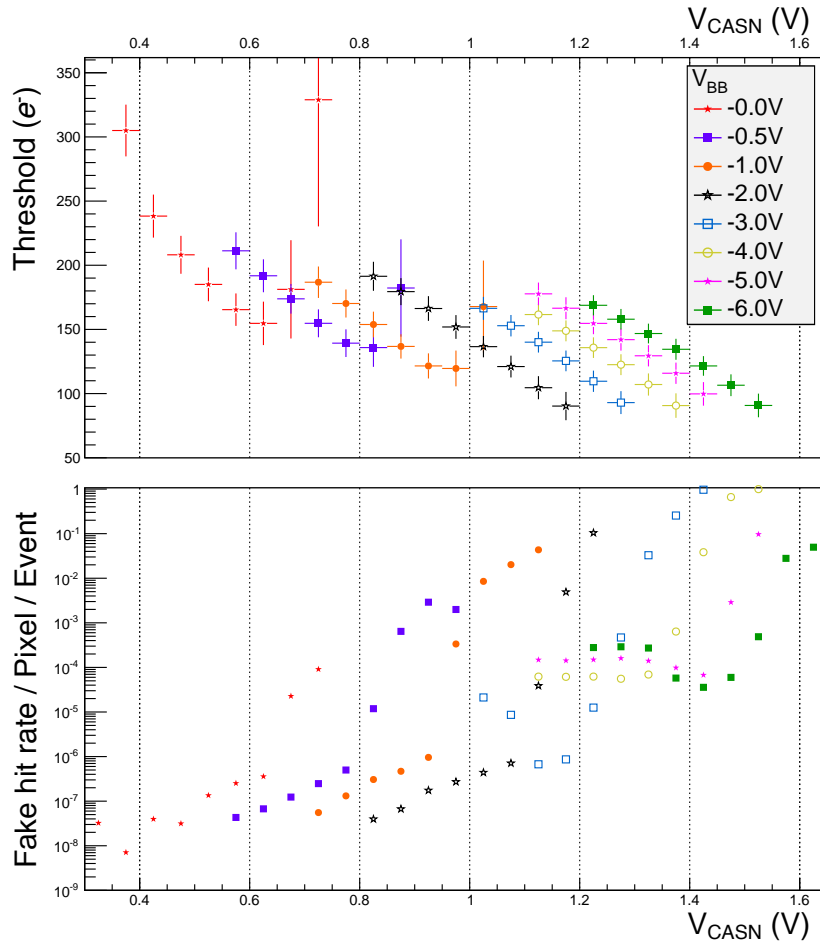

Figure 6.10.: Threshold and fake-hit rate for a pALPIDEss-1a at default settings as a function of V_{CASN} and V_{BB}. Error bars show the threshold RMS.

For both pALPIDEss and pALPIDE-1/2, t_{ACQ} has to be adjusted to cover the shortest expected pulse and the pulse with the longest peaking time. The clipping mechanism of the ALPIDE front-end (cf. Ch. 5.5.1), can lead to very short responses for charges that are a few orders of magnitude higher than the charge deposit of a MIP. A reason to keep t_{ACQ} short, is to reduce pile-up. Within this thesis, only charges of the order of magnitude deposited by a MIP are subject to study and the default t_{ACQ} of the pALPIDE-2 and pALPIDEss of 500 ns and 1.54 µs, respectively, are used.

PMOS reset – V_{RST} and I_{RST} (pALPIDE-1/2)

In pALPIDE-1, the PMOS reset and the discriminator branch were introduced, which are also present in the pALPIDE-2.
For the PMOS reset of pALPIDE-2, the operational V_{RST} range is determined on basis of the analogue pulser response. Before irradiation, the default values for both V_{RST} of 1.2 V and I_{RST} of 5 pA work. After irradiation with 1.7×10^{13} 1 MeV n_{eq}/cm^2 of NIEL, the increased leakage current requires an increase of I_{RST} to 10 pA.

Discriminator Current – I_{DB} (pALPIDE-1/2)

The discriminator current I_{DB} was studied in detail for the pALPIDE-1 [130]. It has little influence on the threshold and TN, but is of relevance for the pulse shape. In the results presented in this thesis, the default value of 10 nA is used.

6.2.3. Comparison of the pALPIDEss Generations and Versions

For the comparison, the charge threshold and TN of several pALPIDEss chips have been measured under nominal bias conditions. This measurement included 12 pALPIDEss-0 prototypes from the March 2013 submission, a single pALPIDEss-0 and two each of pALPIDEss-1a and pALPIDEss-1b from the January 2014 submission. The S-curve scans were performed both in a light-tight enclosure and exposing the chip to light using LEDs. Furthermore, V_{CASP} was varied from the nominal value of 0.6 V to 0 V. The following results are based on the pixels having an octagonally shaped collection electrode. In Fig. 6.11, the threshold (left) and TN (right) values for the different chips at nominal V_{CASP} are shown. The error bars show the pixel-by-pixel variations (RMS) of the corresponding quantity. This spread is largely increased without light (black symbols) for the pALPIDEss-0 generation. While light (red symbols) decreases the threshold of the pALPIDEss-0 generation, it leads to a slight increase for the pALPIDEss-1 generation. The increase of threshold with light for the pALPIDEss-1, resulting in a higher leakage current, is assumed to be due to an increased conductance of the reset diode, leading
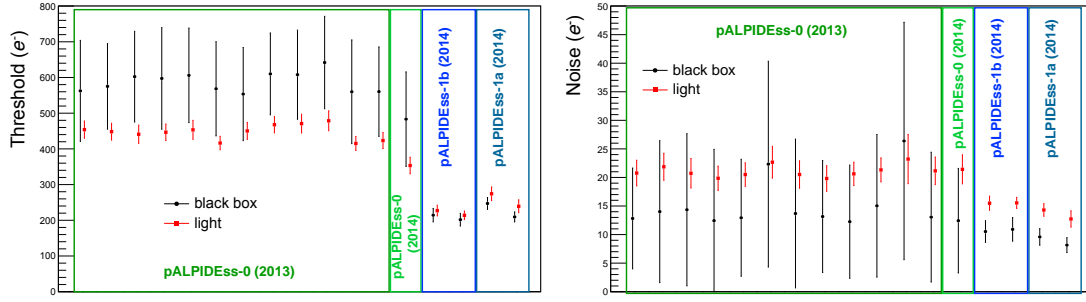
Figure 6.11.: Threshold (left) and noise (right) comparison for $V_{\mathrm{CASP}} = 0.6\,\mathrm{V}$ with (red) and without light (black).
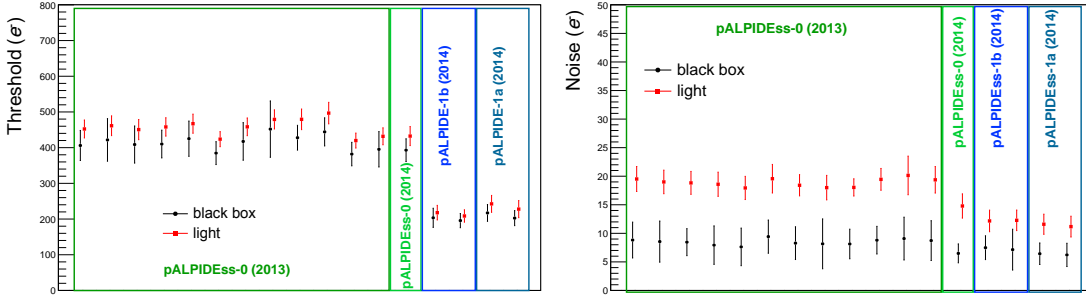
Figure 6.12.: Threshold (left) and noise (right) comparison for $V_{\mathrm{CASP}} = 0\,\mathrm{V}$ with (red) and without light (black).

to a slight clipping of the input charge at the input node. The TN is increased for all chips with light due to the light-induced increase of the leakage current and the resulting increase of shot noise. The 13 pALPIDEss-0 from both submissions show within the corresponding variations a consistent TN and threshold. Furthermore, there is no significant difference between the pALPIDEss-1a and pALPIDEss-1b prototypes (cf. Ch. 5.5.3). The combination of the source follower with the source-to-bulk connection combined with a smaller coupling capacitor C_s does not lead a different charge threshold (cf. Ch. 5.5.3).

Lowering V_{CASP} to $0\,\mathrm{V}$, reduces the influence of light on the pALPIDEss-0 generation drastically as shown for the threshold and noise in Fig. 6.12. The reduction of V_{CASP} leads to a slight reduction of the noise by a few electrons. Without light and $V_{\mathrm{CASP}} = 0\,\mathrm{V}$ all chips have comparable noise of about $8\,e^-$ to $9\,e^-$. The threshold of the pALPIDEss-1 generation is not influenced by the change in V_{CASP} and stays at about $200\,e^-$. For the pALPIDEss-0 the threshold is lower at $V_{\mathrm{CASP}} = 0\,\mathrm{V}$, furthermore the influence of light is inverted and light increases the threshold, which is in line with the behaviour of the pALPIDEss-1 where this is attributed to clipping at the input node.

The reason for the twice as high charge threshold of the pALPIDEss-0 compared to the pALPIDEss-1 is currently not understood. A possible explanation is that the re-layout necessary for moving the input transistor out of the pixel changed the

parasitic capacitances of the front-end circuitry.

In the following, the pALPIDEss-1a is discussed in further detail, as it is the most representative for pALPIDE-2.

6.2.4. Fake-Hit Rate

The fake-hit rate of the pALPIDEss was studied as a function of the time between events, the acquisition time and the threshold, varying V_{CASN} and I_{THR}. For the pALPIDE-2, the influence of the input transistor size and noise induced by readout-activity in the AERD was studied. The fake-hit rates of both pALPIDEss and pALPIDE-2 are compared to the fake-hit rate estimated assuming the fake-hits to be caused by TN following a Gaussian distribution. For the pALPIDEss-1a results presented below, the 20 most noisy pixels of the matrix are masked corresponding a fraction of 6×10^{-4}. Furthermore, all sectors in the matrix are taken into account leading to a measurement sensitivity of

$$R_{\text{FH}}^{\text{min}} = \frac{1}{N_{\text{Pixel}} \times N_{\text{Event}}} = \frac{1}{32768 \times 200} \approx 1.5 \times 10^{-8} \, / \text{event/pixel} \,. \qquad (6.5)$$

For the pALPIDE-2, the fake-hit rate is measured for each sector separately. Using 1.2×10^5 events and the 512×256 pixels per sector lead to a sensitivity of 6.4×10^{-11} /event/pixel.

pALPIDEss

Figure 6.13 shows the fake-hit rate for a pALPIDEss-1a as function of the time between the end of the readout and triggering the next event. In addition to the delay introduced by the software, the communication latency of the PC with the readout system of the order of $100 \, \mu\text{s}$ has to be taken into account. There is no significant rate dependence visible. This behaviour has been achieved by resetting the DMC except for the acquisition and readout period. Otherwise, the capacitor of the DMC would be discharged by leakage currents and show a hit.

The fake-hit rate is found to increase with V_{CASN}, as shown in Fig. 6.14. The V_{CASN}-dependence is stronger with reverse substrate-bias. This can be explained by the reverse substrate bias influencing the characteristics of the NMOS transistor, to whose gate V_{CASN} is connected. A higher I_{THR} can be used to reduce the fake-hit rate. The fake-hit rate as a function of threshold is discussed in more detail below together with the detection efficiency.

As mentioned above, the DMC of the pALPIDEss prototypes can be discharged by leakage currents within the memory cell. Figure 6.15 shows the fake-hit rate as function of the acquisition time t_{ACQ}. For t_{ACQ} smaller of than a few µs, the
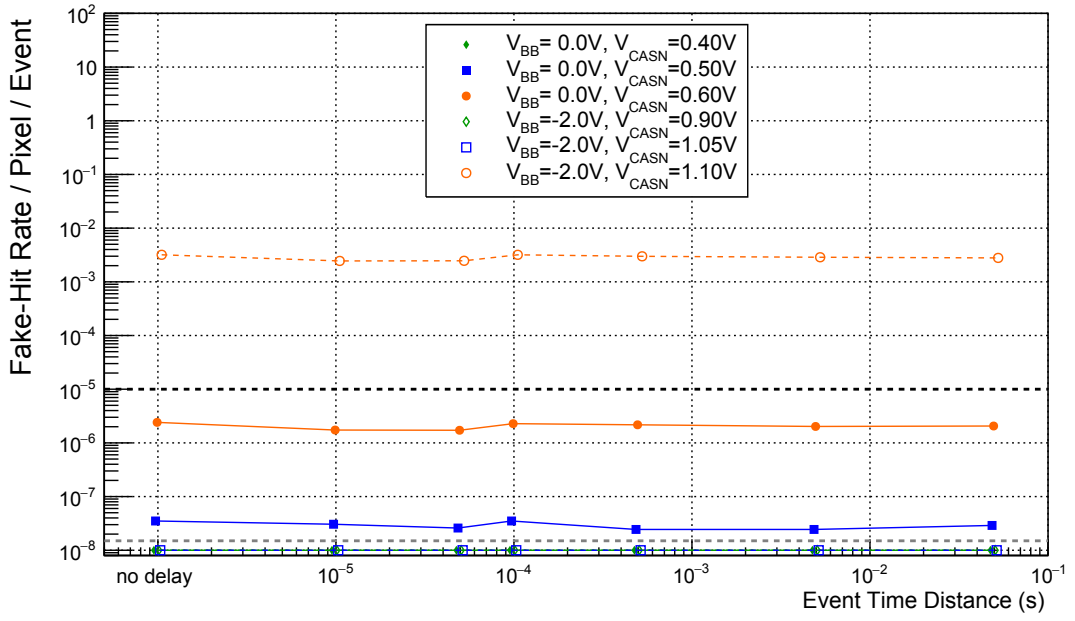
Figure 6.13.: Fake-hit rate of a pALPIDEss-1a at default settings as function the delay between end of readout and triggering the next event. The measurement sensitivity is indicated by the grey dashed line.
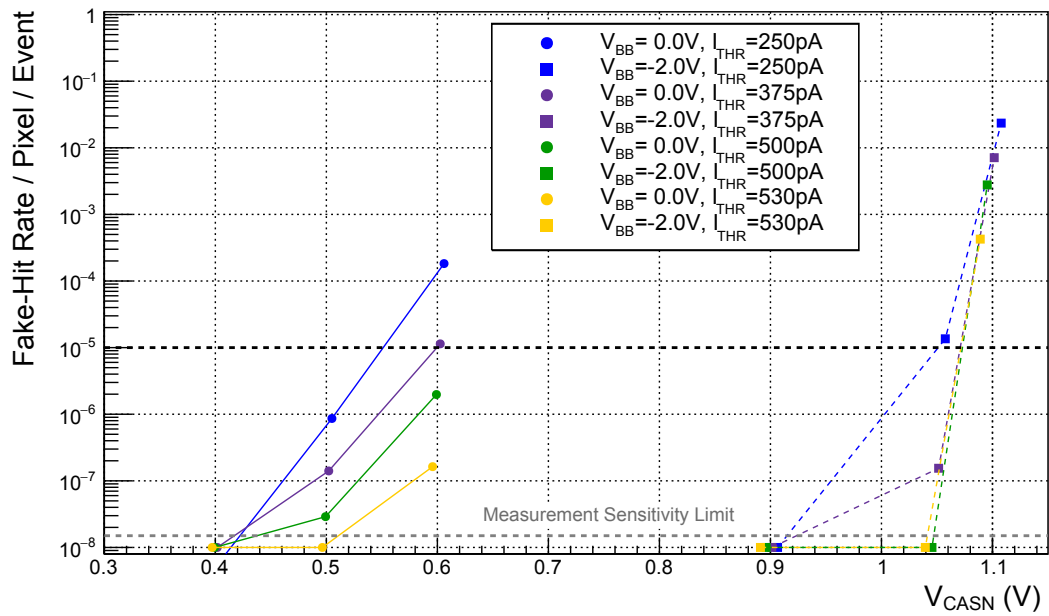
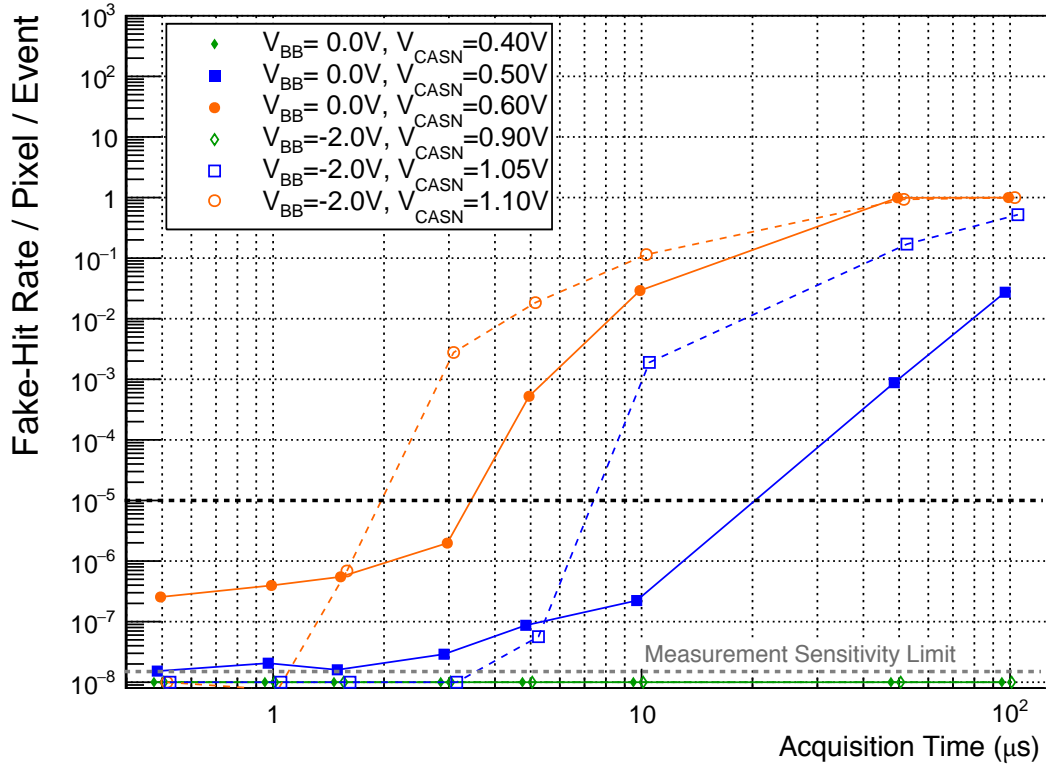**Figure 6.14.:** Fake-hit rate of a pALPIDEss-1a at different settings in terms of I_{THR}, V_{CASN} and V_{BB}.

Figure 6.15.: Fake-hit rate of a pALPIDEss-1a as a function of acquisition time.

fake-hit rate is only slightly influenced by the duration. For larger t_{ACQ}, the fake-hit rate increases exponentially until all pixels fire. This can be understood by a leakage current at the input of the DMC, which is increased for an active `STROBE` signal. This hypothesis is supported by this effect being increased at higher V_{CASN}. This behaviour of the DMC and the only moderately smaller surface needed for the implementation, led to the change to a latch in the full-scale pALPIDE. The advantage of the latch is furthermore its basically instant reaction to an input signal, compared to the discharging time of a few hundred ns of the DMC.

pALPIDE-2

In pALPIDE-2, two sectors, 0 and 1, differ only in the size of their input transistor. Comparing both sectors, the larger input transistor in sector 1, which has four times minimum width by minimum length, performs significantly better in terms of fake-hit rate (cf. Fig. 6.16). At nominal I_{THR} of $500\,\text{pA}$, the sector 0 with the small input transistor reaches a fake-hit rate of 10^{-6} /event/pixel without masking while sector 1 reaches less than 10^{-10} /event/pixel. A masking $0.1\,\%$ of the pixels in sector 0, leads to a fake-hit rate similar to sector 1 without masking. Masking can be used up to the extent for which it deteriorates the detection efficiency and the position resolution. Even assuming only single-pixel clusters, a masking of a
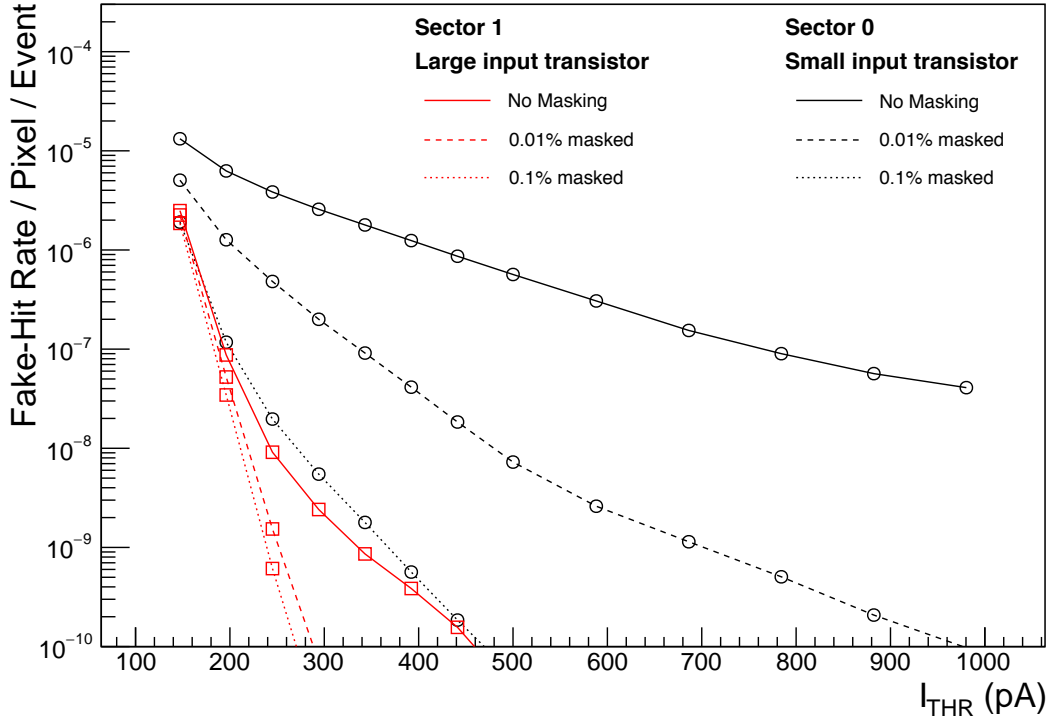
Figure 6.16.: Fake-hit rate averaged over ten pALPIDE-2 as function of I_{THR}, comparing the large-width input transistor (red) and the small-width input transistor (black), $V_{\text{BB}} = -3\,\text{V}$, $V_{\text{CASN}} = 0.95\,\text{V}$.

maximum $1\,\%$ of the pixels would still allow to a achieve a detection efficiency of $99\,\%$, assuming a fully efficient sensor. A masking of $0.1\,\%$ in any case is feasible from this point of view. Additionally, the fake hits have to originate from a reproducible set of pixels to make the masking effective.

Comparing the measured fake-hit rate with the estimate based on the assumption of only noise following a Gaussian distribution causing the fake hits, a large discrepancy is found for both pALPIDEss (cf. Fig. B.2) and pALPIDE-2 (cf. Fig. 6.17). For results before irradiation (circles) in Fig. 6.17, the expected and measured fake-hit rate show a different ordering of the sectors. While the expected values of sector 1 with the wider input transistor are the highest, the measured values are the lowest. After irradiation all sectors show an increased fake-hit rate and there is no advantage of the wider input transistor. The discrepancy of the estimated and measured fake-hit rate decreases with decreasing I_{THR} corresponding to low charge thresholds.

In summary, the fake-hit rate cannot be estimated by a simple model based on Gaussian TN distribution. The reduction of the fake-hit rate due to the wider input transistor points towards Random Telegraph Noise (RTN) [147]. RTN has been identified as source of noise in the analogue prototypes of the ALPIDE family [130] and MAPS of the MIMOSA family [148, 149]. The RTN is known to depend on
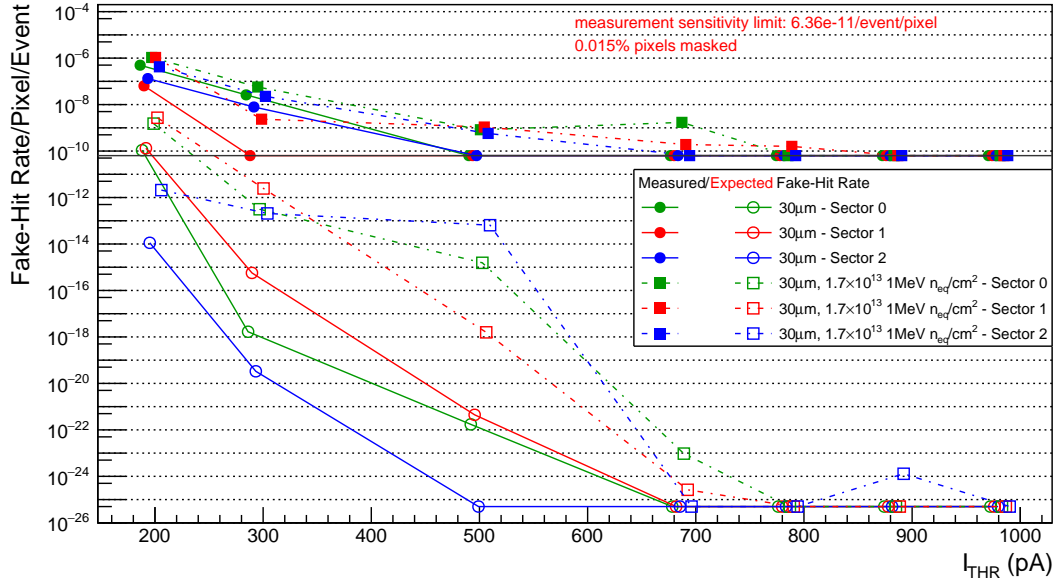
Figure 6.17.: Measured (full symbols) and expected fake-hit rate for a pALPIDE-2 before (circles) and after irradiation with $1.71\,\mathrm{MeV\,n_{eq}/cm^2}$ NIEL (squares) for sectors 0 (small input transistor, $2\,\mu\mathrm{m}$ spacing), sector 1 (larger input transistor, $2\,\mu\mathrm{m}$ spacing) and sector 2 (small input transistor, $4\,\mu\mathrm{m}$ spacing), $30\,\mu\mathrm{m}$ epitaxial layer, $V_{\mathrm{BB}} = -6\,\mathrm{V}$, $V_{\mathrm{CASN}} = 1.12\,\mathrm{V}$.

the transistor geometry and type (NMOS or PMOS). It typically diminishes when increasing the transistor size [130, 150]. A larger input transistor on the other hand leads to a larger contribution of the input transistor to the input capacitance. The larger input capacitance C leads to a smaller signal voltage $\Delta V_{\mathrm{IN}} = Q/C$. However, it is not clear whether the junction or the circuit dominates the input capacitance. Furthermore, a wider gate leads to higher transconductance, which could compensate for the reduced signal. The influence of input transistior size on the detection efficiency is discussed in Ch. 6.2.6.

6.2.5. Pulse Width

pALPIDEss

The maximum pulse width of the pALPIDEss prototypes measured in the laboratory are summarised in Tab. 6.1. The measured maximum pulse width is biased to lower values by the time above threshold needed to discharge the capacitor, which is a few hundred nanoseconds. The strobe-delay step width used for the measurement is 200 ns. At zero reverse substrate bias, the pALPIDEss-0 shows shorter pulses than the pALPIDEss-1a/b, while at $V_{\mathrm{BB}} = -2\,\mathrm{V}$, the pulse widths of pALPIDEss-1a/b are shorter. This is attributed to the NMOS clipping transistor deployed in the pALPIDEss-0, whose performance degrades under reverse substrate bias. A larger

Table 6.1.: Maximum pulse width measured in the laboratory of pALPIDEss prototypes using $t_{\mathrm{ACQ}} = 1.54\,\mu\mathrm{s}$ using strobe-delay steps of $0.2\,\mu\mathrm{s}$.

V_{BB} (V)	I_{THR} (pA)	V_{CASN} (V)	Maximum Pulse Width (µs)		
			pALPIDEss-0	pALPIDEss-1a	pALPIDEss-1b
0.0	500	0.40	3.4	4.8	4.4
0.0	500	0.50	3.2	4.8	4.4
0.0	500	0.60	3.2	4.2	3.8
0.0	250	0.40	4.4	6.6	6.0
0.0	250	0.50	4.2	6.6	5.8
0.0	250	0.60	4.2	5.4	4.8
-2.0	500	0.90	6.6	5.0	4.6
-2.0	500	1.05	6.8	4.8	4.4
-2.0	500	1.10	6.8	4.8	4.2
-2.0	250	0.90	12.0	7.0	6.2
-2.0	250	1.05	11.8	6.8	6.0
-2.0	250	1.10	11.8	6.6	5.8

I_{THR} leads to a shorter pulse, independent of V_{CASN} and V_{BB}. pALPIDEss-0 only shows a marginal influence of V_{CASN} on the pulse width. pALPIDEss-1a/b show a similar behaviour at $V_{\mathrm{BB}} = -2\,\mathrm{V}$. At $V_{\mathrm{BB}} = 0\,\mathrm{V}$, however, the measurements at the highest V_{CASN} show a significantly shorter pulse width. Comparing the maps of the hit-detection probability as function of strobe delay t_S and the injected charge at $V_{\mathrm{CASN}} = 0.4\,\mathrm{V}$ and $V_{\mathrm{CASN}} = 0.6\,\mathrm{V}$, the latter shows less reduction of the pulse width at higher charges. This is most likely due to an earlier activation of the clipping mechanism as expected from a smaller potential difference of the `HIT` and `CURFEED` node caused by the larger V_{CASN}. In pALPIDE-3, the reference voltage for the clipping transistor can be adjusted.

Similar results were obtained by test beam measurements of the detection efficiency as a function the strobe delay t_{s} relative to the arrival time of the trigger at the readout system. In Fig. 6.18, the influence of I_{THR} (left) and V_{BB} (right) is shown. Error bars show the chip-to-chip fluctuations where measurements of multiple chips are available. The pALPIDEss-0 was measured shining light onto the DUT. In comparison to pALPIDEss-0, pALPIDEss-1a/b show a slightly larger peaking time of about $1.5\,\mu\mathrm{s}$ compared to $1.0\,\mu\mathrm{s}$.

In summary, pALPIDEss-1b shows systematically a $0.4\,\mu\mathrm{s}$ to $0.8\,\mu\mathrm{s}$ smaller pulse width than pALPIDEss-1a. This can most likely be attributed to the smaller coupling capacitor C_{s}, which is recharged more quickly after a hit, leading to a faster return of the `HIT` node to the baseline.

Both measurements methods are in agreement with the FWHM of $3.5\,\mu\mathrm{s}$ observed on the analogue output (cf. Fig. 6.1). This an important confirmation of the results obtained using measurement methods based on the discriminated digital output.
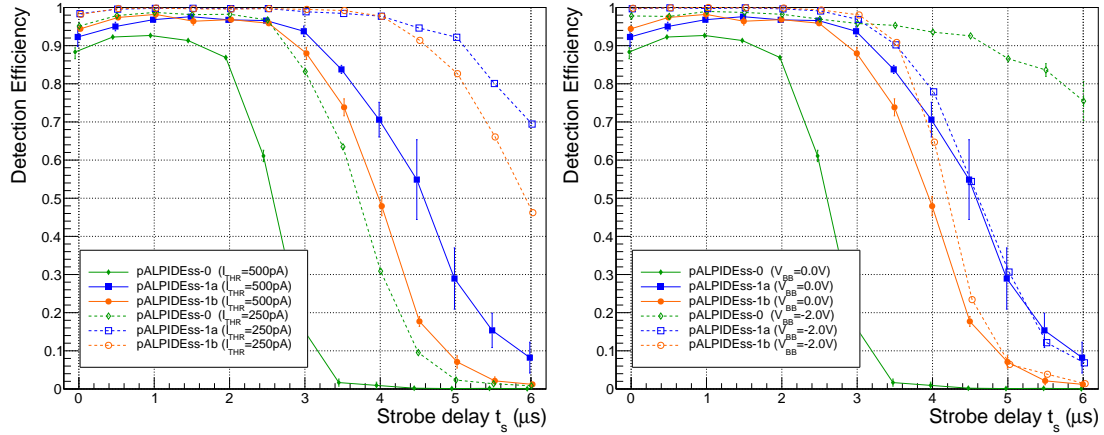
Figure 6.18.: Detection efficiency as function of the strobe delay for pALPIDEss prototypes. Left: influence of I_{THR} at $V_{BB} = 0.0\,\text{V}$, $V_{CASN} = 0.4\,\text{V}$. Right: influence of V_{BB}, for $V_{BB} = 0.0\,\text{V}$ and $V_{CASN} = 0.4\,\text{V}$, as well as $V_{BB} = -2.0\,\text{V}$ and $V_{CASN} = 0.9\,\text{V}$. Both plots were acquired using $t_{ACQ} = 1.54\,\text{µs}$.
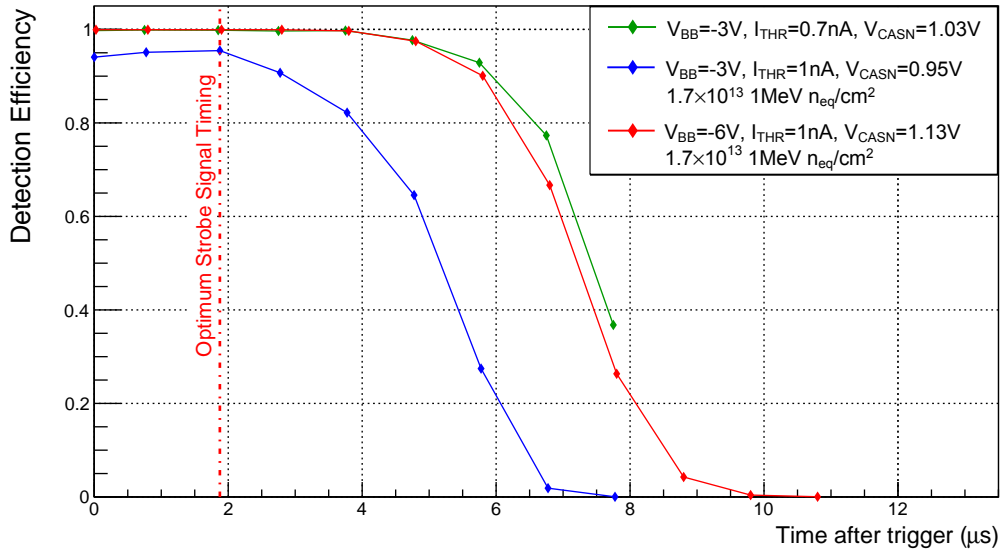

Figure 6.19.: Detection efficiency as function of the strobe delay t_s for pALPIDE-2 settings leading to a particularly short pulse width.

pALPIDE-2

The pALPIDE-2 front-end is close to that of pALPIDE-1, and there is no difference in terms of pulse width expected. The pulse widths of pALPIDE-1 [130] were measured to be significantly longer with about $10\,\text{µs}$ compared to less than $5\,\text{µs}$ in the small-scale prototypes at nominal settings. The peaking time has slightly increased to about $2\,\text{µs}$ at nominal settings. Increasing I_{THR} to $686\,\text{pA}$ leads to a reduction of the pulse width to about $8\,\text{µs}$ and the peaking time to approximately $1.8\,\text{µs}$. Increasing V_{CASN} to $1.03\,\text{V}$ compensates the threshold increase due to the

higher I_{THR}. At the time of the pALPIDE-2 characterisation, an update of the front-end circuit was prepared for pALPIDE-3 [137]. Consequently, the pulse width of the pALPIDE-2 was only measured as a cross-check and to adjust the strobe delay in order to achieve the highest sensitivity. The pulse-width measurements at the test beam, shown in Fig. 6.19, show pulse widths of about 7.5 μs at settings with full detection efficiency (red and green curve). These pulse widths are comparable to measurements obtained for the pALPIDE-1 at similar settings. The usage of MIPs leads to a minimum average charge deposition and in turn the largest peaking time. The peaking time defines the earliest strobe time. It can be inferred from a setting not reaching full detection efficiency (blue) and is in between 1.8 μs to 2.0 μs. Consequently, the strobe delay t_s is chosen 1.9 μs.

6.2.6. Detection Efficiency and Fake-Hit Rate

In the following, emphasis is put on pALPIDE-2. Results on the pALPIDEss, which has also been demonstrated to fulfil the requirements in terms of detection efficiency and fake-hit rate, can be found in App. B. The following plots on pALPIDE-2 are based on the measurement of single chips. The number of reference tracks varies from about 2000 to 12 000, ensuring a statistical uncertainty smaller than 0.5 % in an efficiency regime close to full efficiency. All comparisons of sector 0 and sector 1, which only differ by the input transistor size, confirmed a similar performance in terms of detection efficiency despite the increased gate capacitance of the wider input transistor. Possible explanations are either the input capacitance being dominated by the junction capacitance and not by the gate capacitance of the input transistor or the larger transconductance compensating the larger capacitance. In the following, results of sector 1 with the larger input transistor are shown, as it outperforms the sector 0 in terms of operational margin due to the significantly lower fake-hit rate (cf. Fig. 6.16).

In Fig. 6.20, the two best performing combinations of epitaxial layer and spacing with respect to detection efficiency and fake-hit rate are shown. The combinations are 30 μm epitaxial layer combined with 4 μm spacing in sector 2 with the small input transistor (top) and 25 μm epitaxial layer combined with 2 μm spacing in sector 1 with the larger input transistor (bottom). Both combinations show a wide I_{THR} range from 200 pA to 1000 pA for which the requirements in terms of both detection efficiency and fake-hit rate are fulfilled. Although irradiated with a higher NIEL dose of 1.7×10^{13} 1 MeV $n_{\text{eq}}/\text{cm}^2$ compared to 1.0×10^{13} 1 MeV $n_{\text{eq}}/\text{cm}^2$, the combination of 4 μm spacing (sector 2) and 30 μm epitaxial layer shows less degradation due to radiation effects. The 2 μm spacing (sector 1) and 25 μm epitaxial layer combination shows better performance in terms of fake-hit rate due to the larger input transistor. The larger input transistor, however, can also be combined with a larger spacing leading potentially to a further increase of the operational margin. This will be studied in pALPIDE-3. An advantage of using only 2 μm spacing is
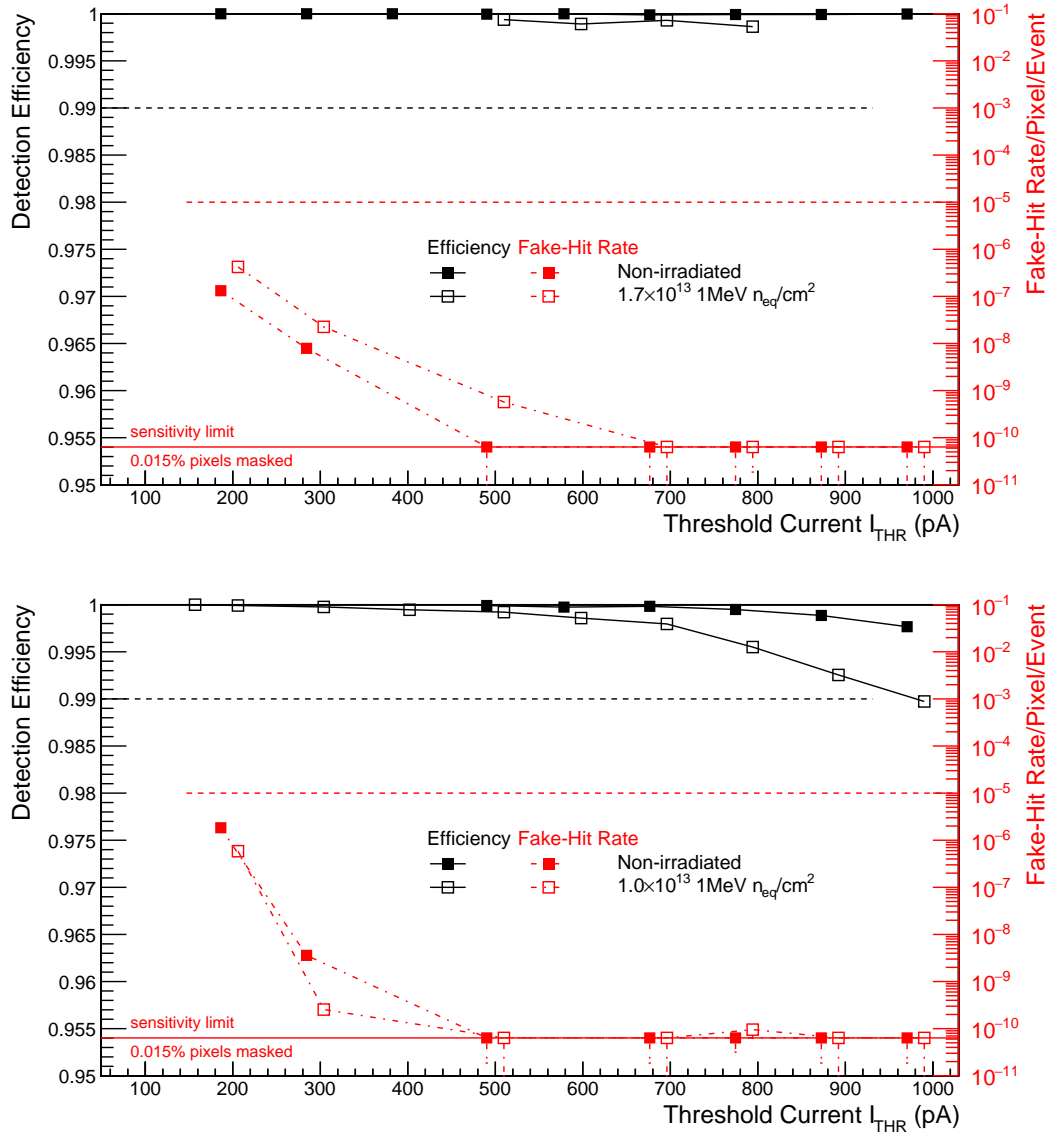
Figure 6.20.: Detection efficiency and fake-hit rate as function of I_{THR}. Top: 30 μm epitaxial layer, 4 μm spacing. Bottom: alternative combination, 25 μm epitaxial layer, 2 μm spacing. Both at $V_{\text{BB}} = -6\,\text{V}$, $V_{\text{CASN}} = 1.12\,\text{V}$.

the increased space for in-pixel circuitry, which is for example of need to integrate multiple hit-buffers in the pixel.

The reverse-substrate-bias dependence is shown in Fig. 6.21 (top). With regard to the detection efficiency, the largest benefit is obtained by going from 0 V to −3 V. $V_{\text{BB}} = -6\,\text{V}$ leads only to a marginal gain for the 4 μm spacing in sector 2 before irradiation shown in Fig. 6.21. After NIEL irradiation, the charge-collection time plays a more important role, as the charge-carrier lifetime is reduced by radiation-induced defects. Additional reverse substrate bias can lead to a larger depletion
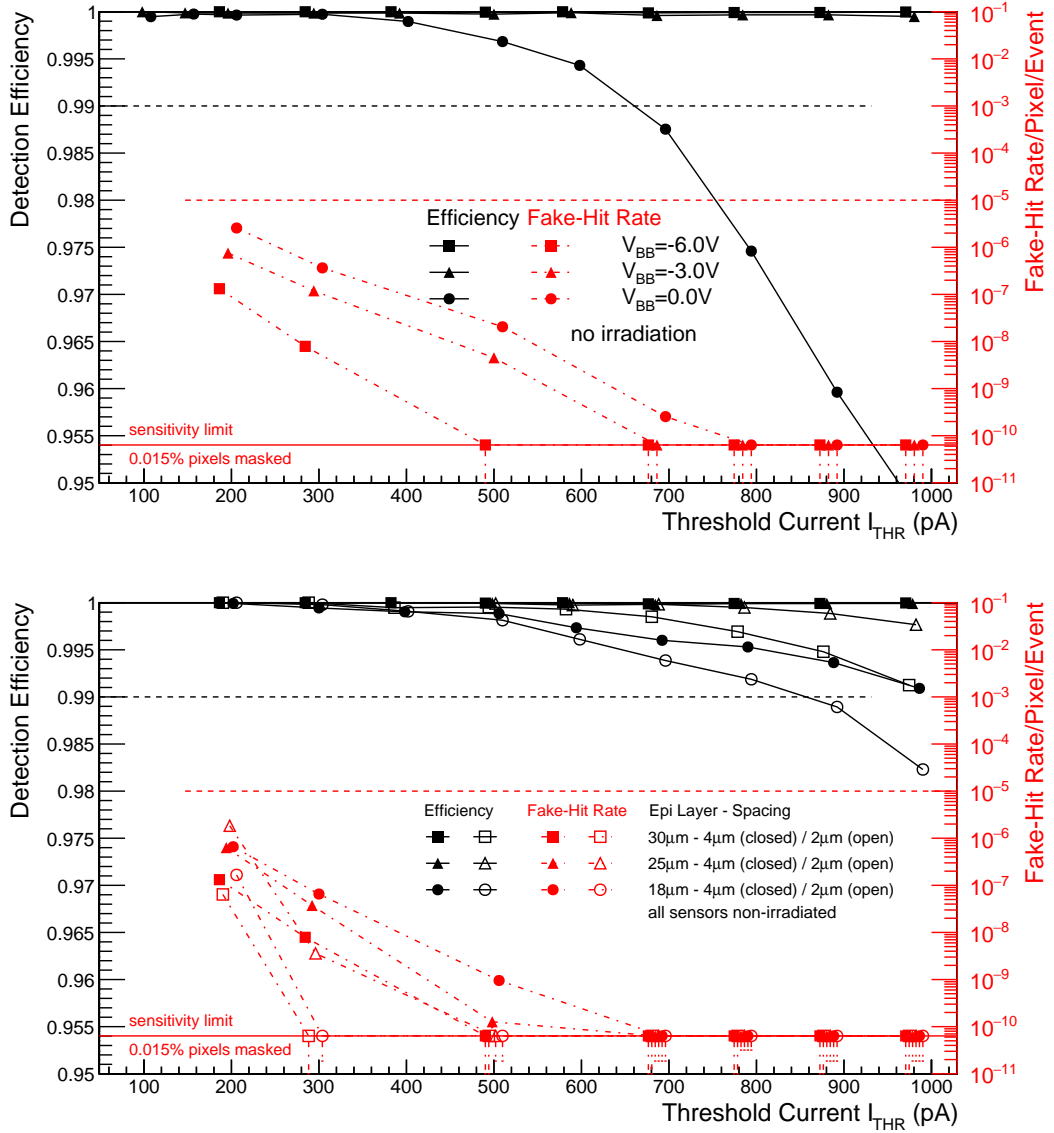
Figure 6.21.: Detection efficiency and fake-hit rate as function of I_{THR}: V_{BB}-dependence for $30\,\mu m$ epitaxial layer, $4\,\mu m$ spacing using $V_{CASN} = 0.4\,V$ for $V_{BB} = 0\,V$, $V_{CASN} = 0.95\,V$ for $V_{BB} = -3\,V$ and $V_{CASN} = 1.12\,V$ for $V_{BB} = -6\,V$. Bottom: epitaxial layer and spacing comparison at $V_{BB} = -6\,V$, $V_{CASN} = 1.12\,V$.

volume resulting to more signal collection by drift and in turn to a faster charge collection. Additionally, the fake-hit rate decreases with additional reverse substrate bias. This can be due to the fact that a higher charge threshold can be applied as the seed signal increases due to the smaller capacitance and the reduced charge sharing (cf. Ch. 5.4.1).

Figure 6.21 (bottom) shows the dependence of detection efficiency and fake-hit rate on the epitaxial-layer thickness and spacing. The spacing of $4\,\mu m$ (full sym-

bols) systematically outperforms the 2 µm spacing (open symbols) in terms of detection efficiency at the same epitaxial-layer thickness. This is expected from the larger depletion region formed together with a wide spacing in the combination with $V_{\text{BB}} = -6\,\text{V}$, leading to larger amount of charge collected in the seed pixel. With 4 µm spacing a thicker epitaxial layer can be beneficial. This is not the case with 2 µm spacing for which the 30 µm epitaxial layer performs worse than the 25 µm epitaxial layer. This can be attributed to larger charge spread due to a smaller relative amount of depleted sensor volume. The additional charge generated in the 30 µm epitaxial layer can therefore only be exploited with the help of the 4 µm spacing. In terms of fake-hit rate, two effects are visible: the larger input transistor in the sector with 2 µm spacing outperforms the minimum-size input transistor in the 4 µm spacing sector. The dependence on the epitaxial-layer thickness in sector 2 is not understood and it would be necessary to study this on multiple instead of single chips per epitaxial-layer thickness.

In Fig. 6.22 (top), the detection efficiency and fake-hit rate is shown as function of the charge threshold for the pixel with the large input transistor, 2 µm spacing and 25 µm epitaxial layer. For this measurement, different combinations of I_{THR} and V_{CASN} were used to set the charge threshold. Although the different combinations can lead to the same threshold, the pulse shape is longer for smaller I_{THR}. The data points with square symbols were measured at V_{CASN} fixed to 1.12 V and I_{THR} was varied within the range of about 200 pA to 1000 pA. The data points with circles were measured using I_{THR} fixed to 785 pA and varying V_{CASN} in the range from 1.00 V to 1.21 V.
The detection efficiencies of settings with the same measured threshold compare well. This is a confirmation of the measured charge threshold and the used strobe delay t_s, as for the right strobe timing the pulse width is expected to be irrelevant. The measured threshold hence can be used to compare measurement results.

The importance of reverse substrate bias for a pixel with 2 µm spacing (sector 1) and 25 µm epitaxial layer after $1.0 \times 10^{13}\,1\,\text{MeV}\,\text{n}_{\text{eq}}/\text{cm}^2$ NIEL irradiation is shown in Fig. 6.22 (bottom). The reverse substrate bias of $-3\,\text{V}$ leads to an operational range of about 30 e^-. Increasing the reverse substrate bias doubles the operational range to about 60 e^-.

Both combinations of spacing and epitaxial layer, sector 1 with 2 µm spacing, larger input transistor and 25 µm epitaxial layer as well as sector 2 with 4 µm spacing, minimum-size input transistor and 30 µm epitaxial layer, show a large operational margin even after irradiation with NIEL under the condition that a reverse substrate bias of $-3\,\text{V}$ is applied. The measurement was carried out with tracks perpendicular to the sensor. For inclined tracks, the path length of the particle in the active volume increases resulting in more generated charge. With the combination pixel pitch and epitaxial-layer thickness of the pALPIDE-2 prototypes, the charge in the seed pixel is not expected to be significantly dependent on the inclination angle.
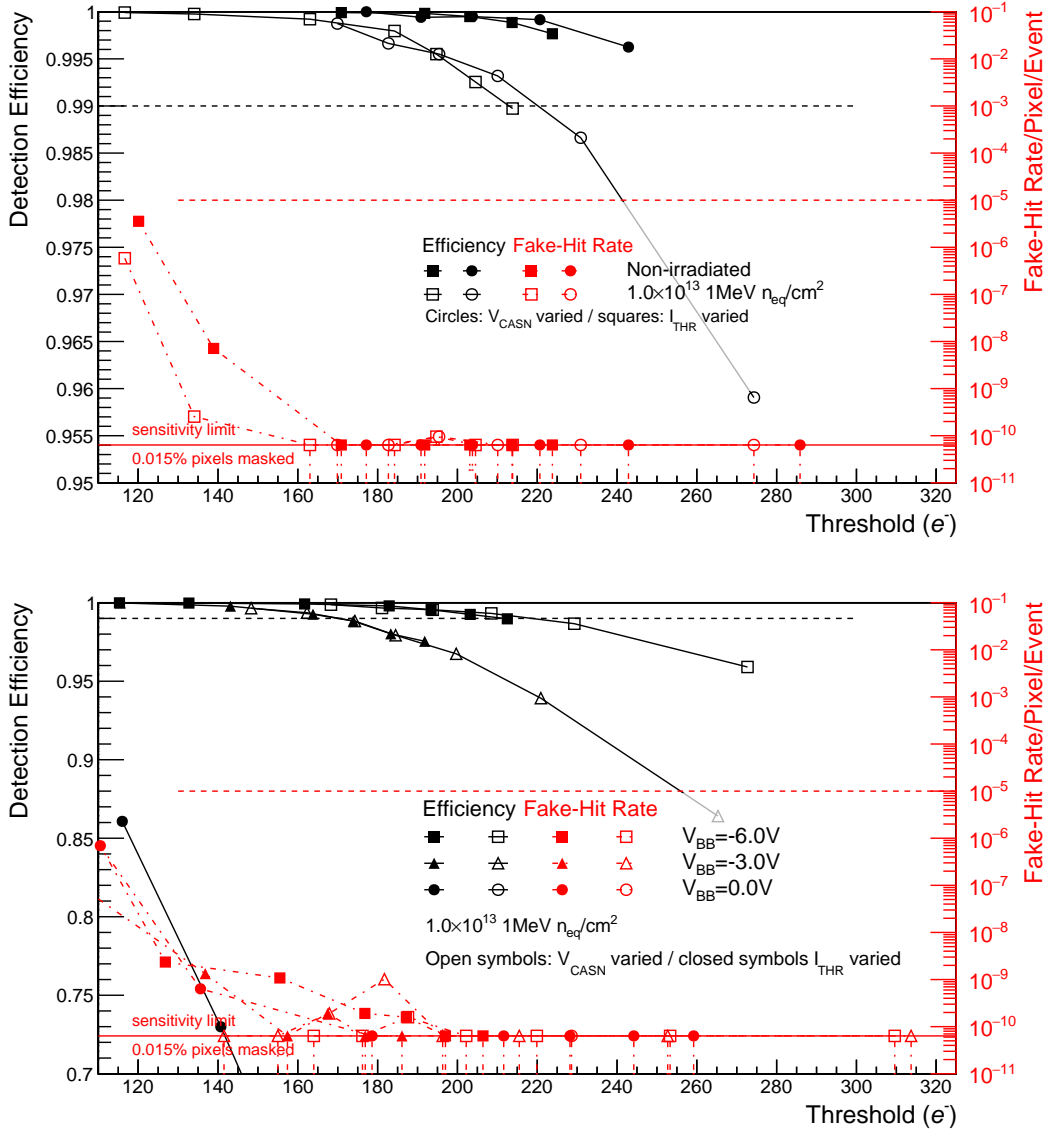
Figure 6.22.: Detection efficiency and fake-hit rate as function of measured threshold for 25 µm epitaxial layer, 2 µm spacing (sector). Top: influence of $1.0 \times 10^{13}\,1\,\text{MeV}\,n_{eq}/\text{cm}^2$ NIEL irradiation at $V_{BB} = -6\,\text{V}$. Bottom: influence of reverse substrate bias after $1.0 \times 10^{13}\,1\,\text{MeV}\,n_{eq}/\text{cm}^2$ NIEL irradiation.

6.2.7. Position Resolution and Cluster Size

In the following, the position resolution and cluster size measured for the pALPIDE-2 are presented. As a reverse substrate bias of $-6\,\text{V}$ resulted in the largest operational marginin terms of detection efficiency and fake-hit rate, it used as the baseline for the study of the position resolution.

In Fig. 6.23, the position resolution and mean cluster size for 30 µm epitaxial layer
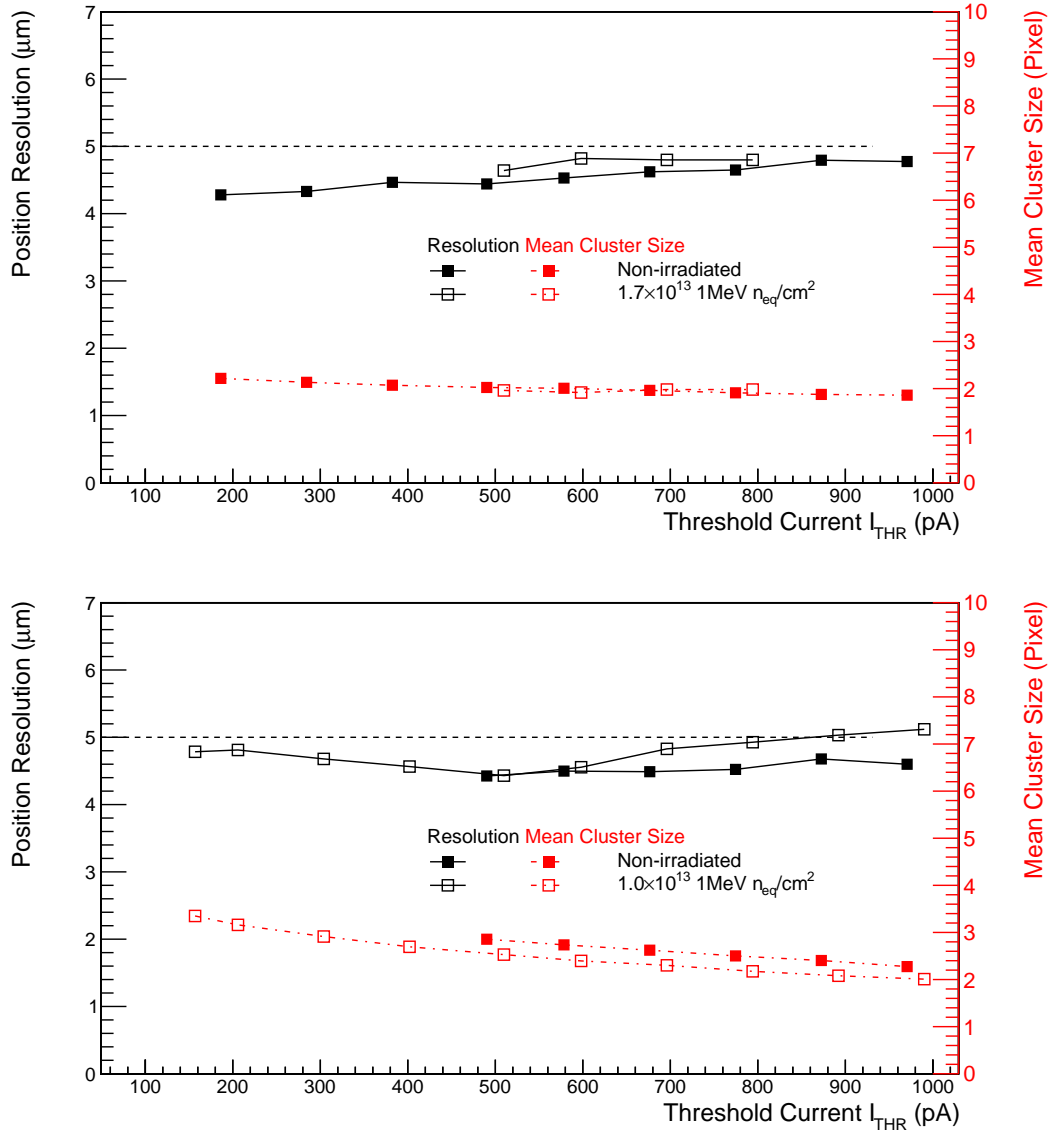
Figure 6.23.: Position resolution and average cluster size as function of I_{THR}. Top: 30 µm epitaxial layer, 4 µm spacing. Bottom: 25 µm epitaxial layer, 2 µm spacing. Both at $V_{BB} = -6\,V$, $V_{CASN} = 1.12\,V$.

combined with 4 µm spacing in sector 2 (top) and 25 µm epitaxial layer combined with 2 µm spacing in sector 1 (bottom) are shown. These are the same combinations as presented in Fig. 6.20. Both combinations achieve a position resolution better than 5 µm. The 4 µm spacing combined with the 30 µm epitaxial layer is less sensitive to irradiation in terms of cluster size. This supports the hypothesis of a larger depletion volume due to the combination of increased spacing and large reverse substrate bias, leading to more charge collection by drift and less diffusion. Charge trapping and recombination are expected to matter mainly in the regions where
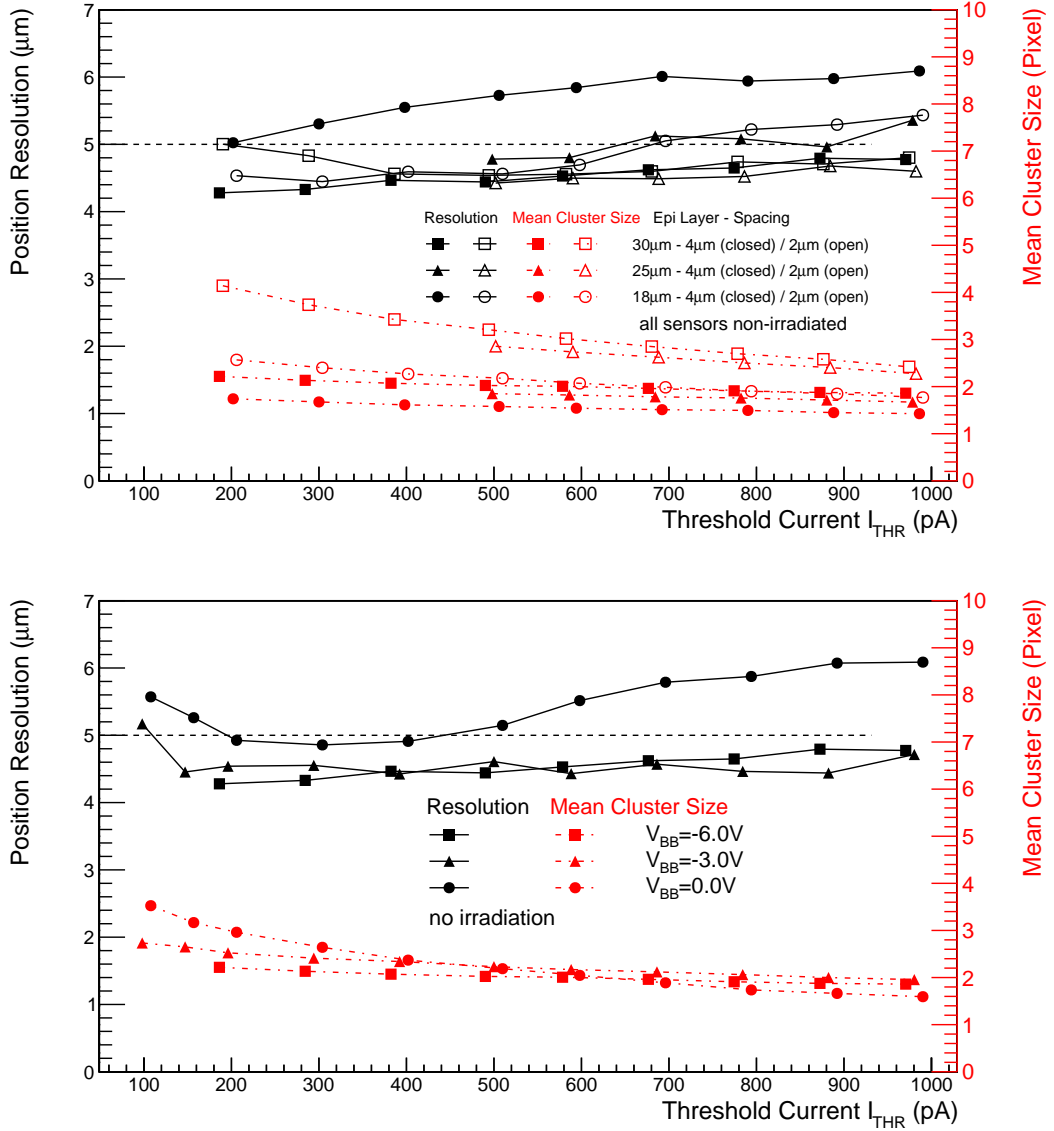
Figure 6.24.: Position resolution and average cluster size as function of I_{THR}. Top: dependence on spacing and epitaxial-layer thickness at $V_{\text{BB}} = -6\,\text{V}$, $V_{\text{CASN}} = 1.12\,\text{V}$. Bottom: dependence on the reverse substrate bias for $4\,\mu\text{m}$ spacing and a $30\,\mu\text{m}$ epitaxial layer.

the charge is collected by diffusion due to the larger charge-collection time. The dependence of the position resolution on I_{THR} and the irradiation effects are less than $10\,\%$ in the presented I_{THR}-range.

The assumptions on the charge collection properties in MAPS are further supported by Fig. 6.24 (top). The average cluster size increases with the epitaxial-layer thickness independent of the spacing. This is expected from the additional charge generated, while the lateral extension of the depletion volume is not expected to

97

strongly depend on the epitaxial-layer thickness. The charge generated in the un-depleted volume is collected by adjacent pixels via diffusion. However, the cluster size will only increase, if the amount of charge arriving at these pixels is above threshold. With smaller spacing and without reverse substrate bias, the cluster size decreases with increasing epitaxial-layer thickness as the charge at individual pixels is too small for detection due to diffusion (cf. Fig. B.13).

A larger spacing leads to smaller clusters due to an increased depletion volume, leading to less charge sharing. The 4 μm spacing combined with 18 μm epitaxial-layer thickness is an example for too little charge sharing, leading to a cluster size resulting in a degraded position resolution (cf. Fig. 6.24, top).

For an epitaxial layer of 25 μm and 30 μm thickness and with reverse substrate bias, the position resolution is largely independent of I_{THR}, spacing and whether a V_{BB} of $-3\,\mathrm{V}$ or $-6\,\mathrm{V}$ is applied (cf. Fig. 6.24, bottom).

In summary, the measurement results match the expected dependence on spacing, epitaxial-layer thickness and reverse substrate bias (cf. Ch. 5.4.1). The required position resolution of 5 μm was achieved. With reverse substrate bias and an epitaxial-layer thickness of 25 μm or 30 μm, the dependence of the position resolution on the front-end settings is less than 10 %.

6.3. Summary

The characterisation results of the pALPIDEss prototypes studied within this thesis show that the ALPIDE architecture is conceptually working. Based on the results obtained in pALPIDEss-0, the light sensitivity has been mitigated and the reverse-substrate-bias tolerance was increased pALPIDEss-1a/b.

pALPIDE-2 was measured to fulfil the requirements in terms of detection efficiency, fake-hit rate and position resolution. Furthermore, the influence of the epitaxial-layer thickness, spacing and reverse substrate bias on the detection efficiency and position resolution in pALPIDE-2 matches the expectations on the charge collection and generation. The wider input transistor in pALPIDE-2 leads to a significant reduction of the fake-hit rate, which is assumed to be dominated by RTN. The operational margin using reverse substrate bias and an epitaxial layer of 25 μm or 30 μm thickness in terms of detection efficiency, fake-hit rate and position resolution also after NIEL irradiation is sufficient.

7. Measurement of $\mathrm{D}^0 \to \mathrm{K}^- \pi^+$ with the Upgraded ITS

In this chapter, the performance gain expected from the upgraded ITS for the measurement of prompt and feed-down D^0 mesons in the decay channel $\mathrm{D}^0 \to \mathrm{K}^- \pi^+$ using cut variations is assessed. This study is carried out using a fast MC simulation scheme called the 'ITS improver'.

The common MC simulation procedure of ALICE starts with a MC generator like PYTHIA [76, 107] or HIJING [105]. The output of these generators, the so-called MC truth, contains the full information of all particles contained in an event and their kinematics at the point of interaction. The particles contained in this event are then propagated through the detector material using GEANT3 [151]. During the propagation through the material, energy loss and multiple scattering are taken into account. Furthermore, long-lived particles are decayed and the detector response based on the energy loss in the active volumes is simulated. Based on the simulated detector response, the same reconstruction, as used for real data, is run. The reconstructed data is the basis of a physics analysis.

The ITS improver allows to modify the detector response while reading the data for analysis. This is achieved by reading the reconstructed helix and MC truth information of a track and calculating the residuals of the reconstructed track p_T and the reconstructed impact parameter d_0 separately in $r\varphi$ and z direction. These residuals δ_current are then scaled according to

$$\delta_\mathrm{up} = \frac{\sigma_\mathrm{up}}{\sigma_\mathrm{current}} \cdot \delta_\mathrm{current} \tag{7.1}$$

in order obtain the expected residuals after the upgrade δ_up using the ratio of the corresponding resolution after the upgrade σ_up over the current resolution σ_current. The track helix is updated according to the scaled residuals σ_up. Based on the new track helices, the secondary vertices of the D^0 candidates are recalculated. With the method being based on existing MC simulations, the sample can be analysed with the normal analysis software, adapted by the ITS improver and re-analysed to assess the upgrade performance at run time. A further detailed description of the ITS improver can be found in Ch. 3 of [111]. The scaling applied by the ITS improver is chosen to reproduce the following detector configuration: the pointing resolution of a single layer is assumed to be $4\,\mu\mathrm{m}$. The radial distance of the innermost layer to the interaction point is $22\,\mathrm{mm}$ and the material budget per layer $0.3\,\%\,\mathrm{X}_0$. The beam pipe radius is assumed to be $20\,\mathrm{mm}$ and the corresponding material budget $0.2\,\%\,\mathrm{X}_0$. Using the parametrisation, the search for secondary vertices is not repeated after the execution of the ITS Improver. Due to the very open cuts used for the search of secondary vertices, the resulting effect is negligible. More selective

cuts are only applied during the actual analysis. A comparison of the performance of the parametrisation and a full MC simulation can be found in [64].

During the course of this thesis, the fast simulation scheme was used to study the performance gain for the feed-down separation using cut variations. The study is carried out on basis of the MC simulations `LHC13d3` and `LHC13d3_plus`. As these simulations are reproducing the conditions of a real data-taking period, the resulting acceptance and efficiency of the ALICE detector system is lower than for an ideal detector.

The choice of cut sets presented in the following study is the same as for the study of p–Pb data described in Ch. 4, with a cut set focusing on prompt D^0 production, a mixed cut set and a cut set focusing on feed-down D^0 mesons. The choice of cut variables is, however, changed. The upgraded ITS will have a similar pointing resolution in xy $(r\varphi)$ and z (cf. Ch. 5.2). Using the 3D decay length and $\cos(\theta_{\text{Pointing}})$ instead of only the xy components as with the current detector makes those variables more effective by exploiting the full performance increase of the upgraded detector. As the description of the decay length resolution was found to be a major contribution to the systematic uncertainty of the measurement (cf. Ch. 4), the decay length is used instead of the normalised decay length. This choice should result in a better matching description of the cut variable in the MC simulation resulting in a smaller systematic uncertainty.

For this upgrade study, the $(\text{Acc} \times \epsilon)$ and the background of the invariant-mass distributions are obtained using the MC simulations modified using the ITS improver. The expected signal is estimated using FONLL calculations [65, 66] scaled using a Glauber model.

7.1. Invariant-Mass Distributions

Due to the signal enhancement in `LHC13d3` and `LHC13d3_plus` described in Ch. 4, the signal has to be scaled in order to be realistic. The cross section for the production of prompt and feed-down D^0 mesons obtained using FONLL calculations [65, 66] scaled using a Glauber model are used to construct the signal. The width of the Gaussian distribution of the signal is extracted from the improved MC simulation. The background shape is also obtained from the improved MC simulation using an exponential fit function, however, due to the signal enhancement, the underlying event of the simulation is biased and the background tends to be overestimated (cf. Ch. 4.3.1). As the scaling of the average background per event is known from the data and MC simulations analysed in Ch. 4, this information is used to scale the background in the improved MC simulation. The change in background shape due to the different underlying event is neglected, as it is assumed that the fit describes the shape well enough and its free of disturbing structures. For all (S/B) estimates the same fit function with a Gaussian distribution describing the signal and an
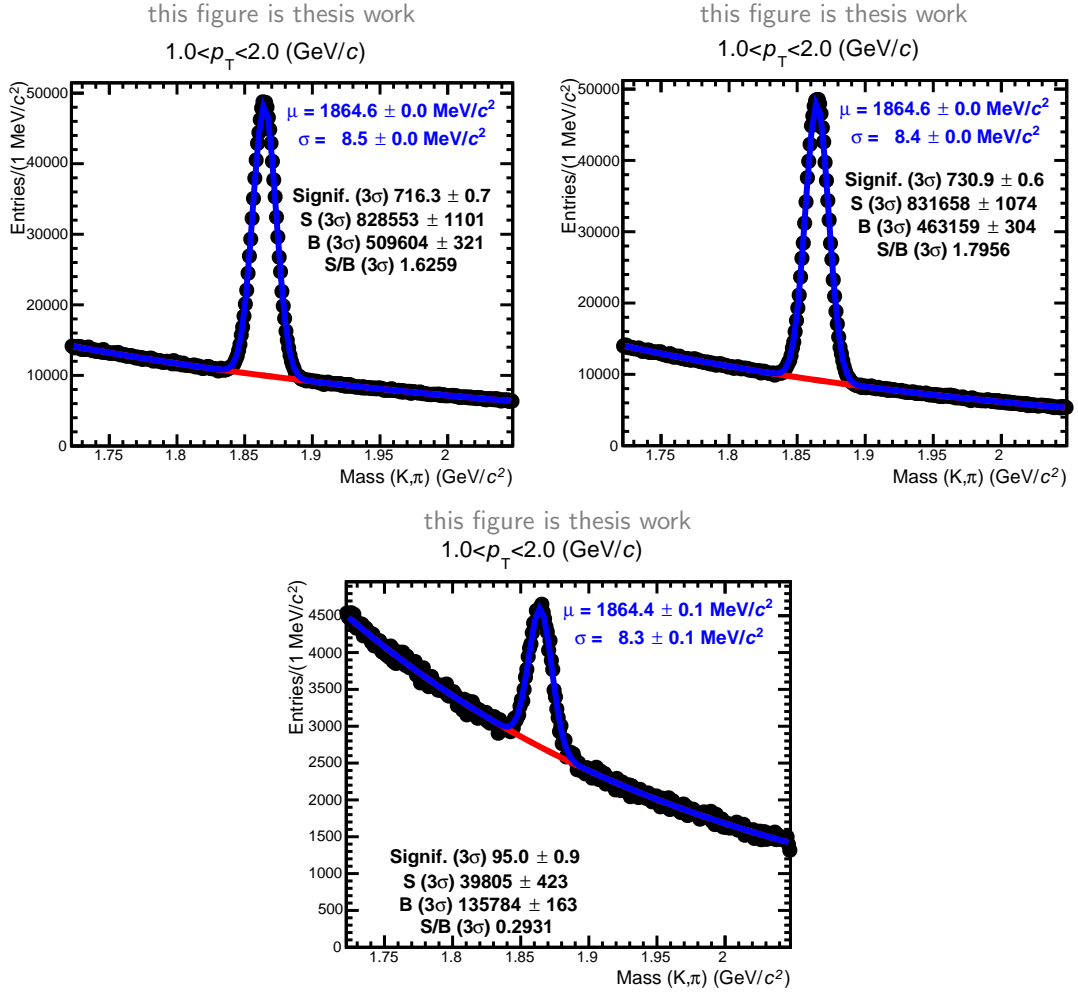
Figure 7.1.: Invariant-mass distributions of D^0 candidates for the prompt-enhanced cut set (top left), mixed cut set (top right) and feed-down-enhanced cut set (bottom centre) in the p_T from $1\,\text{GeV}/c$ to $2\,\text{GeV}/c$.

exponential function describing the background is used.

The signal, constructed based on the cross section from FONLL calculations times the corresponding (Acc $\times$ ϵ), and the estimated background is then used to fill the invariant-mass distributions and a Poisson smearing is applied bin-by-bin. The statistics is scaled to 10^{11} inelastic p–Pb collisions, which are assumed to be recorded after the upgrade of the ITS [64].

An example invariant-mass distribution for the prompt-enhanced (top left), mixed (top right) and feed-down-enhanced cut sets (bottom centre) is shown in Fig. 7.1. The p_T range displayed, from $1\,\text{GeV}/c$ to $2\,\text{GeV}/c$, is of particular interest. With the current detector, it was not possible to define three cut sets leading to reasonable significance values in this p_T bin (cf. Ch. 4). Due to the upgraded ITS and the expected increase in terms of statistics, this p_T region becomes accessible. The complete set of invariant-mass distributions can be found in App. A. As a consequence

Table 7.1.: p_T bins used in the upgrade study.

Bin	1	2	3	4	5	6	7	8	9	10
p_T range (GeV/c)	1–2	2–3	3–4	4–5	5–6	6–7	7–8	8–12	12–16	16–24
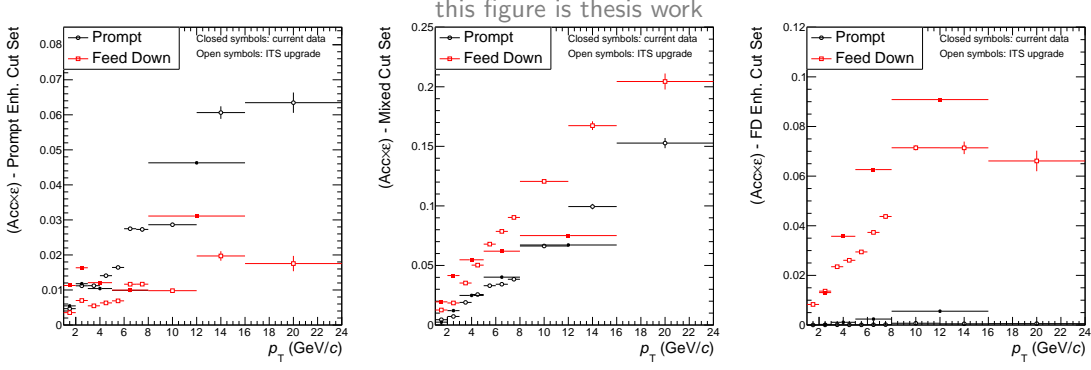
Figure 7.2.: Prompt and feed-down D^0 (Acc$\times\epsilon$) for the prompt-enhanced cut set (left), the mixed cut set (centre) and feed-down-enhanced cut set (right) for the current (closed symbols) and upgraded ITS (closed symbols).

of the increased statistics, it is furthermore possible to use smaller p_T bins and to extend the overall p_T range. The p_T bins chosen for this study are the same as in [94] and shown in Tab. 7.1.

7.2. Acceptance times Efficiency

The (Acc$\times\epsilon$) obtained for the three cut sets using the upgraded ITS (open symbols) along with the (Acc$\times\epsilon$) of the current detector (closed symbols) for the prompt-enhanced (left), mixed (centre) and feed-down (right) enhanced D^0 candidate sets are shown in Fig. 7.2.
Due to the different cut variables, l and $\cos(\theta_\mathrm{Pointing})$ instead of L_xy and $\cos(\theta_\mathrm{Pointing,xy})$, different cut values were chosen aiming for similar (Acc $\times$ ϵ) values as in Ch. 4.
In general, the (Acc $\times$ ϵ) values obtained in the three different cut sets with the upgraded detector show an overall increase in efficiency with increasing D^0 p_T as expected from the larger displacement of the secondary vertex. Although the (Acc$\times\epsilon$) values are at the same order of magnitude as the ones obtained for the current detector, a stronger enhancements of the feed-down and prompt D^0 mesons in the corresponding candidate sets is achieved than in the analysis using the current detector. In the ratio of (Acc $\times$ ϵ)$_\mathrm{FD}$ over (Acc $\times$ ϵ)$_\mathrm{Prompt}$ for the different cut sets shown in Fig. 7.3, the stronger enhancement of prompt (blue symbols) and feed-down (purple symbols) in the corresponding cut sets for the upgrade detector (open symbols) compared to the current detector (closed symbols) becomes evident. The
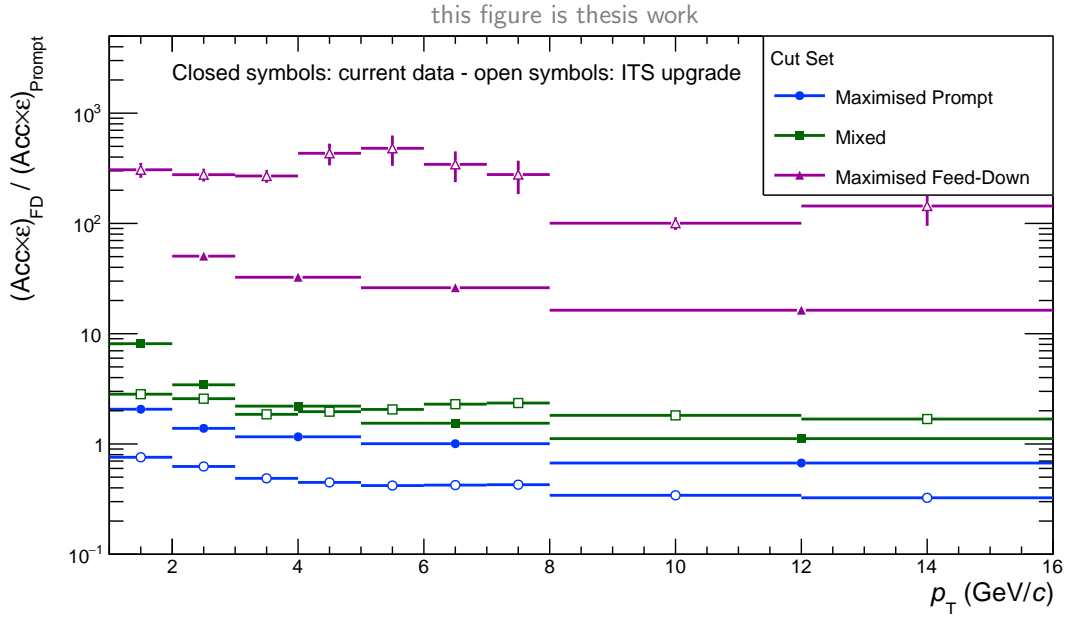
Figure 7.3.: Ratio of the $(\mathrm{Acc} \times \epsilon)$ for feed-down D^0 mesons over that for prompt D^0 mesons for the current (closed symbols) and upgraded ITS (open symbols).

improved pointing resolution of the upgraded detector leads to a better separation of prompt and feed-down D^0 mesons in terms of $\theta_{\mathrm{Pointing}}$ and decay length l, as well as a better rejection of background originating from the primary vertex.

The possible higher separation leads to more freedom in adjusting the significance of the different sets or even to further increase the purity of the feed-down-enhanced D^0 sample. It could even be considered to attempt the analysis of a single feed-down D^0 cut set. However, the stringent cuts needed to achieve a high purity could lead to increased systematic uncertainties.

7.3. Systematic Uncertainties

The systematic uncertainties of the analysis on the upgrade data will be assessed using the same methods as described in Ch. 4.

The systematic uncertainty due to the signal extraction is expected to be less important, as the statistics of the data sample is expected to increase by a factor of about 100 and the improved vertex reconstruction will lead to an improvement of the signal-over-background ratio. The key to a reliable measurement most-likely will be the quality of the simulation of the tracking and vertex-reconstruction performance especially with regard to the decay length and the pointing angle. The use of the decay length instead of the normalised decay length facilitates this description. This is important to reduce the systematic uncertainties observed in the analysis of data acquired with the current detector from the cut variation and the normalisation of the decay length (cf. Ch. 4.7). This point is usually addressed by

studying and comparing data and MC simulations, which is not possible at this point. Furthermore, the exact performance of the detector is not yet known as the pixel chip as well as the detector mechanics are still under development. The expected larger statistics of the data sample, however, allows for more selective track cuts increasing the uniformity of the track sample which can significantly facilitate the MC description. A very uniform track sample can, e.g., be achieved by requiring hits in all seven ITS layers and a large number of TPC clusters leading to the maximum amount of hit points close to the vertex and a long lever arm. The reduced material budget will facilitate the description of the detector response in the MC simulations. Another important point will be the description of the B hadron decays in the MC generators. Expecting MC simulations with higher statistics also more detailed and differential studies concerning the decay-channel dependencies will be possible.

The D^0 p_T range below $1\,\mathrm{GeV}/c$ has been excluded from this study, as in this regime close to $y_{lab} \approx 0$, the D^0-vertex resolution is expected to be strongly D^0 p_T dependent (cf. Fig. 8.1 of [64]). Furthermore, as the mean flight distance of the D^0 is $\gamma\beta c\tau$, at vanishing momentum, there is no xy-displacement of the secondary vertex for prompt D^0 mesons. The performance of this method will significantly depend on actual vertex resolution and its description in the MC simulation.

7.4. Cross Sections

In this section, the expected performance for measuring the cross sections for prompt and feed-down D^0 mesons obtained using cut variations based on the ITS upgrade MC simulations is presented. For the construction of the invariant-mass distribution, the maximum and the central of the FONLL predictions are used for prompt D^0 mesons and feed-down D^0 mesons, respectively. Both the spectrum published in [94] and the spectrum obtained with the cut variation analysis presented in Ch. 4 suggest that the prompt D^0 meson spectrum is closer to the maximum value justifying this choice. In absence of a measurement for the feed-down D^0 meson spectrum, the central prediction value is used. This choice is supported by the agreement of the B-meson measurements of the CMS collaboration and the FONLL prediction [65, 152, 153].

7.4.1. Prompt D^0 Production

The expected measurement of the cross section for prompt D^0 mesons is shown in Fig. 7.4 (left). The data points obtained using the method developed within this thesis based on the MC simulations for the upgraded ITS are shown in black along with the corresponding statistical uncertainty. The published p–Pb result [94] is
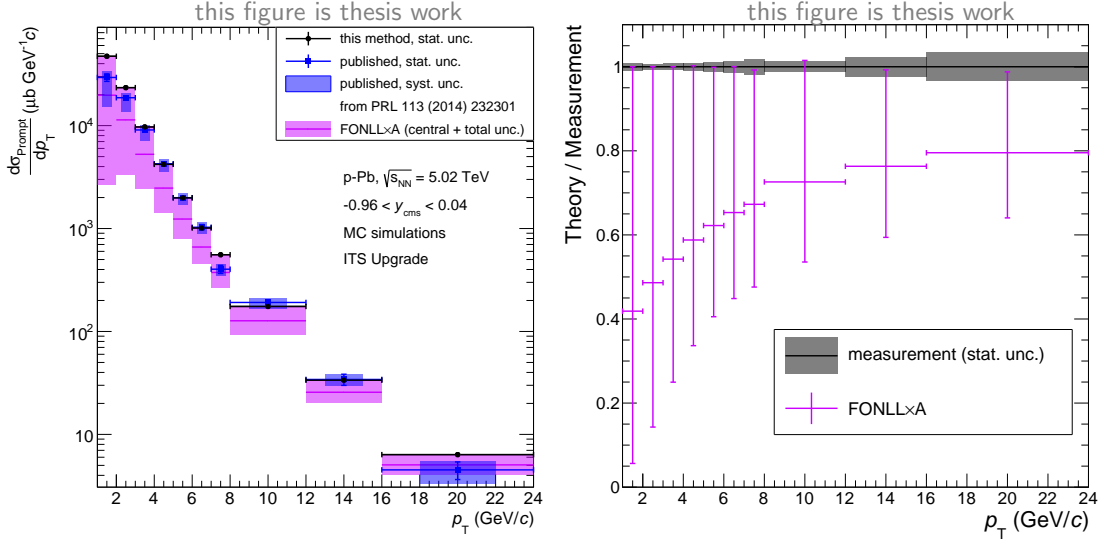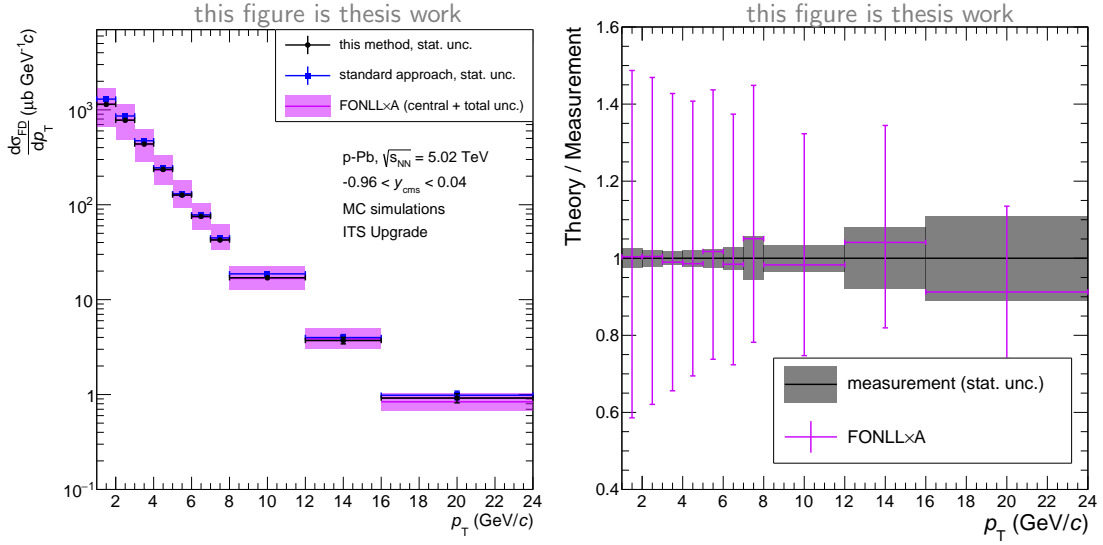
Figure 7.4.: Left: production cross section for prompt D^0 mesons in p–Pb collisions measured in MC simulations for the ITS upgrade using cut variations (black), result published in [94] (blue) and the FONLL prediction (purple). Right: FONLL prediction (purple) over measurement using cut variations (black).

shown in blue. The corresponding statistical uncertainty and the systematic uncertainty are depicted using error bars and light blue boxes, respectively. Furthermore, the FONLL prediction [65, 66] scaled using a Glauber model is shown in purple. The statistical uncertainties of the method developed within this thesis range from about 1 % to 3 % in the last p_T bin (cf. Fig. 7.4, right). The algorithm reproduces the input cross section, the maximum value of the FONLL band.

7.4.2. Feed-Down D^0 Production

The expected measurement of the cross section for feed-down D^0 mesons is shown in Fig. 7.5 (left). The data points obtained using the method developed within this thesis based on the simulation for the upgraded ITS are shown in black. The corresponding statistical uncertainty is depicted using error bars. The blue data points are derived by correcting the feed-down-enhanced cut set for $(\mathrm{Acc} \times \epsilon)$ without subtracting the residual contribution from prompt D^0 mesons. As a consequence, these data points are always above the correct feed-down D^0 production cross section. Due to the stronger enhancement of feed-down D^0 mesons in this cut set, the result deviates less from the fully corrected feed-down cross-section as in the analysis with the current detector (cf. Fig. 4.12). The obtained production cross section for feed-down D^0 mesons is in agreement with the input cross section which is the FONLL prediction [65, 66] scaled using a Glauber model shown in purple. As shown in Fig. 7.5 (right), the statistical uncertainty is smaller than 3 % below a p_T

Figure 7.5.: Left: cross section for feed-down D^0 mesons in p–Pb collisions measured in MC simulations for the ITS upgrade using cut variations (black), and without correction for the residual prompt contribution (blue) and the FONLL prediction (purple). Right: FONLL prediction (purple) over measurement using cut variations (black).

of $7\,\mathrm{GeV}/c$ using a bin width of $1\,\mathrm{GeV}/c$. The larger bin sizes allow to maintain a statistical uncertainty of $8\,\%$ and $11\,\%$ in the two last p_T bins.

7.5. Summary

Thanks to the performance gain expected from the upgraded ITS, the measurement of prompt and feed-down D^0 cross sections is possible in a p_T range from $1\,\mathrm{GeV}/c$ to $24\,\mathrm{GeV}/c$. The improved vertex resolution of the upgraded ITS leads to a feed-down (prompt) enhancement in the corresponding cut set of about a factor 10 (5) stronger than with the current detector at similar (Acc $\times \epsilon$) values. On the basis of 1×10^{11} inelastic p–Pb collisions, the statistical uncertainty is a few percent for prompt and feed-down D^0 mesons. With these statistical uncertainties and assuming comparable systematic uncertainties, not only a measurement of CNM effects will be possible, but also new physics observables like the measurement of correlations of feed-down D^0 mesons will be accessible.

A crucial effort has to be applied on the description of the tracking in the simulation of upgraded ALICE detector in order to reduce the systematic uncertainty. However, the larger data sample is expected to allow for more selective track cuts facilitating the description of the track resolution and in turn the secondary-vertex reconstruction performance in the simulations.

8. Conclusions and Outlook

Within this thesis, studies on the upgrade of the ALICE ITS and the measurement of D^0 mesons via secondary-vertex reconstruction were carried out. With the feed-down separation using cut variations, a new method based on multiple sets of cuts for the separation of prompt and feed-down D^0 mesons was implemented and applied to data from p–Pb collisions at $\sqrt{s_{NN}} = 5.02\,\mathrm{TeV}$. ALPIDE MAPS prototypes for the ITS upgrade were characterised in the laboratory and at the test beam. With simulations reproducing the expected performance of the upgraded ITS, the future potential of the feed-down-separation method using cut variations was studied.

Charm and beauty quarks are important probes for the study of the QGP and the underlying mechanisms of the energy loss in a strongly interacting medium. Charm quarks can be probed, e.g., using the D^0 meson in the decay channel $D^0 \to K^-\pi^+$. There is a significant contribution from B hadron feed-down to the measured yield of D^0 mesons currently subtracted using theory-based methods limited by their respective uncertainties. The feed-down separation using cut variations is an alternative approach splitting the D^0 candidate set in subsets. The cut sets generating the subsets exploit the different vertex topologies of feed-down and prompt D^0 mesons. The cut-set dependent prompt and feed-down D^0 efficiencies are obtained from MC simulations. Using three cut sets generating a prompt-enhanced, mixed and feed-down-enhanced D^0 candidate set, this method shows results comparable with those published in [94]. However, it is more demanding in terms of statistics leading to larger p_T bins and significant systematic uncertainties from the yield extraction. Furthermore, its sensitivity to the precision of the description of the secondary-vertex reconstruction in the MC simulation is higher, as it is based on stricter cuts on the vertex properties than the analysis method published in [94]. A reduction of the corresponding systematic uncertainties requires more detailed studies and improvements to the description of the secondary-vertex reconstruction. Below a D^0 p_T of $2\,\mathrm{GeV}/c$, the smaller displacement leading to a lower D^0 vertex resolution and a smaller efficiency does not allow to define more than two cut sets resulting in an increased systematic uncertainty on the measured cross sections. In contrast to the other methods, this method allows to extract a feed-down D^0 spectrum in addition to the prompt D^0 spectrum. The feed-down D^0 spectrum is within uncertainties in agreement with FONLL calculations scaled using a Glauber model.

The upgraded ITS will be installed during the LS2 in 2019 and 2020. The MAPS pixel chips will be manufactured using the TowerJazz 180 nm CMOS Imaging Sensor process. The characterisation of the small-scale pALPIDEss prototypes carried out within this thesis allowed to validate the front-end circuit and the architecture using in-pixel amplification, shaping and discrimination as well as in-matrix data reduction. The characterised pALPIDE-2 prototypes meet or even pass the requirements of the ITS upgrade in terms of detection efficiency (99 %), fake-hit rate

($\ll 10^{-5}$/pixel/event) and position resolution ($5\,\mu\text{m}$) and have a sufficient operational margin. A NIEL radiation tolerance up to $1.7 \times 10^{13}\,1\,\text{MeV}\,\text{n}_{\text{eq}}/\text{cm}^2$ has been established. Additionally, the beneficial influence of reverse substrate bias and an increased spacing between the collection n-well and the surrounding deep p-well on the detection efficiency was confirmed. A thicker epitaxial layer was found to show an improvement in terms of detection efficiency when combined either with a large spacing or reverse substrate bias. The best performance is achieved in combination with both reverse-substrate bias and large spacing. Increasing the size of the input transistor in the in-pixel front-end leads to a significantly improved fake-hit rate to values below the measurement sensitivity at about 10^{-11}/pixel/event with no measurable penalty in terms of detection efficiency. The position resolution was found to be about the required $5\,\mu\text{m}$ and largely insensitive to the choice of front-end settings, spacing, epitaxial-layer thickness and reverse substrate bias as long as a minimum of charge sharing is maintained.

pALPIDE-2 does not feature the high-speed data link and the multiple in-pixel hit buffers. These features along with further optimisation of the front-end circuit for shorter pulse widths and of the peripheral circuitry reducing its power consumption are implemented in pALPIDE-3.

The upgraded ITS will provide significantly improved vertex reconstruction and tracking at low p_{T}. Furthermore, significantly larger minimum-bias data sets will be acquired. To assess the combined gain, an existing MC data sample has been analysed using the 'ITS improver' to mimic the tracking and vertex-reconstruction performance of the upgraded ITS. The improved vertex resolution allows to define cut sets with stronger enhancement of both prompt and feed-down D^0 mesons without reducing the signal efficiencies. The increase in statistics leads to a more robust signal extraction. The measurement of prompt and feed-down D^0 mesons in p–Pb collisions is expected to lead to statistical uncertainties of a few percent. To achieve similar systematic uncertainties the quality of the description of the secondary-vertex reconstruction needs to be addressed.

In order to study CNM effects and the QGP, the method needs to be extended to data from pp and Pb–Pb collisions. In comparison to data from p–Pb collisions, the smaller multiplicity in pp collisions leads to a reduction of the primary-vertex resolution while the higher multiplicity in Pb–Pb collisions leads to an increase in combinatorial background.

In conclusion, the feed-down separation using cut variations is a promising complementary method to the approaches based on FONLL calculations and the impact-parameter fit allowing the measurement of both prompt and feed-down D^0 mesons. It will profit from the improved tracking and vertex-reconstruction performance of the upgraded ITS. The pALPIDE-2 MAPS prototypes fulfil the requirements concerning detection efficiency, fake-hit rate, position resolution and NIEL irradiation tolerance providing sufficient operational margin.

An idea to further reduce the material budget and facilitate its description in the MC simulations is to build a 'silicon-only' Inner Barrel (IB). The goal would be

to eliminate the electric substrate and move all power distribution and routing to the chips themselves. A layer would then be built from only four large chips each. These chips would be thinned down to $50\,\mu m$ or lower, allowing them to be bend to half-cylinders. Such large chips could be made using so-called stitching. The half-cylinder chips would be mounted on the beam pipe and on top of each other using open-cell carbon-foam rings which act as mechanical support and heat spreader. The detector would be cooled by an air flow through the carbon-foam rings which would be the only material in addition to the beam pipe and the pixel chips themselves inside the active volume. This idea is a potential continuation of the pixel chip R&D coming to an end with the submission of the final chip, which is envisaged for the first quarter of 2016.

A. Additional Analysis Figures and Information

This chapter contains complementary figures to the D^0 analysis method presented in Ch. 4.

A.1. p-Pb Data Sample Details

The data consists two periods, `LHC13b` and `LHC13c` in reconstruction passes three and two, respectively. The software used for the reconstruction is `ROOT` [106] `v5-34-05` and `AliRoot`[1] `v5-03-Rev-20` [154, 155]. The Analysis Object Data (AOD) is `AOD154` produced using `ROOT v5-34-08` and `AliRoot v5-04-Rev-17`. The run list used for the analysis is the following:

LHC13b: 195483, 195482, 195481, 195480, 195479, 195478, 195391, 195390, 195389, 195351, 195346, 195344

LHC13c: 195677, 195675, 195673, 195644, 195635, 195633, 195596, 195593, 195592, 195568, 195567, 195566, 195531, 195529

A.2. Variables for Cut Set Definition

The distributions of the normalised decay length L_{xy} (left) and $\cos(\theta_{\text{Pointing,xy}})$ (right) of the different p_T bins are shown in Fig. A.1 and Fig. A.2. The normalisation leads to almost p_T-independent L_{xy} distributions, while the $\cos(\theta_{\text{Pointing,xy}})$ gains discrimination power with p_T.
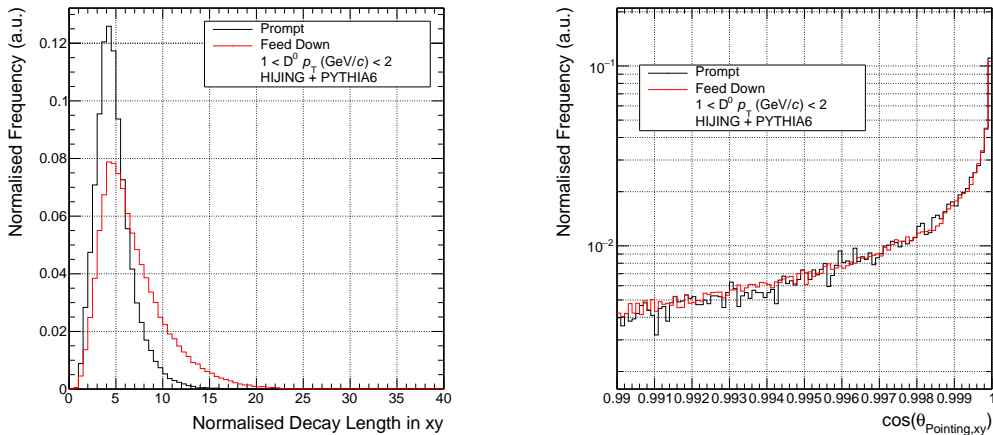
Figure A.1.: Normalised decay length L_{xy} (left) and $\cos(\theta_{\text{Pointing,xy}})$ (right) of the p_T bin $1\,\text{GeV}/c$ to $2\,\text{GeV}/c$.

---

[1] AliRoot and AliPhysics are the ALICE software for simulation, reconstruction and data analysis, which are hosted in Git repositories at `http://git.cern.ch`.
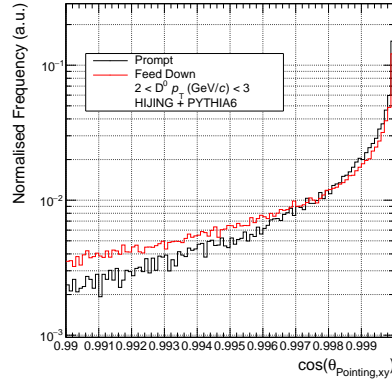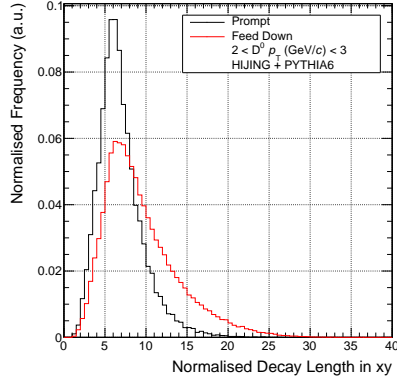
(a) $2\,\mathrm{GeV}/c$ to $3\,\mathrm{GeV}/c$.
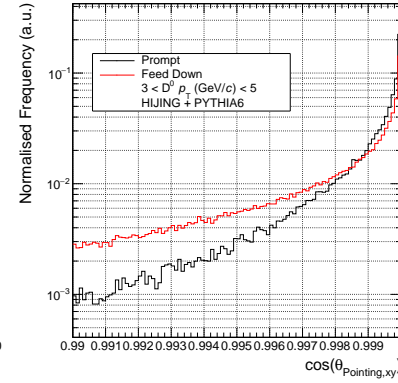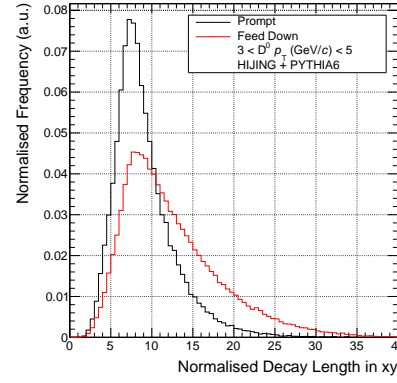
(b) $3\,\mathrm{GeV}/c$ to $5\,\mathrm{GeV}/c$.
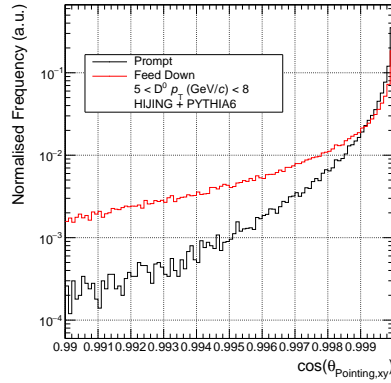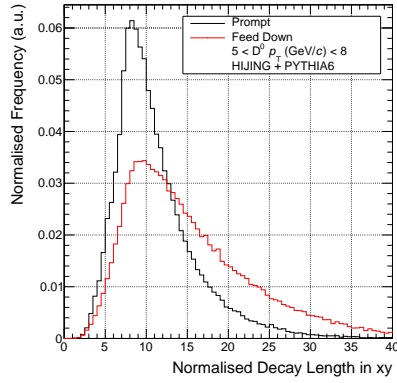
(c) $5\,\mathrm{GeV}/c$ to $8\,\mathrm{GeV}/c$.
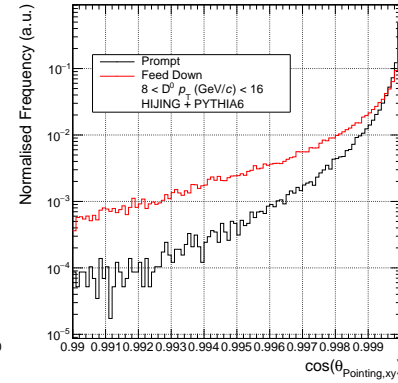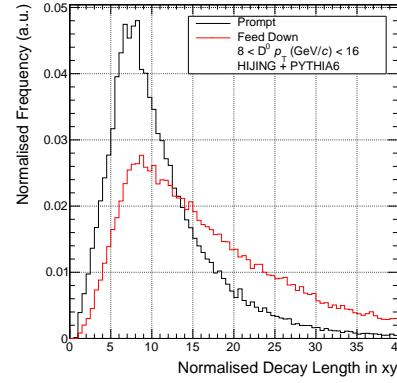
(d) $8\,\mathrm{GeV}/c$ to $16\,\mathrm{GeV}/c$.

Figure A.2.: Normalised decay length L_{xy} (left) and $\cos(\theta_{\mathrm{Pointing,xy}})$ (right) for different p_{T} bins.

A.3. Stability of the Method

The stability of the method was assessed by testing the influence of statistical fluctuations in the measured raw yield and of potential biases on individual efficiencies. Together with the study of the influence of statistical fluctuations, the uncertainty propagation in the minimisation was tested.

A.3.1. Statistical Uncertainty Propagation

The propagation of the statistical uncertainty and the sensitivity to statistical fluctuations in the raw yields was assessed based on a realistic scenario derived from p–Pb data. Using the corrected yields $\boldsymbol{N}$ and the acceptance-times-efficiency matrix $\boldsymbol{\xi}$ obtained in the analysis of p–Pb data and the corresponding MC simulation, the raw yields $\boldsymbol{Y}$ are calculated.

In repeated trials, the calculated raw yields are smeared using a Poisson distribution and are used as input for the minimisation. For each trial, the corrected yield $N^{obtained}$ and the corresponding statistical uncertainty σ_N, the residuals δ defined as

$$\delta = N^{\text{expected}} - N^{\text{obtained}} \tag{A.1}$$

with the corrected yield extracted without smearing $N^{expected}$, and the pulls ν defined as

$$\nu = \frac{\delta}{\sigma_N} = \frac{N^{\text{expected}} - N^{\text{obtained}}}{\sigma_N} \tag{A.2}$$

were obtained separately for prompt and feed-down production. In Fig. A.3, the corresponding distributions for 10000 trials are shown. The width of the Gaussian fit function and the RMS of the corrected yields correspond well to the mean of the corresponding statistical uncertainties. Also the residual distributions show widths corresponding to the expected statistical uncertainty and are centred close to zero compared to their width. The pull distributions show a mean close to zero and a width of 1. The statistical uncertainty propagation by the minimisation is working as expected.
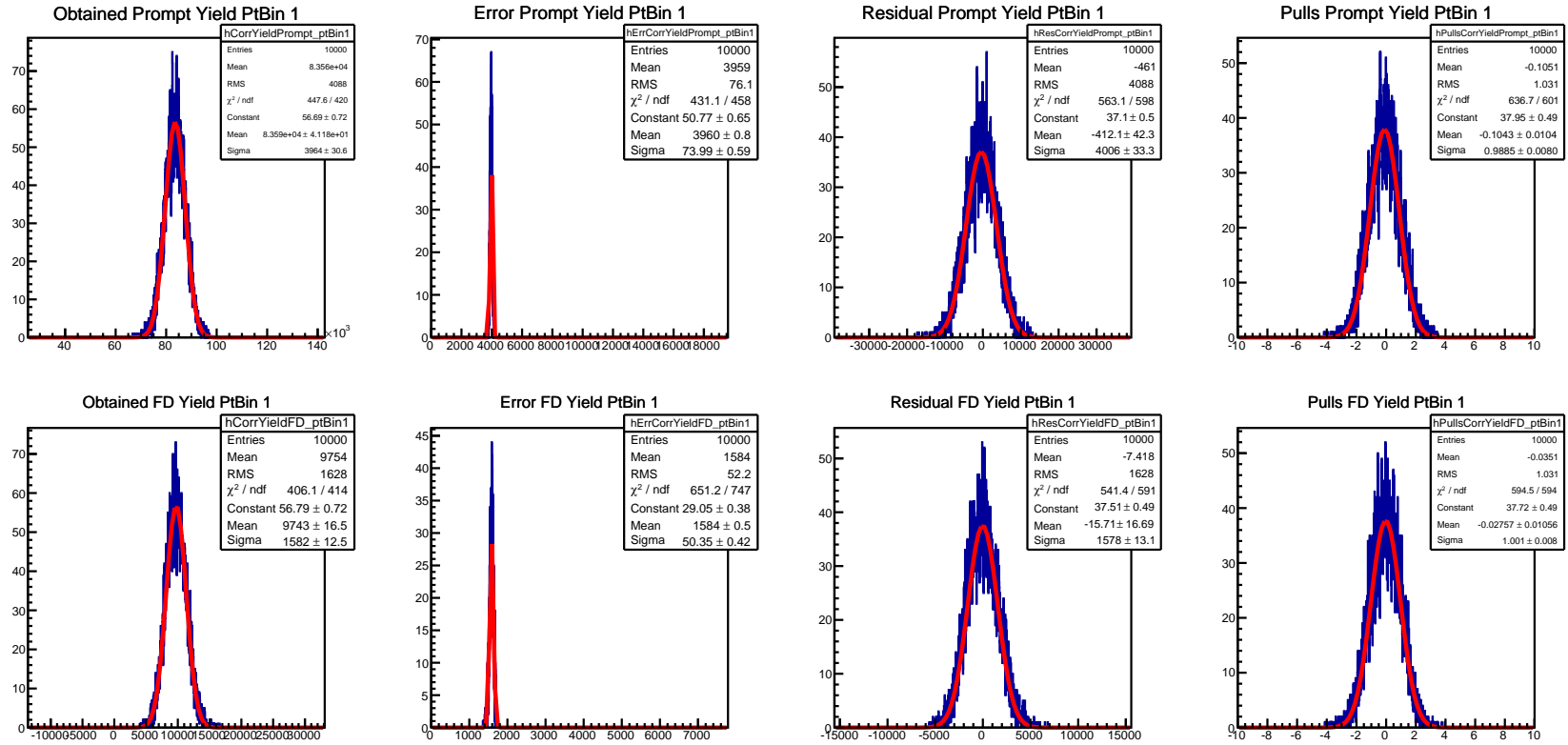
Figure A.3.: Testing the uncertainty propagation of the minimisation: Obtained corrected yield (left), statistical uncertainty (mid left), residual of the corrected yield (mid right), pulls (right) for prompt (top) and feed-down D^0 (bottom) for the p_T range from $2\,\mathrm{GeV}/c$ to $5\,\mathrm{GeV}/c$.

A.3.2. Sensitivity to Biases on Acceptance times Efficiency

An important question is how the minimisation reacts to a bias on one of the six $(\text{Acc} \times \epsilon)$ values. This was studied by artificially biasing individual $(\text{Acc} \times \epsilon)$ values and repeating the minimisation. For comparison of the results, the normalised residual of the corrected yield $\widetilde{\delta}$ is used. It is defined as

$$\widetilde{\delta} = \frac{N^{\text{biased}} - N^{\text{unbiased}}}{N^{\text{unbiased}}} \tag{A.3}$$

with the corrected yields N^{biased} and N^{unbiased} obtained separately for prompt and feed-down D^0 mesons with and without biasing an individual $(\text{Acc} \times \epsilon)$, respectively. The individual $(\text{Acc} \times \epsilon)$ were biased up to a relative bias of $\pm 50\,\%$.

The effect of such biases are presented using the p_T range from $2\,\text{GeV}/c$ to $5\,\text{GeV}/c$ as an example. The largest effect of the biases were found in the prompt and feed-down-enhanced D^0 sets shown in Fig. A.4 and in Fig. A.5, respectively.
In Fig. A.4a, the effect on the corrected yield for prompt D^0, N_{Prompt} (top), and feed-down D^0, N_{FD} (bottom), of a biases on the $(\text{Acc} \times \epsilon)_{\text{Prompt}}$ in the prompt-maximised cut set is shown. An underestimation of $(\text{Acc} \times \epsilon)_{\text{Prompt}}$ leads to an overestimation of N_{Prompt} and an underestimation of N_{FD}. However, the effect on N_{FD} is amplified by a factor of about 10 compared to that on N_{Prompt}.
A bias on $(\text{Acc} \times \epsilon)_{\text{FD}}$ in the prompt-maximised cut set leads to an about a factor of 10 smaller effect on the corrected yields than a bias on $(\text{Acc} \times \epsilon)_{\text{Prompt}}$ (cf. Fig. A.4b). This is expected from the small relative feed-down contribution to the D^0 sample selected by this cut set.
In the feed-down-maximised cut set, the influence of the $(\text{Acc} \times \epsilon)_{\text{FD}}$ (cf. Fig. A.5b) is found to be significantly stronger than that of $(\text{Acc} \times \epsilon)_{\text{Prompt}}$ (cf. Fig. A.5a). Furthermore, the influence on N_{FD} is larger than on N_{Prompt}.

The χ^2 minimisation is not found to artificially amplify the biases of the efficiencies in the corrected yields as long as they do not exceed $50\,\%$. The most crucial $(\text{Acc} \times \epsilon)$ values are $(\text{Acc} \times \epsilon)_{\text{Prompt}}$ in the prompt-enhanced cut set and $(\text{Acc} \times \epsilon)_{\text{FD}}$ in the feed-down-enhanced cut set. Biases on the other $(\text{Acc} \times \epsilon)$ are even suppressed by the minimisation.
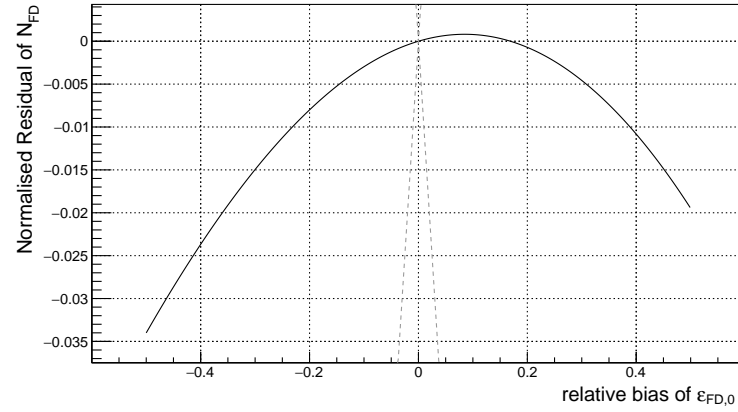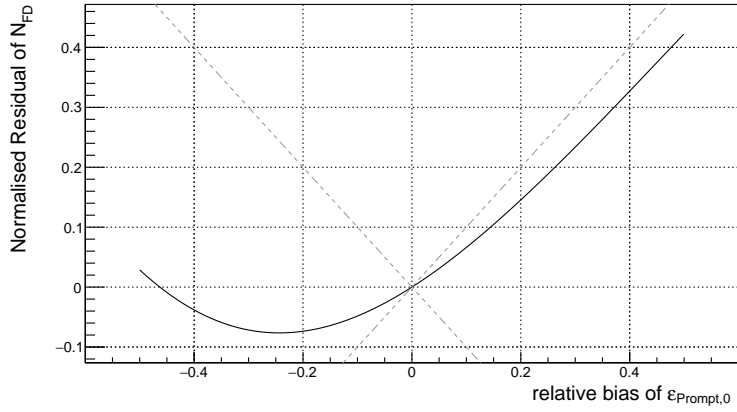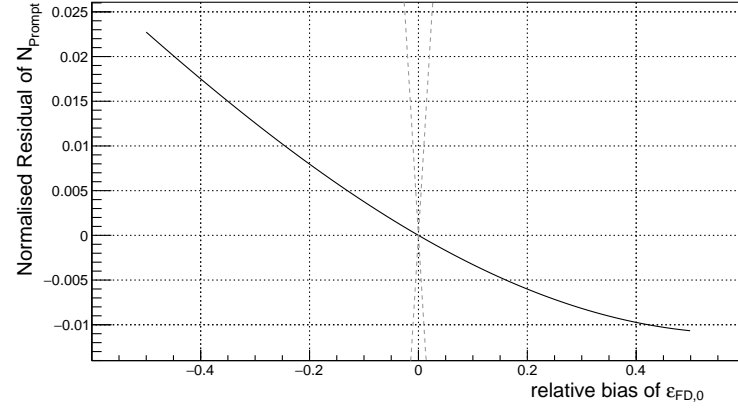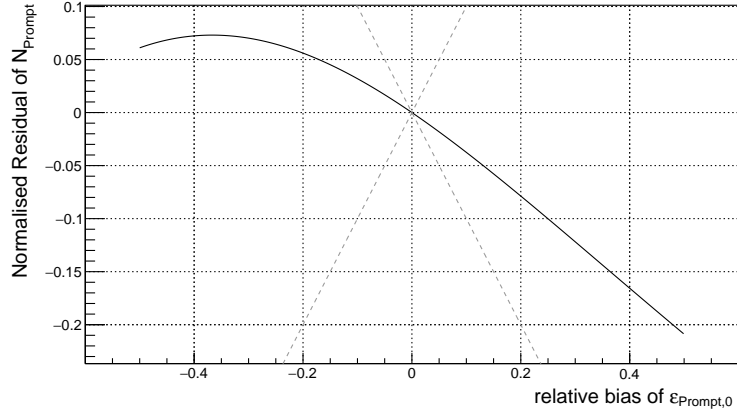
(a) $(\text{Acc} \times \epsilon)_{\text{Prompt}}$.

(b) $(\text{Acc} \times \epsilon)_{\text{FD}}$.

Figure A.4.: Influence of a $(\text{Acc} \times \epsilon)$ bias in the prompt-maximised cut set on the corrected yield in the p_{T} range from $2\,\text{GeV}/c$ to $5\,\text{GeV}/c$.
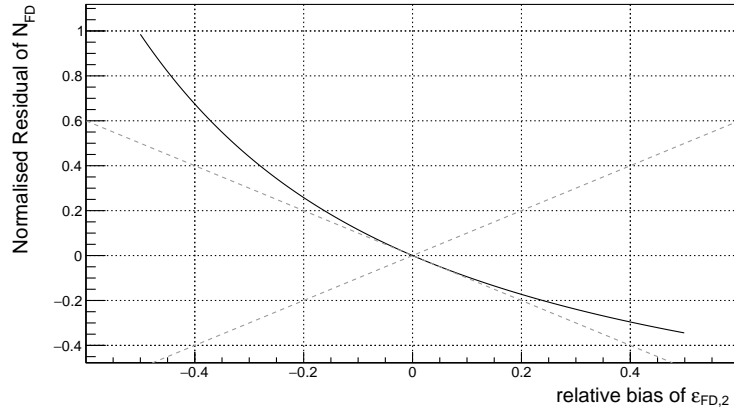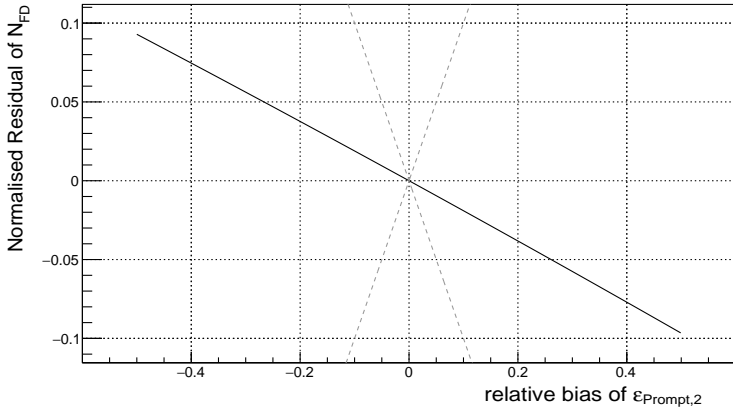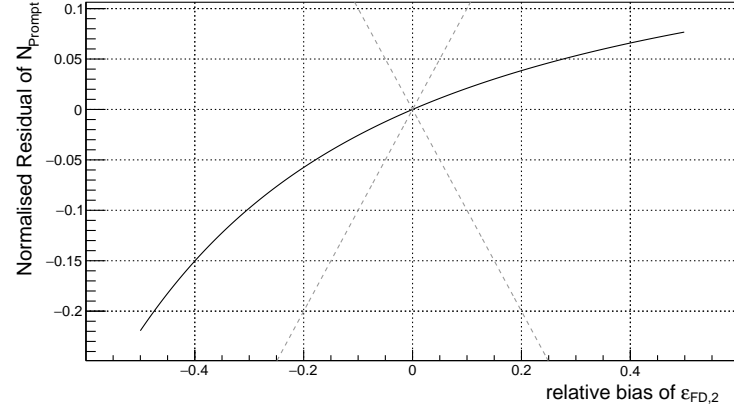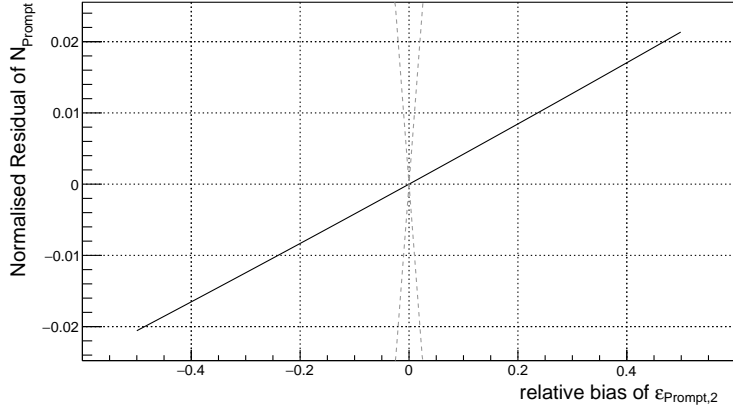
(a) $(\mathrm{Acc} \times \epsilon)_{\mathrm{Prompt}}$.

(b) $(\mathrm{Acc} \times \epsilon)_{\mathrm{FD}}$.

Figure A.5.: Influence of a $(\mathrm{Acc} \times \epsilon)$ bias in the feed-down-maximised cut set on the corrected yield in the p_{T} range from $2\,\mathrm{GeV}/c$ to $5\,\mathrm{GeV}/c$.

A.4. Systematic Uncertainties

A.4.1. Yield Extraction

Figure A.6 and Fig. A.7 are examples of the results obtained during the yield-extraction study. The width of the signal σ (top left), the raw yield (top right), the χ^2/n.d.f. (bottom left) and the distribution of the raw yield (bottom right) are shown. The plot containing the distribution of the raw yield furthermore contains the average and the variance of the distribution. In addition to that the minimum and maximum raw yield and the resulting variance assuming a uniform distribution.
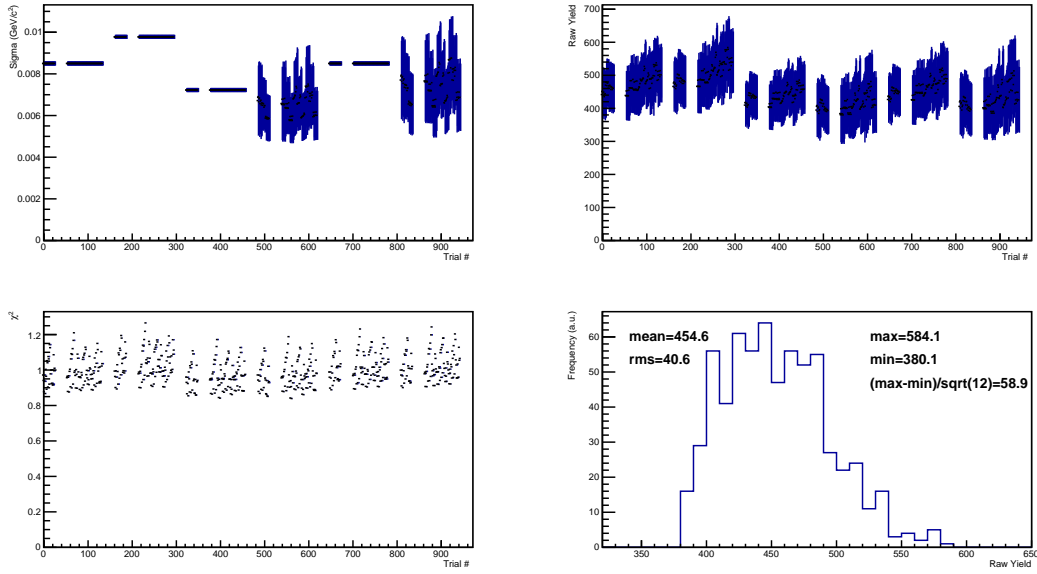
Figure A.6.: Yield-extraction variation results for the prompt-maximised cut set of the p_{T} bin $1\,\mathrm{GeV}/c$ to $2\,\mathrm{GeV}/c$.

A.4.2. Efficiency Determination

In Fig. A.8, the distribution of B decay particles in addition to the D^0 meson in the MC data sample and for the three additional decayers is shown. The MC data sample shows the most obvious difference compared to the three other decayers. This is explainedby the signal enhancement scheme described in Ch. 4.

The dependence of the $(\mathrm{Acc}\times\epsilon)$ for feed-down D^0 on the number of decay particles for the cut set with maximised prompt D^0 contribution, mixed contribution and maximised feed-down contribution is shown in Fig. A.9 to Fig. A.11.
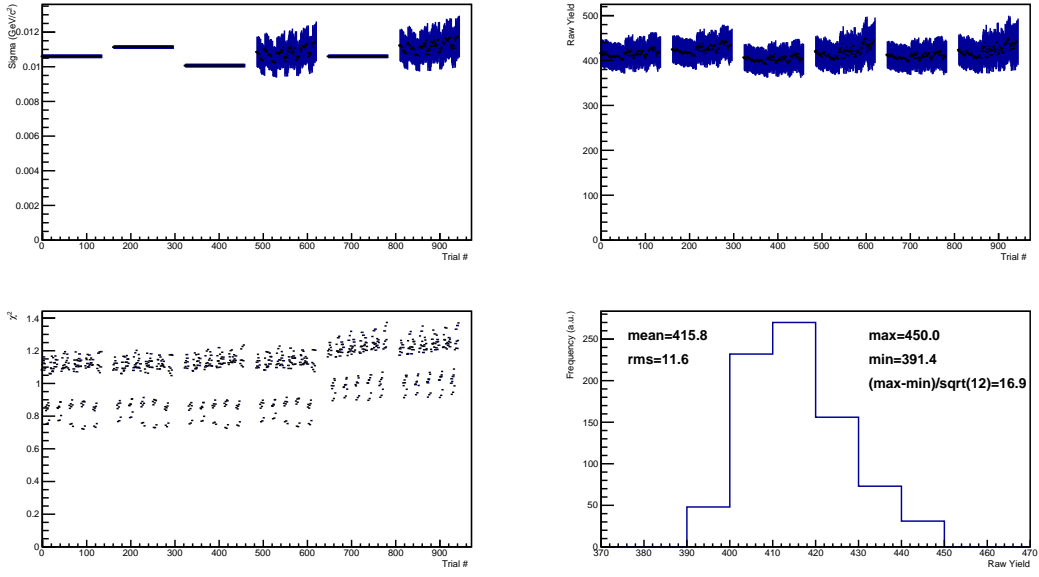
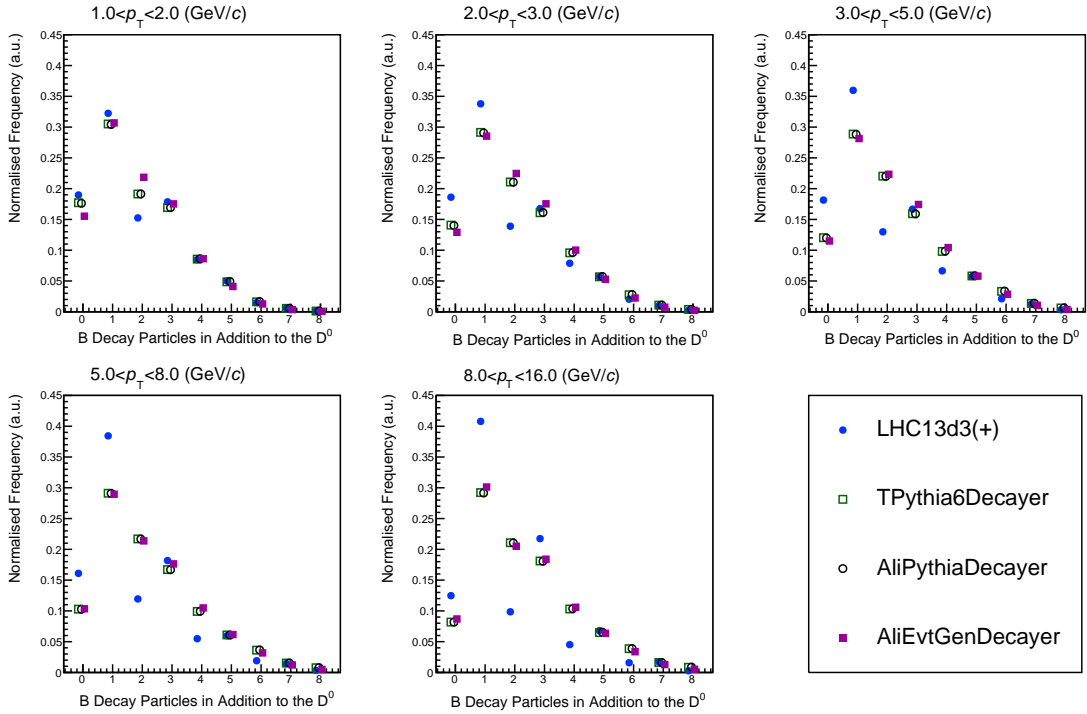**Figure A.7.:** Yield-extraction variation results for the prompt-maximised cut set of the p_T bin $3\,\mathrm{GeV}/c$ to $5\,\mathrm{GeV}/c$.

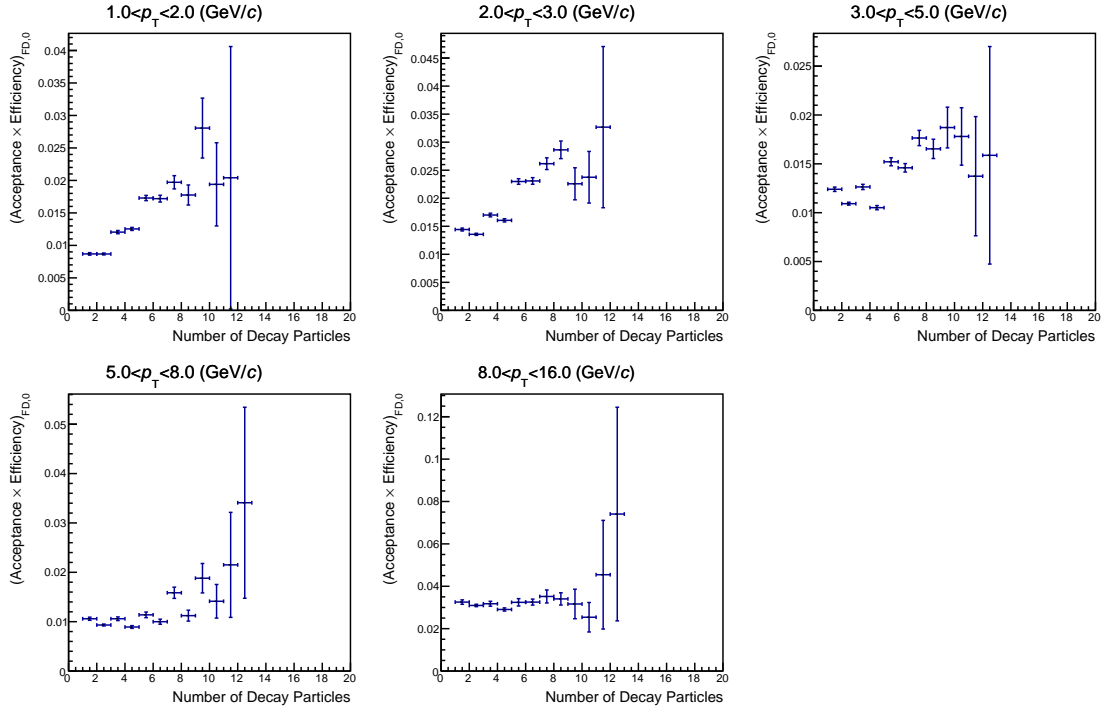**Figure A.8.:** Number of B hadron decay particles in addition to the D^0

Figure A.9.: Decay-particle number dependence of the $(\mathrm{Acc} \times \epsilon)$ for feed-down D^0 of the cut set with maximised prompt D^0 contribution.
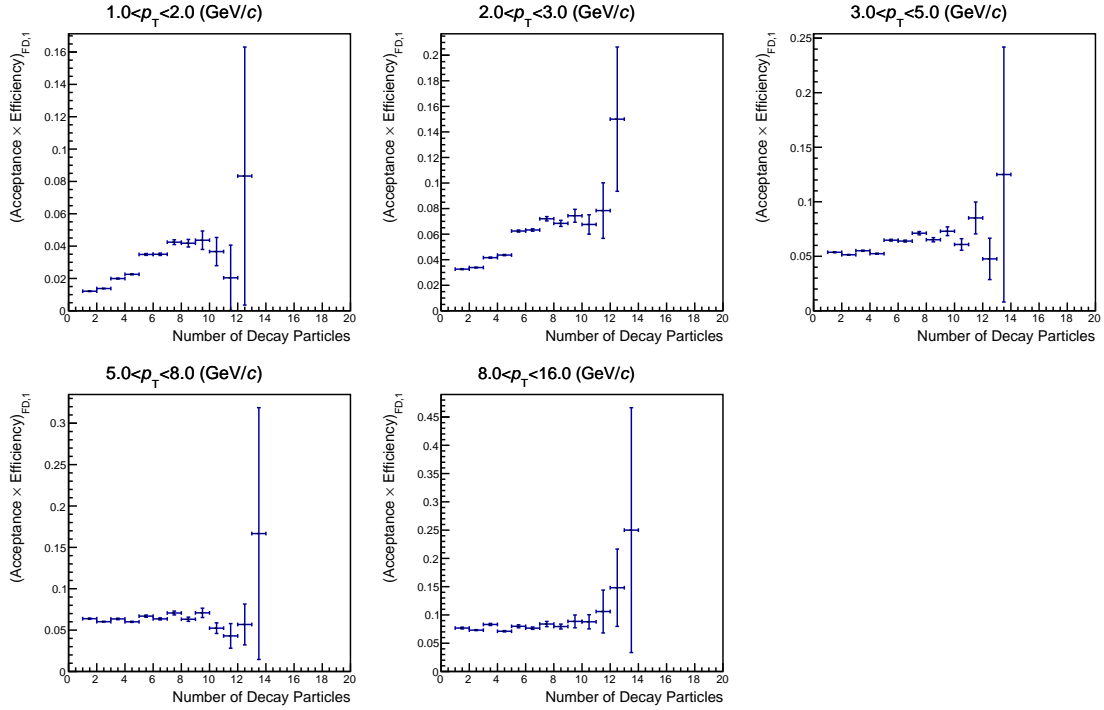

Figure A.10.: Decay-particle number dependence of the $(\mathrm{Acc} \times \epsilon)$ for feed-down D^0 of the cut set with mixed D^0 contribution.
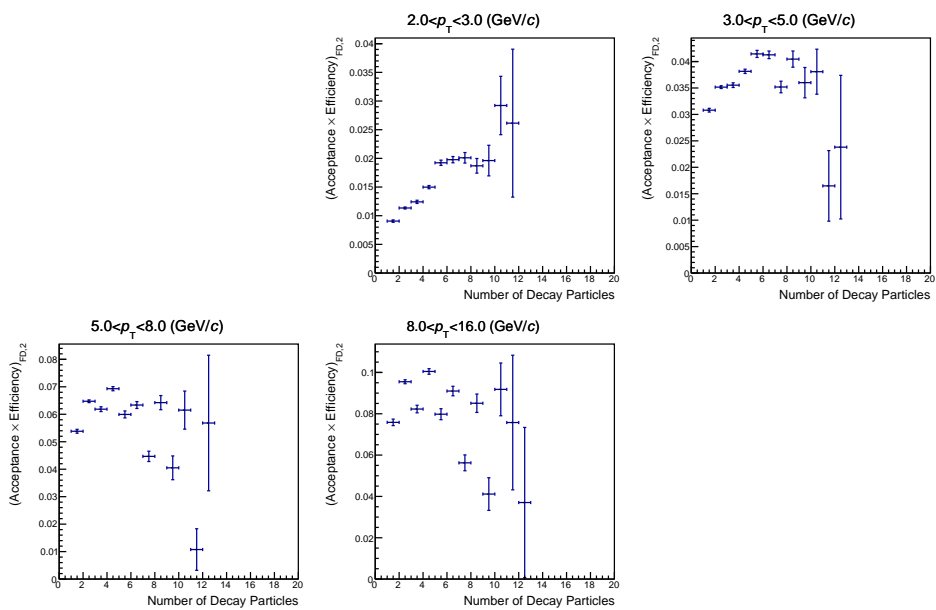
Figure A.11.: Decay-particle number dependence of the $(\mathrm{Acc} \times \epsilon)$ for feed-down D^0 of the cut set with maximised feed-down D^0 contribution.

A.5. Minimisation

The residual vector $\boldsymbol{\delta}$ is shown with different colours for the different components in Fig. A.12 (left). Set 0, 1 and 2, correspond to the prompt-enhanced, mixed and feed-down-enhanced cut set, respectively. In the first p_{T} bin, the residuals are zero, as there are only two cut sets and thus an exact solution. Within their statistical uncertainties, which are the statistical uncertainties of the corresponding raw yields, the residuals are compatible with zero except for the prompt-enhanced cut set in the last p_{T} bin. The residuals normalised by the corresponding raw yields are shown in Fig. A.12 (right).
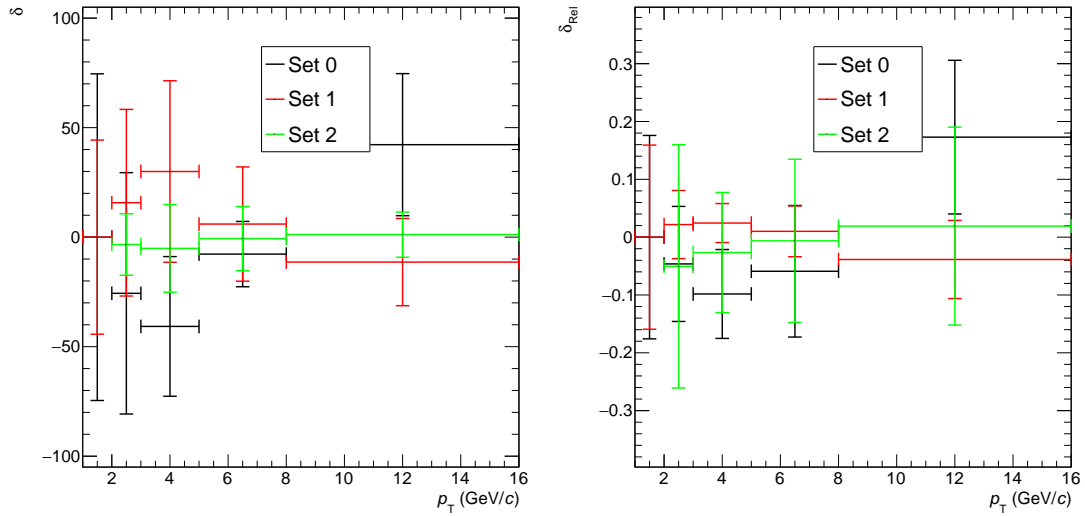

Figure A.12.: Absolute residuals (left) and residuals normalised by the corresponding raw yields (right) obtained using the minimisation algorithm.

A.6. Summary Table

The signal and background values and the corresponding production cross sections for prompt and feed-down D^0 mesons are summarised in Tab. A.1.

Table A.1.: Signal S, background B, S/B and significance as well as the cross section for prompt and feed-down D^0 production along with the corresponding statistical uncertainties.

D^0 p_T (GeV/c)	Cut Set	S (3σ)	B (3σ)	S/B (3σ)	Significance (3σ)	$\frac{d\sigma_{Prompt}}{dp_T}$ ($\frac{\mu b}{GeV/c}$)	$\frac{d\sigma_{FD}}{dp_T}$ ($\frac{\mu b}{GeV/c}$)
1 to 2	Max. Prompt	424 ± 75	5362 ± 28	0.079 ± 0.014	5.57 ± 0.94	$(29.7 \pm 8.9) \times 10^3$	$(2.9 \pm 1.8) \times 10^3$
	Mixed	278 ± 44	1111 ± 15	0.251 ± 0.040	7.47 ± 1.07		
2 to 3	Max. Prompt	584 ± 55	2520 ± 22	0.220 ± 0.022	10.00 ± 0.90	$(15.7 \pm 1.6) \times 10^3$	$(1.61 \pm 0.38) \times 10^3$
	Mixed	723 ± 43	1042 ± 14	0.694 ± 0.042	17.21 ± 0.81		
	Max. FD	67 ± 14	199.8 ± 6.4	0.333 ± 0.071	4.08 ± 0.75		
3 to 5	Max. Prompt	415 ± 32	590 ± 12	0.704 ± 0.056	13.09 ± 0.72	$(5.55 \pm 0.28) \times 10^3$	613 ± 83
	Mixed	1229 ± 41	681 ± 14	1.802 ± 0.070	28.11 ± 0.65		
	Max. FD	193 ± 20	299.3 ± 8.8	0.644 ± 0.070	8.69 ± 0.73		
5 to 8	Max. Prompt	131 ± 15	109.9 ± 5.8	1.19 ± 0.15	8.44 ± 0.71	1012 ± 59	95 ± 20
	Mixed	595 ± 26	232.7 ± 9.0	2.56 ± 0.15	20.67 ± 0.59		
	Max. FD	104 ± 15	162.3 ± 7.3	0.640 ± 0.095	6.37 ± 0.73		
8 to 16	Max. Prompt	244 ± 32	523 ± 17	0.467 ± 0.064	8.82 ± 0.99	109.2 ± 8.7	11.1 ± 3.4
	Mixed	295 ± 20	151.9 ± 7.8	1.94 ± 0.17	13.95 ± 0.64		
	Max. FD	60 ± 10	66.9 ± 4.8	0.90 ± 0.17	5.34 ± 0.70		

A.7. Upgrade Study

In the following, additional figures for the upgrade study in Ch. 7 can be found. The invariant-mass distributions for all p_T bins in the prompt-enhanced, mixed and feed-down-enhanced cut set are shown in Fig. A.13, Fig. A.14 and Fig. A.15, respectively.
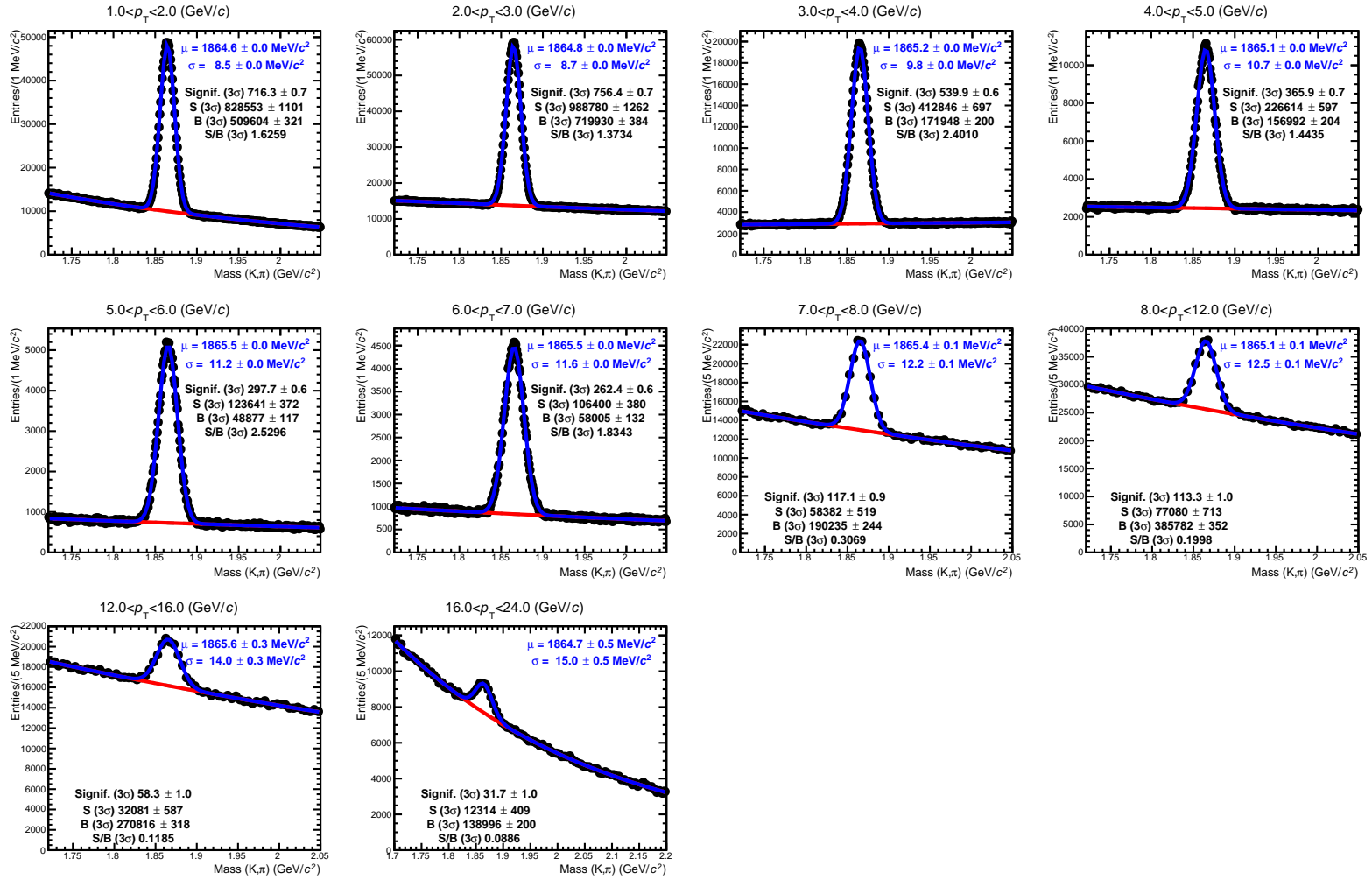
Figure A.13.: Invariant-mass distribution of D^0 candidates for the prompt-enhanced cut set.
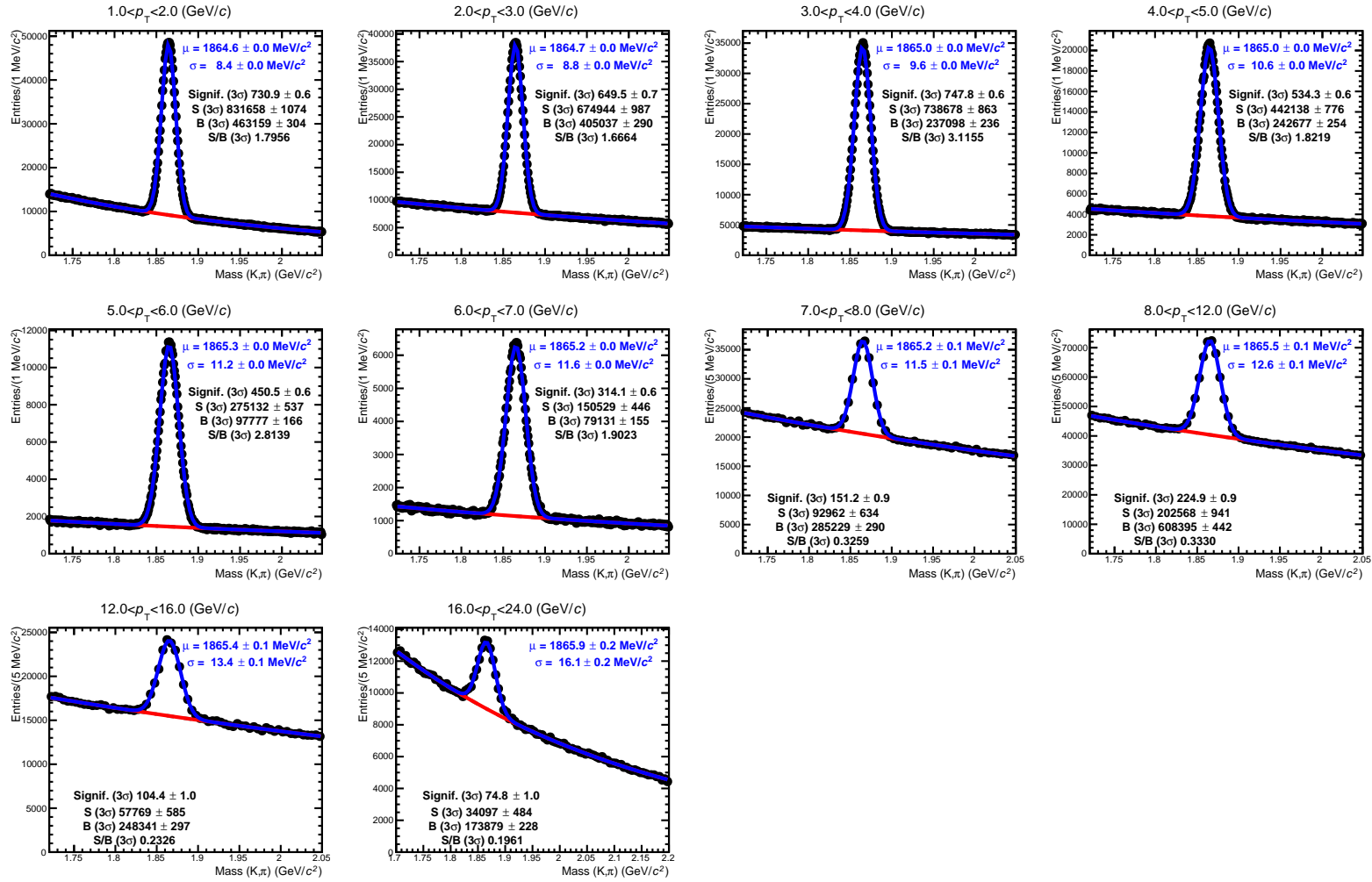
Figure A.14.: Invariant-mass distribution of D^0 candidates for the mixed cut set.
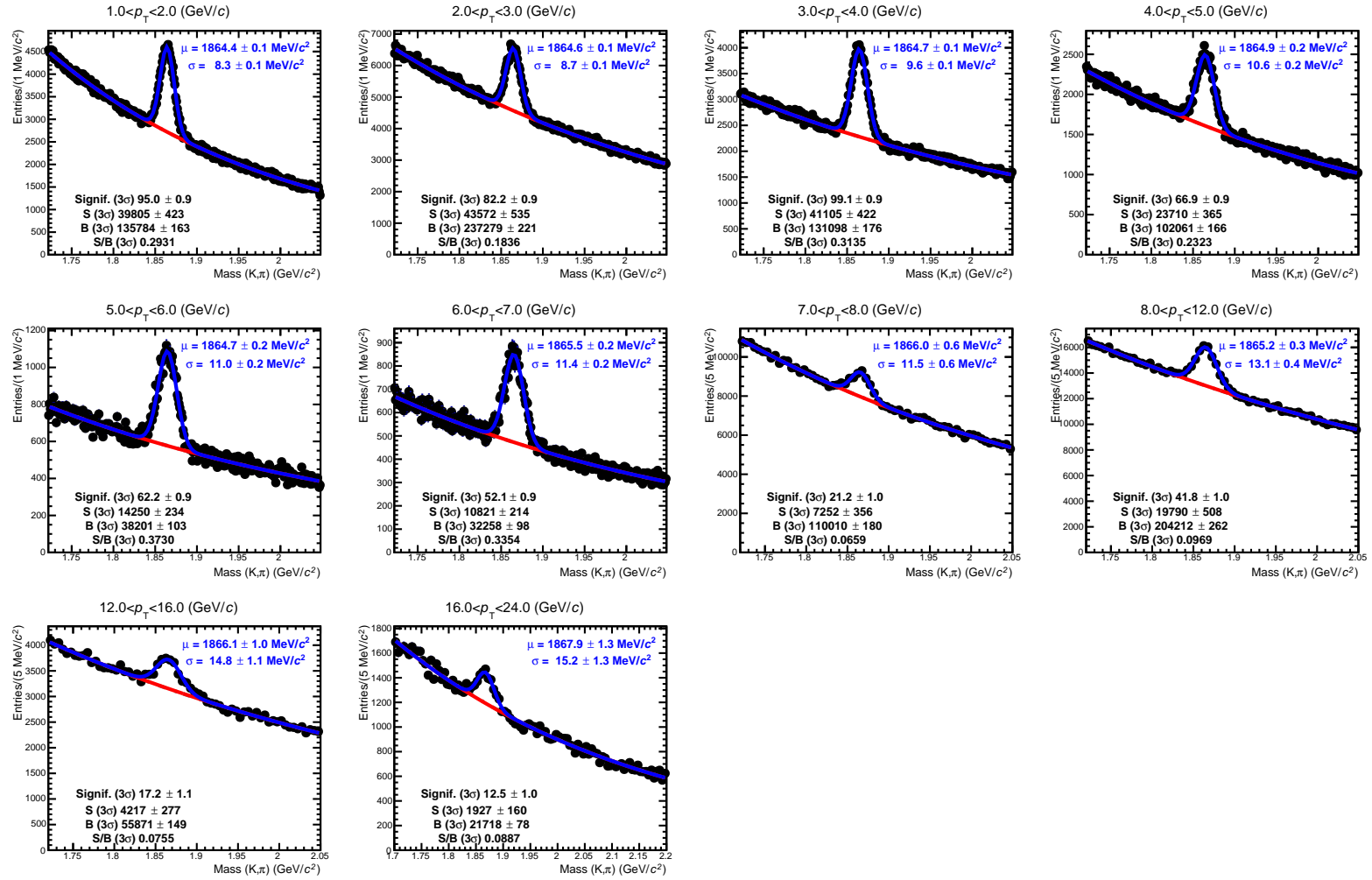
Figure A.15.: Invariant-mass distribution of D^0 candidates for the feed-down-enhanced cut set.

B. Additional Characterisation Information and Figures

B.1. Light Sensitivity of the pALPIDEss-0

As described in Ch. 6.2, pALPIDEss-0 is light sensitive. This behaviour also manifests in the measurement of detection efficiency as shown in Fig. B.1. For pALPIDEss-0, light leads to a significant improvement, while for pALPIDEss-1a the detection efficiency does not change significantly. The error bars are based on the chip-to-chip spread, missing error bars are due to measurement of a single chip only.
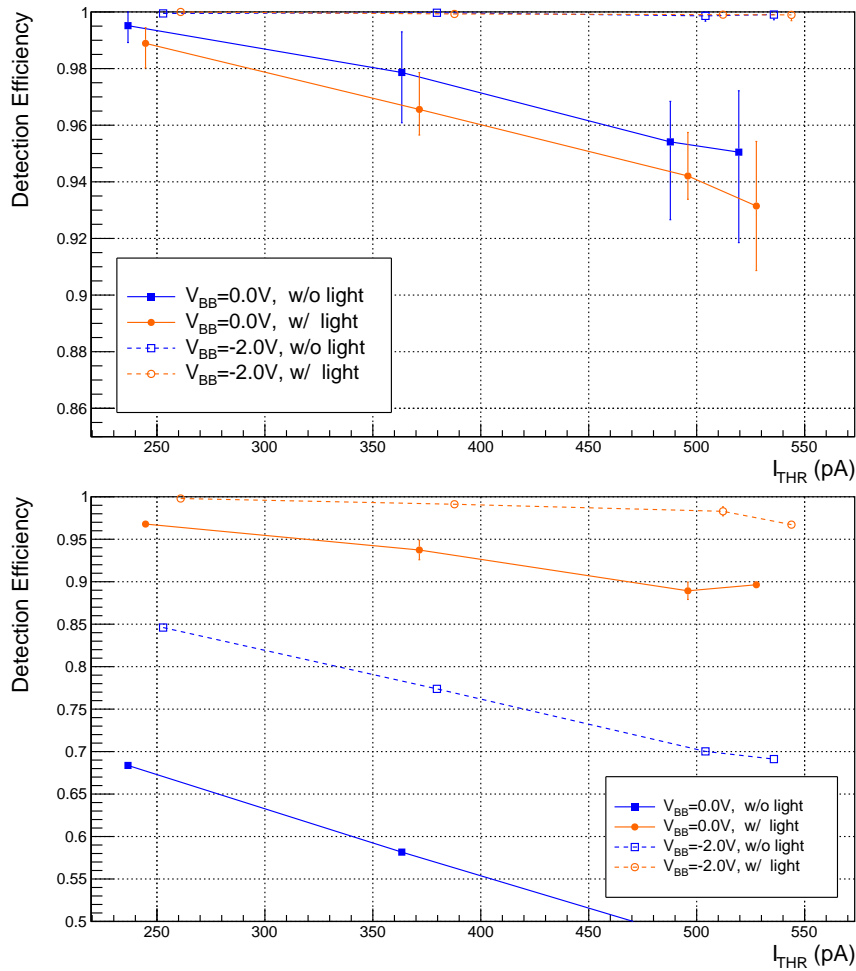

Figure B.1.: Detection efficiency of pALPIDEss-1a (top) and pALPIDEss-0 (bottom) with and without light as a function of threshold current I_{THR}. Error bars indicate the chip-to-chip variations.

B.2. Fake-Hit Rate Model Comparison

The measured fake-hit rate of the pALPIDEss and the expected values estimated using threshold and TN from the S-Curve scan are shown in Fig. B.2. The grey dashed line indicates the measurement sensitivity limit of the fake-hit rate measurement. The red dashed line is a minimum value chosen for plotting. The actual expected values are lower for some settings. Without reverse substrate bias, the measured and expected fake-hit rate deviate by about nine orders of magnitude. At fixed I_{THR}, smaller threshold-to-noise ratios (μ/σ) are accessible with reverse substrate bias (cf. Fig. 6.10). The smaller μ/σ ratios lead to an increase of the estimated fake-hit rate and for high V_{CASN} and at very high fake-hit rates, the expected and measured values are even in agreement.
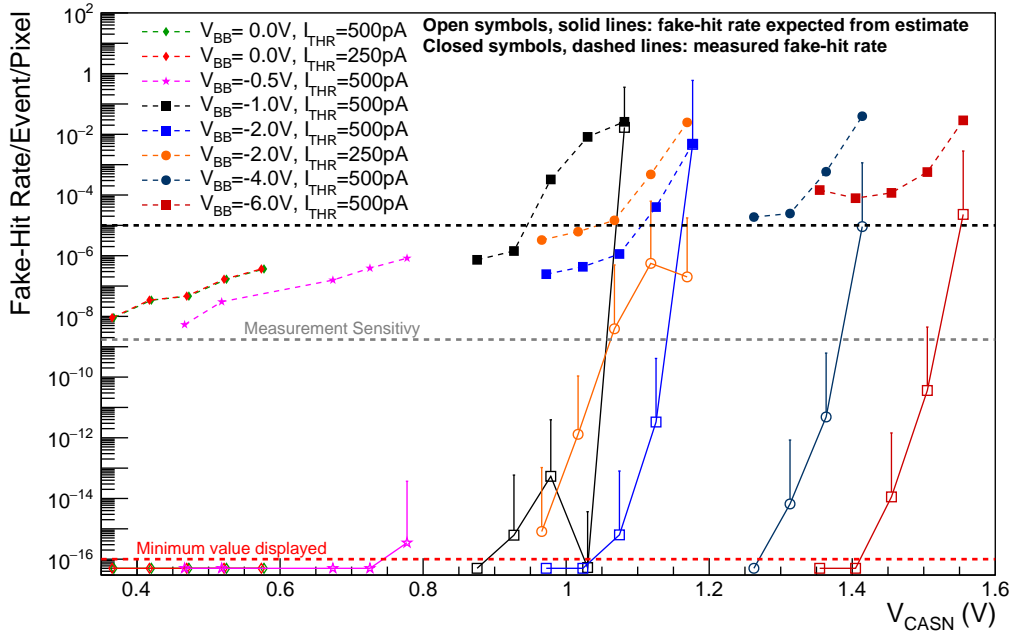

Figure B.2.: Measured (full symbols, dashed line) and expected (open symbols, solid line) fake-hit rate for a pALPIDEss-1a. Uncertainties show the maximum value found for a single pixel.

B.3. Detection Efficiency and Fake-Hit Rate

In the following, complementary figures for the detection efficiency and fake-hit rate of pALPIDEss and pALPIDE-2 are presented.

B.3.1. pALPIDEss

In Fig. B.3, the detection efficiency with (bottom) and without (top) reverse substrate bias as a function of V_{CASN} for the three different pALPIDEss prototypes are shown.
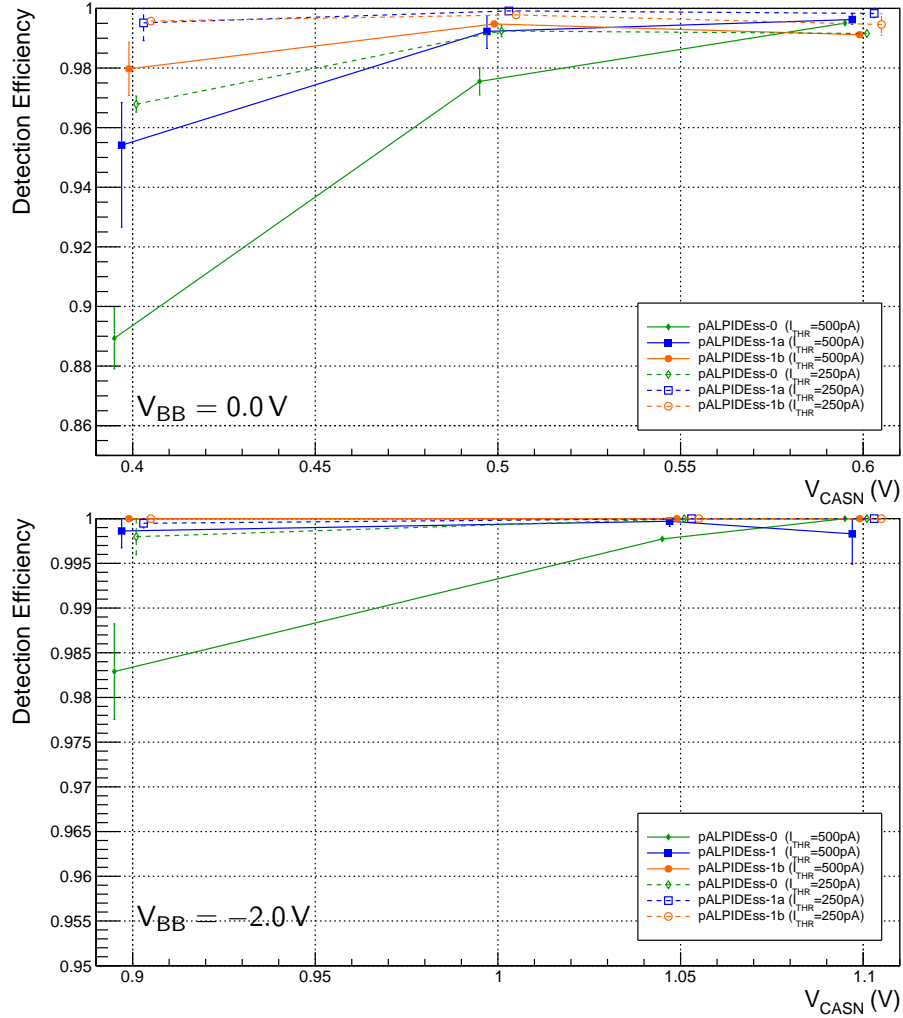

Figure B.3.: Detection efficiency as function of V_{CASN} for the pALPIDEss prototypes. Top: without reverse substrate bias; bottom: with reverse substrate bias $V_{BB} = -2.0\,\text{V}$.
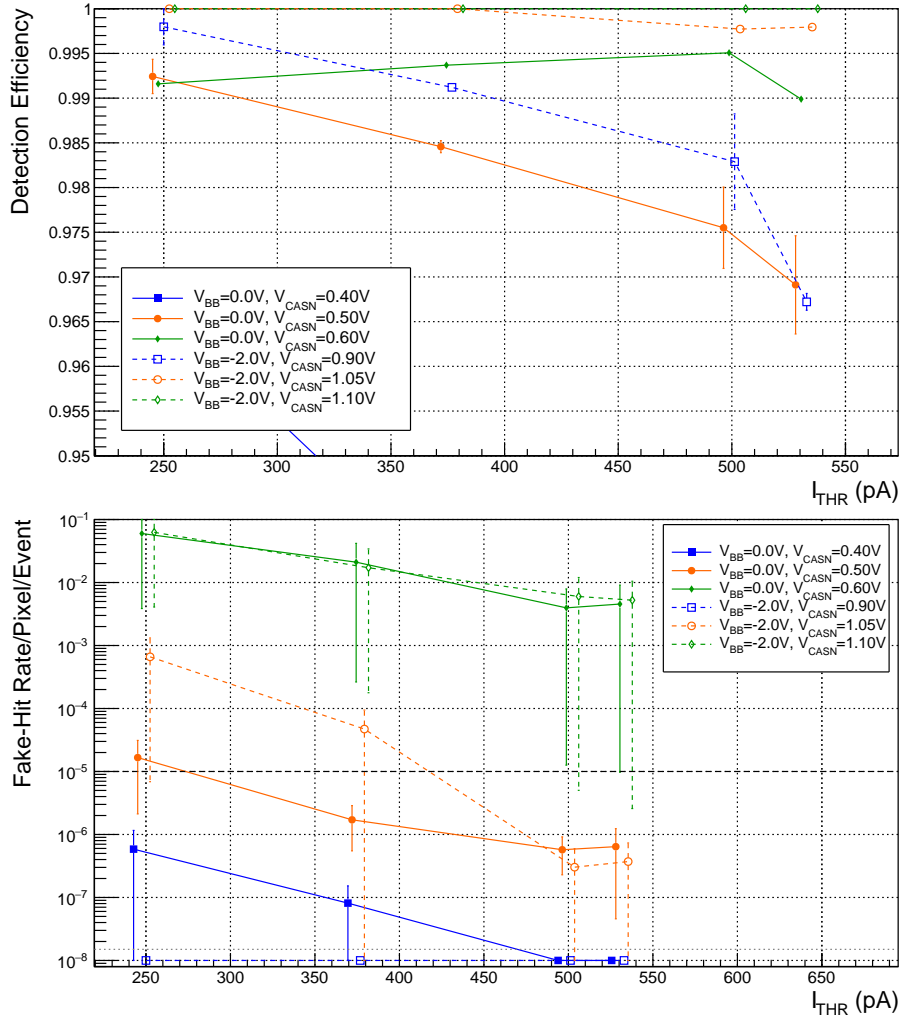
Figure B.4.: Detection efficiency (top) and fake-hit rate (bottom) of a pALPIDEss-0 as function of the threshold current I_{THR}.

As expected, a reduced I_{THR} leads to a higher efficiency. Furthermore, all prototypes perform better under reverse substrate bias for the shown values of V_{CASN}. The performance of the pALPIDEss-0 is in comparison slightly worse than the pALPIDEss-1a/b. There is no significant difference between pALPIDEss-1a and pALPIDEss-1b. All three versions of the pALPIDEss reach 99 % detection efficiency.

The detection efficiency as function of I_{THR} in comparison to the fake-hit rate for the pALPIDEss-0 is shown in Fig. B.4. The error bars show the chip-to-chip variation. Especially, the fake-hit rate shows a large variation. This can be explained by the fact that the baseline and in turn fake-hit rate exponentially depend on V_{CASN} as the corresponding transistor is in weak inversion. This leads to an amplification of even small chip-to-chip variations of the transistor properties. The highest V_{CASN} value (green) for both reverse substrate bias voltages shows a too high fake-hit
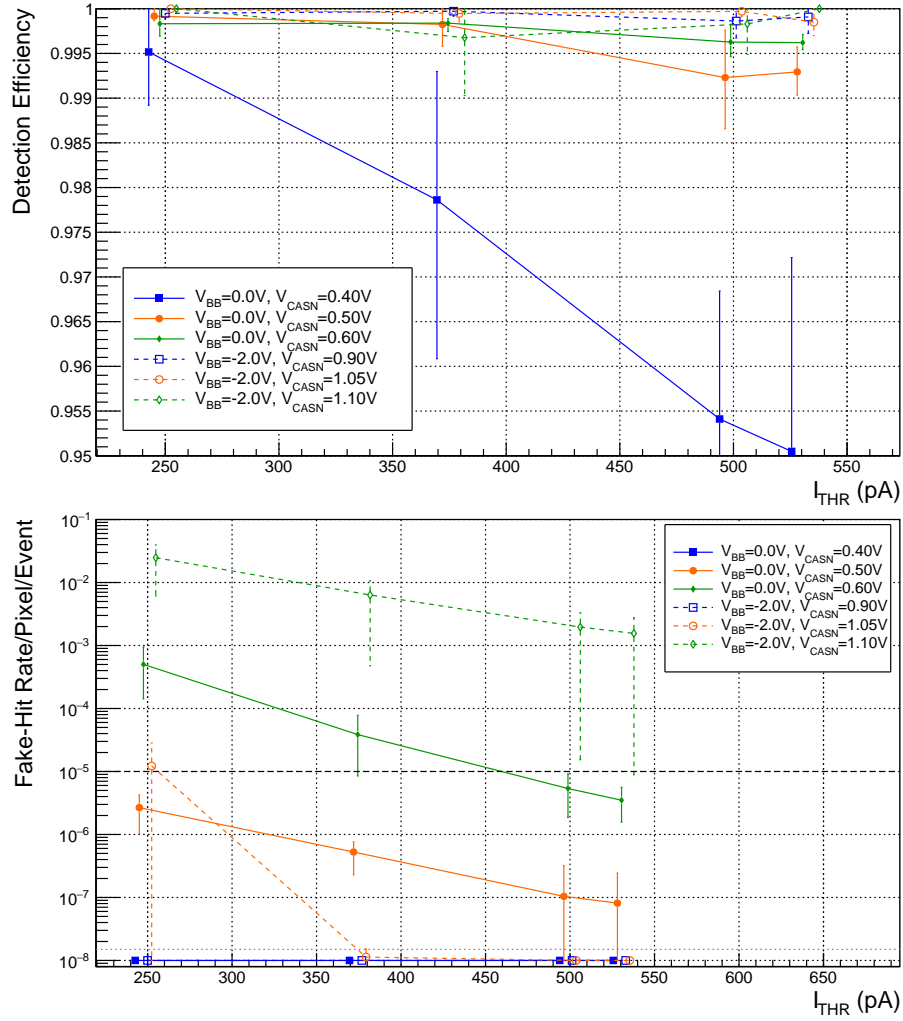
Figure B.5.: Detection efficiency (top) and fake-hit rate (bottom) of a pALPIDEss-1a as function of the threshold current I_{THR}.

rate. Without reverse substrate bias, the pALPIDEss-0 does not achieve 99 % detection efficiency together with a fake-hit rate smaller than 10^{-5} /event/pixel. This improves using $V_{BB} = -2\,\mathrm{V}$.

In Fig. B.5, the detection efficiency (top) and fake-hit rate (bottom) as function of the threshold current I_{THR} of the pALPIDEss-1a is shown. In comparison to the pALPIDEss-0 results (cf. Fig. B.4) there is an obvious improvement with regard to both detection efficiency and fake-hit rate. Only the highest V_{CASN} value (green) has to be excluded due to a too high fake-hit rate. The detection efficiency degrades only for the lowest V_{CASN} and higher I_{THR} at $V_{BB} = 0\,\mathrm{V}$. Using $V_{BB} = -2\,\mathrm{V}$, the pALPIDEss-1a has a lot of operational margin.

In comparison to the pALPIDEss-1a, the pALPIDEss-1b shows a similar performance (cf. Fig. B.6). The pALPIDEss-1a shows slightly better detection efficiency,
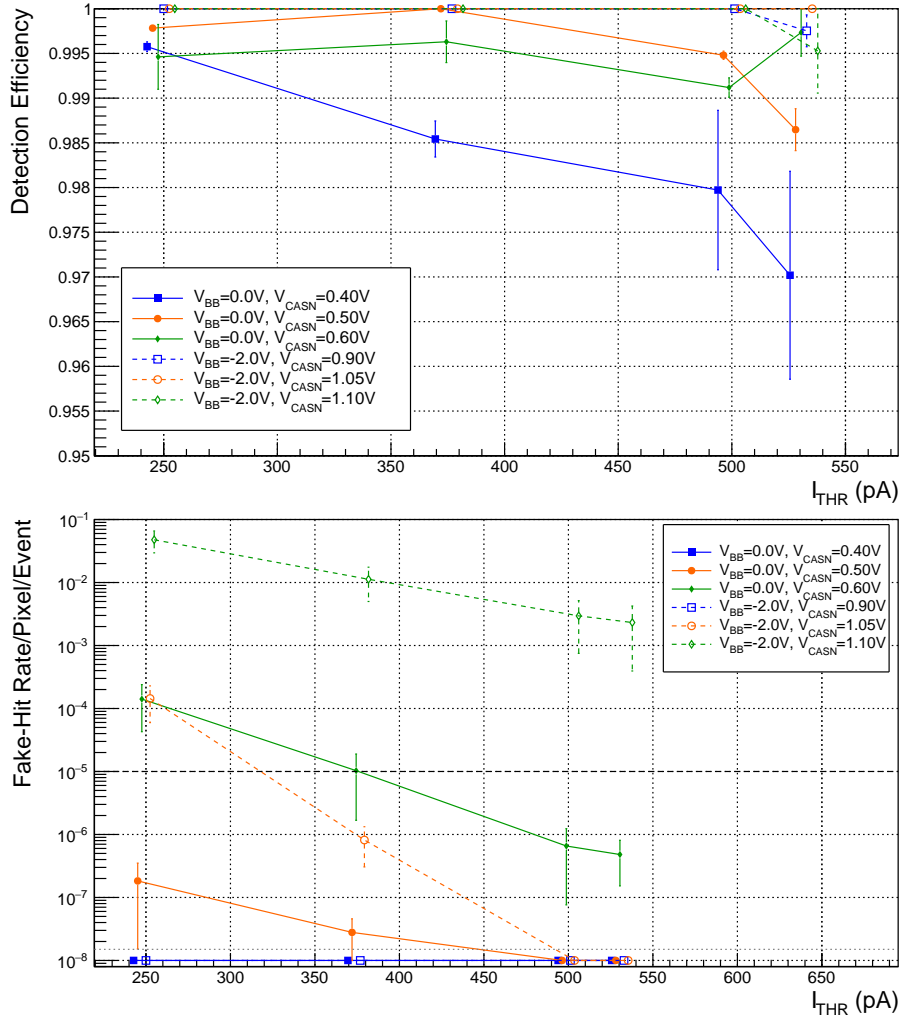
Figure B.6.: Detection efficiency (top) and fake-hit rate (bottom) of a pALPIDEss-1b as function of the threshold current I_{THR}.

while the pALPIDEss-1b shows a lower fake-hit rate. In terms of operational margin, both versions are similar. With the given chip-to-chip variations and only a two measured chips per version, it is not possible to take a decision for a version of pALPIDEss-1 based only on the detection efficiency and fake-hit rate.

B.3.2. pALPIDE-2

The influence of V_{CASN} on the detection efficiency of a pALPIDE-2 is shown in Fig. B.7. Lowering V_{CASN}, the charge threshold of the chip can be increased quickly and the resulting drop in detection efficiency becomes visible.

In Fig. B.8, the performance in terms of detection efficiency and fake-hit rate of the different epitaxial layers at 2 µm spacing as function of the measured threshold after NIEL irradiation is presented. There is a significant difference from 18 µm to 25 µm epitaxial-layer thickness, but no significant difference from 25 µm to 30 µm. However, the 25 µm epitaxial layer chip has experienced only about half the irradiation. The additional charge generated for the thicker epitaxial layer, leads an improved detection efficiency also at higher thresholds. The improvement in terms of fake-hit rate from 18 µm to thicker epitaxial layers is not necessarily expected. This effect has to be studied in further detail using multiple chips.
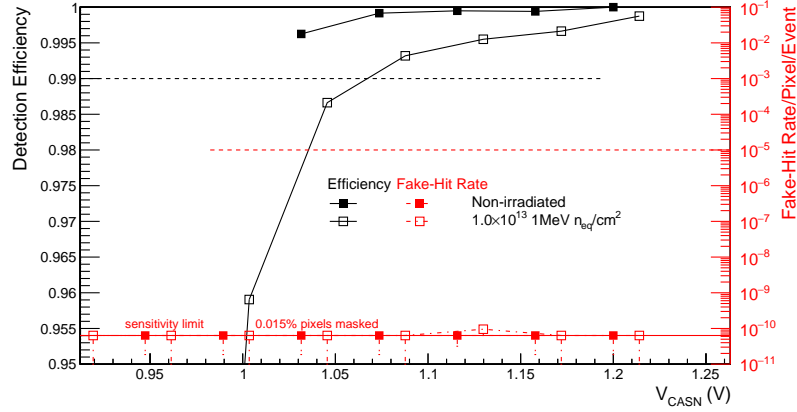
Figure B.7.: Detection efficiency and fake-hit rate as function of V_{CASN} of a pALPIDE-2, 25 µm epitaxial layer, 2 µm spacing (sector 1), $V_{\mathrm{BB}} = -6\,\mathrm{V}$ and $I_{\mathrm{THR}} = 780\,\mathrm{pA}$.

Figure B.8.: Detection efficiency and fake-hit rate as function of measured threshold, epitaxial layer comparison 2 µm spacing (sector 1), $V_{\mathrm{BB}} = -6\,\mathrm{V}$ after irradiation.
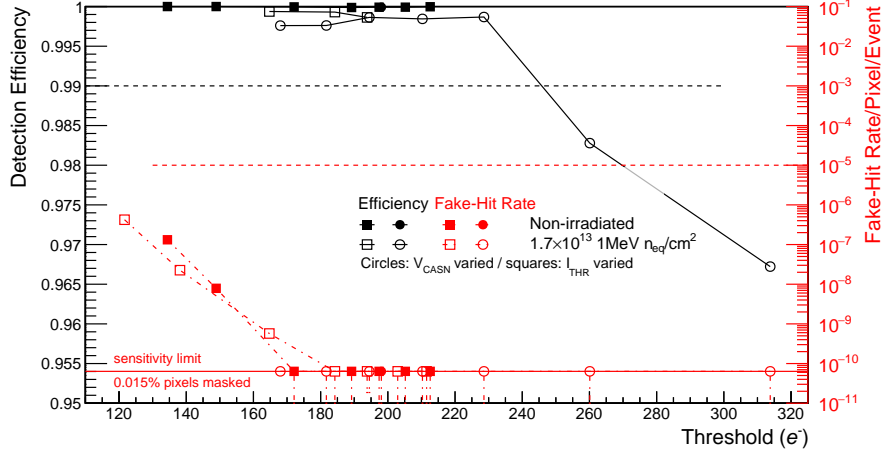
Figure B.9.: Detection efficiency and fake-hit rate as function of measured threshold, 30 μm epitaxial layer, 4 μm spacing (sector 2), $V_{\mathrm{BB}} = -6\,\mathrm{V}$.
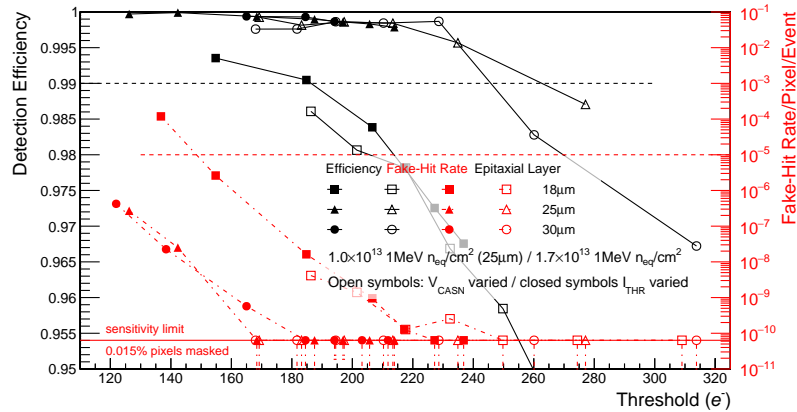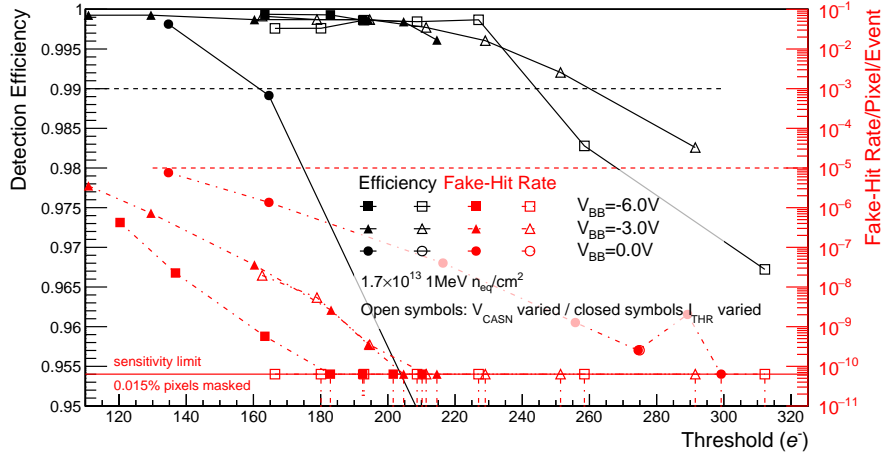

Figure B.10.: Detection efficiency and fake-hit rate as function of measured threshold, 30 μm epitaxial layer comparison, 4 μm spacing (sector 2), V_{BB} comparison.

The detection efficiency and fake-hit rate for the combination of 4 μm spacing (sector 2) and 30 μm epitaxial layer is shown in Fig. B.9. The squares correspond to an I_{THR} range from 200 pA to 1000 pA as shown in Fig. 6.20 (top). For slightly higher threshold values, which can be easily achieved by lowering V_{CASN}, also this combination of spacing and epitaxial layer starts to lose detection efficiency.

In Fig. B.10, the dependence of the detection efficiency and fake-hit rate as function of the measured threshold and reverse substrate bias for 4 μm spacing (sector 2) and 30 μm epitaxial layer is shown. The detection efficiency does not improve from $-3\,\mathrm{V}$ to $-6\,\mathrm{V}$, however, the fake-hit rate still becomes smaller.

B.4. Position Resolution and Cluster Size

For pALPIDE-2, the position resolution and mean cluster size of the two best performing combinations, the 4 µm spacing (sector 2) and 30 µm epitaxial layer as well as the 2 µm spacing (sector 1) and the 25 µm epitaxial layer are shown as a function of the measured threshold in Fig. B.11 and Fig. B.12, respectively. The combination of 2 µm and 25 µm epitaxial layer shows a more pronounced deterioration of both cluster size and position resolution from irradiation.

Figure B.11.: Position resolution and average cluster size as function of measured threshold, 30 µm epitaxial layer, 4 µm spacing (sector 2), $V_{\mathrm{BB}} = -6\,\mathrm{V}$.
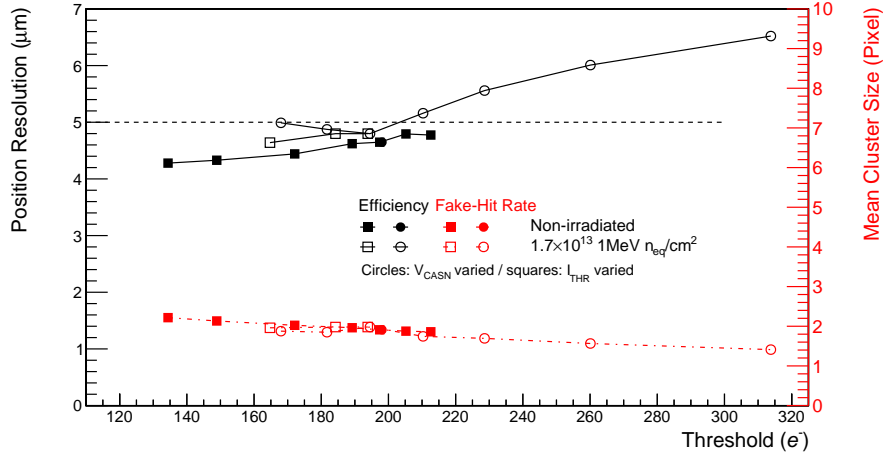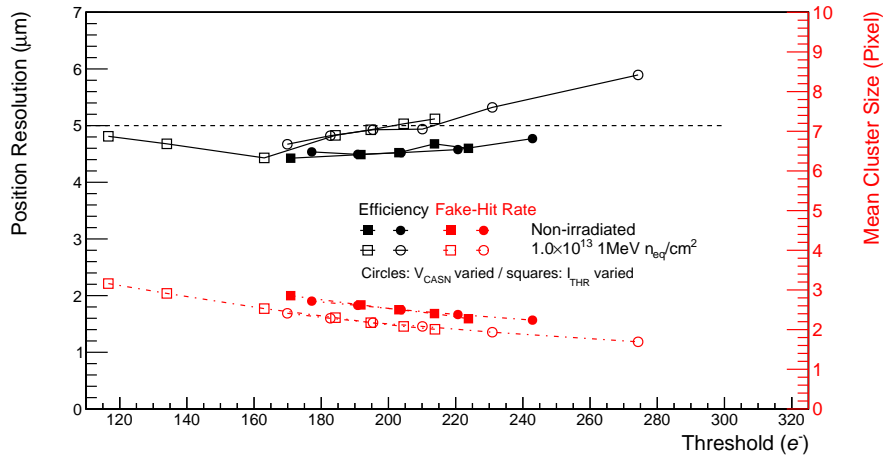

Figure B.12.: Position resolution and average cluster size as function of measured threshold, 25 µm epitaxial layer, 2 µm spacing (sector 1), $V_{\mathrm{BB}} = -6\,\mathrm{V}$.

The negative influence of too large charge sharing without reverse-substrate bias can be observed in Fig. B.13. At 4 µm spacing (sector 2) a thicker epitaxial layer leads to
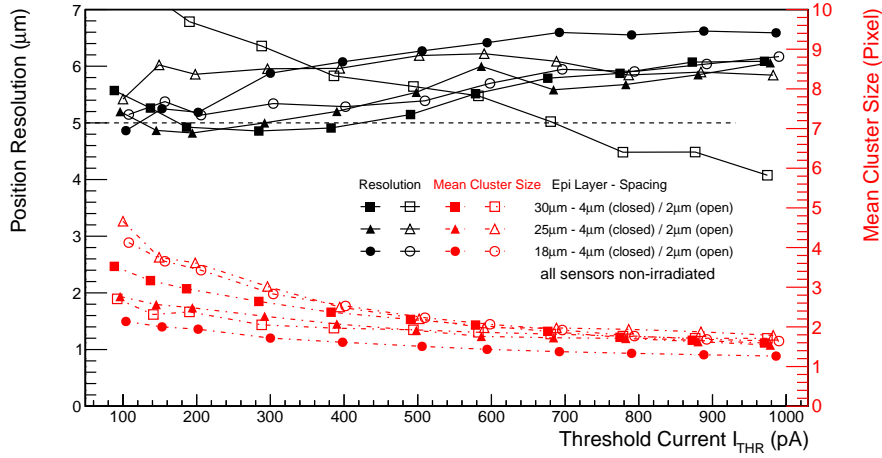
Figure B.13.: Position resolution and average cluster size as function of I_{THR}, dependence on spacing and epitaxial-layer thickness at $V_{BB} = 0\,\text{V}$, $V_{CASN} = 0.4\,\text{V}$.

larger clusters, as observed with reverse substrate bias in Fig. 6.23 (bottom). With $2\,\mu\text{m}$ spacing (sector 1), there is little difference between $18\,\mu\text{m}$ and $25\,\mu\text{m}$ in terms of cluster size, which show both larger clusters and stronger increase towards lower thresholds than the $4\,\mu\text{m}$ spacing (sector 2). For $2\,\mu\text{m}$ spacing and $30\,\mu\text{m}$ epitaxial layer, the cluster size behaves similarly as the combination of $4\,\mu\text{m}$ spacing and $25\,\mu\text{m}$ epitaxial-layer thickness. The smaller clusters compared to the same spacing can be explained by strong charge sharing leading to too small charges at individual pixels. The $2\,\mu\text{m}$ spacing combined with the $30\,\mu\text{m}$ epitaxial layer shows additional a fundamental different behaviour regarding the position resolution, which shows a strong improvement for increasing thresholds.

C. ITS Upgrade SRS Readout System

The ITS Upgrade Scalable Readout System (SRS) consists of a Padova Proximity board and the RD51 collaboration [156] Scalable Readout System (SRS) [157–159]. In the this chapter, relevant features and parts of SRS hardware and firmware will be introduced. Additionally, the main characteristics of the Padova proximity board, used to interface pixel-chip carriers with the SRS, are outlined. Furthermore, the firmware and software implemented during the course of this thesis are described.

C.1. Scalable Readout System

The Scalable Readout System (SRS) [157–159] has been developed within the RD51 collaboration and is a general purpose multi-channel readout platform. It consists of three main components, the Front-End Concentrator (FEC) [160], adapter cards and the Scalable Readout Unit (SRU) (cf. Fig. C.1). The SRU can be used to control and read out multiple FEC cards. Alternatively, the FEC card can be connected directly to a PC using Gigabit Ethernet (GbE). The adapter cards are used to provide application specific interfacing as Analogue-to-Digital Converters (ADCs) or Low-Voltage Differential Signaling (LVDS) I/Os to the front-end electronics.
For the ITS Upgrade SRS readout system, up to two FEC cards are required. One FEC card handles the digital I/Os and another one takes care of the digitisation of analogue signals using an HLVDS and ADC adapter card, respectively.
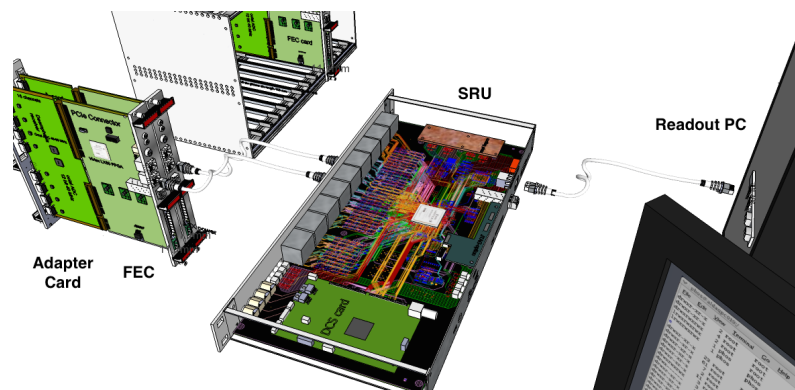
Figure C.1.: Main components of the SRS: adapter card (left), FEC (mid left), and SRU (centre), adapted from [159].
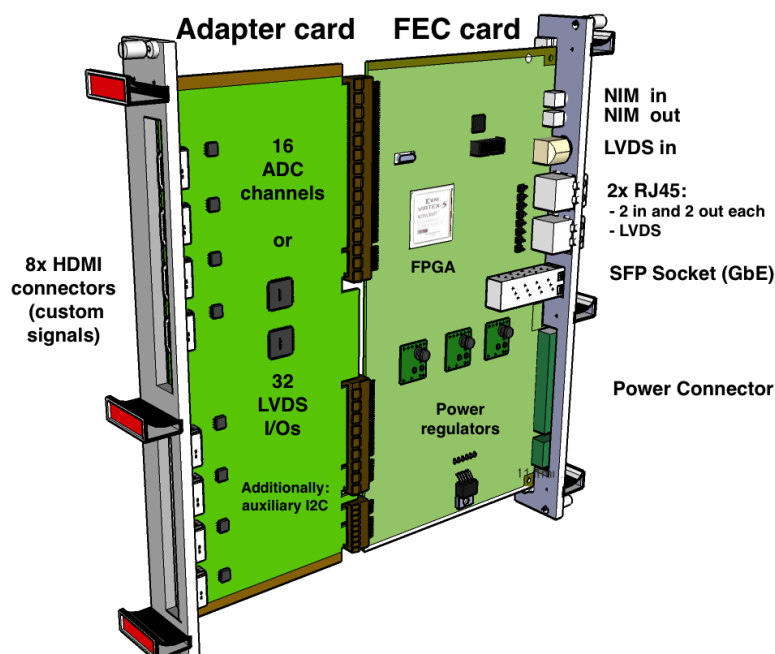
Figure C.2.: SRS components used for the ITS Upgrade readout system, adapted from [159].

C.1.1. Front-End Concentrator Card

The Front-End Concentrator (FEC) [160] (cf. Fig. C.2, right) concentrates the data from several front-end electronic channels and controls the front-end electronics. The core of the FEC card is a Xilinx Virtex-5 LX50T Field-Programmable Gate Array (FPGA). For buffering data, 2 Gbit DDR2 SD-RAM are available. The FEC card contains two EEPROMs, one for storing persistent information and one for the FPGA bit stream. The majority of the I/Os of the FPGA are made available to the adapter card. At the front-panel, furthermore a NIM-standard I/O pair, an LVDS input and two RJ45 connectors featuring two LVDS inputs and outputs each, are available. For high-speed communication an SFP socket is provided. Equipped with a corresponding SFP module, GbE can be used to communicate with a PC. The User Datagram Protocol (UDP) stack is implemented in the FPGA fabric.

C.1.2. Adapter Cards

ADC

The ADC card (cf. Fig. C.2, left) features 16 differential analogue inputs which are digitised by two 12 bit 8 channel ADCs with 40 MSample/s and and input range of $2\,V_{pp}$. All channels have a parallel $100\,\Omega$ input termination and a DC gain of 1.25.

Two ADC channels are connected to each of the eight HDMI connectors. Additionally, each connector provides access to the I^{2}C bus controlled by the FPGA on the FEC card.

HLVDS

The HLVDS adapter card (cf. Fig. C.2, left) features 32 high-speed LVDS lines, whose direction can be selected by mounting the corresponding components to the PCB. There are additional eight auxiliary LVDS inputs. The LVDS transceivers support up to 3.125 Gbps transfer rate, well above the 40 Mbps which are required for the ITS readout system. Four LVDS lines with selectable direction, one LVDS input and an I^{2}C-bus are available through an HDMI connector.

C.1.3. PC Interface

The default firmware provides slow control and data acquisition using the UDP via the GbE interface. The slow-control communication [161] is implemented using a protocol based on requests by the PC which are always answered by the FEC card to ensure a reliable communication. The answer contains either a copy of the data written or the data to read as well as the request ID which was initially send by the PC. The slow-control address space is segmented into different UDP ports which contain registers with a 32 bit address space.

By default, each FEC card has an IP address of the form 10.0.x.2. It expects to send its data to 10.0.x.3 at UDP port 6006. Slow control transactions are expected to originate from port 6007 of 10.0.x.3. The FEC exclusively communicates with the host at 10.0.x.3 and all other packages will be discarded.

In the default firmware, the data acquisition is implemented such, that the FEC continuously sends data to the PC, without the need for an acknowledge or any interaction by the PC. The PC has the option to pause and continue the data transmission using `Xon`/`Xoff` commands.

C.2. Padova Proximity Board

The proximity board is shown in Fig. C.3. It was designed with a flexible interface based on µHDMI connectors and double-row pin headers.

For the digital signals, it contains 64 LVDS to CMOS converters, as well as level shifters, to match the I/O voltage to the supply voltage of the DUT. The direction of groups of 16 channels can be selected using jumpers. Only 32 digital I/Os are available via the µHDMI connectors. The level shifters are directly connected to the DUT.
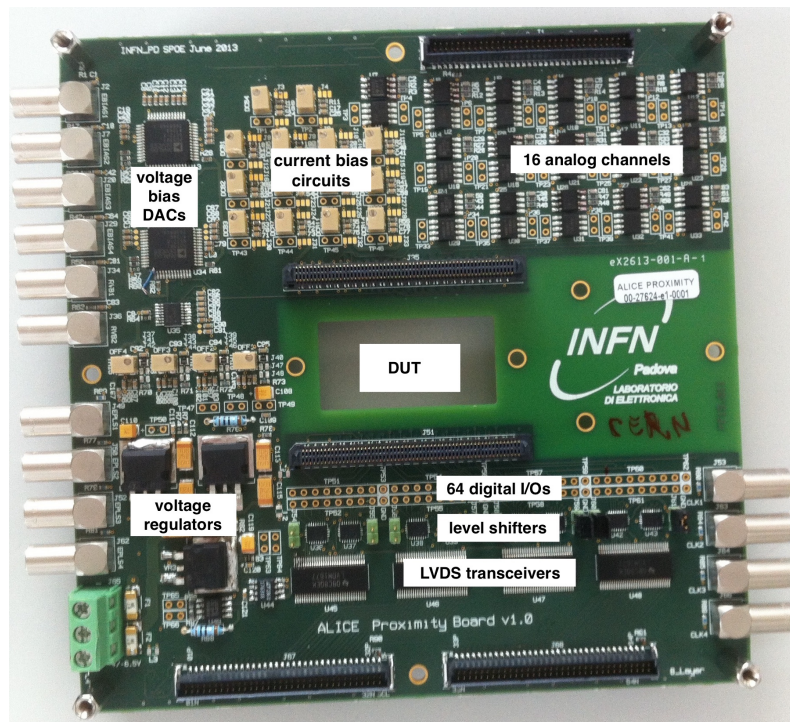
Figure C.3.: Picture of the Padova Proximity Board.

For the measurement of analogue signals, 16 channels with a bandwidth of 45 MHz and a DC gain of -2 are available. Each channel contains two operational amplifiers. The first operational amplifier operates as an inverter and its offset voltage is controlled by a DAC. The second amplifier is a singled-ended to differential signal converter. It is designed for a $100\,\Omega$ termination.

For the biasing of the DUT, two 16 channel voltage DACs and 14 current-bias circuits are available. The DACs are controlled via I^2C. The current-bias circuits are adjusted using a potentiometer and the current can be measured at a series resistor. The current-bias circuits are not designed to be remote controllable. For sweeping the currents of the pALPIDEss, spare channels at the voltage bias DACs were re-wired to be used as reference voltages of the corresponding current-bias circuits. Based on a measured DAC-voltage to current calibration, the DACs are used to adjust the bias currents.

The proximity board contains voltage regulators for the on-board circuitry as well as for the DUT.
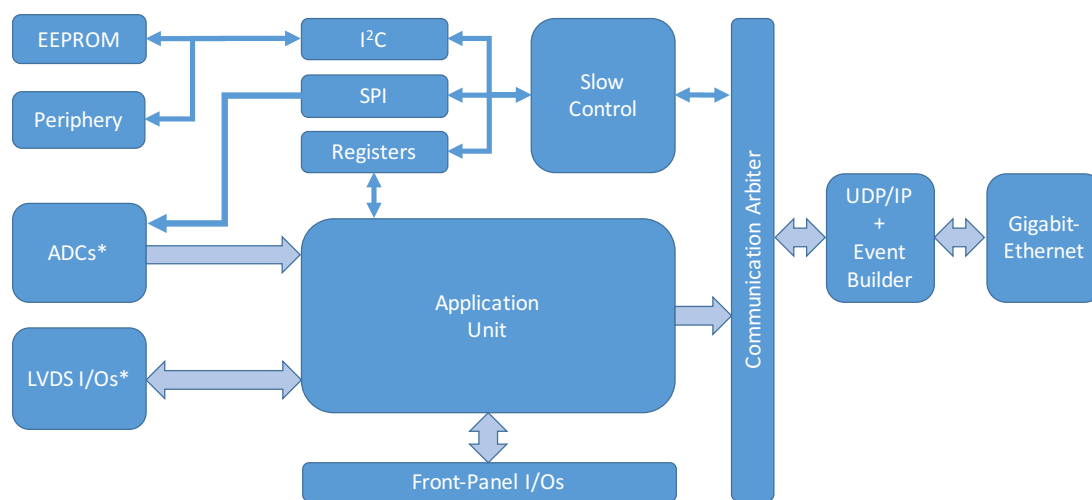
*Firmware contains either ADC or LVDS module

Figure C.4.: Schematic of the data flow in the SRS firmware.

C.3. Firmware

C.3.1. General

The data flow in the SRS firmware is shown in Fig. C.4. The actual organisation of the firmware modules does not directly correspond to the data flow. The SRS firmware for the ITS upgrade was developed by reusing as much code of the standard firmware as possible. As mentioned above, all communication is based on the UDP protocol via the GbE link. All necessary functionality is implemented in the firmware without the need for a micro-controller core. The communication arbiter assigns the transmission bus either to the DAQ or the slow control, which is given priority. The application unit provides the event data and additional information on the number of frames in the event and the size of the frame currently to be sent to the UDP module. The additional information is needed by the UDP module to generate an end-of-event frame after the full event is sent. The actual preparation of the UDP frame payload and the calculation of the frames per event is performed by the application unit. The default firmware was designed only to start sending data, after the full event was acquired. This, however, is not possible for the readout of the Explorer-1 prototypes, as the event size exceeds the capacity of the on-chip memory of the FPGA. As a consequence the firmware was modified in order to allow to start the transmission before the event is fully read from the DUT. This implementation is possible, as the event size was only exceeding the available on-chip memory by about 20 % and the bandwidth necessary to readout the DUT was 25 % lower than the bandwidth available for sending data from the FPGA to the PC. With the new implementation, data is sent as soon as the payload
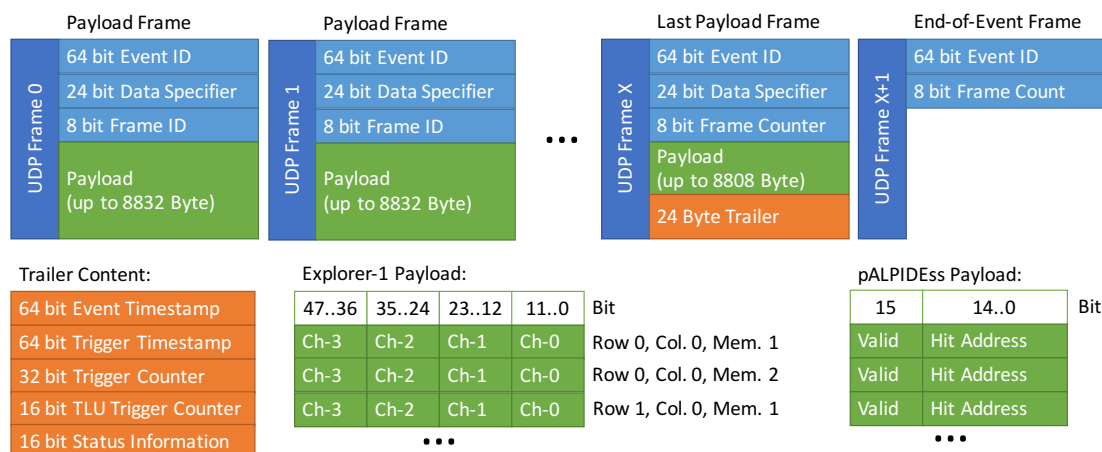
Payload Frame — UDP Frame 0
- 64 bit Event ID
- 24 bit Data Specifier
- 8 bit Frame ID
- Payload (up to 8832 Byte)

Payload Frame — UDP Frame 1
- 64 bit Event ID
- 24 bit Data Specifier
- 8 bit Frame ID
- Payload (up to 8832 Byte)

...

Last Payload Frame — UDP Frame X
- 64 bit Event ID
- 24 bit Data Specifier
- 8 bit Frame Counter
- Payload (up to 8808 Byte)
- 24 Byte Trailer

End-of-Event Frame — UDP Frame X+1
- 64 bit Event ID
- 8 bit Frame Count

Trailer Content:
- 64 bit Event Timestamp
- 64 bit Trigger Timestamp
- 32 bit Trigger Counter
- 16 bit TLU Trigger Counter
- 16 bit Status Information

Explorer-1 Payload:

47..36	35..24	23..12	11..0	Bit
Ch-3	Ch-2	Ch-1	Ch-0	Row 0, Col. 0, Mem. 1
Ch-3	Ch-2	Ch-1	Ch-0	Row 0, Col. 0, Mem. 2
Ch-3	Ch-2	Ch-1	Ch-0	Row 1, Col. 0, Mem. 1
...				

pALPIDEss Payload:

15	14..0	Bit
Valid	Hit Address	
Valid	Hit Address	
Valid	Hit Address	
...		

Figure C.5.: UDP payload data format used for the ITS upgrade.

for one full frame has arrived at the FPGA or the readout of the DUT has finished. In between frames, the data transmission is paused and the transmission channel stays occupied. UDP does not feature a handshake which ensures the arrival of the data packets. The packets could be, e.g., dropped or reshuffled by the operating system due to too high load or full buffers, making the transmission unreliable. In order to detect this, a custom UDP payload format is used. The version of the ITS upgrade (cf. Fig. C.5) differs slightly from the default SRS format. As in the default SRS protocol, every payload frame contains an event ID and a frame ID. The frame ID counts the number of frames starting from zero. The total number of frames of the event is sent using a modified end-of-event frame, which contains only the event ID and the payload-frame count. The end-of-event frame is shorter than the shortest possible data-frame in order to be reliably identified. Furthermore, all data frames contain a header with the event ID and their frame ID. This allows later on to check whether an event has completely arrived at the PC and to sort them. A retransmission of missing data is not foreseen. Hence, incomplete events have to be discarded. The fraction of discarded events was found to be less than a percent if the PC was exclusively used as data acquisition PC.

The slow control module provides registers and reset signals to be used in the application unit and endpoints for I^{2}C and SPI for the control of periphery which can be, e.g., the ADCs on the adapter card, the EEPROM on the FEC or external devices connected to the adapter card.

The default firmware can only send data to the PC using a burst mode. For the ITS upgrade, an event-pulling mode was implemented. In the event-pulling mode, a new event is only acquired and sent after the arrival of a request from the readout PC. At first, this was implemented using a slow-control request. However, it turned out, that the communication arbiter works neither efficiently nor reliably for data and slow-control transmissions alternating at a high frequency. In order to circumvent this problem, the readout-request logic was added to the arbiter itself. This
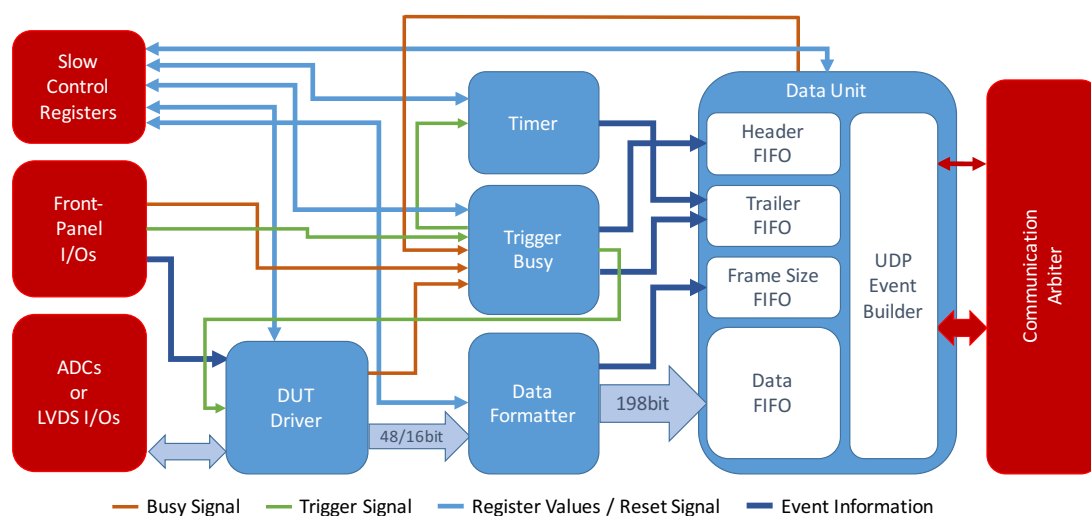
Figure C.6.: Schematic of the modules inside the application unit. External modules are shown in red, modules which are part of the application unit are shown in blue.

has furthermore the advantage, that no slow-control reply is sent for a read request and the transmission channel can stay assigned to the data acquisition. The event-pulling mode helped to reduced the fraction of incompletely received events to less than 1‰. Furthermore, the fraction of incomplete events was found to be independent of the load on the readout PC, which hence also could take care of tasks like zero-suppression and general processing in parallel to the data acquisition.

The actual user logic is implemented in the application unit. For the ITS upgrade, it is organised as shown in Fig. C.6. The `DUT driver` controls the DUT. It generates the steering signals and assembles the data stream with the raw data from the ADC or the LVDS inputs. The input data is 48 bit or 16 bit wide for the Explorer-1 and pALPIDEss, respectively. The `Data Formatter` combines it into 198 bit vectors, which contain 192 bits of data and 6 bits status information. This data vector size is used to exploit the 18 bit-wide internal Block-RAMs of the FPGA in the most efficient way. Additionally, the `Data Formatter` calculates the frame sizes needed, using a maximum payload of 8832 Byte per frame.
The `Timer` records the arrival time of a trigger and the start of the DUT readout time as 64 bit time stamp on the basis of a 40 MHz clock. The `Trigger / Busy` unit, can either trigger upon an external signal, or once all busy inputs are deasserted. As external trigger source, either the NIM input or a EUDET TLU [162] connected via an RJ45 connector can be used. Busy signals are the internal busy flags from the `DUT driver`, the `Data Unit`, the absence of an event request in event-pulling mode or an external busy from the second RJ45 connector. The `Data Unit` gathers all information on an event and stores it in FIFOs. This information is then used by the `UDP Event Builder` to execute the data transmission.
All external I/Os are implemented using registers in the IO-pads, to achieve a
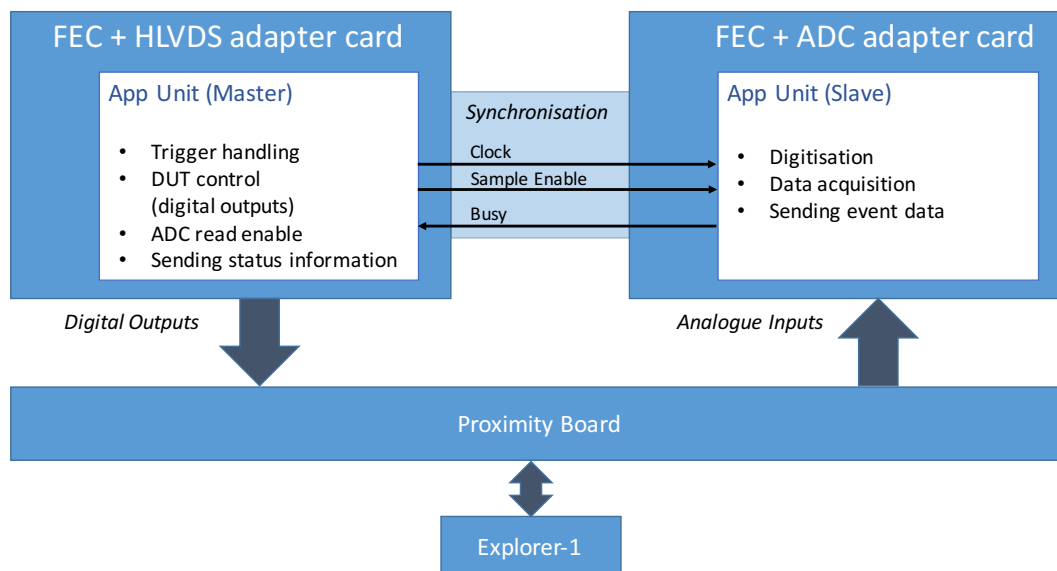
Figure C.7.: Block diagram of the two FEC readout used for the Explorer-1 prototypes.

predictable timing. The peculiarities of the firmware versions of the Explorer-1 and the pALPIDEss are outlined below.

Explorer-1

For the Explorer-1 prototype digital steering signals and ADCs for the digitisation of the analogue output signals are needed. With the available adapter cards this can only be achieved by using two separate adapter cards attached to two FEC cards. As a consequence, a synchronisation of the two FEC cards is necessary (cf. Fig. C.7). This was implemented using one of the two RJ45 connectors. The FEC with the HLVDS adapter card is the master. Using one of the LVDS output lines on the RJ45 connector, it sends its clock to the slave FEC with the ADC card. The second output is used to send a sample-enable signal, which tells the slave FEC to read the output of the ADCs. While reading from the ADCs and sending the data out via UDP, the slave FEC asserts a busy signal which is sent via one of the return LVDS lines on the RJ45 connector. Via slow-control transfers before the start of the data taking, the event IDs of the two FECs are ensured to match. The master FEC sends events which contain only header and trailer without any payload. The EUDET TLU can be connected to both FEC cards. On the slave FEC, the trigger time stamp is only recorded and the data acquisition is still controlled by the sample-enable signal. The sequence signal of the Explorer-1 has a frequency of 10 MHz. The 10 MHz were chosen according to the rise time of the analogue output signals. The application
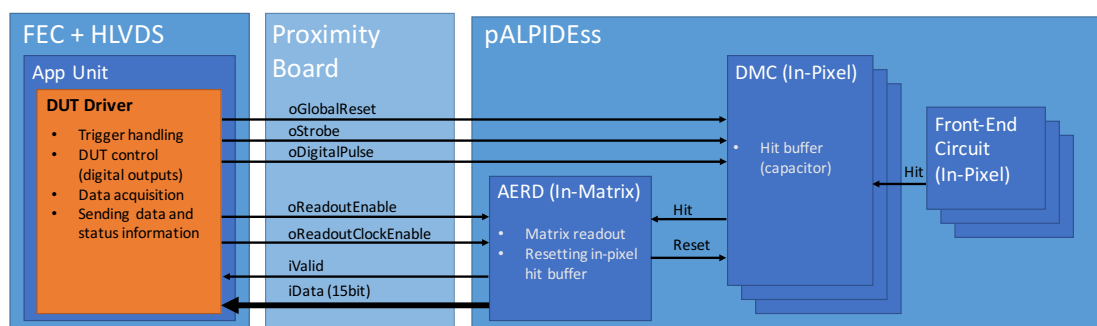
Figure C.8.: Block diagram of the single FEC readout used for the pALPIDEss prototypes.

unit and the ADCs use a 40 MHz clock, in order to be flexible in adjusting the relative phases of the signals. The phases and duty cycles of the control signals were adjusted in order to reduce switching noise during the sampling.

On an Explorer-1 die, four individual Explorer-1 chips are placed next to each other. All four chips receive the same steering signals and their outputs are sampled simultaneously, leading to 48 bit vectors in the payload.

The Explorer prototypes consist of two matrices of in total 11700 pixels with two memories each. The pixels and memories have to be read sequentially, leading to a readout time of 2.34 ms. Further details on the operation of the Explorer-1 prototypes can be found in [130].

pALPIDEss

The pALPIDEss firmware is simpler than the Explorer-1 firmware, as a single FEC card with an HLVDS adapter card is sufficient. Consequently, no inter-FEC synchronisation is necessary. In contrast to the fixed event size of the Explorer-1, the event size of the pALPIDEss depends on the occupancy, as the data is zero-suppressed by the DUT. This leads to a more complex and flexible design of the `Data Unit` and the `Data Formatter`. Furthermore, the readout clock for the pALPIDEss is 40 MHz. In order to allow for oversampling of the input signals and an easy adjustment of the phases and duty cycles, the base frequency of the application unit was increased to 160 MHz. A block diagram of the pALPIDEss readout is shown in Fig. C.8.

The readout sequence for the pALPIDEss is shown in Fig. C.9. The first group of signals are for the interaction with the application unit. Configuration values, as the duration of the different states are not shown. The `pALPIDEss Driver` is initiated by `iReset`. Only after `iEnable` gets invoked, the driver moves on to the `Init` state and starts running. The duration of the `Init` state t_{INIT} is controlled by a counter. `iTriggerMode` determines whether the driver waits for an external trigger

on `iTrigger` before entering the acquisition phase (`iTrigger`= 0, as in Fig. C.9) or proceed directly to the acquisition phase which is kept until the `iValid` signal indicates a hit on the chip. Unless waiting for a trigger, the driver signals busy. `oWriteData` enables the writing of the input on the LVDS lines to the `formatData` module. The length of the `Delay` state t_{DLY} is set by a register. The driver stays in `TriggerWait`, until a trigger signal arrives. The `PreAcq` state is used to set the strobe delay t_S. During the `ACQ` state, `oStrobe` is asserted. The default strobe duration is $t_{ACQ} = 1.54\,\mu s$. The `RdoWait` allows to introduce a wait time t_{RD} between the acquisition and the readout. In order to cope with the signal propagation time to the DUT and from the DUT to the readout system t_{PD}, the `RdoStart` state is used. In order to reduce the clock frequency send to the DUT, `Pause` states can be added to the readout. The readout is terminated either after the readout of 32768 hits or after the deassertion of the `iValid` signal. The limit of 32768 hits corresponds to all pixels firing and prevents the readout from getting stuck due to a malicious DUT behaviour.

Many of the Finite-State Machine (FSM) states were introduced to investigate the influence of the switching noise of the control signals in the acquisition and readout phase by adding wait cycles. During these studies, it was discovered, that fake-hits due to leakage in the DMC are dominant (c.h. Ch. 6.2.4). During normal data taking the `Delay`, `RdoWait` and `PostEvtDly` states are configured to a length of one clock cycle, as a larger delay does not improve the fake-hit rate and only increases the readout time of an event.

The global reset controlled by $\overline{\text{oGlobalReset}}$ is used to keep the DMCs in a well defined state, while they are not used. It resets all DMCs simultaneously. Its value is controlled using a register with a bit for each FSM state. The configuration shown in Fig. C.9 was found to be the best performing one.

C.4. Software

The laboratory software for the SRS readout system is organised in a git repository [163]. In the following, the main components are briefly outlined.

Slow Control:
> The slow control is also implemented as Python classes resembling read and write requests as well as their replies. The core is the slow-control class which implements a server listening on port 6007 for replies for the FEC. For each FEC, an object has to be instanced. Wrapper functions for reading single addresses, consecutive addresses and lists of addresses as well as reading bursts and lists ease the usage. Furthermore, high-level Python scripts are provided to control the bias DACs on the proximity board, the EEPROM on the FEC, resetting and rebooting the FECs, configuring the DUT driver and application unit as well as reading status registers in the application unit.
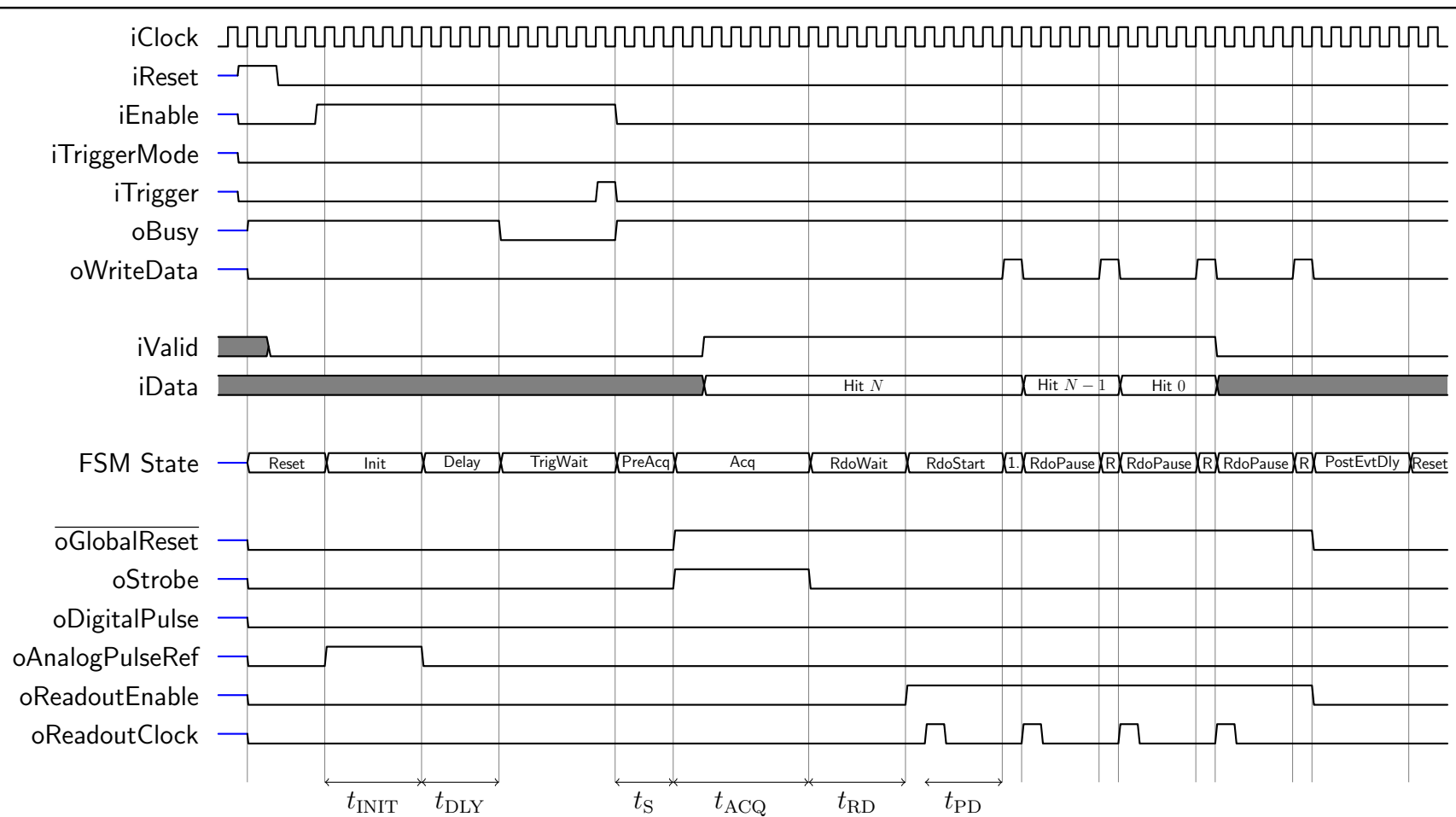
Figure C.9.: Timing diagram of the pALPIDEss readout sequence. The first group of signals is for communication within the application unit. The second group are the input signals from the DUT followed by the FSM state. The last group are the output signals to the DUT. State durations in terms of clock cycles are not to scale.

DAQreceiver:

The DAQreceiver is written in Python. It listens on port 6006 and writes the raw data to the disk. The data is not processed or checked for consistency. In order to make the data transmission more reliable, large enough buffers to accommodate a full event are used.

For the readout of the Explorer-1, two separate threads for receiving the data from each FEC is used.

In the continuous readout mode, the DAQreceiver simply writes the raw data sent from the SRS to the disk. In the event pulling mode, a new event request is sent after receiving and end-of-event frame or a time out. The end-of-event frame is identified by its unique size of nine bytes.

DAQreader:

The DAQreader processes the raw data. It reads the raw data, sorts the frames of an event and checks it for consistency. The payload is then converted to a data format based on `ROOT TTrees`. For the 12-bit data words of the explorer, Python was found to be a factor ten slower than an equivalent application written using C in reading and processing the input data. As a consequence, the version written in C is used to read the raw data from disk and to convert it into `TTrees`.

For the analogue Explorer-1 data, a zero-suppression algorithm can optionally be used. Based on the a pedestal run, signals with a configurable height above threshold are identified. Only squares of a specified size in pixels around these identified signals are stored.

Analysis:

The analysis code is based on `ROOT` macros written in C. They are grouped into different measurement types using the same base for common tasks as clustering.

EUDAQ Integration:

`EUDAQ` [142, 143] is used as test-beam data-acquisition framework. For the `EUDAQ` integration, the data receiver was integrated in a so-called producer written in C++. For the slow control, the existing Python scripts are used.

In order to achieve a high level of reproducibility, all standard measurements are automated. The automation concerns the control of the readout system, the biasing of the DUT and external devices like power supplies, pulse generators and linear stages moving the radioactive sources or the laser in position. Like this parameter scans and consecutive noise and radioactive source measurements are possible without interaction.

D. Acronyms and Technical Terms

ADC	Analogue-to-Digital Converter
AERD	Address-Encoder Reset-Decoder
ALICE	A Large Ion Collider Experiment
ATLAS	A Toroidal LHC ApparatuS
AOD	Analysis Object Data
CERN	Centre Européen pour la Recherche Nucléaire
CGC	Colour Glass Condensate
CKM	Cabibbo-Kobayashi-Maskawa
CMS	Compact Muon Solenoid
CNM	Cold Nuclear Matter
CTP	Central Trigger Processor
DAC	Digital-to-Analogue Converter
DAQ	Data Acquisition system
DCA	Distance of Closest Approach
DESY	Deutsches Elektronen Synchrotron
DMC	Dynamic Memory Cell
DUT	Device Under Test
FEC	Front-End Concentrator
FONLL	Fixed next-to leading Order Next-to-Leading Logarithm
FPGA	Field-Programmable Gate Array
FPN	Fixed-Pattern Noise
FSM	Finite-State Machine
FWHM	Full-Width Half Maximum
GBL	General Broken Line
GbE	Gigabit Ethernet
GEM	Gas Electron Multiplier
HLT	High-Level Trigger system
HV-MAPS	High-Voltage MAPS
IB	Inner Barrel
ITS	Inner Tracking System
LHC	Large Hadron Collider
LO	Leading Order
LS2	Long Shutdown 2
LVDS	Low-Voltage Differential Signaling
MAPS	Monolithic Active Pixel Sensor
MC	Monte Carlo
MFT	Muon Forward Tracker
MIP	Minimum Ionising Particle
MRPC	Multi-gap Resistive Plate Chamber
MWPC	Multi-Wire Proportional Chamber

NIEL	Non-Ionising Energy Loss
NLO	Next-to-Leading Order
OB	Outer Barrel
PCB	Printed Circuit Board
PDF	Parton Distribution Function
PID	Particle Identification
PS	Proton Synchrotron
RTN	Random Telegraph Noise
QCD	Quantum Chromodynamics
pQCD	perturbative Quantum Chromodynamics
QFT	Quantum Field Theory
QGP	Quark-Gluon Plasma
RHIC	Relativistic Heavy Ion Collider
RMS	Root Mean Square
R&D	Research and Development
SDD	Silicon Drift Detectors
SRS	Scalable Readout System
SPD	Silicon Pixel Detector
SRU	Scalable Readout Unit
SRS	Scalable Readout System
SSD	Silicon Strip Detector
STAR	Solenoidal Tracker at RHIC
TID	Total Ionising Dose
TN	Temporal Noise
TOF	Time-of-Flight detector
TPC	Time-Projection Chamber
TRD	Transition Radiation Detector
UDP	User Datagram Protocol
ZDC	Zero-Degree Calorimeter

E. Bibliography

[1]   K. A. Olive et al. "Review of Particle Physics". In: *Chin. Phys.* C38 (2014), p. 090001. DOI: 10.1088/1674-1137/38/9/090001.

[2]   W. J. Marciano and H. Pagels. "Quantum Chromodynamics: A Review". In: *Phys. Rept.* 36 (1978), p. 137. DOI: 10.1016/0370-1573(78)90208-9.

[3]   R. K. Ellis, W. J. Stirling and B. R. Webber. "QCD and Collider Physics". In: *Camb. Monogr. Part. Phys. Nucl. Phys. Cosmol.* 8 (1996), pp. 1–435.

[4]   N. Cabibbo and G. Parisi. "Exponential hadronic spectrum and quark liberation ". In: *Phys. Lett.* B59 (1975), pp. 67–69. DOI: 10.1016/0370-2693(75)90158-6.

[5]   J. C. Collins and M. J. Perry. "Superdense Matter: Neutrons or Asymptotically Free Quarks ?" In: *Phys. Rev. Lett.* 34.21 (1975), pp. 1353–1356. DOI: 10.1103/PhysRevLett.34.1353.

[6]   P. Braun-Munzinger and J. Stachel. "The quest for the quark-gluon plasma". In: *Nature* 448.7151 (2007), pp. 302–309. URL: http://dx.doi.org/10.1038/nature06080.

[7]   L. Evans and P. Bryant. "LHC Machine". In: *JINST* 3 (2008), S08001. DOI: 10.1088/1748-0221/3/08/S08001.

[8]   B. Müller, J. Schukraft and B. Wyslouch. "First Results from Pb+Pb collisions at the LHC". In: *Ann. Rev. Nucl. Part. Sci.* 62 (2012), pp. 361–386. DOI: 10.1146/annurev-nucl-102711-094910. arXiv: 1202.3233 [hep-ex].

[9]   A. Bazavov et al. "Equation of state in (2+1)-flavor QCD". In: *Phys. Rev.* D90.9 (2014), p. 094503. DOI: 10.1103/PhysRevD.90.094503. arXiv: 1407.6387 [hep-lat].

[10]   S. Borsanyi et al. "Full result for the QCD equation of state with 2+1 flavors". In: *Phys. Lett.* B730 (2014), pp. 99–104. DOI: 10.1016/j.physletb.2014.01.007. arXiv: 1309.5258 [hep-lat].

[11]   The ALICE Collaboration. "The ALICE experiment at the CERN LHC". In: *JINST* 3 (2008), S08002. DOI: 10.1088/1748-0221/3/08/S08002.

[12]   The ATLAS Collaboration. "The ATLAS Experiment at the CERN Large Hadron Collider". In: *JINST* 3 (2008), S08003. DOI: 10.1088/1748-0221/3/08/S08003.

[13]   The CMS Collaboration. "The CMS experiment at the CERN LHC". In: *JINST* 3 (2008), S08004. DOI: 10.1088/1748-0221/3/08/S08004.

[14]   The LHCb Collaboration. "The LHCb Detector at the LHC". In: *JINST* 3 (2008), S08005. DOI: 10.1088/1748-0221/3/08/S08005.

[15] D. J. Gross and F. Wilczek. "Ultraviolet Behavior of Non-Abelian Gauge Theories". In: *Phys. Rev. Lett.* 30.26 (1973), pp. 1343–1346. DOI: `10.1103/PhysRevLett.30.1343`.

[16] H. D. Politzer. "Reliable Perturbative Results for Strong Interactions?" In: *Phys. Rev. Lett.* 30.26 (1973), pp. 1346–1349. DOI: `10.1103/PhysRevLett.30.1346`.

[17] S. Bethke. "Experimental Tests of Asymptotic Freedom". In: *Prog. Part. Nucl. Phys.* 58 (2013), pp. 351–386. DOI: `10.1016/j.ppnp.2006.06.001`. arXiv: `hep-ex/0606035 [hep-ex]`.

[18] J. Kapusta, B. Müller and J. Rafelski. *Quark-Gluon Plasma: Theoretical Foundations.* Elsevier, 2003. ISBN: 0444511105.

[19] J. Bartke. *Introduction to Relativistic Heavy Ion Physics.* World Scientific, 2009. ISBN: 9810212313.

[20] W. Florkowski. *Phenomenology of Ultra-Relativistic Heavy-Ion Collisions.* World Scientific, 2010. ISBN: 9789814280662.

[21] V. Koch. "Aspects of chiral symmetry". In: *Int. J. Mod. Phys.* E6 (1997), pp. 203–250. DOI: `10.1142/S0218301397000147`. arXiv: `nucl-th/9706075 [nucl-th]`.

[22] A. Chodos et al. "Baryon Structure in the Bag Theory". In: *Phys. Rev.* D10 (1974), p. 2599. DOI: `10.1103/PhysRevD.10.2599`.

[23] T. A. DeGrand et al. "Masses and Other Parameters of the Light Hadrons". In: *Phys. Rev.* D12 (1975), p. 2060. DOI: `10.1103/PhysRevD.12.2060`.

[24] A. Andronic et al. "Hadron Production in Ultra-relativistic Nuclear Collisions: Quarkyonic Matter and a Triple Point in the Phase Diagram of QCD". In: *Nucl. Phys.* A837 (2010), pp. 65–86. DOI: `10.1016/j.nuclphysa.2010.02.005`. arXiv: `0911.4806 [hep-ph]`.

[25] J. Stachel et al. "Confronting LHC data with the statistical hadronization model". In: *J. Phys. Conf. Ser.* 509 (2014), p. 012019. DOI: `10.1088/1742-6596/509/1/012019`. arXiv: `1311.4662 [nucl-th]`.

[26] P. Braun-Munzinger et al. "Properties of hot and dense matter from relativistic heavy ion collisions". In: *submitted to Elsevier* (2015). arXiv: `1510.00442 [nucl-th]`.

[27] K. Adcox et al. "Formation of dense partonic matter in relativistic nucleus-nucleus collisions at RHIC: Experimental evaluation by the PHENIX collaboration". In: *Nucl. Phys.* A757 (2005), pp. 184–283. DOI: `10.1016/j.nuclphysa.2005.03.086`. arXiv: `nucl-ex/0410003 [nucl-ex]`.

[28] U. Heinz and R. Snellings. "Collective flow and viscosity in relativistic heavy-ion collisions". In: *Ann. Rev. Nucl. Part. Sci.* 63 (2013), pp. 123–151. DOI: `10.1146/annurev-nucl-102212-170540`. arXiv: `1301.2826 [nucl-th]`.

[29] P. Braun-Munzinger, K. Redlich and J. Stachel. "Particle production in heavy ion collisions". In: (2003). arXiv: nucl-th/0304013 [nucl-th].

[30] J. Schukraft. "Heavy ion physics at the Large Hadron Collider: what is new? What is next?" In: *Phys. Scripta* T158 (2013), p. 014003. DOI: 10.1088/0031-8949/2013/T158/014003. arXiv: 1311.1429 [hep-ex].

[31] The ALICE Collaboration. "Charged-Particle Multiplicity Density at Midrapidity in Central Pb–Pb Collisions at $\sqrt{s_{NN}} = 2.76$ TeV". In: *Phys. Rev. Lett.* 105 (25 Dec. 2010), p. 252301. DOI: 10.1103/PhysRevLett.105.252301.

[32] R. J. Glauber. "High-energy collision theory". In: *Lectures in Theoretical Physics* 1.315 (1959). Ed. by L. G. Dunham W. E. Brittin.

[33] M. L. Miller et al. "Glauber modeling in high energy nuclear collisions". In: *Ann. Rev. Nucl. Part. Sci.* 57 (2007), pp. 205–243. DOI: 10.1146/annurev.nucl.57.090506.123020. arXiv: nucl-ex/0701025 [nucl-ex].

[34] The ALICE Collaboration. "Freeze-out radii extracted from three-pion cumulants in pp, p–Pb and Pb–Pb collisions at the LHC". In: *Phys. Lett.* B739 (2014), pp. 139–151. DOI: http://dx.doi.org/10.1016/j.physletb.2014.10.034.

[35] The ALICE Collaboration. "Elliptic flow of identified hadrons in Pb–Pb collisions at $\sqrt{s_{\mathrm{NN}}} = 2.76$ TeV". In: *JHEP* 06 (2015), p. 190. DOI: 10.1007/JHEP06(2015)190. arXiv: 1405.4632 [nucl-ex].

[36] C. Shen et al. "Thermal photons as a quark-gluon plasma thermometer reexamined". In: *Phys. Rev.* C89 (2014), p. 044910. DOI: 10.1103/PhysRevC.89.044910.

[37] The ALICE Collaboration. "Direct photon production in Pb–Pb collisions at $\sqrt{s_{\mathrm{NN}}} = 2.76$ TeV". In: *Submitted to PLB* (2015). arXiv: 1509.07324 [nucl-ex].

[38] D. G. d'Enterria and D. Peressounko. "Probing the QCD equation of state with thermal photons in nucleus-nucleus collisions at RHIC". In: *EPJ* C46 (2006), pp. 451–464. DOI: 10.1140/epjc/s2006-02504-0. arXiv: nucl-th/0503054 [nucl-th].

[39] M. Gyulassy and M. Plümer. "Jet quenching in dense matter". In: *Phys. Lett.* B243 (1990), pp. 432–438. DOI: 10.1016/0370-2693(90)91409-5.

[40] R. Baier et al. "Radiative energy loss and p_{T}-broadening of high energy partons in nuclei". In: *Nucl. Phys.* B484 (1997), pp. 265–282. DOI: 10.1016/S0550-3213(96)00581-0.

[41] M. H. Thoma and M. Gyulassy. "Quark damping and energy loss in the high temperature QCD". In: *Nucl. Phys.* B351 (1991), pp. 491–506. DOI: 10.1016/S0550-3213(05)80031-8.

[42] E. Braaten and M. H. Thoma. "Energy loss of a heavy quark in the quark-gluon plasma". In: *Phys. Rev.* D44 (1991), R2625–R2630. DOI: 10.1103/PhysRevD.44.R2625.

[43] N. Armesto. "Nuclear shadowing". In: *J. Phys.* G32 (2006), R367–R394. DOI: 10.1088/0954-3899/32/11/R01. arXiv: hep-ph/0604108 [hep-ph].

[44] H. Fujii, F. Gelis and R. Venugopalan. "Quark pair production in high energy pA collisions: General features". In: *Nucl. Phys.* A780 (2006), pp. 146–174. DOI: 10.1016/j.nuclphysa.2006.09.012. arXiv: hep-ph/0603099 [hep-ph].

[45] Z.-B. Kang et al. "Multiple scattering effects on heavy meson production in p+A collisions at backward rapidity". In: *Phys. Lett.* B740 (2015), pp. 23–29. DOI: 10.1016/j.physletb.2014.11.024. arXiv: 1409.2494 [hep-ph].

[46] J. W. Cronin et al. "Production of hadrons with large transverse momentum at 200, 300, and 400 GeV". In: *Phys. Rev.* D11 (1975), pp. 3105–3123. DOI: 10.1103/PhysRevD.11.3105.

[47] R. Sharma, I. Vitev and B.-W. Zhang. "Light-cone wave function approach to open heavy flavor dynamics in QCD matter". In: *Phys. Rev.* C80 (2009), p. 054902. DOI: 10.1103/PhysRevC.80.054902. arXiv: 0904.0032 [hep-ph].

[48] A. Andronic et al. "Heavy-flavour and quarkonium production in the LHC era: from proton-proton to heavy-ion collisions". In: *Submitted to EPJC* (2015). arXiv: 1506.03981 [nucl-ex].

[49] J. Uphoff et al. "Heavy-quark production in ultrarelativistic heavy-ion collisions within a partonic transport model". In: *Phys. Rev.* C82 (2010), p. 044906. DOI: 10.1103/PhysRevC.82.044906. arXiv: 1011.6183.

[50] C.-M. Zhang B.-W.and Ko and W. Liu. "Thermal charm production in a quark-gluon plasma in Pb-Pb collisions at $\sqrt{s_{\mathrm{NN}}} = 5.5\,\mathrm{TeV}$". In: *Phys. Rev.* C77 (2008), p. 024901. DOI: 10.1103/PhysRevC.77.024901. arXiv: 0709.1684 [nucl-th].

[51] F. Liu and S. Liu. "Quark-gluon plasma formation time and direct photons from heavy ion collisions". In: *Phys. Rev.* C89.3 (2014), p. 034906. DOI: 10.1103/PhysRevC.89.034906. arXiv: 1212.6587 [nucl-th].

[52] Y. L. Dokshitzer and D. E. Kharzeev. "Heavy quark colorimetry of QCD matter". In: *Phys. Lett.* B519 (2001), pp. 199–206. DOI: 10.1016/S0370-2693(01)01130-3. arXiv: hep-ph/0106202 [hep-ph].

[53] N. Armesto, C. A. Salgado and U. A. Wiedemann. "Medium induced gluon radiation off massive quarks fills the dead cone". In: *Phys. Rev.* D69 (2004), p. 114003. DOI: 10.1103/PhysRevD.69.114003. arXiv: hep-ph/0312106 [hep-ph].

[54] M. Djordjevic and M. Gyulassy. "Heavy quark radiative energy loss in QCD matter". In: *Nucl. Phys.* A733 (2004), pp. 265–298. DOI: `10.1016/j.nuclphysa.2003.12.020`. arXiv: `nucl-th/0310076 [nucl-th]`.

[55] B.-W. Zhang, E. Wang and X.-N. Wang. "Heavy quark energy loss in nuclear medium". In: *Phys. Rev. Lett.* 93 (2004), p. 072301. DOI: `10.1103/PhysRevLett.93.072301`. arXiv: `nucl-th/0309040 [nucl-th]`.

[56] S. Wicks et al. "Heavy quark jet quenching with collisional plus radiative energy loss and path length fluctuations". In: *Nucl. Phys.* A783 (2007), pp. 493–496. DOI: `10.1016/j.nuclphysa.2006.11.102`. arXiv: `nucl-th/0701063 [nucl-th]`.

[57] N. Armesto et al. "Testing the color charge and mass dependence of parton energy loss with heavy-to-light ratios at RHIC and CERN LHC". In: *Phys. Rev.* D71 (2005), p. 054027. DOI: `10.1103/PhysRevD.71.054027`. arXiv: `hep-ph/0501225 [hep-ph]`.

[58] The ALICE Collaboration. "Centrality dependence of high-$p_{\rm T}$ D meson suppression in Pb–Pb collisions at $\sqrt{s_{NN}} = 2.76$ TeV". In: *Submitted to JHEP* (2015). arXiv: `1506.06604 [nucl-ex]`.

[59] The CMS Collaboration. "Suppression of non-prompt J/ψ, prompt J/ψ, and $\Upsilon(1S)$ in PbPb collisions at $\sqrt{s_{NN}} = 2.76$ TeV". In: *JHEP* 1205 (2012), p. 063. DOI: `10.1007/JHEP05(2012)063`. arXiv: `1201.5069 [nucl-ex]`.

[60] M. Djordjevic. "Heavy flavor puzzle at LHC: a serendipitous interplay of jet suppression and fragmentation". In: *Phys. Rev. Lett.* 112.4 (2014), p. 042302. DOI: `10.1103/PhysRevLett.112.042302`. arXiv: `1307.4702 [nucl-th]`.

[61] The ALICE Collaboration. "Transverse momentum dependence of D-meson production in Pb–Pb collisions at $\sqrt{s_{NN}} = 2.76$ TeV". In: (2015). arXiv: `1509.06888 [nucl-ex]`.

[62] The ALICE Collaboration. "Production of charged pions, kaons and protons at large transverse momenta in pp and Pb–Pb collisions at $\sqrt{s_{NN}} =2.76$ TeV". In: *Phys. Lett.* B736 (2014), pp. 196–207. DOI: `10.1016/j.physletb.2014.07.011`. arXiv: `1401.1250 [nucl-ex]`.

[63] The ALICE Collaboration. "Measurement of charm production at central rapidity in proton-proton collisions at $\sqrt{s} = 7$ TeV". In: *JHEP* 01 (2012), p. 128. DOI: `10.1007/JHEP01(2012)128`. arXiv: `1111.1553 [hep-ex]`.

[64] The ALICE Collaboration. "Technical Design Report for the Upgrade of the ALICE Inner Tracking System". In: *J. Phys.* G41 (2014), p. 087002. DOI: `10.1088/0954-3899/41/8/087002`. URL: `http://cds.cern.ch/record/1625842`.

[65] M. Cacciari et al. "Theoretical predictions for charm and bottom production at the LHC". In: *JHEP* 10 (2012), p. 137. DOI: `10.1007/JHEP10(2012)137`. arXiv: `1205.6344 [hep-ph]`.

[66]   M. Cacciari, M. L. Mangano and P. Nason. "Gluon PDF constraints from the ratio of forward heavy quark production at the LHC at $\sqrt{s} = 7$ and 13 TeV". In: *Eur. Phys. J.* C75 (2015), p. 610. DOI: `10.1140/epjc/s10052-015-3814-x`. arXiv: `1507.06197 [hep-ph]`.

[67]   E. Norrbin and T. Sjostrand. "Production and hadronization of heavy quarks". In: *EPJ* C17 (2000), pp. 137–161. DOI: `10.1007/s100520000460`. arXiv: `hep-ph/0005110 [hep-ph]`.

[68]   M. Cacciari, M. Greco and P. Nason. "The p_T spectrum in heavy flavor hadroproduction". In: *JHEP* 05 (1998), p. 007. DOI: `10.1088/1126-6708/1998/05/007`. arXiv: `hep-ph/9803400 [hep-ph]`.

[69]   M. Cacciari, S. Frixione and P. Nason. "The p_T spectrum in heavy flavor photoproduction". In: *JHEP* 03 (2001), p. 006. DOI: `10.1088/1126-6708/2001/03/006`. arXiv: `hep-ph/0102134 [hep-ph]`.

[70]   M. Cacciari, P. Nason and C. Oleari. "A Study of heavy flavored meson fragmentation functions in $e^+ e^-$ annihilation". In: *JHEP* 04 (2006), p. 006. DOI: `10.1088/1126-6708/2006/04/006`. arXiv: `hep-ph/0510032 [hep-ph]`.

[71]   P. M. Nadolsky et al. "Implications of CTEQ global analysis for collider observables". In: *Phys. Rev.* D78 (2008), p. 013004. DOI: `10.1103/PhysRevD.78.013004`. arXiv: `0802.0007 [hep-ph]`.

[72]   M. Artuso, E. Barberio and S. Stone. "*B* Meson Decays". In: *PMC Phys.* A3 (2009), p. 3. DOI: `10.1186/1754-0410-3-3`. arXiv: `0902.3743 [hep-ph]`.

[73]   N. Cabibbo. "Unitary Symmetry and Leptonic Decays". In: *Phys. Rev. Lett.* 10 (12 1963), pp. 531–533. DOI: `10.1103/PhysRevLett.10.531`.

[74]   M. Kobayashi and T. Maskawa. "CP Violation in the Renormalizable Theory of Weak Interaction". In: *Prog. Theor. Phys.* 49 (1973), pp. 652–657. DOI: `10.1143/PTP.49.652`.

[75]   G. Brandenburg et al. "Charged track multiplicity in B meson decay". In: *Phys. Rev.* D61 (2000), p. 072002. DOI: `10.1103/PhysRevD.61.072002`.

[76]   T. Sjöstrand, S. Mrenna and P. Skands. "PYTHIA 6.4 Physics and Manual". In: *JHEP* 05 (2006), p. 026. DOI: `10.1088/1126-6708/2006/05/026`. arXiv: `hep-ph/0603175 [hep-ph]`.

[77]   B. Hippolyte. "Bulk matter physics and its future at the Large Hadron Collider". In: *Hot Quarks 2008*. Ed. by EPJ. Vol. C62. 2008, pp. 237–242. DOI: `10.1140/epjc/s10052-009-0910-9`. arXiv: `0901.3176 [hep-ex]`.

[78]   The ATLAS Collaboration. "The ATLAS Experiment at the CERN Large Hadron Collider". In: *JINST* 3 (2008), S08003. DOI: `10.1088/1748-0221/3/08/S08003`.

[79] The ALICE TPC collaboration. "The ALICE TPC, a large 3-dimensional tracking device with fast readout for ultra-high multiplicity events". In: *NIM* A622.1 (2010), pp. 316–367. DOI: 10.1016/j.nima.2010.04.042. arXiv: 1001.1950 [physics.ins-det].

[80] The ALICE Collaboration. "Performance of the ALICE Experiment at the CERN LHC". In: *Int. J. Mod. Phys.* A29 (2014), p. 1430044. DOI: 10.1142/S0217751X14300440. arXiv: 1402.4476 [nucl-ex].

[81] G. Contin. "Performance of the present ALICE Inner Tracking System and studies for the upgrade". In: *JINST* 7 (2012), p. C06007. DOI: 10.1088/1748-0221/7/06/C06007.

[82] G. Aglieri Rinella, A. Kluge and F. Pancher. "Development and implementation of the level 0 Pixel Trigger System for the ALICE silicon pixel detector". In: *NSS/MIC 2007*. Vol. 3. 2007, pp. 2141–2144. DOI: 10.1109/NSSMIC.2007.4436576.

[83] V. Altini. "Trigger performance of the ALICE silicon pixel detector". In: *NIM* A650 (2011), pp. 30–32. DOI: 10.1016/j.nima.2010.11.167.

[84] The ALICE Collaboration. *Upgrade of the ALICE Time Projection Chamber.* Tech. rep. CERN-LHCC-2013-020. ALICE-TDR-016. Geneva: CERN, 2013. URL: http://cds.cern.ch/record/1622286.

[85] A. Akindinov et al. "Performance of the ALICE Time-Of-Flight detector at the LHC". In: *EPJ+* 128 (2013), p. 44. DOI: 10.1140/epjp/i2013-13044-x.

[86] P. Billoir. "Track Fitting with Multiple Scattering: A New Method". In: *NIM* A225 (1984), pp. 352–366. DOI: 10.1016/0167-5087(84)90274-6.

[87] P. Billoir, R. Frühwirth and M. Regler. "Track Element Merging Strategy and Vertex Fitting in Complex Modular Detectors". In: *NIM* A241 (1985), pp. 115–131. DOI: 10.1016/0168-9002(85)90523-6.

[88] M. Ivanov et al. "Track reconstruction in high density environment". In: *NIM* A566 (2006), pp. 70–74. DOI: 10.1016/j.nima.2006.05.029.

[89] Y. Belikov et al. "TPC tracking and particle identification in high density environment". In: *eConf* C0303241 (2003), TULT011. arXiv: physics/0306108 [physics].

[90] The ALICE Collaboration. "Particle identification in ALICE: a Bayesian approach". In: *submitted to EPJ+* (2016). arXiv: 1602.01392 [physics.data-an].

[91] The ALICE Collaboration. "Measurement of charm production at central rapidity in proton-proton collisions at $\sqrt{s} = 2.76$ TeV". In: *JHEP* 07 (2012), p. 191. DOI: 10.1007/JHEP07(2012)191. arXiv: 1205.4007 [hep-ex].

[92] The ALICE Collaboration. "D_s^+ meson production at central rapidity in proton–proton collisions at $\sqrt{s} = 7$ TeV". In: *Phys. Lett.* B718 (2012), pp. 279–294. DOI: 10.1016/j.physletb.2012.10.049. arXiv: 1208.1948 [hep-ex].

[93] The ALICE Collaboration. "Measurement of charm and beauty production at central rapidity versus charged-particle multiplicity in proton-proton collisions at $\sqrt{s} = 7$ TeV". In: *JHEP* 09 (2015), p. 148. DOI: 10.1007/JHEP09(2015)148. arXiv: 1505.00664 [nucl-ex].

[94] The ALICE Collaboration. "Measurement of prompt *D*-meson production in p–Pb collisions at $\sqrt{s_{NN}} = 5.02$ TeV". In: *Phys. Rev. Lett.* 113 (2014), p. 232301. DOI: 10.1103/PhysRevLett.113.232301. arXiv: 1405.3452 [nucl-ex].

[95] The ALICE Collaboration. "Suppression of high transverse momentum D mesons in central Pb–Pb collisions at $\sqrt{s_{NN}} = 2.76$ TeV". In: *JHEP* 09 (2012), p. 112. DOI: 10.1007/JHEP09(2012)112. arXiv: 1203.2160 [nucl-ex].

[96] The ALICE Collaboration. "D meson elliptic flow in non-central Pb–Pb collisions at $\sqrt{s_{NN}} = 2.76$TeV". In: *Phys. Rev. Lett.* 111 (2013), p. 102301. DOI: 10.1103/PhysRevLett.111.102301. arXiv: 1305.2707 [nucl-ex].

[97] The ALICE Collaboration. "Azimuthal anisotropy of D meson production in Pb–Pb collisions at $\sqrt{s_{\mathrm{NN}}} = 2.76$ TeV". In: *Phys. Rev.* C90 (2014), p. 034904. DOI: 10.1103/PhysRevC.90.034904. arXiv: 1405.2001 [nucl-ex].

[98] The ALICE Collaboration. "Measurement of D_s^+ production and nuclear modification factor in Pb–Pb collisions at $\sqrt{s_{\mathrm{NN}}} = 2.76$ TeV". In: (2015). arXiv: 1509.07287 [nucl-ex].

[99] D. J. Lange. "The EvtGen particle decay simulation package". In: *NIM* A462 (2001), pp. 152–155. DOI: 10.1016/S0168-9002(01)00089-4.

[100] The ALICE Collaboration. "Measurement of pion, kaon and proton production in proton–proton collisions at $\sqrt{s} = 7$ TeV". In: *EPJ* C75 (2015), p. 226. DOI: 10.1140/epjc/s10052-015-3422-9. arXiv: 1504.00024 [nucl-ex].

[101] The CMS Collaboration. "Transverse-momentum and pseudorapidity distributions of charged hadrons in *pp* collisions at $\sqrt{s} = 7$ TeV". In: *Phys. Rev. Lett.* 105 (2010), p. 022002. DOI: 10.1103/PhysRevLett.105.022002. arXiv: 1005.3299 [hep-ex].

[102] A. Rossi. private communication.

[103] G. Cramer. *Introduction A L'Analyse Des Lignes Courbes Algébriques*. Cramer and Philibert, 1750. URL: http://eudml.org/doc/203906.

[104] The ALICE Collaboration. "Centrality dependence of particle production in p-Pb collisions at $\sqrt{s_{\mathrm{NN}}} = 5.02$ TeV". In: *Phys. Rev.* C91 (2015), p. 064905. DOI: 10.1103/PhysRevC.91.064905. arXiv: 1412.6828 [nucl-ex].

[105] X.-N. Wang and M. Gyulassy. "HIJING : A Monte Carlo model for multiple jet production in *pp*, *pA*, and *AA* collisions". In: *Phys. Rev.* D44 (1991), pp. 3501–3516. DOI: 10.1103/PhysRevD.44.3501.

[106] R. Brun and F. Rademakers. "ROOT —An object oriented data analysis framework". In: *NIM* A389 (1997), pp. 81–86. DOI: 10.1016/S0168-9002(97)00048-X.

[107] T. Sjostrand, S. Mrenna and P. Z. Skands. "A Brief Introduction to PYTHIA 8.1". In: *Comput. Phys. Commun.* 178 (2008), pp. 852–867. DOI: 10.1016/j.cpc.2008.01.036. arXiv: 0710.3820 [hep-ph].

[108] The ALICE Collaboration. "Measurement of visible cross sections in proton-lead collisions at $\sqrt{s_{NN}} = 5.02$ TeV in van der Meer scans with the ALICE detector". In: *JINST* 9 (2014), P11003. DOI: 10.1088/1748-0221/9/11/P11003. arXiv: 1405.1849 [nucl-ex].

[109] The ALICE Collaboration. "Upgrade of the ALICE Experiment: Letter Of Intent". In: *J. Phys.* G41 (2014), p. 087001. DOI: 10.1088/0954-3899/41/8/087001. URL: http://cds.cern.ch/record/1475243.

[110] J. M. Jowett, M. Schaumann and R. Versteegen. "Heavy ion operation from run 2 to HL-LHC". In: *RLIUP: Review of LHC and Injector Upgrade Plans* (2014). DOI: 10.5170/CERN-2014-006.167. URL: https://cds.cern.ch/record/1977371.

[111] The ALICE Collaboration. *Upgrade of the Inner Tracking System Conceptual Design Report.* Tech. rep. CERN-LHCC-2012-013. LHCC-P-005. Geneva: CERN, 2012. URL: http://cds.cern.ch/record/1475244.

[112] The ALICE Collaboration. *Upgrade of the ALICE Readout & Trigger System.* Tech. rep. CERN-LHCC-2013-019. ALICE-TDR-015. Geneva: CERN, 2013. URL: http://cds.cern.ch/record/1592659.

[113] The ALICE Collaboration. *Technical Design Report for the Muon Forward Tracker.* Tech. rep. CERN-LHCC-2015-001. ALICE-TDR-018. Geneva: CERN, Jan. 2015. URL: http://cds.cern.ch/record/1981898.

[114] The ALICE Collaboration. *Addendum to the Technical Design Report for the Upgrade of the ALICE Time Projection Chamber.* Tech. rep. CERN-LHCC-2015-002. ALICE-TDR-016-ADD-1. Geneva: CERN, 2015. URL: http://cds.cern.ch/record/1984329.

[115] The ALICE Collaboration. *Technical Design Report for the Upgrade of the Online-Offline Computing System.* Tech. rep. CERN-LHCC-2015-006. ALICE-TDR-019. Geneva: CERN, 2015. URL: http://cds.cern.ch/record/2011297.

[116] L. Musa. private communication.

[117] The ATLAS Collaboration. *Letter of Intent for the Phase-II Upgrade of the ATLAS Experiment.* Tech. rep. CERN-LHCC-2012-022. LHCC-I-023. Geneva: CERN, 2012. URL: http://cds.cern.ch/record/1502664.

[118] J. Schambach et al. "A MAPS Based Micro-Vertex Detector for the STAR Experiment". In: *Phys. Procedia* 66 (2015), pp. 514–519. DOI: 10.1016/j.phpro.2015.05.067.

[119] L. Greiner et al. "A MAPS based vertex detector for the STAR experiment at RHIC". In: *NIM* A650 (2011), pp. 68–72. DOI: 10.1016/j.nima.2010.12.006.

[120] URL: www.jazzsemi.com.

[121] H. Hillemanns et al. "Radiation hardness and detector performance of new 180nm CMOS MAPS prototype test structures developed for the upgrade of the ALICE Inner Tracking System". In: *IEEE NSS/MIC* (2013). DOI: 10.1109/NSSMIC.2013.6829475.

[122] W. R. Leo. *Techniques for nuclear and particle physics experiments: a how-to approach.* 2nd ed. Berlin: Springer, 1994. ISBN: 0387572805. DOI: 10.1007/978-3-642-57920-2. URL: http://cds.cern.ch/record/302344.

[123] K. Kleinknecht. *Detectors for Particle Radiation.* 2nd ed. Cambridge, Univ. Press, 1998. ISBN: 0521648548.

[124] L. Landau. "On the energy loss of fast particles by ionization". In: *J. Phys.(USSR)* 8 (1944), pp. 201–205.

[125] H. Bichsel. "Straggling in thin silicon detectors". In: *Rev. Mod. Phys.* 60 (3 1988), pp. 663–699. DOI: 10.1103/RevModPhys.60.663.

[126] W. Snoeys. "Monolithic pixel detectors for high energy physics". In: *NIM* A731 (2013), pp. 125–130. DOI: 10.1016/j.nima.2013.05.073.

[127] W. Shockley. "Currents to Conductors Induced by a Moving Point Charge". In: *J. Appl. Phys.* 9 (1938), pp. 635–636. DOI: 10.1063/1.1710367.

[128] S. Ramo. "Currents induced by electron motion". In: *Proc. Ire.* 27 (1939), pp. 584–585. DOI: 10.1109/JRPROC.1939.228757.

[129] L. Rossi et al. *Pixel Detectors.* Springer-Verlag, 2006. ISBN: 9783540283324. DOI: 10.1007/3-540-28333-1.

[130] J. W. van Hoorne. "Study and Development of a Novel Silicon Pixel Detector for the Upgrade of the ALICE Inner Tracking System". PhD thesis. CERN-THESIS-2015-255: TU Wien, 2015. URL: https://cds.cern.ch/record/2119197.

[131] H. Spieler. *Semiconductor detector systems.* Oxford Univ. Press, 2005. DOI: 10.1093/acprof:oso/9780198527848.001.0001.

[132] I. Perić. "A novel monolithic pixelated particle detector implemented in high-voltage CMOS technology". In: *NIM* A582 (Dec. 2007), pp. 876–885. DOI: http://dx.doi.org/10.1016/j.nima.2007.07.115.

[133] I. Perić et al. "Overview of HVCMOS pixel sensors". In: *JINST* 10 (2015), p. C05021. DOI: 10.1088/1748-0221/10/05/C05021.

[134] S. M. Sze and Kwok. K. Ng. *Physics of Semiconductor Devices*. 3rd Edition. Wiley, 2006. ISBN: 978-0-471-14323-9. DOI: 10.1002/0470068329.

[135] G. Deptuch. "New Generation of Monolithic Active Pixel Sensors for Charged Particle Detection". Theses. Université Louis Pasteur - Strasbourg I, Sept. 2002. URL: https://tel.archives-ouvertes.fr/tel-00011109.

[136] M. Kofarago. "under preparation". PhD thesis. Universiteit Utrecht, 2016.

[137] D. Kim et al. "Front-end Optimization for the Monolithic Active Pixel Sensor of the ALICE Inner Tracking System upgrade". to be published in: TWEPP 2015 conference proceedings. 2016.

[138] J. M. Miller. "Dependence of the input impedance of a three-electrode vacuum tube upon the load in the plate circuit". In: *Scientific Papers of the Bureau of Standards* 15 (1920), pp. 367–385. URL: http://web.mit.edu/klund/www/papers/jmiller.pdf.

[139] U. Tietze, C. Schenk and E. Gamm. *Halbleiter-Schaltungstechnik*. 14. Aufl. Springer, 2012. ISBN: 9783642310256.

[140] R. J. Baker. *CMOS Circuit Design, Layout, and Simulation*. 3rd Ed. Wiley, IEEE Press, 2010. ISBN: 9780470881323. DOI: 10.1002/9780470891179.

[141] P. Yang et al. "Low-power priority Address-Encoder and Reset-Decoder data-driven readout for Monolithic Active Pixel Sensors for tracker system". In: *NIM* A785 (2015), pp. 61–69. DOI: http://dx.doi.org/10.1016/j.nima.2015.02.063.

[142] H. Perrey. "EUDAQ and EUTelescope: Software Frameworks for Test Beam Data Acquisition and Analysis". In: *PoS* TIPP2014 (2014), p. 353.

[143] URL: https://eudaq.github.io.

[144] URL: http://eutelescope.web.cern.ch.

[145] H. Tian, B. Fowler and A. E. Gamal. "Analysis of temporal noise in CMOS photodiode active pixel sensor". In: *IEEE Journal of Solid-State Circuits* 36 (2001), pp. 92–101. DOI: 10.1109/4.896233.

[146] C. Kleinwort. "General Broken Lines as advanced track fitting method". In: *NIM* A673 (2012), pp. 107–110. DOI: 10.1016/j.nima.2012.01.024. arXiv: 1201.4320 [physics.ins-det].

[147] K. K. Hung et al. "Random telegraph noise of deep-submicrometer MOSFETs". In: *Electron Device Letters, IEEE* 11 (1990), pp. 90–92. DOI: 10.1109/55.46938.

[148] M. Deveaux. "Development of fast and radiation hard Monolithic Active Pixel Sensors (MAPS) optimized for open charm meson detection with the CBM - vertex detector". PhD thesis. 2007.

[149] M. Deveaux et al. "Random telegraph signal in monolithic active pixel sensors". In: *IEEE NSS/MIC/RTSD*. 2008, pp. 3098–3105. DOI: 10.1109/NSSMIC. 2008.4775010.

[150] A. Lahav et al. "Optimization of random telegraph noise non uniformity in a CMOS pixel with a pinned-photodiode". In: *Proc. Int. Image Sens. Workshop*. 2007, pp. 230–234.

[151] R. Brun et al. *GEANT 3: user's guide Geant 3.10, Geant 3.11; rev. version*. CERN-DD-EE-84-01. CERN, 1987. URL: http://cds.cern.ch/record/ 1119728.

[152] The CMS Collaboration. "Measurement of the B^0 production cross section in pp Collisions at $\sqrt{s} = 7$ TeV". In: *Phys. Rev. Lett.* 106 (2011), p. 252001. DOI: 10.1103/PhysRevLett.106.252001. arXiv: 1104.2892 [hep-ex].

[153] The CMS Collaboration. "Measurement of the B^+ Production Cross Section in pp Collisions at $\sqrt{s} = 7$ TeV". In: *Phys. Rev. Lett.* 106 (2011), p. 112001. DOI: 10.1103/PhysRevLett.106.112001. arXiv: 1101.0131 [hep-ex].

[154] URL: http://alidoc.cern.ch/.

[155] URL: http://aliroot-docs.web.cern.ch/.

[156] URL: http://rd51-public.web.cern.ch/RD51-Public/.

[157] S. Martoiu et al. "Development of the scalable readout system for micro-pattern gas detectors and other applications". In: *JINST* 8 (2013), p. C03015. DOI: 10.1088/1748-0221/8/03/C03015.

[158] S. Martoiu, H. Müller and J. Toledo. "Front-end electronics for the Scalable Readout System of RD51". In: *Proceedings, 2011 IEEE Nuclear Science Symposium and Medical Imaging Conference (NSS/MIC 2011)*. 2011, pp. 2036–2038. DOI: 10.1109/NSSMIC.2011.6154414.

[159] URL: https://espace.cern.ch/rd51-wg5/srs/default.aspx.

[160] J. Toledo et al. "The Front-End Concentrator card for the RD51 Scalable Readout System". In: *JINST* 6 (2011), p. C11028. DOI: 10.1088/1748-0221/6/11/C11028.

[161] URL: https://espace.cern.ch/rd51-wg5/srs/Documentation/SRS_ Slow_Control_Manual.pdf.

[162] URL: http://www.eudet.org/e26/e28/e42441/e57298/EUDET-MEMO-2009-04.pdf.

[163] URL: https://git.cern.ch/web/alice-its-upgrade-srs-software. git.

Acknowledgements

First and foremost, I want to thank Prof. Dr. Johanna Stachel for supervising my PhD thesis and giving me the opportunity to work in this exciting field. Second, I am grateful to Dr. Luciano Musa, my supervisor at CERN, for his guidance, the discussions and the opportunity to become part of the ITS upgrade team. I am thankful to Prof. Dr. Peter Fischer, who agreed to be the second referee of this thesis.

I would like to thank Dr. Magnus Mager very much for all the fruitful discussions, advice and critical assessment of my ideas and work, not only on the pixel-chip characterisation. I am grateful to Dr. Andrea Rossi for the supervision of my D^0 analysis, the related upgrade study and all the enlightening discussions.
During my work on the ITS upgrade characterisation and the D^0 analysis, I collaborated with many people. I would like to thank all members and especially the conveners for the discussions and feedback within the context of the ITS Upgrade WP5, WP1&2 and the PWG-HF as well as the PAG-D2H. I owe many thanks to Dr. Jacobus van Hoorne, who closely collaborated with me on the pixel-chip characterisation, for all the fruitful discussions and his support. I would like to thank Michael Winn very much for all the enlightening discussions on heavy-ion physics and analysis-related topics. Many thanks go to PD Dr. Markus Keil for his help with the full-scale prototypes. I wish to thank all colleagues who participated in the test beams and in particular Dr. Paolo Martinengo as our test-beam coordinator. I would like to express my gratitude to Dr. Walter Snoeys and Dr. Thanushan Kugathasan for always being available to discuss my questions concerning the pixel chips. I want to thank Mónika Kőfaragó for introducing me to the test-beam data analysis using EUTelescope. Thanks go to Johannes Stiller, Dr. Zaida Consesa del Valle and Dr. Francesco Prino for discussions concerning the D^0 analysis and technical support. I appreciated the interesting discussions on physics analysis with Dr. Jochen Klein and Dr. Alexander Kalweit. Many thanks go to Dr. Hans Müller and his RD51 colleagues for their precious help with the SRS. I would like to thank my office mates Adam Szczepankiewicz, Andrés Sánchez González, Krzysztof Sielewicz and all my colleagues at CERN and from the Heidelberg group for providing a great working atmosphere.

For proofreading and discussions concerning my thesis, I would like to thank Michael Winn, Dr. Jochen Klein, Dr. Jacobus van Hoorne, Dr. Andrea Rossi, Dr. Magnus Mager, Dr. Hartmut Hillemanns, PD Dr. Markus Keil, Prof. Dr. Peter Glässel, PD Dr. Kai Schweda, Dr. Walter Snoeys, Prof. Dr. Klaus Reygers, Dr. Thanushan Kugathasan, Krzysztof Sielewicz and Mónika Kőfaragó.

Last but not least, I want to thank my family and friends, especially Eléonore, for their support and never-ending patience.